Springer Series in Materials Science 175

Bekir Aktaş
Faik Mikailzade *Editors*

Nanostructured Materials for Magnetoelectronics

Springer

Springer Series in Materials Science

Volume 175

For further volumes:
www.springer.com/series/856

The Springer Series in Materials Science covers the complete spectrum of materials physics, including fundamental principles, physical properties, materials theory and design. Recognizing the increasing importance of materials science in future device technologies, the book titles in this series reflect the state-of-the-art in understanding and controlling the structure and properties of all important classes of materials.

Bekir Aktaş • Faik Mikailzade
Editors

Nanostructured Materials for Magnetoelectronics

Springer

Editors
Bekir Aktaş
Department of Physics
Gebze Institute of Technology
Gebze-Kocaeli, Turkey

Faik Mikailzade
Department of Physics
Gebze Institute of Technology
Gebze-Kocaeli, Turkey

ISSN 0933-033X Springer Series in Materials Science
ISBN 978-3-642-34957-7 ISBN 978-3-642-34958-4 (eBook)
DOI 10.1007/978-3-642-34958-4
Springer Heidelberg New York Dordrecht London

Library of Congress Control Number: 2013930538

Printed on acid-free paper

Springer is part of Springer Science+Business Media (www.springer.com)

Preface

The research and development of nanoscale magnetic materials is one of the most promising fields in today's science and is a base for new branches of high-tech industry. In recent decades intensive investigations in this field have promoted great progress in the technological applications of magnetism in various areas. Nanoscale magnetic materials exhibit new and interesting physical properties that cannot be found in the bulk matter. Many of these unique properties have high potential for technical applications in magnetic storage media, magnetic heads of computer hard disk drives, single-electron devices, microwave electronic devices, and magnetic sensors. New terminologies, such as magnetoelectronics and spintronics, have recently been introduced to refer to aspects of the field involving magnetic phenomena at the nanoscale.

The technical progress of recent years involved the preparation of multilayer thin films and nanowires, resulting in the discovery of the giant magnetoresistance (GMR) and tunnel magnetoresistance (TMR) phenomena, consisting in an extraordinary change in the resistance/impedance of a material on application of an external magnetic field. GMR and TMR materials have already found applications as sensors of low magnetic fields, computer hard disk read heads, magnetoresistive random access memory (RAM) chips, etc. The most recent investigations in the field of magnetic nanostructured materials introduced the new progressive field of spintronic devices, which utilize not only the electrical charge but also the spin of electrons and optical spin manipulation.

The dynamic behavioral features of magnetic nanostructures, especially the speed of magnetization reversal and the physical limitations, are crucial issues in magnetic data storage and spintronics, as they determine the functionality and frequency response of devices. The need to increase the data transfer rates in magnetic mass storage devices pushes the relevant switching frequencies far into the gigahertz (GHz) regime. The enormous power dissipation in current semiconductor-based microprocessors has resulted in a search for low-power alternatives, for example, magnetic logic circuits, which provide the advantage of an inherent data non-volatility. The successful operation of future "magnetic processors" at GHz frequencies must

be based on careful control and tuning of the microscopic mechanisms governing the magnetic switching process.

During the last decade, spin-transfer torque physics has attracted much scientific interest after the transfer of spin momentum by spin-polarized currents was predicted and observed in the wake of the seminal discovery of GMR, which kicked off the fast-paced development of spintronics. Whereas the GMR effect is well suited for sensing and detecting magnetization states, the spin-transfer torque provides a means to act on the magnetization, thus complementing GMR and extending the toolbox for spintronics.

There are two different approaches for realizing spintronic devices. One is metal-based spintronics which uses ferromagnetic metals. The second one is semiconductor-based spintronics consisting of ferromagnetic semiconductors, for which much effort has focused on producing ferromagnetism in semiconductors above room temperature. If successful, this new class of spintronic devices could be integrated much more easily with conventional semiconductor technology. The key requirement in the development of such devices is the efficient injection, transfer, and detection of spin-polarized current from a ferromagnetic material into a semiconductor. Because of the well-known problem of a resistance mismatch at metal/semiconductor interfaces, hindering an effective spin injection, much interest is now concentrated on the development of room-temperature ferromagnetic semiconductors.

In recent years there has been a considerably growing interest in multilayered GMR nanostructures due to their wide magnetoelectronics applications. Obviously, the magnetic anisotropy and interlayer exchange coupling play the most important roles in these structures. Oscillatory interlayer exchange coupling between ferromagnetic layers is an indirect exchange interaction of localized spins in magnetic layers mediated by conducting electrons of nonmagnetic spacers. As the need for ultra high density data recording increases, the size of the films used in spintronic applications must decrease. Therefore, accurate magnetic characterization is one of the major issues related to magnetic multilayer structures.

Another important field is that of interfacial phenomena in perovskite oxide superlattices, which have the potential to provide unique functional properties for a diverse range of applications, including sensing, energy conversion, and information technology. In these systems, the antiferromagnetic and ferromagnetic order parameters display dissimilar dependences on sublayer thickness and temperature due to the competition between different magnetic interactions. For a small range of sublayer thicknesses, a robust spin-flop coupling is observed such that the alignment of the magnetization of the ferromagnetic layer with a magnetic field leads to the reorientation of the magnetic moments in the antiferromagnetic layer to maintain the proper orientation between different moments.

The science and technology of functional nanostructured materials received great impetus by the ability to produce structures on a sub-micrometer scale. Nanofabrication and nanotechnology allowed the manipulation of materials and the engineering of innovative materials and devices, both for fundamental studies and for applications in various fields. One of the major obstacles in the miniaturization of

nanoelectronic devices has been the fabrication of interconnects having diameters compatible with the size of the devices they connect. In solid state electronics as well as in nanoelectronics, interconnecting nano or molecular devices has remained a challenge for several decades. Although the search for feasible interconnects in nanoelectronics is continuing, nanosized Si nanowires appear to be an attractive 1D material because of their well-known silicon-based microelectronic fabrication technology and their ability to be used directly on the Si-based chips. Electronic and spintronic devices with conducting interconnects between them can be fabricated on a single Si nanowire at a desired order.

One of the most effective methods of nanotechnology and nanofabrication is the self-assembling of nanoparticles or nanospheres, a low-cost alternative patterning technology particularly well suited to the preparation of arrays of dots or antidots covering a surface area of several square millimeters (mm^2) or larger. While nanoparticles with a sharp size (diameter) distribution can be synthesized by several bottom-up chemical processes, and can even be functionalized for different purposes, their dispersion over large substrates results in well-ordered, short-range periodic templates, with a lack of long-range order and without a precise orientation on the macroscopic scale of the whole sample, of the periodic structure. Self-assembling of polystyrene nanospheres is a powerful technique to prepare large area (several mm^2) nanostructured thin films. Compared to conventional lithographic techniques, which have more resolution and are more versatile, but are limited to very small surface areas, self-assembling of polystyrene nanospheres allows the preparation of large nanostructured samples. This technique limits the shaping to only circular dot and antidot geometries which can be obtained in a hexagonal close-packed configuration.

Another prospective field for research and application of magnetic nanostructures is the fabrication and investigation of magnetic nanoparticles for biomedical applications. Magnetic nanoparticle hyperthermia (MNH) treatment of tumors is at an advanced stage of development; it has been through phase I human clinical trials and is currently being tested in phase II in combination with other therapies. Currently the use of MNH for the treatment of tumors is restricted by the heating performance of the available nanoparticle ferrofluids. Although a massive amount of important biochemical and clinical work is also required to develop this therapy, the heating issue is fundamental and must be solved. Of course, this is just the start of the process, as the magnetic nanoparticles must be made biocompatible, hidden from the immune system, targeted, tested in vivo, etc., but it is clear that MNH will be able to make significant strides towards becoming a stand-alone treatment, and that it is potentially a very low morbidity and generic therapy.

This book is intended to provide a review of the latest developments and the fundamental concepts in the above-mentioned fields of research and application of nanostructured magnetic materials as well as in the emerging fields of magnetoelectronics and spintronics. The idea for this book was born at the Fifth International Conference on Nanoscale Magnetism (ICNM-2010) held on September 28–October 2, 2010 in Gebze-Istanbul, Turkey. The meeting was organized by the Department of Physics of the Gebze Institute of Technology (GIT). The scope of the

contributions extends from fundamental magnetic properties at the nanometer scale to fabrication and characterization of nanoscale magnetic materials and structures as well as the physics behind the behavior of these structures.

We would like to thank all the authors for their contributions. We also acknowledge the great efforts of our collaborators and research fellows from the Department of Physics and Nanomagnetism and Spintronics Research Center (NASAM) of GIT and others who made major contributions to the organization of the ICNM-2010 Conference and made this publication possible. We are very grateful to Prof. C. Ascheron for his great support, help, and patience during the publishing of this book.

Gebze-Kocaeli, Turkey B. Aktaş
F. Mikailzade

Contents

Contributors

Numan Akdoğan Department of Physics, Gebze Institute of Technology, Kocaeli, Turkey

Bekir Aktaş Department of Physics, Gebze Institute of Technology, Gebze-Kocaeli, Turkey

Chris Binns Department of Physics and Astronomy, University of Leicester, Leicester, UK

Luca Boarino Electromagnetics Division, INRIM, Torino, Italy

Daniel Bürgler Peter Grünberg Institut, Electronic Properties (PGI-6) and Jülich-Aachen Research Alliance, Fundamentals for Future Information Technology (JARA-FIT), Research Center Jülich GmbH, Jülich, Germany

Federica Celegato Electromagnetics Division, INRIM, Torino, Italy

Salim Ciraci UNAM-Institute of Materials Science and Nanotechnology, Bilkent University, Ankara, Turkey; Department of Physics, Bilkent University, Ankara, Turkey

Marco Coïsson Electromagnetics Division, INRIM, Torino, Italy

Natascia De Leo Electromagnetics Division, INRIM, Torino, Italy

Engin Durgun UNAM-Institute of Materials Science and Nanotechnology, Bilkent University, Ankara, Turkey

Mustafa Erkovan Department of Physics, Gebze Institute of Technology, Gebze-Kocaeli, Turkey

Riccardo Hertel Peter Grünberg Institut, Electronic Properties (PGI-6) and Jülich-Aachen Research Alliance, Fundamentals for Future Information Technology (JARA-FIT), Research Center Jülich GmbH, Jülich, Germany; Institut de Physique et Chimie des Matériaux de Strasbourg, CNRS UMR 7504, Université de Strasbourg, Strasbourg, France

Atilla Kákay Peter Grünberg Institut, Electronic Properties (PGI-6) and Jülich-Aachen Research Alliance, Fundamentals for Future Information Technology (JARA-FIT), Research Center Jülich GmbH, Jülich, Germany

Ronald Lehndorff Peter Grünberg Institut, Electronic Properties (PGI-6) and Jülich-Aachen Research Alliance, Fundamentals for Future Information Technology (JARA-FIT), Research Center Jülich GmbH, Jülich, Germany; Sensitec GmbH, Mainz, Germany

Mustafa Özdemir Department of Physics, Faculty of Science and Letters, Marmara University, Istanbul, Turkey

Claus Schneider Peter Grünberg Institut, Electronic Properties (PGI-6) and Jülich-Aachen Research Alliance, Fundamentals for Future Information Technology (JARA-FIT), Research Center Jülich GmbH, Jülich, Germany

Volker Sluka Peter Grünberg Institut, Electronic Properties (PGI-6) and Jülich-Aachen Research Alliance, Fundamentals for Future Information Technology (JARA-FIT), Research Center Jülich GmbH, Jülich, Germany; Institute of Ion Beam Physics and Materials Research, Helmholtz-Zentrum Dresden-Rossendorf e.V., Dresden, Germany

Yayoi Takamura Department of Chemical Engineering and Materials Science, University of California at Davis, Davis, CA, USA

Paola Tiberto Electromagnetics Division, INRIM, Torino, Italy

Ramazan Topkaya Department of Physics, Gebze Institute of Technology, Gebze-Kocaeli, Turkey

Franco Vinai Electromagnetics Division, INRIM, Torino, Italy

Hartmut Zabel Institut für Experimentalphysik/Festkörperphysik, Ruhr-Universität Bochum, Bochum, Germany

Chapter 1
From Magnetodynamics to Spin Dynamics in Magnetic Heterosystems

Claus M. Schneider

Abstract The dynamic behavior of magnetic systems covers a broad range of length and time scales and is of both fundamental interest and technological relevance. The particular challenge in magnetic heterosystems is the need to disentangle the responses of the individual magnetic and chemical components. In this contribution we discuss the results of two complementary experimental approaches addressing element-selective magnetization and spin dynamics. Time-resolved X-ray photoemission electron microscopy (TR-XPEEM) is employed to image the temporal evolution of the magnetization in interlayer exchange-coupled trilayers in the picosecond regime with high lateral resolution. In order to address the femtosecond time scale with element selectivity, we developed a novel pump-probe magneto-optical Kerr effect (MOKE) technique involving higher harmonic generation (HHG) in the extreme ultraviolet regime. We are able to map the spin dynamics of the individual constituents in Permalloy ($Ni_{80}Fe_{20}$) with a time resolution of better than 100 fs. Combining PEEM with HHG excitation may pave the way to an element-selective magnetic imaging technique in the lab offering femtosecond time resolution.

1.1 Introduction

The dynamic behavior of magnetic systems involves a wide variety of physical phenomena and covers a broad range of time scales of more than 23 orders of magnitude. Moreover, this enormous dynamic range is also of high technological relevance. The long-term end of the time axis is marked by the data storage retention time defined by the magnetic storage industry. It relates to the thermal stability of a written bit of information for a period of at least 10 years. Another technologically important regime is located between 10^{-9} and 10^{-12} s and governs fast magnetic

C.M. Schneider (✉)
Peter Grünberg Institut (PGI-6), Forschungszentrum Jülich, 52425 Jülich, Germany
e-mail: c.m.schneider@fz-juelich.de

C.M. Schneider
Fakultät f. Physik und CENIDE, Universität Duisburg-Essen, 47048 Duisburg, Germany

B. Aktaş, F. Mikailzade (eds.), *Nanostructured Materials for Magnetoelectronics*, Springer Series in Materials Science 175, DOI 10.1007/978-3-642-34958-4_1,

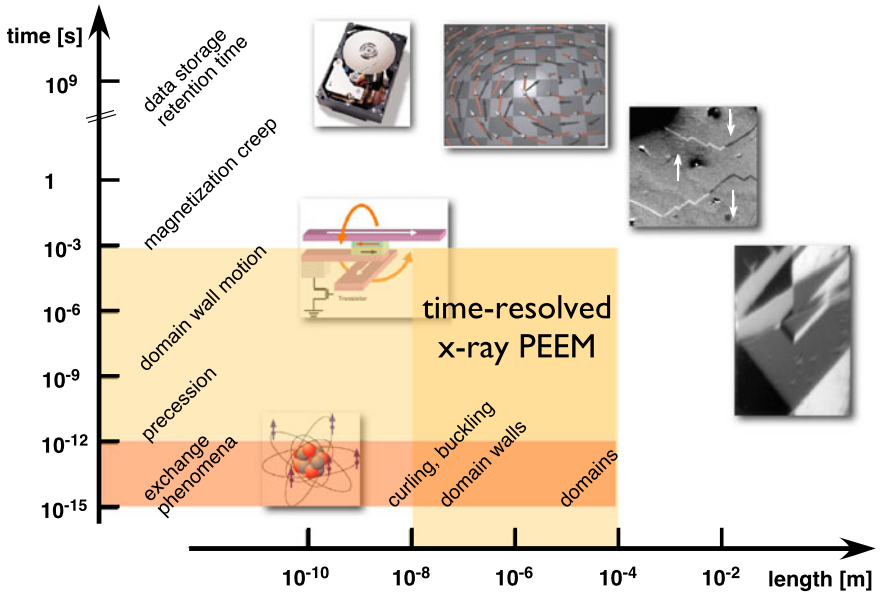

Fig. 1.1 Time and length scales in magnetization and spin dynamics. The *lightly shaded area* marks the region accessible in X-ray photoemission microscopy. The *darker shading* marks a possible extension into the femtosecond region

switching processes (Fig. 1.1). The speed in magnetization reversal and particularly its physical limitations are crucial issues in magnetic data storage and spintronics, as they determine the functionality and frequency response of hard disk drive systems and other devices [1, 2]. The need to increase the data transfer rates in magnetic mass storage devices pushes the relevant switching frequencies far into the gigahertz (GHz) regime. The enormous power dissipation in current semiconductor-based microprocessors spurs the search for low-power alternatives, for example, magnetic logic circuits which provide the advantage of an inherent data non-volatility [3]. The successful operation of future "magnetic processors" at GHz frequencies must be based on a careful control and tuning of the microscopic mechanisms governing the magnetic switching process.

Beyond these technological issues it is particularly the regime of short and ultrashort time scales which combines interesting scientific perspectives with considerable challenges. Pushing the speed of magnetization reversal to its physical limits is only possible if reversal or precessional processes on the nano- and picosecond time scales are understood in detail [4]. However, this understanding will be incomplete without an exploration of the nature of magnetic damping effects [5]. Of specific importance for the details of the dynamic response is also the nature of the excitation, either in the classical manner via a magnetic field pulse, or via spin-transfer torque phenomena involving a spin-polarized current [6].

The femtosecond regime becomes accessible by means of ultrashort-pulse laser sources, which have matured into convenient table-top systems nowadays. The laser

pulses may be employed to strongly excite the electronic system of a sample on a time scale of less than 100 fs [7]. Extending studies of spin and magnetization dynamics into the femtosecond regime has two consequences. First, spin and electron dynamics are intimately connected and can no longer be treated separately. Second, this interplay may open new channels for energy and angular momentum transfer processes. In this limit, the magnetization $\mathbf{M}(\mathbf{r})$ can no longer be represented by a vector of constant length $|\mathbf{M}|$. In order to capture the influence of finite temperature, for example, during ultrafast demagnetization experiments, the vector field $\mathbf{M}(\mathbf{r}, \mathbf{t})$ must include variations of *both* direction and length of the local magnetization vector. Since the pioneering experiments on Ni [8] which revealed an ultrafast demagnetization on the 100 fs time scale driven by strong optical pump pulses, most of the studies have focused on this phenomenon and the underlying microscopic processes. A variety of mechanisms have been invoked, ranging from phonon-, electron-, and magnon-mediated spin-flip processes [9–13], through direct laser-induced spin flips [14] or relativistic spin-light interaction [15] to superdiffusive spin transport [16]. Recently some results appeared which demonstrated a certain control of the magnetization direction by ultrashort light pulses [17–20]. Although the underlying mechanisms still need to be clarified, ultrafast optical switching of magnetic elements may come within reach.

Magnetic heterosystems form the basis for technological magnetic and spintronic devices [21]. Their inherent chemical and magnetic complexity, which also creates coupling phenomena on different length scales, poses another challenge to dynamic studies. In this case we need to disentangle the dynamic responses of the individual magnetic and chemical components in the heterosystems. However, it is generally accepted that even in chemically and magnetically simple confined systems the macrospin picture is often not sufficient to fully describe the dynamic response [22]. This is due to nonuniform magnetization distributions in the transient states or already in the ground state. In order to map the behavior of the magnetization distribution, spatially resolving techniques are needed, and they must be paired with element or chemical selectivity to discriminate the contributions of the individual chemical and magnetic constituents in the heterosystems.

In this contribution we will focus on X-ray photoemission electron microscopy (XPEEM), which has matured into a high-resolution magnetic imaging technique in the picosecond regime. We compile selected results for the dynamic phenomena observed in magnetic heterosystems, and we will discuss a possible extension of the technique into the femtosecond regime.

1.2 Magnetodynamic Imaging on the Picosecond Time Scale

1.2.1 Time-Resolved Photoemission Microscopy

In our experiments we employed time-resolved X-ray photoemission electron microscopy (TR-XPEEM) to image the temporal evolution of the magnetization following a short field pulse excitation. The details of the electron optics of such an

immersion lens microscope have been described in several review articles [23–25]. In general, the instruments fall into two classes differing in the electron-optical concept. The strong electric field between the sample and the objective lens system, which is a characteristic of the immersion lens approach, is realized either by putting the sample on high negative potential or the objective lens on high positive potential. The first solution allows the use of electromagnetic lens elements, but limits the access to the sample. In the second variant, the sample is kept on ground. This is very convenient for magnetodynamics studies, as the sample can be easily subjected to short electrical current and magnetic field pulses generated by fast pulse generators. Thus, this is also the geometry of choice in our experiments.

The samples consist of small magnetic elements, which are prepared by optical and electron beam lithography techniques on coplanar waveguides of up to 100 μm width [26]. The high-frequency behavior of the waveguide is chosen so as to provide a close impedance match to commercial pulse generators. The shortest current (*pump*) pulses realized in this way have a rise time of less than 100 ps. For even shorter pulses the waveguide is connected to an Auston switch which can be controlled by a femtosecond pulse laser system. Both the pulse generator and the femtosecond laser are synchronized with the synchrotron radiation pulse train (*probe*) via an electronic circuit which keeps the timing jitter between pump and probe pulses below 10 ps. If the repetition rate of pump and probe pulses is the same, no further selection mechanism in the microscope is needed. In most cases, however, the repetition rate of the pump pulses may be lower in order to allow the magnetic system to return to the ground state after each excitation pulse. In order to select those synchrotron probe pulses which correspond to a given pump pulse sequence, a gating scheme has been implemented in the microscope column [27]. It allows one to blank the electron beam for those synchrotron pulses which do not contribute to the selected time window. The time resolution of this imaging approach being limited by the timing jitter in the electronic synchronization and the pulse width of the synchrotron radiation reaches down to about 10 picoseconds.

The combination of element selectivity and magnetic sensitivity is provided by soft X-ray magnetodichroic phenomena predominantly at the transition metal L edges. Magnetic X-ray circular dichroism (MXCD) [28, 29] serves as a contrast mechanism for ferromagnetic samples, whereas magnetic X-ray linear dichroism (MXLD) [30, 31] yields magnetic contrast for certain antiferromagnetic spin structures. The MXCD signal A_C is sensitive to the projection of the magnetization $\mathbf{M}$ onto the helicity vector of the circularly polarized light $\boldsymbol{\zeta}$, i.e.,

$$A_C \sim \mathbf{M} \cdot \boldsymbol{\zeta}. \tag{1.1}$$

Therefore, MXCD yields the highest contrast for $\mathbf{M}$ being oriented parallel or antiparallel to the direction of light incidence. It thus determines a *spin orientation* in space. MXLD, however, depends on the orientation of the spin quantization axis with respect to the electric field vector $\mathbf{E}$ of the linearly polarized light. It therefore can determine only the *spin alignment* direction. The angular dependence in MXLD is usually system dependent and more complicated as crystalline and orbital symmetries have to be considered [32, 33]. The combination of MXCD and MXLD

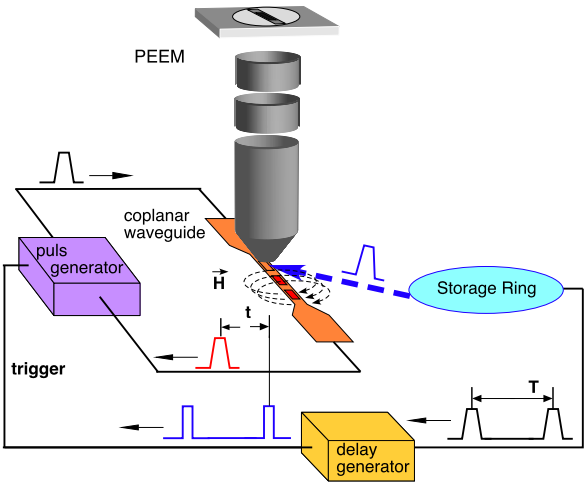

Fig. 1.2 Principle of a time-resolved PEEM experiment with magnetic field pulse excitation (taken from Ref. [37])

provides convenient access to heteromagnetic systems, as has been demonstrated for static micromagnetic structures in several cases [34–36].

1.2.2 Imaging Magnetization Dynamics in Single Magnetic Thin Films

In order to demonstrate and explain the principle of the time-resolved PEEM technique, we will first focus on results obtained from single magnetic layers.

1.2.2.1 Example I: Permalloy ($Ni_{80}Fe_{20}$) Layers

As a first example, we briefly discuss the results obtained on a single Permalloy ($Ni_{80}Fe_{20}$) microstructured element of 40 nm thickness, which has been subjected to a 10 ns wide field pulse (Fig. 1.2). The experiments have been performed using the 16-bunch mode at the ESRF, which provides a repetition period of 200 ns [37]. This time structure of the excitation ensures that the magnetization distribution has relaxed into the ground state after each excitation pulse. Each image shown in the sequence of Fig. 1.3 reflects the MXCD contrast at the Ni L_3 edge and represents an average over 10^8 pump-probe cycles. As a consequence, the image shows a clear contrast only in those regions of the magnetization distribution which reproducibly appear at the same lateral position at each pump pulse event. The electrical pulse passing along the coplanar waveguide changes the potential landscape between sample and immersion lens. This leads to a transient change of the imaging magnification; i.e., the image "breathes." This effect can be conveniently employed to determine not only the reference point on the time axis marking the onset of the

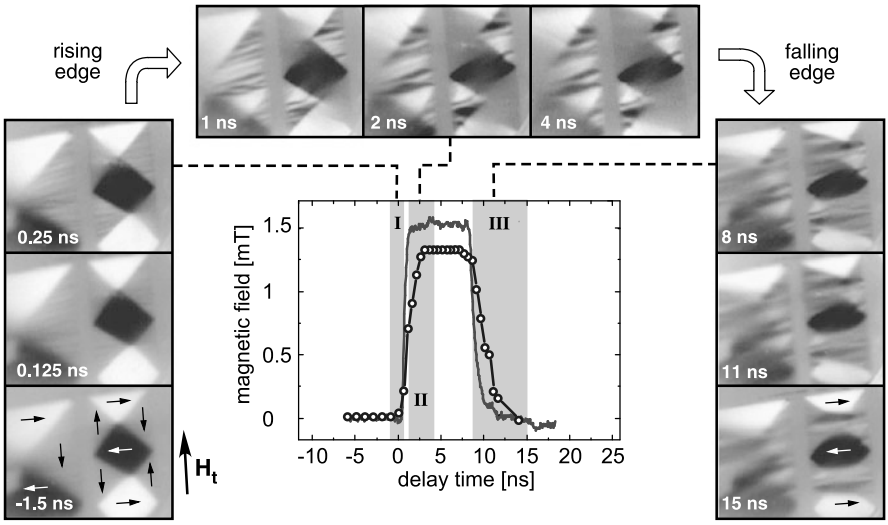

Fig. 1.3 Evolution of the magnetization pattern in a micrometer-sized Permalloy thin film element following the excitation with a magnetic field pulse. The pulse shape supplied by the pulse generator (*solid line*) is only slightly broadened, when the pulse (○) arrives at the element. The *arrows* indicate the orientation of the local magnetization vector. From [37]

magnetic field pulse, but also the pulse shape of the magnetic excitation (data points in Fig. 1.3) [38].

The image shows the domain distribution in a rectangular element (right, $16 \times 8\ \mu m^2$) and part of a square element (left, $16 \times 16\ \mu m^2$). In the ground state, i.e., before the field pulse sets in, the elements assume simple Landau flux closure domain structures. This indicates that the domain pattern is dominated by the tendency of the system to reduce the magnetic stray field outside the particle. The arrows indicate the orientations of the local magnetization vector in the individual domains. As soon as the magnetic pulse field $\mathbf{H}_p(t)$ acts on the element, the domain configuration starts to change in a characteristic manner (region I). In the following, we will denote the ground state magnetization distribution at delay time $t < 0$ by $\mathbf{M}_0(\mathbf{r})$ and the transient magnetization distribution at $t > 0$ as $\mathbf{M}_t(\mathbf{r})$. The most pronounced changes appear in those triangular domains for which the ground state magnetization direction points antiparallel to the pulse field, $\mathbf{M}_0(\mathbf{r}) \downarrow\uparrow \mathbf{H}_p(t)$. Exhibiting an intermediate gray contrast level in the ground state, they develop a clear stripe-like pattern, which indicates the formation of a network of small domains with transient magnetization $\mathbf{M}_t(\mathbf{r}) \perp \mathbf{H}_p(t)$. This phenomenon is known as incoherent magnetization rotation [39].

A coherent magnetization rotation, by contrast, appears in those domains whose ground state magnetization fulfills $\mathbf{M}_0(\mathbf{r}) \perp \mathbf{H}_p(t)$, because they are subject to the highest magnetization torque $\tau(\mathbf{r}, t) \sim \mathbf{M}(\mathbf{r}) \perp \mathbf{H}_p(t)$. They appear as black and white contrast levels in the images. In particular in the regions of the 90°-domain walls separating domains with $\mathbf{M}_0(\mathbf{r}) \perp \mathbf{H}_p(t)$ and $\mathbf{M}_0(\mathbf{r}) \parallel \mathbf{H}_p(t)$, the magnetiza-

tion rotates, effectively increasing the area of the domains with $\mathbf{M}_0(\mathbf{r}) \parallel \mathbf{H}_\mathrm{p}(t)$. As a consequence the domain wall seems to smear out. This process is most pronounced close to the central vortices and weaker at those positions where the domain wall meets the boundary of the element. The edges of the element act as pinning sites for the domain walls and stabilize the local magnetization against the coherent rotation. Consequently, on the plateau of the field pulse (region II), the domain with $\mathbf{M}_0(\mathbf{r}) \parallel \mathbf{H}_\mathrm{p}(t)$ has taken a W-like shape, whereas the black and white domains with $\mathbf{M}_0(\mathbf{r}) \perp \mathbf{H}_\mathrm{p}(t)$ have reduced in size. We also note that most of these changes take place along the rising edge of the field pulse during the first few hundred picoseconds.

On the plateau of the field pulse the transient domain structure stabilizes, as can be seen by comparing the MXCD images taken at delay times $t = 2$ ns and $t = 4$ ns. A temporary equilibrium state is formed, which is determined by the local effective field $\mathbf{H}_\mathrm{eff}(t) = \mathbf{H}_\mathrm{dip}(t) + \mathbf{H}_\mathrm{p}(t)$, which contains the contributions of the dipolar and pulse fields. This configuration has an important consequence which becomes visible along the falling edge of the field pulse. The reduction of the pulse field also causes a formation of the stripe-like phase in the previously unaffected regions with $\mathbf{M}_0(\mathbf{r}) \parallel \mathbf{H}_\mathrm{p}(t)$. This behavior can be understood in the following manner: The reduction of the pulse field acts on the temporary equilibrium state as if a hypothetical magnetic field $\mathbf{H}_\mathrm{hyp}(t)$ is applied into the direction opposite to $\mathbf{H}_\mathrm{p}(t)$. The W-shaped domains with $\mathbf{M}_0(\mathbf{r}) \parallel \mathbf{H}_\mathrm{p}(t)$ are then subject to the condition $\mathbf{M}_\mathrm{r}(\mathbf{r}) \downarrow\uparrow \mathbf{H}_\mathrm{hyp}(t)$, which also causes an incoherent magnetization rotation in these domains. As a consequence, the stripe-like areas expand through the entire element. As this process involves the creation of many partial domain walls, the resulting structure is relatively stable, even after the field pulse has completely decayed. The domain wall motion is considerably slower than the magnetization rotation. Therefore, it takes more than 10 ns for the transient magnetization configuration to relax back into the ground state.

1.2.2.2 Example II: Fe(001) Layers

In contrast to the polycrystalline Permalloy thin films described above, single crystal layers usually possess a strong magnetocrystalline anisotropy. This has important consequences, as demonstrated in Fig. 1.4. The sample comprises a 20×10 μm^2 sized Fe(001) thin film element (thickness 10 nm), which has been grown on a Ag(001) coplanar waveguide on a GaAs(001) substrate. It is well known that the magnetocrystalline anisotropy requires the easy axes of magnetization in single-crystalline iron to lie along the [001] crystalline directions [41]. The element has been structured such that the easy axes agree with the boundaries of the elements. Therefore, the ground state domain pattern is very similar to the pattern of the Permalloy element discussed before, because magnetocrystalline and dipolar (shape) anisotropy act in the same directions. The direction of light incidence is pointing along the long axis of the element, generating the strongest magnetodichroic contrast from the top and bottom triangular domains. The domain pattern

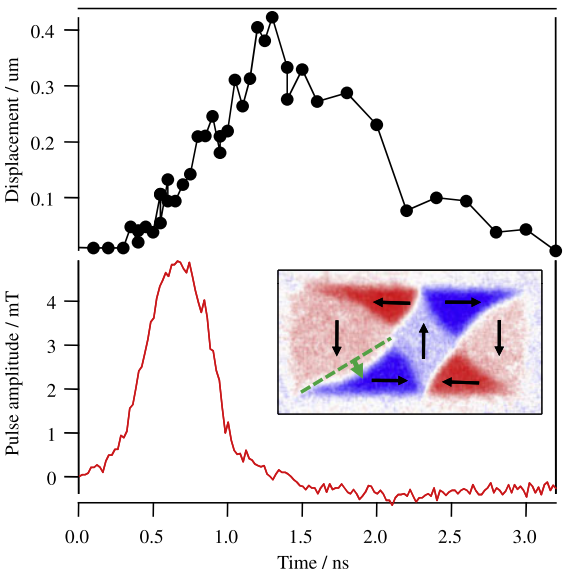

Fig. 1.4 Domain wall bulging in a $20 \times 10\ \mu m^2$ Fe element (*inset*) as a response to the magnetic field pulse (*bottom*). *Arrows* indicate local magnetization direction. *Broken green line* marks the position of the domain wall in the ground state, i.e., the static case. From [40]

is reproduced in a false color representation (blue–red instead of black–white) to highlight small changes occurring during the dynamic response.

The field pulse in the dynamic experiment (pulse field $\mathbf{H}_p(t)$ is pointing from top to bottom along the short axis of the element) is shorter by a factor of 10 than that in Fig. 1.3. Thus, we first verified that incoherent rotation also occurs in Permalloy films under these conditions [40]. The most obvious finding in Fe(001) is thus the *absence* of incoherent rotation processes. Evidently, the field pulse is not strong enough to overcome the magnetocrystalline anisotropy and to locally rotate the magnetization out of the easy axis. The field pulse generates the largest magnetization torque in the blue and red colored domains. This leads to a coherent magnetization rotation in these domains, which in turn leads to a *bulging* of the domain walls with respect to the ground state configuration.

In Fig. 1.4 we have analyzed this behavior more quantitatively by plotting the time dependence of the displacement in the center of the wall normal to the wall axis. The comparison to the shape of the field pulse reveals an astonishing finding: There is a considerable time lag between the field pulse and the wall response. In particular, the maximum of the bulging motion is located at around $t \approx 1.2$ ns, i.e., a delay time at which the field pulse itself has already decayed. More quantitatively, there is a time delay of $\tau_B = 700$ ps between the maximum of the field excitation and the maximum domain wall displacement. This behavior can be attributed to the interplay of two mechanisms. First, the field pulse stores Zeeman energy in the magnetization distribution which in the low-anisotropy material Permalloy leads to large-angle rotations of the local magnetization. The stronger magnetocrystalline anisotropy in Fe(100) suppresses large-angle rotations and leaves only the much slower domain wall motion as a pathway to reduce the energy of the system. Thus, the wall bulging proceeds as long as it is driven by the excess energy in the spin sys-

tem. Second, the long decay of the excitation is also promoted by a small magnetic damping in iron for which a Gilbert damping factor of $\alpha = 3 \times 10^{-3}$ has been reported [42]. The characteristic time scale on which the Zeeman energy is dissipated via domain wall motion is given by [43]

$$\tau_{\mathrm{DW}} = \frac{1}{\gamma \mu_0 M_{\mathrm{S}} \alpha} \tag{1.2}$$

with γ denoting the gyromagnetic ratio. Taking the value $\mu_0 M_{\mathrm{S}} = 2.2$ T for the saturation magnetization of iron yields a time constant of $\tau_{\mathrm{Fe}} = 850$ ps, which compares favorably with the preceding value of $\tau_{\mathrm{B}} = 700$ ps. A further analysis of the time dependence in Fig. 1.4 reveals that the domain wall bulging builds up with an almost constant wall velocity of $v_{\mathrm{w}} \approx 400$ m/s, but relaxes significantly more slowly with a domain wall speed of $v_{\mathrm{w}} \approx 100$ m/s. The constant wall velocity in the initial rise may be due to the Walker limit [44]. The Walker breakdown field in iron is estimated to be about 3.3 mT, which agrees well with the external field value at the position where the domain wall velocity levels off into a constant value. We have also verified the main results of our interpretation by means of micromagnetic simulations within the OOMMF environment [45].

1.2.3 Imaging Magnetization Dynamics in Interlayer-Coupled Trilayers

After seeing the variety of dynamic processes which can be revealed by photoemission microscopy on single magnetic layers, we can take the technique a step further to investigate more complicated magnetic heterostructures. In the following we are focusing on trilayer structures composed of two different ferromagnetic layers FM1 and FM2 sandwiching a nonmagnetic interlayer. Exploiting the well-known phenomena of interlayer exchange coupling [46, 47], we can tune the magnetic coupling character between FM1 and FM2 from ferromagnetic to antiferromagnetic by adjusting the thickness of the interlayer appropriately. In this way we can study the influence of the interlayer coupling onto the magnetodynamics, but we must be able to separate the response of the two layers FM1 and FM2. This is achieved via the element selectivity of the MXCD effect if both layers have different chemical constituents and the thicknesses of the top layer and interlayer are in the nanometer regime. In this case the magnetodichroic signal resulting from the bottom layer can still be discerned.

Our magnetodynamics studies encompassed several material systems comprising layers of single magnetic elements or binary compounds [48–50]. In the following we will discuss results on the dynamic response obtained from a polycrystalline trilayer of the type $Fe_{20}Ni_{80}$(2nm)/Cr(2.5nm)/$Fe_{50}Co_{50}$(5nm). In this case, the interlayer coupling is weak and leads to a ferromagnetic alignment of the local magnetization direction of both layers. This can be seen in Fig. 1.5, which displays MXCD maps taken at the Ni and Co L_3 absorption edges, which directly translate into the

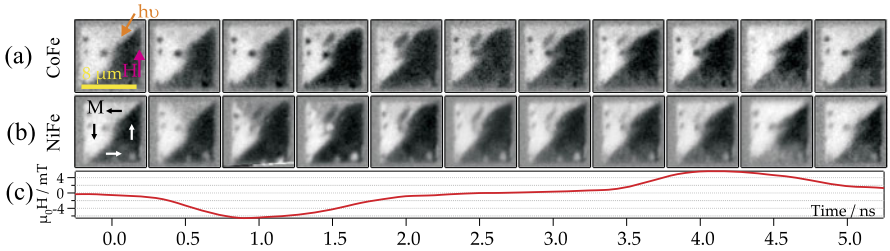

Fig. 1.5 Evolution of the layer-resolved magnetization patterns in a micrometer-sized pseudo-spin valve element following the excitation with a bipolar magnetic field pulse. The layer structure comprises $Fe_{20}Ni_{80}$(2 nm)/Cr(2.5 nm)/$Fe_{50}Co_{50}$(5 nm). From [50]

magnetization distribution of the top and bottom magnetic layers, respectively. A direct comparison of the domain patterns at delay time $t = 0$ reveals the same contrast distribution and hence a ferromagnetic coupling between the $Fe_{20}Ni_{80}$ and the $Fe_{50}Co_{50}$ layers. The domain pattern corresponds closely to a Landau–Lifshitz flux closure pattern with four triangular domains and a central vortex (cf. Fig. 1.3). The magnetization vectors in all four domains make an angle of about 45° and therefore have about the same projection onto the direction of light incidence. Because of the angular dependence of the MXCD, the left and top and the right and bottom domains, respectively, show almost the same magnetic contrast. The dark circular dots appearing in the left-hand domain are defects on the sample surface.

This pseudo-spin valve structure is subjected to a magnetic field pulse with a maximum amplitude of 6 mT. We found out that a unipolar pulse often left the system in a metastable transient state which severely impairs a repetitive pump-probe measurement. Apparently, the restoring force by the demagnetizing field was not strong enough to restore the initial state before the pulse excitation, in contrast to the observation in single Permalloy layers. Only a bipolar pulse ensured that the system reproducibly returned back to the initial state even after a train of 10^9 repetitive field pulses. and bottom the element-resolved magnetization character determines the dynamic response.

Following the temporal evolution of the magnetization pattern in the Permalloy and $Fe_{50}Co_{50}$ layers, we can discern three different processes taking place on different time scales. The fastest response takes place in the top and bottom domains and appears as a change of the contrast level in the entire domain. This contrast change is related to a rotation of the local magnetization vector in the direction of the external or rather effective magnetic field (see also Fig. 1.6(a)). The second process, which takes place on a longer time scale, is a domain wall propagation which causes the domain with $\mathbf{M}_0(\mathbf{r}) \parallel \mathbf{H}_p(t)$ to expand at the expense of the neighboring domains (cf. Fig. 1.6(b)). The third process is slowest and leads to the nucleation and expansion of a small domain in the top domain (cf. Fig. 1.6(c)). Judging from the contrast level, the magnetization vector in this domain is also parallel to the external field.

Although at first glance the responses look similar for the top and bottom ferromagnetic layers, a closer inspection of the data in Fig. 1.3 reveals an interesting difference, which gives more insight on the microscopic mechanisms governing the

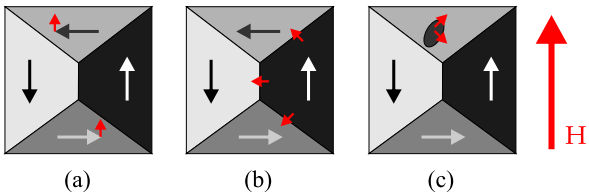

Fig. 1.6 Graphical representation of the magnetodynamic response taking place in different parts of the domain patterns displayed in Fig. 1.5: (**a**) magnetization rotation, (**b**) domain wall displacement, and (**c**) domain nucleation and growth. The respective direction of motion is indicated by the *small red arrows* in panels (**a**) to (**c**)

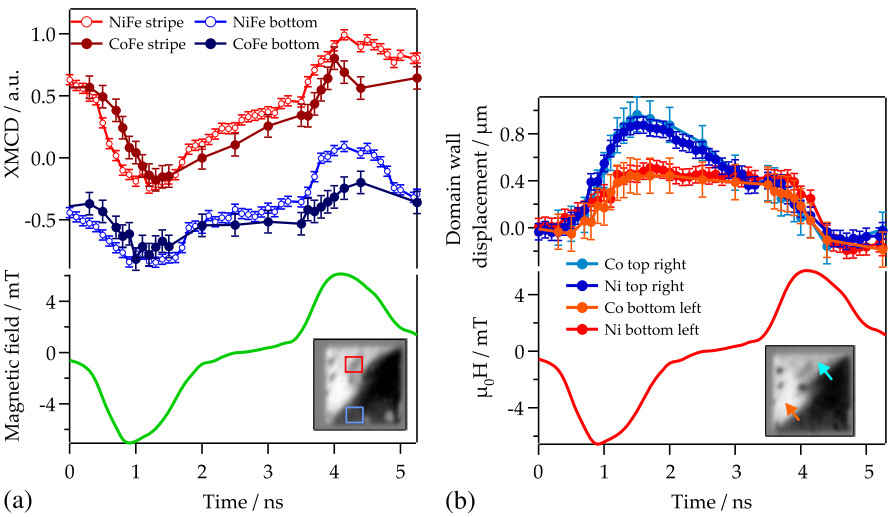

Fig. 1.7 (**a**) Evolution of the magnetization rotation in the top and bottom domains along the magnetic field pulse for the top (Permalloy) and bottom ($Fe_{50}Co_{50}$) layers (*squares* mark the area of averaging). (**b**) Layer-resolved domain wall motion (position indicated by the *arrows*) driven by the magnetic field pulse. From [48]

magnetization dynamics. In the following we will focus on the magnetization rotation and the domain wall motion. Figure 1.7 compiles a quantitative assessment of the two processes, which is based on the analysis of the temporal variation of the MXCD contrast levels in both ferromagnetic layers.

The temporal evolution of the magnetization rotation in both magnetic layers is compared in Fig. 1.7(a). The data have been obtained by averaging the magnetic contrast over an extended area in the top and bottom triangular domains. The rotation angle of **M** was then determined from the angular dependence of the MXCD signal (cf. (1.1)). At the onset of the field pulse (negative excursion) the rotational motion also sets in and increases with the magnetic field. However, there is a characteristic phase shift between the responses in the two layers. The rotation in the FeCo layer lags behind that in the Permalloy layer by about 250 ps. This time lag also

affects the further temporal development, as the relaxation in the CoFe layer is also delayed and the rotation in the CoFe layer is smaller during the positive excursion of the field pulse. This behavior is similar for both the top and the bottom domains. As a consequence, the magnetization vectors $\mathbf{M}_{\mathrm{FeNi}}$ and $\mathbf{M}_{\mathrm{CoFe}}$ are not rotating as a unit, but develop a dynamic twist during the magnetic field pulse excitation. The interpretation of this behavior can be traced back to the coercive fields of the individual layers, which differ by about a factor of 10 ($H_{\mathrm{C,FeNi}} = 0.5$ mT, $H_{\mathrm{C,CoFe}} = 5$ mT). According to the empirical model of Doyle et al. [51], the switching time τ can be related to the layer-specific coercivity $H_{\mathrm{C},n}$,

$$\frac{1}{\tau} = \frac{1}{S_{\mathrm{w}}}(H - H_{\mathrm{C},n}), \tag{1.3}$$

of the respective layer n via the switching coefficient $S_{\mathrm{w}} \approx 2(1+\alpha^2)/(\alpha\gamma)$. The above quasi-statically determined coercivity values can be regarded as lower bounds only to the dynamic coercivity [52], which precludes any quantitative interpretation. Qualitatively, however, the switching time in the CoFe layer should be significantly higher than in the Permalloy layer, in agreement with the experimental observation.

The data on the domain wall motion along the field pulse are compiled in Fig. 1.7(b) and exhibit a different behavior. A comparison of the motion in the FeNi and CoFe layers reveals a different amplitude, but the same time dependence during the negative part of the bipolar field pulse. In particular, there is no time delay in the initial phase of the domain wall motion; i.e., the domain walls in the top and bottom layers move simultaneously. This may be understood by the fact that a domain wall generates an additional stray field, which can increase the effective coupling through the nonmagnetic interlayer [53]. Also, keep in mind that the domain wall motion is considerably slower than the magnetization rotation. The scatter in the experimental data points may simply mask a potential difference of the order of 100 ps in the onset of the domain wall displacement in Fig. 1.7(b). The finite domain wall velocity also causes the system to relax slowly and still be in a transient state when the positive component of the magnetic field pulse starts to act. Consequently, we observe only a weak domain wall displacement in the opposite direction, although the positive and negative components of the bipolar pulse are of comparable magnetic field strength.

1.3 Addressing the Femtosecond Time Scale

The area of magnetization dynamics discussed in the previous section reaches its limits in the picosecond regime. The fastest process available in this regime is the precessional motion of the magnetization vector, which is well described by the Landau–Lifshitz–Gilbert (LLG) equation. An important precondition in the LLG treatment is that the length of the magnetization vector remains essentially unchanged during the motion, i.e., $|\mathbf{M}| = \mathrm{const}$.

Pioneering laser experiments in the mid-1990s showed that there may be even faster excitation channels resulting in magnetization or rather spin dynamics down

to the femtosecond regime [8]. In this case the magnetic system is excited by a strong light pulse from an amplified femtosecond pulse laser, e.g., a Ti:sapphire oscillator. This light pulse may be as short as 50 fs and transfers an energy of up to several microjoules (μJ) to the magnet. The wavelength of this pump pulse is usually around $\lambda = 800$ nm; i.e., it leads to excitations of electrons mainly around the Fermi level resulting in a transient nonequilibrium electron distribution which differs strongly from the Fermi distribution in thermodynamical equilibrium. This situation also affects the magnetic order, i.e., the spin system. Consequently, an ultrafast demagnetization, i.e., a reduction of the magnetization vector on a time scale of the order of 100 fs, takes place. In other words, in these experiments the magnetization vector is no longer of constant length, but rather varies in time, i.e., $|\mathbf{M}| = f(t)$. The interpretation of such experiments usually follows the three-temperature model [8, 54], in which the solid is described by three interacting subsystems with well-defined temperatures for the electron (T_e), spin (T_s), and lattice (T_l) subsystems. This phenomenologically derived model assumes an ultrafast dissipation channel for the spin angular momentum in order to explain a demagnetization time of a few hundred femtoseconds. Various approaches are currently discussed controversially to explain such a fast spin-flip process; among them are inelastic magnon scattering, Elliot–Yafet type mechanisms [11], photon-induced spin flips [14, 55], spin-flip Coulomb scattering [10], and relativistic quantum-electrodynamic processes [15]. On the other hand, spin-dependent transport processes driven by the nonequilibrium electron distribution may generate sizable contributions to the ultrafast demagnetization without invoking an angular momentum dissipation channel at all [16, 56]. Moreover, recent theories suggest that the demagnetization time τ_M is related to the Gilbert damping factor α [57], which also appears in the LLG equation.

Recently, an ultrafast all-optical switching of the magnetization has been reported in GdFeCo alloys. In this case the magnetization is found to reverse its orientation by 180° as a response to the irradiation with a circularly polarized femtosecond laser pulse [19]. Whether this effect involves the ultrafast demagnetization or is related to other microscopic mechanisms is currently still a matter of intense debate. In any case, the preceding examples show that spin dynamics on ultrafast time scales is a highly interesting area of research. All of the ultrafast experiments performed up to now, however, lack lateral resolution. Investigating ultrafast spin dynamics with photoemission microscopy is a real challenge and requires several experimental problems to be solved. Two of them—the questions of an appropriate light source for femtosecond pulses and a suitable magnetic contrast mechanism—will be addressed below.

1.3.1 Femtosecond Pulse Soft X-Ray Sources

In order to introduce element selectivity into ultrafast spin dynamics studies, we need soft X-ray light sources providing femtosecond pulses. At present, this quality of radiation can be provided by at least three different types of sources: (i) free electron lasers (FELs), (ii) femtosecond slicing procedures, and (iii) higher harmonic

generation (HHG). Free electron lasers provide femtosecond light pulses with an extremely high peak brilliance which is a factor of up to 10^7 higher than that of storage ring light sources [58]. This corresponds to up to 10^{13} photons per 30 fs pulse. On the one hand, this photon density may lead to severe sample damage even after a single-shot exposure [59]. On the other hand, in electron-based spectroscopies and microscopies the peak brilliance translates into a high photoelectron density which may lead to space-charge phenomena resulting in severely deteriorated spectral and lateral resolution of the instruments [60]. At the other end of the photon density scale we find the femtosecond slicing approaches [61]. They are based on the modulation of the electron bunches in the storage ring by means of intense photon pulses from an external laser source. The limited efficiency of this slicing technique results in very low photon fluxes, but allows for repetitive pump-probe experiments. The first results on element-selective studies of ultrafast demagnetization at the L_3 edges of Ni have been obtained recently [62, 63]. Nevertheless, the complexity of the slicing experiment and the rather limited accessibility to such a source at the moment allow only for selected experiments.

In contrast to the accelerator-based sources described above, the HHG technique involves essentially a table-top laser setup. The pulses of a Ti:sapphire amplifier are focused into a noble gas medium such as Ar or Ne. The strong electromagnetic field of the light pulse causes the valence electrons to oscillate in the Coulomb potential of the core with partial ionization and recombination events. During the recombination photons of higher energies corresponding to integer multiples of the fundamental laser energy are emitted [64]. With argon as a medium the higher harmonic upconversion may easily reach photon energies of 100 eV (the phase-matching cutoff for Ne), thereby covering the transition metal M absorption edges. This energy range is also often referred to as extreme ultraviolet (EUV). The radiation produced by the HHG process retains the polarization and coherence properties of the driving laser and may reach pulse lengths down to less than 10 fs [65]. In addition, each HHG light pulse has a well-defined phase relation to the corresponding light pulse at the fundamental wavelength, therefore providing the means for inherently synchronized pump-probe experiments with femtosecond time resolution.

1.3.2 Magnetodichroic Effects in the EUV Regime

In order to perform element-selective studies in the EUV regime, an appropriate magnetodichroic phenomenon is needed which delivers a magnetic signal at these photon energies. As the HHG source provides only linearly polarized light, MXCD-type effects like those used in the PEEM experiments described above are not accessible. However, studies on iron with synchrotron radiation by Pretorius et al. have shown that an effect similar to the transverse magneto-optical Kerr effect (T-MOKE) can be observed in resonant excitation at the Fe M edge [66].

In Fig. 1.8 we show corresponding data for such a resonant reflectivity experiment on a thin Co film using linearly polarized synchrotron light. The electric

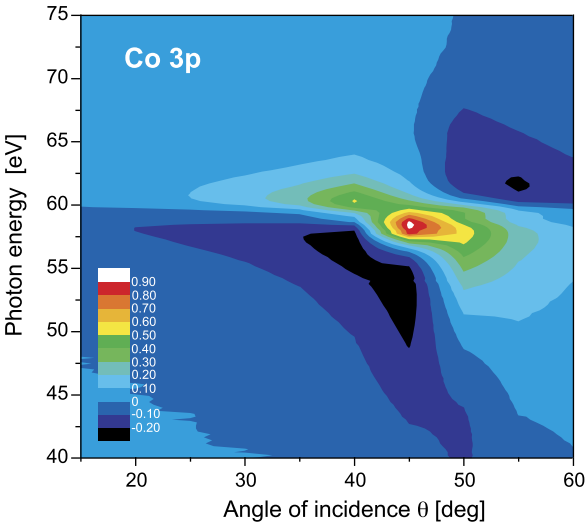

Fig. 1.8 Magnetic resonant reflectivity in the EUV regime at the Co *M* edge as a function of scattering angle and photon energy. The color encodes the value of the magnetodichroic asymmetry A_R

field vector of the linearly polarized light is oriented within the scattering plane, whereas the magnetization vector is oriented perpendicular to this plane. The magnetodichroic signal in reflection is displayed as an asymmetry

$$A_R = \left(I^+ - I^-\right)/\left(I^+ - I^-\right) \tag{1.4}$$

with I^+ and I^- denoting the intensity of the reflected light for opposite directions of the magnetization or external magnetic field. The variation of A_R with angle of incidence θ and photon energy $\hbar\omega$ reveals a pronounced maximum at around $\hbar\omega \approx 58$ eV, close to the position of the Co 3p core level, and $\theta \approx 45°$, corresponding to the Brewster angle. Under these conditions the magnetodichroic signal A_R reaches peak values of more than 90 %. This property makes the resonant magnetic reflectivity or T-MOKE in the EUV regime a very useful tool for the study of magnetic heterosystems [67, 68].

This is briefly demonstrated in Fig. 1.9, which shows the spectral distribution of the HHG light reflected off a Permalloy grating and the corresponding T-MOKE asymmetry A_R. The HHG intensity spectrum exhibits the characteristic comb structure and covers both the Fe and Ni *M* edges. A reversal of the magnetization direction introduces a strong change in the harmonics, particularly around $\hbar\omega \approx 66$ eV, corresponding to the Ni edge. Similar changes occur at the Fe edge at around $\hbar\omega \approx 54$ eV. This is also reflected in the magnetodichroic asymmetry, which exhibits pronounced maxima at these two photon energies. The sign of the asymmetry is the same for both edges and underlines the fact that the Fe and Ni magnetic moments are strongly exchange-coupled in the alloy and align parallel to each other. We also compare the HHG data to measurements with synchrotron radiation performed on the same sample system and note an overall fair agreement. The remaining differences in the asymmetry spectra are due to differences in the experimental geometry in the HHG and synchrotron experiments.

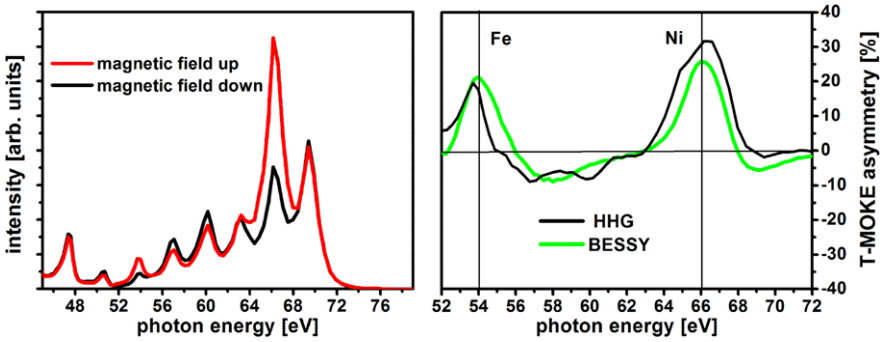

Fig. 1.9 Magnetic resonant reflectivity in the EUV regime at the Fe and Ni *M* edges in a Permalloy layer. Intensity distribution for opposite magnetization directions (*left*) and resulting magnetodichroic asymmetry (*right*) acquired with HHG and synchrotron radiation

In performing synchrotron pump-probe reflectometry experiments we have also already answered the question of to what extent this EUV T-MOKE signal can also be used for magnetodynamics studies in the picosecond regime [69]. For this purpose, we prepared magnetic heterosystems on a coplanar waveguide with an integrated Auston switch on GaAs substrates. The switch was driven by a Ti:sapphire fs-pulse laser (pulse width 20 fs) electronically synchronized with the synchrotron radiation pulses (50 ps FWHM) and generated magnetic field pulses of 10 ps (FWHM) at a repetition frequency of 100 MHz. These short field pulses caused a small-angle precession of the magnetization in the Permalloy and Co layers, which was recorded by the time traces in the element-selective T-MOKE signals, which are reproduced for the Co layer in Fig. 1.10. These time traces reflect the contribution of several precessional modes, the ratio of which can be changed by a static external field, as clearly visible in the experimental data. Although in the case of the small-angle precession the change in the resonant magnetic reflectivity signal is much smaller than for a full magnetization reversal (cf. Figs. 1.8 and 1.9), it can be conveniently used to map the temporal evolution of the precessional motion and distinguish different excitation modes.

1.3.3 HHG Pump-Probe Experiments

An experiment addressing ultrafast demagnetization in an element-selective manner without lateral resolution is sketched in Fig. 1.11. Both the HHG radiation and the fundamental pump pulse are focused by a toroidal mirror onto the sample. The sample comprises a Permalloy ($Ni_{80}Fe_{20}$) film which has been microstructured into an optical grating. It is placed into a Helmholtz coil system which generates the magnetic field for magnetization reversal. The sample disperses the HHG spectrum onto a CCD camera; the fundamental light at a wavelength of $\lambda = 760$ nm is blocked by

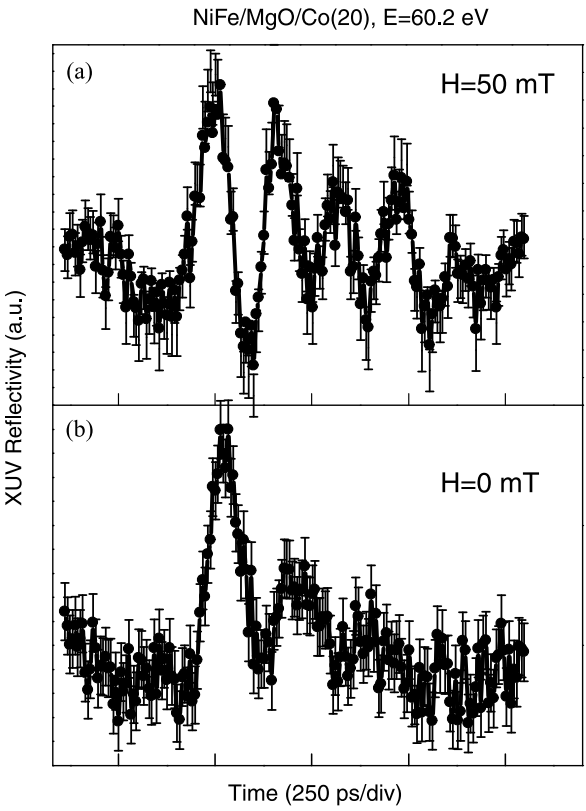

Fig. 1.10 Time-resolved T-MOKE signal of the Co(20)/MgO/NiFe sample at the Co M absorption edge (60.2 eV) and for static external magnetic fields 50 mT (**a**) and 0 mT (**b**). From [69]

an Al filter. In this way the magnetic dichroism can be measured in parallel for all relevant photon energies.

The results on the ultrafast demagnetization from this Permalloy sample are shown in Fig. 1.12. The data represent the time evolution of the magnetodichroic response at the Fe and Ni edges, and at a point in between the edges where the magnetodichroic signal disappears (the positions of the respective harmonics are indicated in the inset). In the temporal evolution we observe the fast reduction of the magnetodichroic response on a time scale of about $\tau_M \approx 150$ fs, followed by a much slower recovery of the signal due to spin-lattice relaxation. At the photon energy $\hbar\omega \approx 58$ eV there is no change of the dichroic signal. Within the experimental uncertainty, the demagnetization times for Fe and Ni appear the same. At first glance, this seems plausible because of the strong exchange coupling in this intermetallic compound which ties the magnetic moments of Fe and Ni together. However, recent studies with improved time resolution suggest that a small difference in the demagnetization of different constituents in a heteromagnetic system may exist. In the Permalloy system a small time delay of the order of a few tens of femtoseconds is observed for the onset of demagnetization of Ni and Fe [71]. This results in the Ni demagnetization lagging behind the Fe demagnetization in a char-

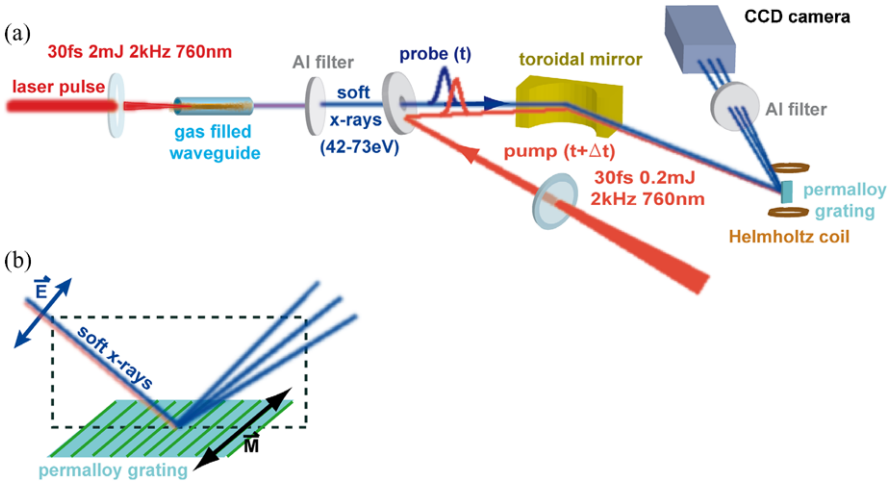

Fig. 1.11 Setup of the HHG pump-probe experiment (**a**). The sample itself serves as an optical grating to disperse the radiation onto a CCD camera (**b**). From [70]

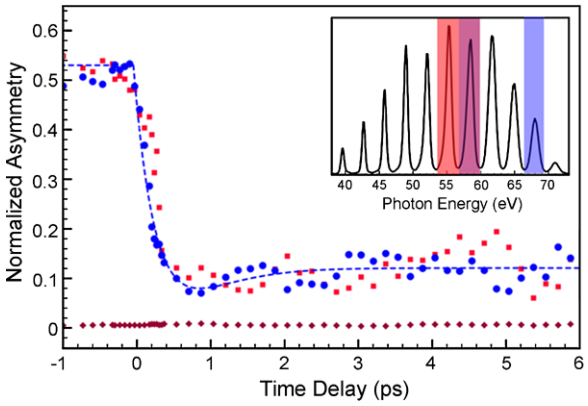

Fig. 1.12 Ultrafast demagnetization in Permalloy ($Ni_{80}Fe_{20}$) measured element-selectively at the Fe (*red*) and Ni (*blue*) *M* absorption edges. The *purple data points* refer to a photon energy of $\hbar\omega \approx 58$ eV, where the magnetodichroic signal disappears. *Inset*: HHG spectrum with color markers for the harmonics selected for the element-selective data acquisition. Taken from [72]

acteristic fashion. Reducing the exchange coupling between Fe and Ni by doping with Cu increases this time lag, the microscopic origin of which still needs to be explained.

In the context of magneto-optical pump-probe techniques often the question arises as to what extent the magneto-optical signal—in our case the T-MOKE asymmetry—represents changes in the magnetization rather than changes in the electronic structure. This is a nontrivial issue, as the pump pulse puts the electron system in a nonequilibrium state which may affect the optical response and the magneto-optical coupling constants. It turns out that it is possible to avoid most of those optical side effects by taking advantage of the fact that they are symmetric under magnetic field reversal, whereas the magnetic contribution is antisymmetric. Therefore, in magneto-optical pump-probe experiments, the magnetic response

of the sample is extracted by taking the sample response for two magnetic fields aligned in opposite directions; subsequently, assuming that the optical constants are not affected by the magnetic field, the optical response can be eliminated by subtracting the two responses. A thorough discussion of possible effects influencing the magneto-optical response can be found in [73]. The question of whether the signal from the T-MOKE at the $M_{2,3}$ edges of a magnetic material is purely magnetic or is perturbed by nonmagnetic artifacts was addressed in detail in [74]. There it was shown that the magnetic asymmetry obtained with EUV photons in the T-MOKE geometry is predominantly of magnetic origin and that any transient nonmagnetic contribution to the asymmetry parameter is small (0.2 %) compared to the amplitude of the demagnetization changes (20 %) at the same pump fluence. This highlights the importance of T-MOKE in the EUV regime for the investigation of ultrafast magnetization dynamics.

1.3.4 Future Development

The T-MOKE phenomenon described in Sect. 1.3.2 has a pronounced angular dependence as is apparent from Fig. 1.8, with the maximum asymmetry appearing around a 45° angle of light incidence. In PEEM experiments the angle of light incidence ranges between 15° and 25° depending on the instrument's geometry. At these angles the T-MOKE signal in the reflected light is significantly reduced, which opens up a possibility for magnetodichroic effects in the absorption channel. In a pioneering PEEM experiment Hillebrecht et al. have shown indeed that even under these geometrical constraints a sizable magnetodichroic signal of up to 5 % in the total electron yield appears and can be successfully employed for magnetic domain imaging [75]. On the other hand, PEEM imaging even with light pulses as short as 200 as has been demonstrated recently [76]. In this case, however, the spectral width of the harmonics is more than 10 eV wide, which deteriorates the lateral resolution of the microscope due to the chromatic aberration of the immersion lens. If we use 20 fs pulses instead, as in the above HHG experiments, the spectral width of the harmonics drops to less than 1 eV, which considerably reduces the effect of chromatic aberration. Nevertheless, we may still have to cope with the issue of space charges in the microscope, which can be counteracted by optimizing the light pulse train with respect to pulse height and repetition frequency. For PEEM imaging an increase in pulse dispersion and repetition rate is certainly more favorable than an increase in pulse height. This opens a pathway to realize element-selective magnetic microscopy with femtosecond time resolution in the laboratory.

1.4 Conclusions

The magnetodynamics in magnetic heterosystems is determined by a complex interplay of competing length and time scales as well as the magnetic coupling mechanism. Element- and layer-selective techniques are mandatory to discriminate the

individual microscopic processes governing the dynamic behavior. Our experiments show that time-resolved soft X-ray photoemission microscopy has matured as a versatile tool to address the various aspects of magnetization dynamics on small length scales and down to the picosecond regime. A further extension of this imaging approach into the subpicosecond regime seems feasible with the use of higher harmonic generation-based light sources. This will give a laterally resolved access to the highly interesting area of ultrafast demagnetization phenomena and optically driven switching processes.

Acknowledgements This review covers extensive research activities which have run for several years involving a large number of collaborators. I am indebted to R. Adam, P. Grychtol, D. Rudolf, S. Cramm, I. Krug, and C. Wiemann, as well as M. Aeschlimann (University of Kaiserlautern), S. Mathias (University of Kaiserlautern), T. Silva (NIST Boulder), J.M. Shaw (NIST Boulder), H.T. Nembach (NIST Boulder), C. La-O-Vorakiat (JILA Boulder), E. Turgut (JILA Boulder), M.M. Murnane (JILA Boulder), H.C. Kapteyn (JILA Boulder) A. Kaiser (ALS Berkeley), A. Krasyuk (MPI Halle), and G. Schönhense (University of Mainz) for their collaboration and scientific discussions.

Thanks are due to B. Küpper, C. Bickmann, J. Lauer, H. Pfeifer, and F.-J. Köhne for expert technical assistance. A particular acknowledgement goes to R. Schreiber for skillful sample growth and preparation.

Financial support by the German Ministry of Education and Research (BMBF) under Grant No. 05KS7UK1 and the German Research Foundation (DFG) through Collaborative Research Centre SFB 491 is gratefully acknowledged.

References

1. R. Wood, J. Magn. Magn. Mater. **321**, 555 (2009)
2. K.Z. Gao, O. Heinonen, Y. Chen, J. Magn. Magn. Mater. **321**, 495 (2009)
3. I.C.T. Results. New logic: the attraction of magnetic computation (2008). http://www.sciencedaily.com/releases/2008/07/080708094128.htm
4. S.E. Russek, R.D. McMichael, M.J. Donahue, S. Kaka, in *Spin Dynamics in Confined Magnetic Structures*, vol. II (Springer, Berlin, 2003)
5. D.L. Mills, S.M. Rezende, in *Spin Dynamics in Confined Magnetic Structures*, vol. II (Springer, Berlin, 2003)
6. M.D. Stiles, J. Miltat, in *Spin Dynamics in Confined Magnetic Structures*, vol. III (Springer, Berlin, 2006)
7. G.P. Zhang, W. Hübner, E. Beaurepaire, J.Y. Bigot, in *Spin Dynamics in Confined Magnetic Structures*, vol. I (Springer, Berlin, 2002)
8. E. Beaurepaire, J.C. Merle, A. Daunois, J.Y. Bigot, Phys. Rev. Lett. **76**, 4250 (1996)
9. E. Carpene, E. Mancini, C. Dallera, M. Brenna, E. Puppin, S. De Silvestri, Phys. Rev. B **78**, 174422 (2008)
10. M. Krauss, T. Roth, S. Alebrand, D. Steil, M. Cinchetti, M. Aeschlimann, H.C. Schneider, Phys. Rev. B **80**, 180407 (2009)
11. B. Koopmans, G. Malinowski, F. Dalla Longa, D. Steiauf, M. Fähnle, T. Roth, M. Cinchetti, M. Aeschlimann, Nat. Mater. **9**, 259 (2010)
12. K. Carva, M. Battiato, P.M. Oppeneer, Phys. Rev. Lett. **107**, 207201 (2011)
13. B.Y. Mueller, T. Roth, M. Cinchetti, M. Aeschlimann, B. Rethfeld, New J. Phys. **13**, 123010 (2011)
14. G.P. Zhang, W. Huebner, G. Lefkidis, Y. Bai, T.F. George, Nat. Phys. **5**, 499 (2009)
15. J.Y. Bigot, M. Vomir, E. Beaurepaire, Nat. Phys. **5**, 515 (2009)

16. M. Battiato, K. Carva, P.M. Oppeneer, Phys. Rev. Lett. **105**, 027203 (2010)
17. A.V. Kimel, A. Kirilyuk, A. Tsvetkov, R.V. Pisarev, T. Rasing, Nature **429**, 850 (2004)
18. A.V. Kimel, A. Kirilyuk, P.A. Usachev, R.V. Pisarev, A.M. Balbashov, T. Rasing, Nature **435**, 655 (2005)
19. C.D. Stanciu, F. Hansteen, A.V. Kimel, A. Kirilyuk, A. Tsukamoto, A. Itoh, T. Rasing, Phys. Rev. Lett. **99**, 047601 (2007)
20. K. Vahaplar, A.M. Kalashnikova, A.V. Kimel, D. Hinzke, U. Nowak, R. Chantrell, A. Tsukamoto, A. Itoh, A. Kirilyuk, T. Rasing, Phys. Rev. Lett. **103**, 117201 (2009)
21. H. Zabel, S.D. Bader, *Magnetic Heterostructures: Advances and Perspectives in Spinstructures and Spintransport*. Springer Tracts in Modern Physics, vol. 228 (2008)
22. F. Wegelin, D. Valdaitsev, A. Krasyuk, S.A. Nepijko, G. Schönhense, H.J. Elmers, I. Krug, C.M. Schneider, Phys. Rev. B **76**, 134410 (2007)
23. J. Stöhr, S. Anders, IBM J. Res. Dev. **44**, 535 (2000)
24. E. Bauer, J. Phys. Condens. Matter **13**, 11391 (2001)
25. G. Schönhense, H.J. Elmers, S.A. Nepijko, C.M. Schneider, Adv. Imaging Electron Phys. **142**, 159 (2006)
26. H.A. Dürr, C.M. Schneider, in *Handbook of Magnetism and Advanced Magnetic Materials*, ed. by H. Kronmüller, S. Parkin, vol. III (Wiley, Chichester, 2007), p. 1367
27. C. Wiemann, A.M. Kaiser, S. Cramm, C.M. Schneider, Rev. Sci. Instrum. **83**, 063706 (2012)
28. G. Schütz, W. Wagner, W. Wilhelm, P. Kienle, R. Zeller, R. Frahm, G. Materlik, Phys. Rev. Lett. **58**, 737 (1987)
29. C. Chen, F. Sette, Y. Ma, S. Modesti, Phys. Rev. B **42**, 7262 (1990)
30. B. Thole, G. van der Laan, G. Sawatzky, Phys. Rev. Lett. **55**, 2086 (1985)
31. G. van der Laan, B. Thole, G. Sawatzky, J. Goedkoop, J. Fuggle, J. Esteva, R. Karnatak, J. Remeika, H. Dabkowska, Phys. Rev. B **34**, 6529 (1986)
32. E. Arenholz, G. van der Laan, R.V. Chopdekar, Y. Suzuki, Phys. Rev. Lett. **98**, 197201 (2007)
33. M.W. Haverkort, N. Hollmann, I.P. Krug, A. Tanaka, Phys. Rev. B **82**, 094403 (2010)
34. F. Nolting, A. Scholl, J. Stöhr, J. Fompeyrine, H. Siegwart, J.P. Locquet, S. Anders, J. Lüning, E. Fullerton, M. Toney, M.R. Scheinfein, H.A. Padmore, Nature **405**, 767 (2000)
35. I.P. Krug, F.U. Hillebrecht, H. Gomonaj, M.W. Haverkort, A. Tanaka, L.H. Tjeng, C.M. Schneider, Europhys. Lett. **81**, 17005 (2008)
36. I.P. Krug, F.U. Hillebrecht, M.W. Haverkort, A. Tanaka, L.H. Tjeng, H. Gomonay, A. Fraile-Rodriguez, F. Nolting, S. Cramm, C.M. Schneider, Phys. Rev. B **78**, 064427 (2008)
37. C. Schneider, A. Kuksov, A. Krasyuk, A. Oelsner, D. Neeb, S. Nepijko, G. Schönhense, J. Morais, I. Mönch, R. Kaltofen, C.D. Nadaï, N. Brookes, Appl. Phys. Lett. **85**, 2562 (2004)
38. D. Neeb, A. Krasyuk, A. Oelsner, S.A. Nepijko, H.J. Elmers, A. Kuksov, C.M. Schneider, G. Schönhense, J. Phys. Condens. Matter **17**, S1381 (2005)
39. W.K. Hiebert, G.E. Ballentine, L. Lagae, R.W. Hunt, M.R. Freeman, J. Appl. Phys. **92**, 392 (2002)
40. A. Kaiser, C. Wiemann, S. Cramm, C.M. Schneider, J. Phys. Condens. Matter **21**, 314008 (2009)
41. K. Honda, S. Kaya, Sci. Rep. Tohoku Univ. **15**, 721 (1926)
42. C. Scheck, L. Cheng, W.E. Bailey, Appl. Phys. Lett. **88**, 252510 (2006)
43. S.W. Yuan, H.N. Bertram, Phys. Rev. B **44**, 12395 (1991)
44. N.L. Schryer, L.R. Walker, J. Appl. Phys. **45**, 5406 (1974)
45. M.J. Donahue, D.G. Porter, OOMMF user's guide, version 1.0. Tech. rep., National Institute of Standards and Technology, Gaithersburg, MD, 1999
46. P. Grünberg, R. Schreiber, Y. Pang, M. Brodsky, H. Sowers, Phys. Rev. Lett. **57**, 2442 (1986)
47. D.E. Bürgler, P. Grünberg, S. Demokritov, M. Johnson, in *Handbook of Magnetic Materials*, ed. by K. Buschow, vol. 13 (Elsevier Science, Amsterdam, 2001), p. 3
48. C.M. Schneider, A. Kaiser, C. Wiemann, C. Tieg, S. Cramm, J. Electron Spectrosc. Relat. Phenom. **181**, 159 (2010)
49. A. Kaiser, C. Wiemann, S. Cramm, C.M. Schneider, J. Appl. Phys. **109**, 07D305 (2011)

50. A.M. Kaiser, C. Schöppner, F.M. Römer, C. Hassel, C. Wiemann, S. Cramm, F. Nickel, P. Grychtol, C. Tieg, J. Lindner, C.M. Schneider, Phys. Rev. B **84**, 134406 (2011)
51. W.D. Doyle, E. Stinnett, C. Dawson, L. He, J. Magn. Soc. Jpn. **22**, 91 (1998)
52. T.A. Moore, M.J. Walker, A.S. Middleton, J.A.C. Bland, J. Appl. Phys. **97**, 053903 (2005)
53. J. Vogel, S. Cherifi, S. Pizzini, F. Romanens, J. Camarero, F. Petroff, S. Heun, A. Locatelli, J. Phys. Condens. Matter **19**, 476204 (2007)
54. F. Dalla Longa, J.T. Kohlhepp, W.J.M. de Jonge, B. Koopmans, Phys. Rev. B **75**, 224431 (2007)
55. G. Lefkidis, G.P. Zhang, W. Huebner, Phys. Rev. Lett. **103**, 217401 (2009)
56. G. Malinowski, F. Dalla Longa, J.H.H. Rietjens, P.V. Paluskar, R. Huijink, H.J.M. Swagten, B. Koopmans, Nat. Phys. **4**, 855 (2008)
57. B. Koopmans, J.J.M. Ruigrok, F.D. Longa, W.J.M. de Jonge, Phys. Rev. Lett. **95**, 267207 (2005)
58. W. Ackermann, G. Asova, V. Ayvazyan, A. Azima, N. Baboi, J. Bähr, V. Balandin, B. Beutner, A. Brandt, A. Bolzmann, R. Brinkmann, O.I. Brovko, M. Castellano, P. Castro, L. Catani, E. Chiadroni, S. Choroba, A. Cianchi, J.T. Costello, D. Cubaynes, J. Dardis, W. Decking, H. Delsim-Hashemi, A. Delserieys, G.D. Pirro, M. Dohlus, S. Düsterer, A. Eckhardt, H.T. Edwards, B. Faatz, J. Feldhaus, K. Flöttmann, J. Frisch, L. Fröhlich, T. Garvey, U. Gensch, C. Gerth, M. Görler, N. Golubeva, H.J. Grabosch, M. Grecki, O. Grimm, K. Hacker, U. Hahn, J.H. Han, K. Honkavaara, T. Hott, M. Hüning, Y. Ivanisenko, E. Jaeschke, W. Jalmuzna, T. Jezynski, R. Kammering, V. Katalev, K. Kavanagh, E.T. Kennedy, S. Khodyachykh, K. Klose, V. Kocharyan, M. Körfer, M. Kollewe, W. Koprek, S. Korepanov, D. Kostin, M. Krassilnikov, G. Kube, M. Kuhlmann, C.L.S. Lewis, L. Lilje, T. Limberg, D. Lipka, F. Löhl, H. Luna, M. Luong, M. Martins, M. Meyer, P. Michelato, V. Miltchev, W.D. Möller, L. Monaco, W.F.O. Müller, O. Napieralski, O. Napoly, P. Nicolosi, D. Nölle, T. Nuñez, A. Oppelt, C. Pagani, R. Paparella, N. Pchalek, J. Pedregosa-Gutierrez, B. Petersen, B. Petrosyan, G. Petrosyan, L. Petrosyan, J. Pflüger, E. Plönjes, L. Poletto, K. Pozniak, E. Prat, D. Proch, P. Pucyk, P. Radcliffe, H. Redlin, K. Rehlich, M. Richter, M. Roehrs, J. Roensch, R. Romaniuk, M. Ross, J. Rossbach, V. Rybnikov, M. Sachwitz, E.L. Saldin, W. Sandner, H. Schlarb, B. Schmidt, M. Schmitz, P. Schmüser, J.R. Schneider, E.A. Schneidmiller, S. Schnepp, S. Schreiber, M. Seidel, D. Sertore, A.V. Shabunov, C. Simon, S. Simrock, E. Sombrowski, A.A. Sorokin, P. Spanknebel, R. Spesyvtsev, L. Staykov, B. Steffen, F. Stephan, F. Stulle, H. Thom, K. Tiedtke, M. Tischer, S. Toleikis, R. Treusch, D. Trines, I. Tsakov, E. Vogel, T. Weiland, H. Weise, M. Wellhöfer, M. Wendt, I. Will, A. Winter, K. Wittenburg, W. Wurth, P. Yeates, M.V. Yurkov, I. Zagorodnov, K. Zapfe, Nat. Photonics **1**, 336 (2007)
59. H.N. Chapman, A. Barty, M.J. Bogan, S. Boutet, M. Frank, S.P. Hau-Riege, S. Marchesini, B.W. Woods, S. Bajt, W.H. Benner, R.A. London, E. Plonjes, M. Kuhlmann, R. Treusch, S. Dusterer, T. Tschentscher, J.R. Schneider, E. Spiller, T. Moller, C. Bostedt, M. Hoener, D.A. Shapiro, K.O. Hodgson, D. van der Spoel, F. Burmeister, M. Bergh, C. Caleman, G. Huldt, M.M. Seibert, F.R.N.C. Maia, R.W. Lee, A. Szoke, N. Timneanu, J. Hajdu, Nat. Phys. **2**, 839 (2006)
60. A. Locatelli, T.O. Mentes, M.A. Nino, E. Bauer, Ultramicroscopy **111**, 1447 (2011)
61. S. Khan, K. Holldack, T. Kachel, R. Mitzner, T. Quast, Phys. Rev. Lett. **97**, 074801 (2006)
62. C. Stamm, T. Kachel, N. Pontius, R. Mitzner, T. Quast, K. Holldack, S. Khan, C. Lupulescu, E.F. Aziz, M. Wietstruk, H.A. Durr, W. Eberhardt, Nat. Mater. **6**, 740 (2007)
63. C. Boeglin, E. Beaurepaire, V. Halte, V. Lopez-Flores, C. Stamm, N. Pontius, H.A. Durr, J.Y. Bigot, Nature **465**, 458 (2010)
64. T. Pfeifer, C. Spielmann, G. Gerber, Rep. Prog. Phys. **69**, 443 (2006)
65. T. Popmintchev, M.C. Chen, P. Arpin, M.M. Murnane, H.C. Kapteyn, Nat. Photonics **4**, 822 (2010)
66. M. Pretorius, J. Friedrich, A. Ranck, M. Schroeder, J. Voss, V. Wedemeier, D. Spanke, D. Knabben, I. Rozhko, H. Ohldag, F.U. Hillebrecht, E. Kisker, Phys. Rev. B **55**, 14133 (1997)
67. P. Grychtol, R. Adam, S. Valencia, S. Cramm, D.E. Buergler, C.M. Schneider, Phys. Rev. B **82**, 054433 (2010)

68. P. Grychtol, R. Adam, A.M. Kaiser, S. Cramm, D.E. Buergler, C.M. Schneider, J. Electron Spectrosc. Relat. Phenom. **184**, 287 (2011)
69. R. Adam, P. Grychtol, S. Cramm, C.M. Schneider, J. Electron Spectrosc. Relat. Phenom. **184**, 291 (2011)
70. C. La-O-Vorakiat, M. Siemens, M.M. Murnane, H.C. Kapteyn, S. Mathias, M. Aeschlimann, P. Grychtol, R. Adam, C.M. Schneider, J.M. Shaw, H. Nembach, T.J. Silva, Phys. Rev. Lett. **103**, 257402 (2009)
71. S. Mathias, C. La-O-Vorakiat, P. Grychtol, P. Granitzka, E. Turgut, J.M. Shaw, R. Adam, H.T. Nembach, M.E. Siemens, S. Eich, C.M. Schneider, T.J. Silva, M. Aeschlimann, M.M. Murnane, H.C. Kapteyn, Proc. Natl. Acad. Sci. USA **109**, 4792 (2012)
72. S. Mathias, C. La-O-Vorakiat, P. Grychtol, R. Adam, S. Mark, J.M. Shaw, H. Nembach, M. Aeschlimann, C.M. Schneider, T. Silva, M.M. Murnane, H.C. Kapteyn, *OSA Technical Digest* (CD) (Optical Society of America, 2010), p. TuE33
73. B. Koopmans, M. van Kampen, J.T. Kohlhepp, W.J.M. de Jonge, Phys. Rev. Lett. **85**, 844 (2000)
74. C. La-O-Vorakiat, E. Turgut, C.A. Teale, H.C. Kapteyn, M.M. Murnane, S. Mathias, M. Aeschlimann, C.M. Schneider, J.M. Shaw, H.T. Nembach, T.J. Silva, Phys. Rev. X **2**(1), 011005 (2012)
75. F. Hillebrecht, T. Kinoshita, D. Spanke, J. Dresselhaus, C. Roth, H. Rose, E. Kisker, Phys. Rev. Lett. **75**, 2224 (1995)
76. A. Mikkelsen, J. Schwenke, T. Fordell, G. Luo, K. Klunder, E. Hilner, N. Anttu, A.A. Zakharov, E. Lundgren, J. Mauritsson, J.N. Andersen, H.Q. Xu, A. L'Huillier, Rev. Sci. Instrum. **80**, 123703 (2009)

Chapter 2
Spin-Transfer Torque Effects in Single-Crystalline Nanopillars

D.E. Bürgler, R. Lehndorff, V. Sluka, A. Kákay, R. Hertel, and C.M. Schneider

Abstract We review our recent work on spin-transfer torque (STT) effects in single-crystalline, all-metal nanopillars. The experiments deal with current-driven magnetization switching and excitation of steady-state high-frequency magnetic oscillatory modes. The interplay between the magnetocrystalline anisotropy and STT gives rise to a two-step switching mechanism and to zero-field magnetic precession. Both are manifestations of the angular STT asymmetry and are explained within Slonczewski's theory for currents and torques in metallic multilayers. The normal and inverse torques observed in a double spin-valve nanopillar are related to spin-dependent interface resistances and confirm ab initio calculations by Stiles and Penn. The magnetization of a nanodisk of suitable aspect ratio can be switched by STT between the quasi-uniform and the vortex configuration. The STT-excited gyrotropic mode of the vortex emits more microwave power than the standing-wave mode and can be locked to an external high-frequency signal in a wide frequency range.

D.E. Bürgler (✉) · R. Lehndorff · V. Sluka · A. Kákay · R. Hertel · C.M. Schneider
Peter Grünberg Institut, Electronic Properties (PGI-6) and Jülich-Aachen Research Alliance, Fundamentals for Future Information Technology (JARA-FIT), Research Center Jülich GmbH, 52425 Jülich, Germany
e-mail: d.buergler@fz-juelich.de

Present address:
R. Lehndorff
Sensitec GmbH, Hechtsheimerstr. 2, 55131 Mainz, Germany

Present address:
V. Sluka
Institute of Ion Beam Physics and Materials Research, Helmholtz-Zentrum Dresden-Rossendorf e.V., 01314 Dresden, Germany

Present address:
R. Hertel
Institut de Physique et Chimie des Matériaux de Strasbourg, CNRS UMR 7504, Université de Strasbourg, 23 rue du Loess, BP 43, 67034 Strasbourg, France

B. Aktaş, F. Mikailzade (eds.), *Nanostructured Materials for Magnetoelectronics*, Springer Series in Materials Science 175, DOI 10.1007/978-3-642-34958-4_2,

2.1 Introduction

During the last decade spin-transfer torque (STT) physics has attracted a lot of scientific interest after the transfer of spin momentum by spin-polarized currents was predicted and observed in the wake of the seminal discovery of giant magnetoresistance (GMR), which kicked off the fast-paced development of spintronics. Whereas the GMR effect is well suited for sensing and detecting magnetization states, STT provides a means to act on the magnetization, thus complementing GMR and extending the toolbox for spintronics.

From a fundamental point of view, STT represent a completely new means to affect and excite the magnetization of nanomagnets without applying an external magnetic field and in realms that are not reachable by magnetic fields alone. The major effects of current-induced magnetization dynamics are (i) current-induced magnetization switching, (ii) current-driven excitation of steady magnetization oscillations, and (iii) current-driven domain wall motion.

Obviously, these effects are of outmost interest for present and future spintronic applications, because they provide a smart means to locally and individually control the magnetization state of nanoscale magnets, for instance (i) in magnetic random access memories (MRAMs) for the writing process, (ii) in spin-torque oscillators (STOs) for the tunable generation of microwave signals in a nanoscale, solid-state, and CMOS-compatible environment, and (iii) in racetrack memories for the position control of the domain wall pattern that represents the stored information. For instance, STOs are discussed as major components for intra- and inter-chip communication with less dissipation as well as for microwave-assisted hard disk drive (HDD) write heads that push the superparamagnetic limit to yet higher storage densities.

For a comprehensive introduction to STT physics, its theoretical framework ranging from ab initio calculations to micromagnetic simulations, the experimental procedures and challenges, and prospective applications, the reader is referred to a series of review articles on various aspects of STT [1–9].

Here, we review our work on STT effects in single-crystalline nanopillars. Section 2.2 gives an introduction to STTs with an emphasis on developing a physical picture for the origin of the effect. The Slonczewski model is introduced to set the stage for the analysis of our experiments. The sample fabrication leading to single-crystalline nanopillars is described in Sect. 2.3. In Sect. 2.4 we show experimentally that the nanomagnets exhibit magnetocrystalline anisotropy due to their single-crystallinity that endures the fabrication process. We demonstrate normal and inverse magnetization switching in a single nanopillar, which provides strong support for the theoretical description based on spin-dependent resistivities. Section 2.5 addresses the interplay between magnetocrystalline anisotropy and STT, which leads to a two-step switching process and to zero-field excitations of steady magnetization oscillations. Both effects are manifestations of the angular spin torque asymmetry introduced in Slonczewski's model. In Sect. 2.6, we study STT-driven vortex dynamics in the nanopillar geometry. In a given nanopillar we excite either the gyrotropic or the standing-wave mode and compare the STO properties, which turn out

to be superior for the vortex STO. In addition, we demonstrate the injection locking of the gyrotropic vortex excitation to an external high-frequency signal, which is a prerequisite for the synchronization of arrays of STOs. A summary is given in Sect. 2.7.

2.2 Spin-Transfer Torque (STT)

In 1996 Slonczewski [10] and Berger [11] predicted that a spin-polarized current propagating into a ferromagnetic (FM) layer exerts a torque on the magnetization of the layer, due to the exchange interaction between the electrons and the local magnetic moments. In layered metallic systems with alternating magnetic and nonmagnetic layers, a current flowing perpendicular to the plane of the layers (CPP geometry) is polarized by one FM layer and transfers spin angular momentum to another FM layer, where the transferred momentum acts as a torque on the magnetization; this is called the *spin-transfer torque* (STT). For this torque to be sufficient to perturb the magnetization from equilibrium, large current densities (e.g., $>10^7$ A/cm^2 for metallic systems) are required.

2.2.1 Phenomenology

The STT due to currents of opposite polarity can reversibly switch the magnetization between equilibrium states, e.g., the two stable equilibria due to a uniaxial anisotropy. This process is called *current-induced magnetization switching* and does not require an external magnetic field to induce switching. In Fig. 2.1(b) we consider two FM layers separated by a non-ferromagnetic (NM) spacer with a thickness below its spin diffusion length. The FM layers are different in such a way (e.g., the thickness or coercive field), that one of them can be remagnetized more easily than the other. We distinguish the two layers by calling them "free" and "fixed," respectively. When electrons flow from the fixed to the free layer,[1] the magnetization of the free layer $\vec{M}_{\text{free}}$ aligns parallel to the magnetization of the fixed layer $\vec{M}_{\text{fixed}}$ and this alignment is stabilized [Fig. 2.1(b) left side]. When the current direction is reversed, however, the antiparallel alignment is more stable and is therefore taken [Fig. 2.1(b) right side]. Thus, a magnetization reversal can be induced by reversing the polarity of the DC current flowing through the layers.

Changes of the relative magnetization alignment in FM/NM/FM trilayers can be detected via the giant magnetoresistance (GMR) effect, which describes the phenomenon where the magnetization alignment controls the electric resistance, i.e., the current flow [Fig. 2.1(a)]. Therefore, the current-induced magnetization reversal

[1] Whenever we refer to the direction of a current, we mean the direction of the electron flux rather than the (opposite) technical current direction.

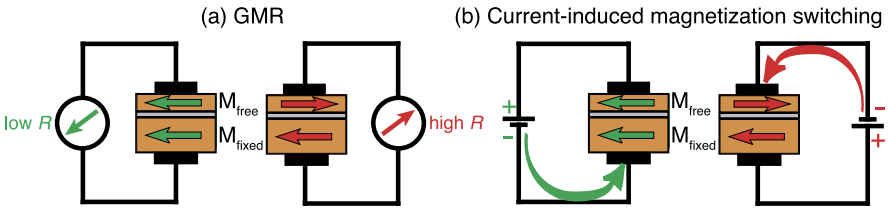

Fig. 2.1 Phenomenology of (**a**) GMR and (**b**) current-induced magnetization switching. (**a**) The electric resistance of a trilayer structure depends on the alignment of the layer magnetizations. (**b**) The stable alignment of the magnetizations depends on the polarity of the current flowing perpendicularly through the trilayer

can be electrically measured by recording the resistance U/I (or differential resistance dU/dI) while sweeping the DC current I. The result is a current hysteresis loop, as shown for instance in Fig. 2.10. Current-induced magnetization switching was first observed in 1999 by Myers et al. [12] and Katine et al. [13].

The direct comparison of GMR and STT in Fig. 2.1 suggests that they are reciprocal effects in the sense of Newton's third law "*actio* equals *reactio*": GMR describes the fact that the magnetization alignment controls the current flow, whereas STT allows the current to control the magnetization alignment.

In a more general approach we have to consider the STT as an additional term in the equation of motion of a magnetization, the Landau–Lifshitz–Gilbert (LLG) equation. Thus, current-induced magnetization switching is a special case of current-induced magnetization dynamics. The STT acting on the free layer has been calculated by Slonczewski [10] as

$$\frac{1}{M_S}\frac{d\vec{M}_{\text{free}}}{dt} = \frac{I}{A}\cdot g(\theta)\cdot \vec{m}_{\text{free}} \times (\vec{m}_{\text{free}} \times \vec{m}_{\text{fixed}}), \tag{2.1}$$

where $\vec{m}_{\text{free,fixed}}$ are the normalized magnetization vectors of the free and the fixed layer, respectively, and M_S is the saturation magnetization. I/A is the current density. The linear dependence on I yields the reversed STT upon reversing the current direction. $g(\theta)$ is the material-dependent STT efficiency function, which is a measure of the conversion of current into STT. In general it depends on the angle θ between $\vec{M}_{\text{free}}$ and $\vec{M}_{\text{fixed}}$. The materials enter via the spin polarization P, spin-dependent volume and interface resistivities, and other transport properties. The double cross product is proportional to $\sin(\theta)$ and indicates that the STT is perpendicular to both $\vec{M}_{\text{fixed}}$ and $\vec{M}_{\text{free}}$. If $\vec{M}_{\text{fixed}}$ is aligned with the effective field, then the STT is—depending on the sign of the prefactor—parallel or antiparallel to the Gilbert damping torque. Therefore, the STT can act as an additional damping or—the more interesting case—as an antidamping, i.e., excitation, which can reduce or compensate the Gilbert damping. It turns out that under certain conditions, e.g., when the degeneracy of the parallel and antiparallel alignment of a trilayer with uniaxial anisotropy is lifted by a strong external field, the STT completely compensates the Gilbert damping torque and gives rise to steady-state oscillatory modes, as first reported by Kiselev et al. [14]. In this manner new oscillatory dynamic modes can

be excited that are not attainable with magnetic fields alone. An example is that of large-angle precessional modes with excitation angles as large as 180°. Any oscillatory motion of $\vec{M}_{\text{free}}$ with respect to $\vec{M}_{\text{fixed}}$ results, due to the GMR effect, in a variation of the resistance. Therefore, the DC current that gives rise to the STT effect generates an AC voltage with typical frequencies in the GHz range that can be measured with a suitable high-frequency setup. Such devices are called *spin-torque oscillators* (*STOs*) and will be discussed in Sects. 2.5 and 2.6.

2.2.2 Physical Picture: Absorption of the Transverse Spin Current Component

In view of the high current densities, one might suppose that the Oersted field generated by the current is responsible for the current-induced magnetization switching and dynamics. However, the Oersted field has the wrong symmetry. Its circular field lines lie in the plane of the sample and favor a vortex-like magnetization state with the sense of rotation depending on the current polarity. The resistance change due to GMR when a clockwise or anti-clockwise circulating vortex is formed in the free layer is the same. Therefore, a resistance increase would appear symmetrically for both current polarities in clear contrast to the experimentally observed behavior. The strongest Oersted field occurs at the pillar circumference and scales like I/d, where I is the current and d the pillar diameter. The STT, on the other hand, scales like the current density I/d^2. Therefore, the STT effect becomes stronger below a certain structure size d_c. Theoretical estimates and available experiments suggest a d_c of the order of 100 nm. This fundamental size restriction fortunately coincides with the possibilities of e-beam lithography and at the same time yields the needed current densities at technically convenient current amplitudes [10 mA flowing through an area of $(100\ \text{nm})^2$ correspond to $10^8\ \text{A/cm}^2$]. In practice, one must always be aware of the presence of the Oersted field and take into account its possible influence.

In order to develop a physical picture for the origin of the STT, we start by considering the fate of a polarized current that enters from a metallic NM into a FM. The situation is sketched in Fig. 2.2(a). We assume that the incident current is polarized along an axis tilted by the angle θ with respect to the magnetization $\vec{M}$ of the FM. The normalized spinor Ψ_{in} of an incident electron can be written as a superposition of spin-up and spin-down components with respect to the quantization axis defined by $\vec{M}$. The amplitudes are $\cos(\theta/2)$ and $\sin(\theta/2)$, respectively, and correspond to a transverse component of the spin vector given by $\sin(\theta)$. At the interface to the FM the potential experienced by the electron changes and becomes spin-dependent. Inside the FM this gives rise to the spin-split density of states, and at the interface it leads to spin-dependent transmission and reflection. Therefore, the transmitted and reflected spinors, Ψ_{trans} and Ψ_{ref}, are modified superpositions compared to the incident spinor. This leads unavoidably to different transverse spin components and, thus, to a discontinuity in the transverse spin current. The "missing" transverse spin current is absorbed at the interface and acts as a current-induced torque on $\vec{M}$. This

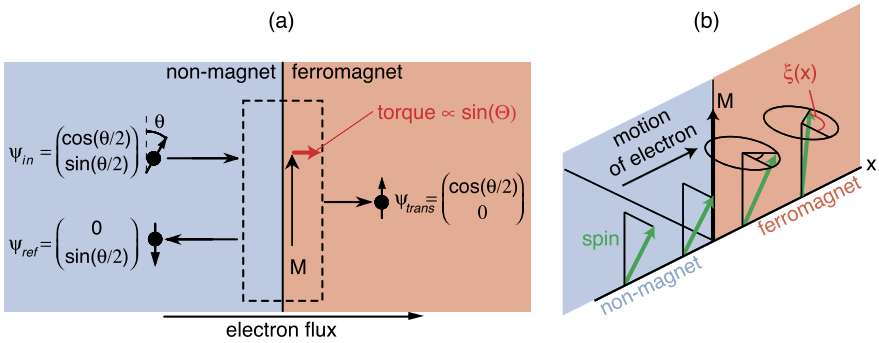

Fig. 2.2 Two effects contributing to the absorption of the transversal spin current component in the interface region (*dashed box*) between an NM and an FM. (**a**) Spin filtering: The incoming Ψ_{in}, transmitted Ψ_{trans}, and reflected Ψ_{ref} spinors for the idealized case of perfect spin filtering are indicated. The absorbed transversal spin current is proportional to $\sin(\theta)$ and acts as a torque on the interface magnetization. (**b**) Spatial precession of the spin in the ferromagnet: The phase ξ is constant in the non-magnet, but increases in the FM with distance x from the interface

effect occurs for each electron and is called *spin filtering* [10]. Figure 2.2(a) shows the spinors in the extreme case of perfect spin filtering. This means that only one spin orientation (here spin-up) can propagate in the FM, whereas the other cannot and therefore is completely reflected at the interface. For realistic ferromagnets like the 3d transition metals (i.e., Fe and Co) and their alloys, roughly 50 % of the transversal component is absorbed, and the transmitted as well as reflected spinors still carry transversal components [15].

The actual current polarization of the transmitted and reflected currents is given by the sum over all electronic states contributing to the transport. This introduces two additional effects. The first one arises because the reflection and transmission amplitudes at the interface may be complex. This means that the spin of an incoming electron rotates upon reflection and transmission. The angle of rotation is generally different for each state under consideration, as it depends on the k vector of the incoming electron. The cancellation, which occurs when we sum over all the resulting different spin vectors, reduces the net outgoing transverse spin current. This is an entirely quantum mechanical phenomenon, for which there is no classical analog. A second effect arises because spin-up and spin-down components of an electron have the same wave vector $k^{\uparrow,\downarrow}$ in the NM, but different wave vectors when they are transmitted into the FM, $\Delta k = k^{\downarrow} - k^{\uparrow} \neq 0$. This is a consequence of the spin-split density of states. The two components are coherent, and a spatial phase $\xi(x) = \xi_0 + \Delta k x$ builds up. This corresponds to a precession of the spin vector in space [Fig. 2.2(b)]. The precession frequency is different for electrons from different portions of the Fermi surface due to different Δk. After summing over all conduction electrons, almost complete cancellation of the transverse spin occurs after propagation into the FM by a few lattice constants.

Combining all three effects—(i) spin filtering, (ii) rotation of the reflected and transmitted spin, and (iii) spatial precession of the spin in the FM—, to a good

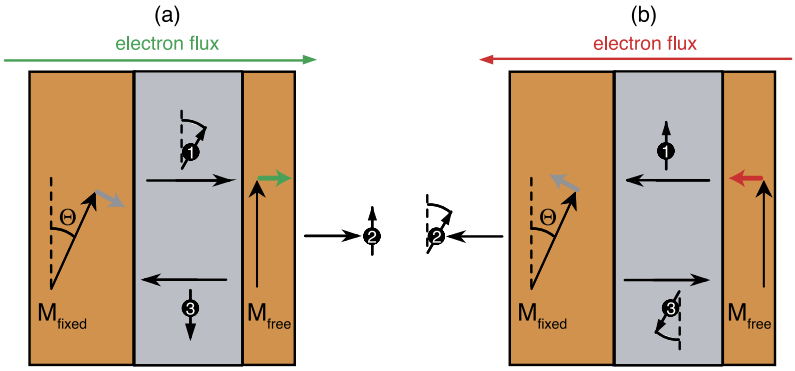

Fig. 2.3 Physical picture of the current-induced magnetization switching. Orange regions represent the two FM layers. Due to the assumed asymmetry, $\vec{M}_{\text{fixed}}$ does not respond to the torque (*short gray arrows*) acting on it, whereas $\vec{M}_{\text{free}}$ can follow the torque (*short green* and *red arrows*). The *numbers* in the spins refer to the sequence of the description. (**a**) and (**b**) show the situation for opposite electron flux directions (see footnote 1), which result in stable or unstable parallel alignment, respectively

approximation, the transverse component of the transmitted and reflected spin currents are zero for most systems of interest (the completeness of the cancellations depends on the actual band structures). Thus, the incoming transverse spin current is absorbed at the interface to the FM and acts as a current-induced torque on the magnetization. A comprehensive theoretical treatment of these effects is given in Ref. [15].

In Fig. 2.3 we consider a fixed and a free FM layer, which differ for instance in their coercivities. $\vec{M}_{\text{fixed}}$ and $\vec{M}_{\text{free}}$ are assumed to enclose an angle θ. The current is spin-polarized in the first FM layer, passes through the spacer layer, which is much thinner than its spin-flip length, and enters into the second FM layer, where the current is repolarized according to the local quantization axis given by the local magnetization. The repolarization process proceeds by the mechanisms described above. In Fig. 2.3(a) the electrons flow from the fixed to the free layer (see footnote 1). A current polarized by the fixed layer (1) hits the free layer and transfers its transversal component as a torque to the free layer. Part of the current is transmitted (2) and another part is reflected (3). This reflected current can now be considered as a polarized current impinging on the fixed layer. Again, the transversal component will be absorbed and acts as a torque on the fixed layer. However, we assume that for the fixed layer the torque is not sufficient to induce a coherent rotation of $\vec{M}_{\text{fixed}}$. Instead incoherent spin waves are generated to dissipate the energy and angular momentum associated with the exerted torque. Therefore, $\vec{M}_{\text{fixed}}$ resists the torque, and only $\vec{M}_{\text{free}}$ starts to rotate due to its lower coercivity in order to reach the stable parallel alignment with $\vec{M}_{\text{fixed}}$. For the opposite current polarity in Fig. 2.3(b), we obtain a similar situation, but the resulting torques point in opposite directions. Therefore, the stable state corresponds to the antiparallel alignment of $\vec{M}_{\text{free}}$ and $\vec{M}_{\text{fixed}}$. Note that in this case the torque acting on $\vec{M}_{\text{free}}$ arises from the current, which has been

reflected (3) from the fixed layer. Obviously, the asymmetry (fixed ↔ free) plays an important role, which is very reasonable because "left" and "right" flowing current cannot be distinguished in the symmetric case.

Up to now we have assumed that the polarization of the FM layers is positive; i.e., the current is polarized in the direction of the majority electrons. It is obvious from Fig. 2.3 that the torques acting on the free layer reverse when the fixed layer transmits/reflects a current with opposite polarization [rotate arrow (1) in Fig. 2.3(a) and arrow (3) Fig. 2.3(b) by 180°]. In contrast, the sign of polarization of the free layer has no influence on the direction of the torques. Therefore, normal (inverse) current-induced switching is expected for positive (negative) polarization of the fixed layer.

2.2.3 Slonczewski's Model

We have chosen Fe and Ag for our work not only because of their good epitaxial match (see Sect. 2.3), but also because of the specific spin-dependent transport properties of Ag/Fe(001) interfaces. According to Stiles and Penn [16] the spin-dependent interface resistances $R^{+,-}$ differ by more than one order of magnitude, $AR^{+}_{\mathrm{Fe/Ag(100)}} = 1.07 \times 10^{-15}\ \Omega\,\mathrm{m}^2$ and $AR^{-}_{\mathrm{Fe/Ag(100)}} = 12.86 \times 10^{-15}\ \Omega\,\mathrm{m}^2$, where A is the pillar cross section. Therefore, we can apply Slonczewski's theory [17] for a unified description of GMR and STT, which is based on two main assumptions: (i) negligible interfacial reflection for majority spin electrons and (ii) electrically symmetric trilayer system. Assumption (i) is fulfilled because $AR^{+}_{\mathrm{Fe/Ag(100)}} \ll AR^{-}_{\mathrm{Fe/Ag(100)}}$, and (ii) is fulfilled even for trilayers with unequal Fe thicknesses because the interface resistances are much larger than the volume resistance.

In Slonczewski's theory, the angular dependences of the CPP-GMR effect expressed by the normalized resistance $r(\theta)$ and the magnitude of the STT $L_{\mathrm{STT}}(\theta)$ on the angle θ between the two layer magnetizations are given by [17]

$$r(\theta) = \frac{R(\theta) - R(0°)}{R(180°) - R(0°)} = \frac{1 - \cos^2(\theta/2)}{1 + \chi \cos^2(\theta/2)} \tag{2.2}$$

$$L_{\mathrm{STT}}(\theta) = \frac{\hbar I P \Lambda}{4Ae} \frac{\sin(\theta)}{\Lambda \cos^2(\theta/2) + \Lambda^{-1} \sin^2(\theta/2)} \tag{2.3}$$

$$\text{with } \Lambda^2 = \chi + 1 = AG \frac{R^+ + R^-}{2}. \tag{2.4}$$

$R(\theta)$ is the dependence of the resistance on θ, $G = e^2 k_f^2 / \sqrt{3}\pi h$ the conductance of the interlayer, and $R^{+(-)}$ is the total (interface and bulk) resistance for spin-up (spin-down) electrons of one half of the trilayer system consisting of lead, FM, and interfaces (NM/FM and FM/lead).

$$P = \frac{R^- - R^+}{R^- + R^+} \tag{2.5}$$

is the spin polarization. The spin-torque asymmetry parameter Λ (or χ) is a mea-

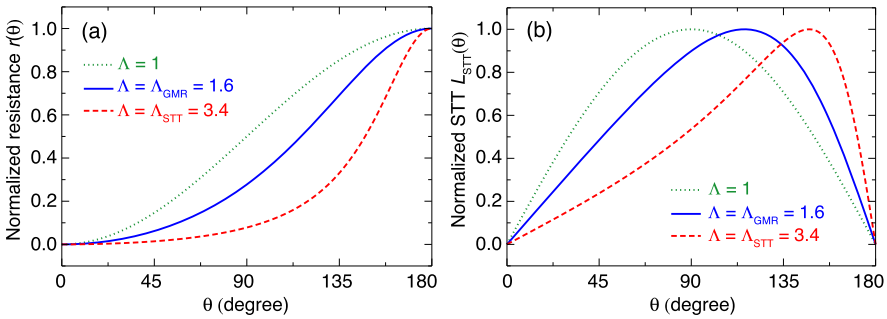

Fig. 2.4 Angular variations of the normalized resistance (**a**) and the magnitude of the STT (**b**) according to (2.2)–(2.4) for three different Λ values. The *dotted lines* show the symmetric behavior ($\Lambda = 1$). The *solid* and *broken lines* correspond to the asymmetry parameters that we determine from GMR ($\Lambda_{\mathrm{GMR}} = 1.6$) and STT ($\Lambda_{\mathrm{STT}} = 3.4$) experiments, respectively; see Sect. 2.5.1

sure of the deviation from the symmetric behavior, which is given by $\Lambda = 1$ ($\chi = 0$). Λ^2 expresses the ratio of the spin-averaged resistance of one FM layer including lead and interfaces to the intrinsic interlayer resistance. If it deviates from unity, the resistance of the FM parts is different from the interlayer resistance, which leads to an enhanced spin accumulation. The expectations according to (2.2) and (2.3) are plotted in Fig. 2.4 for various values of Λ. The dotted lines for $\Lambda = 1$ represent the symmetric case. The GMR effect is then given by $r(\theta) = \sin^2(\theta/2)$ with point symmetry about the value at $\theta = 90°$ as known for current-in-plane GMR. The angular dependence of the STT is reduced to $L_{\mathrm{STT}}(\theta) \propto \sin(\theta)$ and is thus mirror symmetric about $\theta = 90°$. Having $\Lambda \neq 1$ breaks these symmetries.

For the Fe/Ag(001) interfaces studied in this work, based on theoretical calculations [16], we expect an asymmetry parameter $\Lambda = 4.0$ yielding a strongly asymmetric behavior as well as a large polarization $P = 0.85$, which should result in strong STT effects. Corresponding results are presented in Sect. 2.5.

2.3 Sample Fabrication

The generation of STT is an interface effect in the sense that most of the spin momentum transferred by the spin-polarized current is absorbed within a few atomic layers at the NM/FM interface; see Fig. 2.2(b) in Sect. 2.2.2. Defects at the interfaces, in the bulk, and at the edges of the nanostructures can cause additional scattering and tend to reduce the spin polarization in the NM spacer layer and can act as magnetic pinning centers that influence the magnetization dynamics. Clean and well-defined layers and interfaces are therefore of crucial importance for optimizing the STT effects and also for meaningful comparisons with theoretical models, i.e., band structure calculations for the determination of transport properties such as spin-dependent interface resistances and micromagnetic simulations of the magnetization dynamics. Magnetic and electric properties, e.g., magnetization, anisotropy,

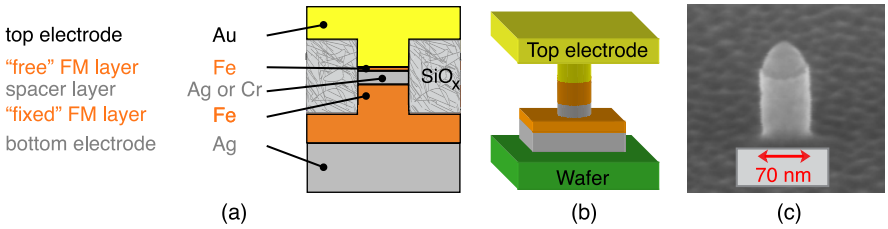

Fig. 2.5 (**a**) Sequence, thicknesses, and functions of the layers within the multilayer stack. (**b**) 3D view of the final nanopillar structure and the electrodes. (**c**) SEM micrograph of a free-standing nanopillar after ion beam etching

and resistivity, are expected to be spatially more homogeneous in the absence of grain boundaries. For these reasons we aim, in contrast to most previous studies, at preparing single-crystalline nanopillars. This is achieved by combining the growth of the FM and NM layers by thermal evaporation on well-defined crystalline substrates in a molecular beam epitaxy (MBE) system under ultra-high vacuum (UHV) conditions with a mixed optical and e-beam lithographic process that is performed after completing the deposition of all relevant layers including a Au protection layer.

2.3.1 MBE Growth of Single-Crystalline Multilayers

We choose bcc-Fe(001) as material for the FM layers and Ag(001) and Cr(001) for the spacer layers. Bottom electrodes are fabricated from the 150 nm thick Ag(001) layer that we grow as a buffer on GaAs(001) wafers. All these materials—GaAs(001), Ag(001), Fe(001), Cr(001)—and Au(001), which we use as a protective cap layer, have a low lattice mismatch of the order of 1–2 %, if rotational epitaxy is taken into account. Fe(001), for instance, grows 45° rotated on Ag(001) such that Fe(001) $\langle 100 \rangle \parallel$ Ag(001)$\langle 110 \rangle$. The GaAs(001) substrates (10×10 mm^2) are precleaned by annealing them under UHV conditions for 60 min at 580 °C to desorb the native oxide. Then we deposit 1 nm Fe as a seed layer, which improves the growth of the subsequent 150 nm thick Ag(001) buffer layer. Thicknesses are controlled by quartz crystal monitors. The growth temperature is 100 °C and the buffer system is post-annealed at 300 °C for 60 min to obtain a smooth surface [18]. The Fe(001) layers are 2 to 20 nm thick, whereas typical spacer thicknesses range between 0.9 nm for Cr(001) and 6 nm for Ag(001). The layer sequence is shown in Fig. 2.5(a). The Fe layers have a bcc structure and exhibit cubic magnetocrystalline anisotropy. The shape anisotropy of the thin film geometry keeps the magnetization mainly in the plane of the film, where it is subject to a fourfold anisotropy of magnetocrystalline origin. The easy axes correspond to the Fe(001)$\langle 100 \rangle$ crystallographic axes. These layers as well as the final 50 nm thick Au(001) capping layer are grown at room temperature. The single-crystalline growth and the epitaxial relationship are confirmed by low-energy electron diffraction (LEED) after each layer. The spots characteristic of (001) surfaces slightly broaden with increasing total thickness, but still indicate high crystalline quality, even for the Au(001) capping

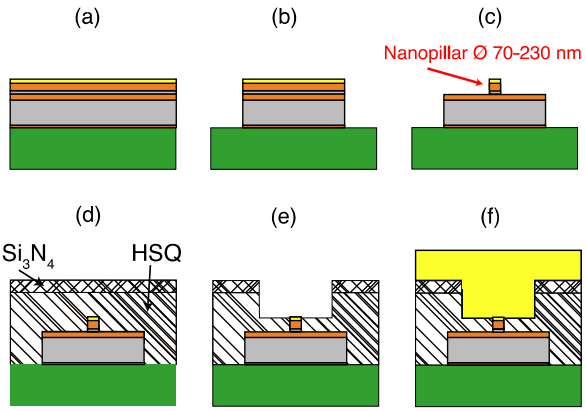

Fig. 2.6 Lithographic process: (**a**) Extended epitaxial multilayer grown by MBE, (**b**) definition of about 50 µm wide bottom electrodes by optical lithography and IBE, (**c**) definition of nanopillars of 70–230 nm diameter by e-beam lithography and IBE, (**d**) planarization by HSQ and additional insulation by Si_3N_4; e-beam exposure converts HSQ into insulating SiO_x, (**e**) opening of a 10×10 µm^2 window to the top of the nanopillar by IBE, and (**f**) definition of the top electrodes by optical lithography and lift-off. The colors of different materials correspond to those of Fig. 2.5

layer. Therefore, the crucial interfaces for the STT effects in the FM/NM/FM trilayer are well protected against oxidation, when the samples are brought to air for the lithographic patterning, which is performed in a cleanroom. In some cases, the laterally extended multilayer is magnetically characterized by magneto-optic Kerr effect (MOKE) or Brillouin light scattering (BLS) prior to the next fabrication step, for instance, in order to determine anisotropy and coupling constants.

2.3.2 Lithographic Process

We developed a mixed optical and e-beam lithographic process to define nanopillars with circular cross section and diameters ranging from 70 to 230 nm. This is achieved by e-beam lithography and ion beam etching (IBE) [19]. The much larger structures of the top and bottom electrodes that connect the nanopillar to contact pads of 300×300 µm^2 or coplanar waveguides of similar dimensions are patterned by optical lithography and lift-off. As DC currents of up to 50 mA will be applied to the structures and weak high-frequency (HF) signals of the order of nW in the GHz range are to be detected simultaneously, proper electrical insulation, thermal contact to the environment, and impedance considerations are important design issues.

The lithographic fabrication procedure is sketched in Fig. 2.6 and starts with the extended, Au-capped multilayer [Fig. 2.6(a)]. First the areas of the prospective bottom electrodes are covered with resist by optical lithography. The uncovered material is then removed with IBE [Fig. 2.6(b)]. In the following e-beam lithography step, resist dots of the desired diameter (50 to 230 nm) are placed into the

$15 \times 15\ \mu m^2$ contact area located in the middle of the previously defined structures. We employ a hydrogen silsesquioxane (HSQ) electron beam resist (fOx-12). Successively, the layers are milled down either to the spacer layer or to the bottom electrode by IBE, resulting in nanopillars with diameters slightly larger (70 to 230 nm) than those of the resist dots [Fig. 2.6(c)]. If both FM layers are (at least partially) laterally confined as sketched in Fig. 2.5(a), significant dipolar coupling arises from the stray fields emanating from the edges of the FM elements. This sometimes unwanted coupling is strongly reduced when the etching is stopped within the spacer layer such that the bottom FM layer remains extended over several micrometers [sketch in Fig. 2.5(b)]. This, however, requires control of the etching depth at the nanometer scale that can only be achieved via precise calibration of etching rates. A scanning electron microscope (SEM) picture of a 70 nm diameter free-standing nanopillar is shown in Fig. 2.5(c). In order to laterally insulate these structures from each other and planarize the sample surface again, HSQ is used prior to the deposition of a 50 nm thick Si_3N_4 layer that grows on inclined surfaces [Fig. 2.6(d)]. The Si_3N_4 layer prevents electrical shortings at the sharp edges of the bottom electrodes that were formed in the first IBE step. The sample is then covered with optical resist apart from $10 \times 10\ \mu m^2$ contact windows above the nanopillars, which are opened by IBE so that the pillar tops are cleared from the insulating material [Fig. 2.6(e)]. A short reactive ion etching (RIE) step is additionally performed to selectively remove some remaining HSQ. Finally the top Au electrode is deposited by a negative optical lithography step and subsequent lift-off [Fig. 2.6(f)]. During this step a "Au–Au interface" is formed between the electrode material and the Au capping layer previously grown in the MBE system. The RIE step ensures clean conditions to avoid unwanted scattering centers or even a tunneling barrier. All other interfaces, in particular those between the FM and NM spacer, are formed under UHV conditions and are untouched by the lithographic process.

This fabrication process yields well-defined layered pillar structures that are well embedded in an insulator matrix, which provides good mechanical and thermal stability allowing for measurements over expanded periods of time and at high current densities. The SiO_x insulation also provides good protection against oxidation such that some samples could be measured even several years after fabrication and storage under ambient conditions.

Finally, note that this procedure can be applied to any multilayer structure grown by any deposition method as long as there is a thick enough buffer layer to form the bottom electrode and a protective cap layer, preferentially made from Au.

2.4 Normal and Inverse Current-Induced Switching in a Single Pillar

As a first example we consider current-induced magnetization switching in a single-crystalline double spin valve comprising three FM layers and two different spacer layers, namely Fe(14 nm)/Cr(0.9 nm)/Fe(10 nm)/Ag(6 nm)/Fe(2 nm). The different

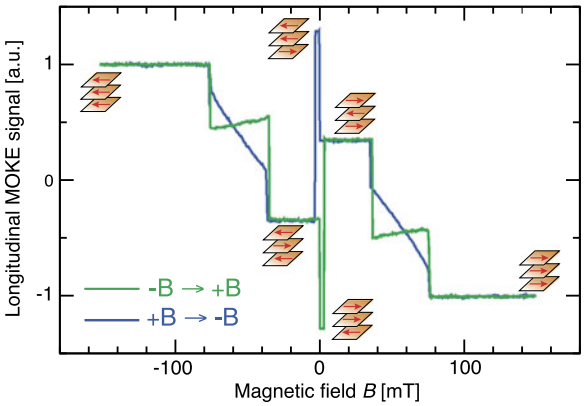

Fig. 2.7 MOKE hysteresis loop of the extended Fe/Cr/Fe/Ag/Fe layered system measured with the external magnetic field parallel to an easy axis of Fe. The interlayer exchange coupling stabilizes the fully antiferromagnetic state between ±3 and ±35 mT

material combinations at the FM/NM interfaces (Fe/Ag and Fe/Cr) allow observing of normal and inverse current-induced magnetization switching in a single device [19]. The multilayer is structured into a nanopillar such that all three FM layers have circular cross sections with a diameter of about 150 nm.

2.4.1 Evidence for Magnetocrystalline Anisotropy in Nanopillars

The layer sequence is designed such that the bottom and central FM layers [Fe(14 nm) and Fe(10 nm)] are antiferromagnetically coupled by interlayer exchange coupling over the Cr interlayer. Therefore, the central Fe(10 nm) layer is magnetically harder with respect to the top Fe(2 nm) layer. We employ the longitudinal MOKE to confirm this picture and measure the magnetic properties of the samples. Figure 2.7 shows the hysteresis loop with the magnetic field applied in the film plane and parallel to one of the easy axes of the Fe layers. The saturation field of the system is $|B_S| = 76$ mT. For smaller fields the central Fe(10 nm) layer remagnetizes via a canted state to the fully antiferromagnetic configuration of the trilayer stack below ±35 mT. After reversing the field direction, a further jump of the signal corresponds to the reversal of the topmost 2 nm-thick Fe layer at ±0.3 mT. At ±3 mT the two coupled Fe layers reverse simultaneously due to their unequal thicknesses. By fitting the MOKE measurements and additional BLS measurements [20] (not shown here) we extract the magnetic properties of each layer. The saturation magnetization M_S and the crystalline anisotropy constant K_1 of the Fe(14 nm) and Fe(10 nm) layers have bulk values, $M_S = 1.75 \times 10^6$ A/m and $K_1 = 56$ kJ/m^3 [21, 22], and indicate the high layer quality. The thin Fe(2 nm) layer has reduced $M_S = 1.6 \times 10^6$ A/m and $K_1 = 33$ kJ/m^3, which can be understood by the lower thickness and the reduced growth quality. The interface anisotropy constant is $K_S = 0.5$ mJ/m^2 for the thick Fe layers and $K_S = 0.3$ mJ/m^2 for Fe(2 nm). The bilinear and biquadratic coupling constants of interlayer exchange coupling across the Cr spacer are $J_1 = -0.97$ mJ/m^2 and $J_2 = -0.01$ mJ/m^2. The Fe layers are not coupled across the Ag spacer, i.e., $J_1 = J_2 \approx 0$.

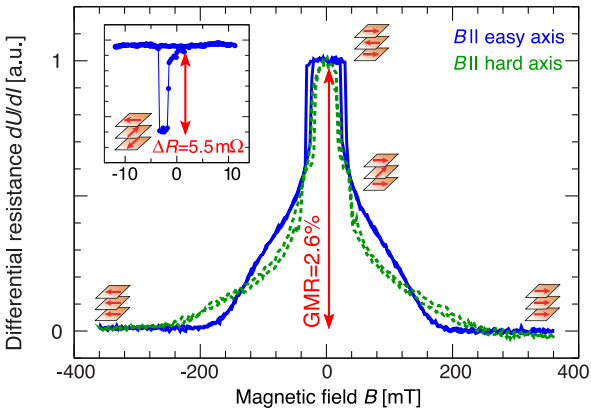

Fig. 2.8 CPP-GMR hysteresis loop with magnetic field parallel to an easy (*solid blue*) and hard (*dashed green*) axis. *Inset*: Minor GMR loop. Only in the first half of the loop ($+B \rightarrow -B$) does the resistance drop to a smaller value corresponding to a canted magnetization state. In the second half of the loop ($-B \rightarrow +B$) the resistance stays at the maximum value

The magnetoresistance loop of an Fe/Cr/Fe/Ag/Fe nanopillar is shown in Fig. 2.8. The solid blue (dashed green) line represents the data with magnetic field along easy (hard) axes of Fe(001), showing completely different behaviors. This immediately indicates that the nanomagnets are single-crystalline and exhibit fourfold in-plane magnetocrystalline anisotropy. The saturation field of the structured sample is 190 mT, which is more than twice the saturation field of the extended layers (see Fig. 2.7). Another difference becomes obvious in the minor loop (inset of Fig. 2.8), where the absolute resistance is measured with a small DC current of 1 mA. Coming from a large positive magnetic field, the resistance drops to a smaller value at small reversed fields between 1 and 3 mT and jumps back to the high resistance state at larger negative fields. For the reversed sweep direction, the resistance is constant at the maximum value. The drop in the first half of the cycle does not occur in every measurement. Thus, the patterning has modified the magnetic configuration, and the structured Fe(2 nm) nanomagnet is presumably coupled to the rest of the system by dipolar stray fields at the edges. This is a common feature in these devices and is also seen in Co nanopillars [23]. Due to this effect, we cannot separate the contributions of the Fe/Ag/Fe and Fe/Cr/Fe subsystems to the total GMR; therefore, we cannot gauge the resistance jumps measured under the influence of a large DC current shown in Fig. 2.9. The overall GMR ratio defined as $(R_{\mathrm{AP}} - R_{\mathrm{P}})/R_{\mathrm{P}}$, where R_{AP} is the highest resistance value in the fully antiferromagnetic configuration and R_{P} denotes the smallest resistance in the saturated state, amounts to 2.6 % at RT and 5.6 % at 4 K. The dramatic increase in the saturation field can be explained by the competition between the interlayer exchange coupling, external, and dipolar fields.

2.4.2 Normal and Inverse Switching

Figure 2.9 shows the differential resistance as a function of the DC bias current for different external fields. Positive current corresponds to an electron flow from the "free" Fe(2 nm) to the "fixed" Fe(10 nm) layer. We observe a parabolic background,

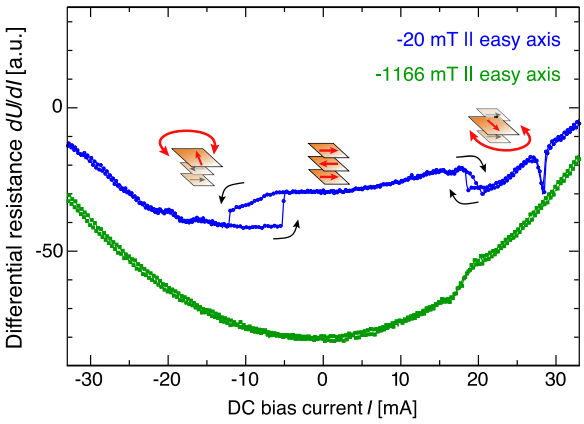

Fig. 2.9 DC current loops with magnetic field parallel to an easy axis. At high magnetic fields of −1166 mT a single step occurs at positive bias currents. At −20 mT, we observe hysteretic magnetization switching at both current polarities, which is related to the opposite spin scattering asymmetries of the Fe/Cr and Fe/Ag interface, respectively

which has been measured previously [23–26] and is usually explained by Joule heating of the pillar. On top of this background, we measure field-dependent resistance changes that can be attributed to STT effects. At −20 mT, the resistance drops at $I_C^+ = +18.2$ mA from the high-resistive to an intermediate state. After reducing the current again, the resistance jumps back to the large value. But also at negative bias the resistance changes at $I_C^- = -12.1$ mA from large to small. With an estimated junction diameter of $d = 150$ nm the corresponding critical current densities are $j_c^+ = 1 \times 10^8$ A/cm^2 and $j_c^- = -0.7 \times 10^8$ A/cm^2.

At large magnetic fields exceeding the saturation field [e.g., −1166 mT in Fig. 2.9], the two thick layers [Fe(14 nm) and Fe(10 nm)] are more strongly stabilized by the Zeeman energy than the Fe(2 nm) layer, and therefore only one step-like resistance change due to magnetic excitations of Fe(2 nm) at $I > 0$ is observed under these conditions.

The occurrence of jumps at both polarities of the current at small fields is at first glance surprising, but it can be explained by considering that both Fe/CrFe and Fe/Ag/Fe subsystems contribute. The spin-dependent interface resistances of Fe/Ag(100) and Fe/Cr(100) interfaces have been calculated by Stiles and Penn [16]. The values for Fe/Ag(001) have already been given in Sect. 2.2.3 and yield with (2.5) a polarization $P_{\mathrm{Fe/Ag(100)}} = 0.85$. For Fe/Cr(100) interfaces $AR^-_{\mathrm{Fe/Cr(100)}} = 0.77 \times 10^{-15}\ \Omega\,\mathrm{m}^2$ and $AR^+_{\mathrm{Fe/Cr(100)}} = 2.87 \times 10^{-15}\ \Omega\,\mathrm{m}^2$ [16]. Therefore, this type of interface exhibits a negative polarization $P_{\mathrm{Fe/Cr(100)}} = -0.58$. As discussed in Sect. 2.2.2 and as (2.1) and (2.3) make clear, this leads to inverse current-induced magnetization switching for the Fe/Cr subsystem. The situation is somewhat similar to inverse GMR [27, 28]. However, the type of GMR—normal or inverse—depends on the scattering spin asymmetries (here represented by P) of both interfaces of a $\mathrm{FM_1/NM/FM_2}$ trilayer. The inverse effect only occurs if the product of the asymmetries of the $\mathrm{FM_1/NM}$ and $\mathrm{FM_2/NM}$ interfaces is negative. In our case, the two subsystems Fe/Ag/Fe and Fe/Cr/Fe are symmetric and both exhibit a normal GMR effect. However, the type of STT depends on the polarization of the fixed layer only

(Sect. 2.2.2). Therefore, Fe/Ag/Fe and Fe/Cr/Fe show normal and inverse STT, respectively.

The data in Fig. 2.9 can now be explained by taking into account that the STTs in the two subsystems for a given current polarity act in opposite directions. For instance, a negative current stabilizes the parallel state for Fe/Ag/Fe and the antiparallel state for Fe/Cr/Fe. At low fields, the central Fe(10 nm) layer points opposite to the external magnetic field (Fig. 2.7). At positive currents, the spin-transfer torque generated in the Fe/Cr subsystem destabilizes this direction and switches the Fe(10 nm) layer [Fig. 2.9]. At negative currents, the Fe(2 nm) layer becomes unstable by the torque created from the Fe/Ag subsystem, while the Fe/Cr subsystem is even more strongly stabilized in the antiparallel state.

Our layer sequence suggests that the opposite polarizations arise from *interface* scattering because all involved FM layers consists of iron grown by MBE at room temperature. Therefore, we do not expect different spin-dependent resistances in the *bulk* of the FM layers. This justifies the restriction to spin-dependent interface resistances in the above discussion and in Sect. 2.2.3. In addition, for the given material and FM layer thickness the bulk resistances are much lower than the interface resistances. However, in the general case, both interface and bulk scattering spin asymmetries may contribute. AlHajDarwish et al., for instance, have induced an inversion of the bulk scattering spin asymmetry by diluting Fe with 5 % of Cr [29].

2.5 Interplay Between Magnetocrystalline Anisotropy and STT

The GMR data in the previous section has clearly shown that the patterned nanomagnets exhibit a fourfold in-plane anisotropy as expected from the bulk anisotropies. In this section we address the interplay between STT and anisotropy. We study a Fe(001) nanomagnet of 2 nm thickness and 70 nm diameter separated by 6 nm Ag(001) from an extended 20 nm thick fixed layer (inset of Fig. 2.10).

2.5.1 Two-Step Switching Process

Figure 2.10 shows the differential resistance through the pillar *versus* DC current taken at a magnetic field of 7.9 mT applied roughly along a hard axis. This field is much weaker than the anisotropy field of about 40 mT. Therefore, both magnetizations are aligned along an easy axis, and the measurement starts at zero DC current in a low resistive state. In contrast to the usually observed behavior [12, 13] the switching occurs here in two steps via an intermediate resistance level. At a positive current I_{c1} the free layer starts to rotate with respect to the fixed layer. The anisotropy energy minimum at 90° stabilizes the orthogonal state. However, at an even higher current I_{c2} the local energy minimum is overcome, and the free layer switches to the antiparallel alignment. Upon reversing the current, a similar behavior is observed. At first glance, it is surprising that there are two switching events

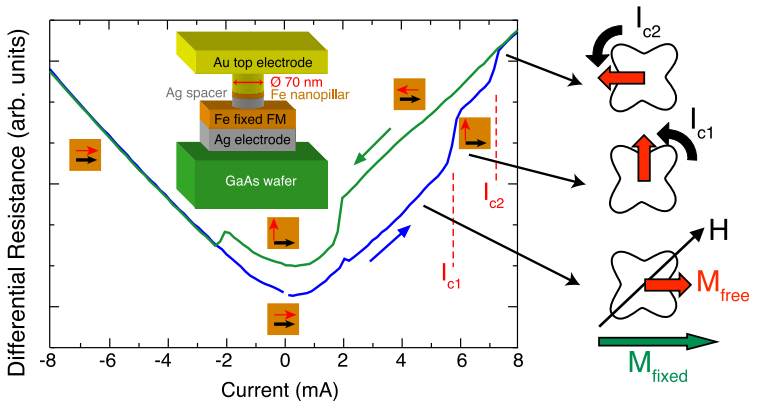

Fig. 2.10 Two-step current-induced magnetization switching of a single-crystalline Fe/Ag/Fe(001) nanopillar measured at 5 K. $\vec{M}_{\text{free}}$ switches first from parallel to perpendicular and then to antiparallel alignment relative to $\vec{M}_{\text{fixed}}$ and vice versa for the decreasing current branch (*green*). A static magnetic field of 7.9 mT, which is weaker than the in-plane anisotropy field, is applied roughly along a hard axis. The diagrams that look like cloverleaves represent the in-plane anisotropy energy landscape. The four minima correspond to easy axis directions

at different critical currents, because the anisotropy energy barriers to overcome are the same in both cases. The different current densities arise from the angular dependence of the STT efficiency function $g(\theta)$, as can be seen in the macrospin simulations of Fig. 2.11. The trajectory of the first switching step from parallel to perpendicular with respect to the fixed magnetization is shown in Fig. 2.11(a). The direction of the damping torque (red) and the STT (blue) during the switching are shown in Fig. 2.11(c). The viewing direction is along the $-x$-direction. As expected, the STT always points outward and, thus, acts as an excitation. Therefore, the cone angle of the precession around the initial state increases, until the anisotropy energy barrier between the initial and the 90°-state is overcome. Figure 2.11(d) shows the torques after the switching; now with the viewing direction in the $-y$-direction [note the different abscissae of Figs. 2.11(c) and (d)]. The symmetry of the STT after switching is completely different. For $m_x < 0$ [right half of Fig. 2.11(d)] the STT is still pointing outward and is an exciting torque. However, for $m_x > 0$ [left half of Fig. 2.11(d)] the STT points towards the precession axis and damps the oscillatory motion. The total action of the STT along one revolution tends to cancel out. Therefore, the magnetization relaxes towards the $+x$-direction after the first switching step, as can also be seen in Fig. 2.11(a). The simulation also reproduces the second switching step at a higher DC current from the 90°-state to the antiparallel state [Fig. 2.11(b)]. Again, the angle of the precession around the initial state increases until the switching occurs. (In this specific simulation the switching is a bit more complicated, because the magnetization overcomes the energy barrier on the "wrong" side of the trajectory, which requires it to reach the final state via a "detour".) But how can the STT in Fig. 2.11(d) excite the magnetization at a higher current and induce the switching? The answer can be found in the magnitude of the

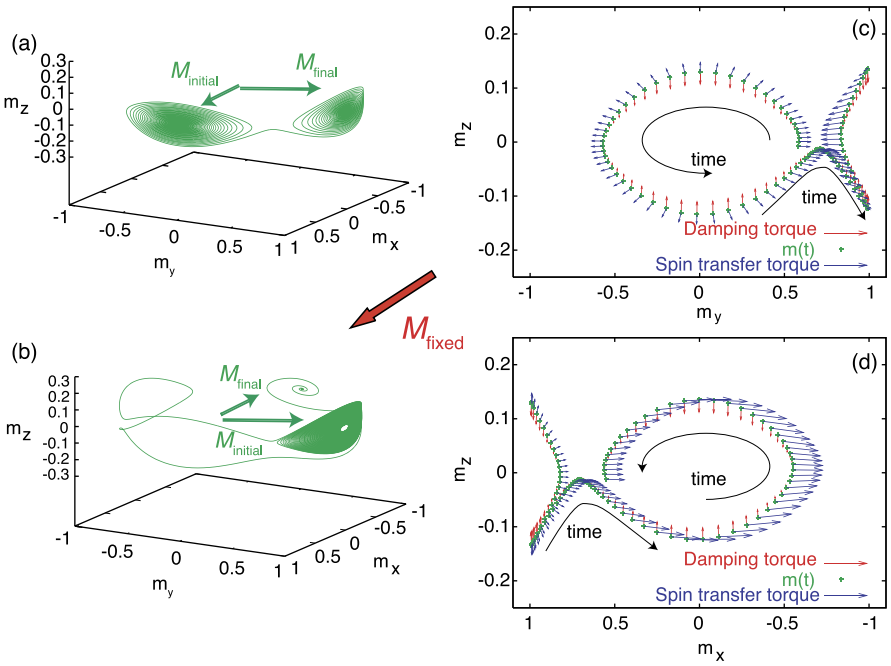

Fig. 2.11 STT-induced switching of a macrospin in the presence of cubic magnetocrystalline anisotropy and demagnetizing field. $\vec{M}_{\text{free}}$ switches under the influence of a persistent DC current first from a parallel ($+x$-direction) to a 90°-orientation ($+y$-direction) with respect to $\vec{M}_{\text{fixed}}$ and then from the 90°-orientation to the antiparallel alignment ($-x$-direction). (**a**), (**b**) Trajectories of the two switching events. (**c**), (**d**) representation of the STT (*blue arrows*) and damping torque (*red arrows*) viewed against (**b**) the initial, parallel and (**c**) the 90°-orientation of the macrospin. Only a fraction of the trajectory in the immediate vicinity of the switching event (**a**) is shown in (**c**) and (**d**)

STT, which is not constant along the trajectory. In fact, the STT for $m_x < 0$ [right half of Fig. 2.11(d)] is stronger than for $m_x > 0$ [left half of Fig. 2.11(d)]. Therefore, the total action along one revolution does not completely cancel out, and a small exciting net torque remains. For a large enough critical current I_{c2} this net torque is sufficient to overcome the damping torque and induces the second switching step.

This asymmetry of the magnitude of the STT is a consequence of Slonczewski's unified theory for GMR and STT: For an asymmetry parameter $\Lambda > 1$ the maximum of the STT occurs for angles larger than $\theta = 90°$ (see blue or red curve in Fig. 2.4(b)). From a comparison between the experimentally determined ratio of the critical currents I_{c2}/I_{c1} with corresponding values extracted from simulations with varying asymmetry parameter Λ, we obtain $\Lambda_{\text{STT}} = 3.4$ [30].

According to Slonczewski's model, a $\Lambda \neq 1$ should result in a deviation of the GMR curve from the $\sin^2(\theta/2)$ behavior [Fig. 2.4(a)]. Figure 2.12 shows the normalized resistance $r(\theta)$ [see (2.2)] as a function of the magnetic field applied along a hard axis of the Fe layers. The red lines are simulations for which we assume single-

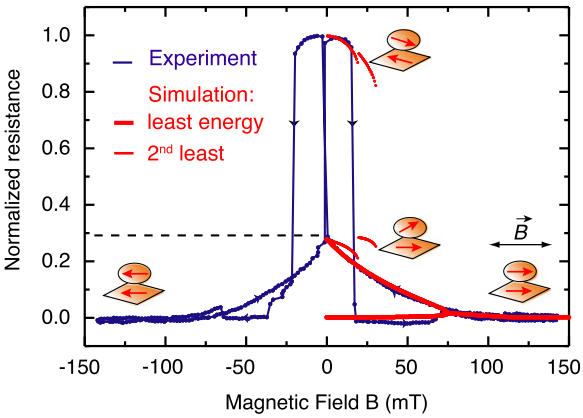

Fig. 2.12 CPP-GMR data (*blue*) measured at 5 K with the magnetic field applied along a hard axis of the single-crystalline Fe layers. *Thick* and *thin red lines* are least and second least energy solutions of a Stoner–Wohlfarth fit, respectively. *Pairs of red arrows* indicate the relative alignment of magnetizations as derived from the fit

domain behavior for both Fe layers (Stoner–Wohlfarth model). The experimental curve is well reproduced and yields the relative alignment of the magnetizations as a function of the external field (icons with pairs of arrows). An interesting magnetic configuration occurs after decreasing the field to zero, where the two magnetizations rest in two different easy axes and, thus, include an angle of $\theta = 90°$. For a standard, symmetric angular dependence of the GMR $r(90°)$ would be 0.5. Instead we find a much lower value of 0.3 (dashed line). This deviation originates from enhanced spin accumulation at the Fe/Ag(001) interfaces and yields with (2.2) and (2.4) an asymmetry parameter—this time for GMR—$\Lambda_{\mathrm{GMR}} = 1.6$.

These experiments represent the first direct determination of the asymmetry parameter Λ for GMR and STT in the same sample. The deviations between the calculated value of Λ (4.0) and those determined from GMR and STT data (1.6 and 3.4, respectively) most likely arise from imprecise knowledge of material parameters and from simplifying assumptions of the model, such as the complete neglect of the minority channel, which is only approximately fulfilled for Fe/Ag(001). Further work on this subject is required.

2.5.2 Zero-Field Excitations in the 90°-State

The simulations in Fig. 2.11 suggest that a steady-state oscillatory mode can be excited at a low external field, if the system is prepared in the 90°-state and a DC current between I_{c1} and I_{c2} is applied. Figure 2.14 shows microwave spectra measured under these conditions using the HF setup described in Fig. 2.13. The frequencies of the observed modes slightly shift with increasing current strength to higher frequencies. A corresponding macrospin simulation is shown in Fig. 2.15. We indeed find a precessional trajectory around the $+y$-direction, which is the static direction of the free magnetization in the 90°-state. The analysis of the torques in Fig. 2.15(b) yields a similar picture as for the second switching step in Fig. 2.11: The integrated action of the STT along one revolution almost cancels out. Only a relatively small

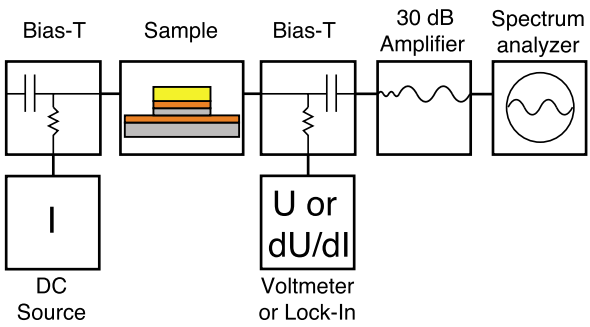

Fig. 2.13 Experimental setup for the measurement of microwave signals generated by STT in a nanopillar. The bias-T separates the applied DC current and the HF output signal. The voltmeter or lock-in amplifier allows for a simultaneous measurement of (differential) DC resistance changes in four-point geometry

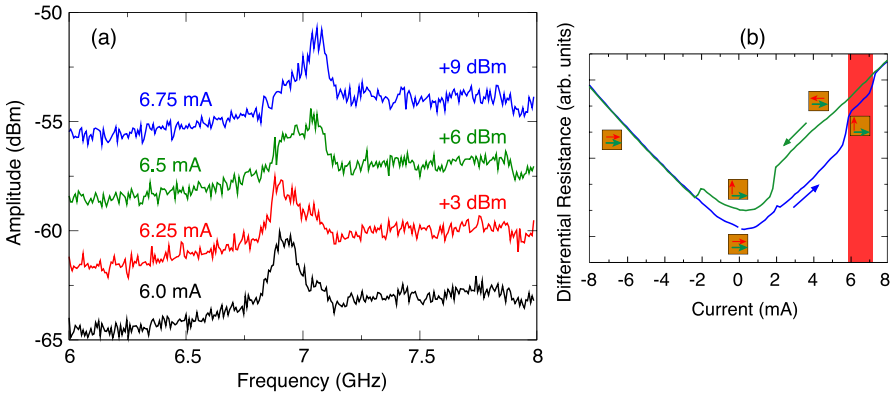

Fig. 2.14 (**a**) Low-field precession: microwave spectra recorded at 5 K with a weak field of 5 mT applied at an angle of 15° relative to an easy axis and at different DC currents as indicated. All curves are taken at DC currents that correspond to the 90°-state [*red shaded range* in (**b**)]

net excitation remains due to the asymmetry of the STT magnitude as a function of the angle θ. The excitation of the STT on the right-hand part of the trajectory is larger than the damping on the left-hand part. The relatively small cone angle of the trajectory in Fig. 2.15(a) and the weak peaks in Fig. 2.14(a) reflect the weak excitation.

The observation of a steady-state precession at low external or even zero field is of importance from an application point of view; the usual need for an external field exceeding the coercivity of the oscillating layer is disadvantageous, as it increases the complexity and cost of spin-torque oscillators (STOs). There are different ways to circumvent the necessity of an external field. One recently presented possibility is to shape the angular dependence of the STT by using different magnetic materials as the free and the fixed layer [31]. If these provide complementary spin scattering parameters, a reversal of the sign (direction) of the STT between the parallel and the antiparallel alignment of the magnetizations can be achieved. Both alignments are therefore destabilized/stabilized by the given current polarity and can cause a steady

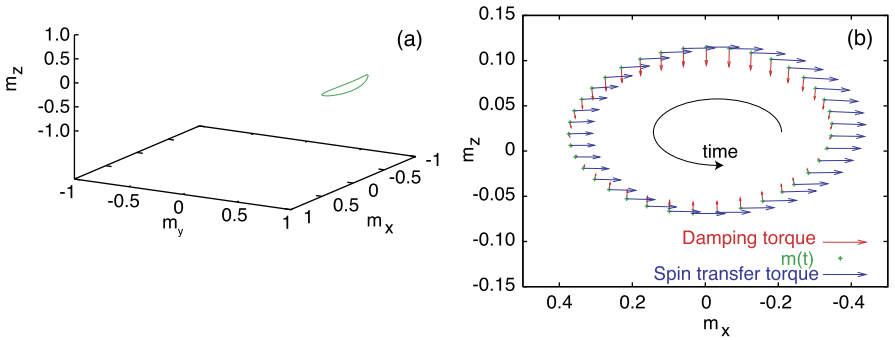

Fig. 2.15 STT-induced excitation of low-field precession in the 90°-state in the presence of cubic magnetocrystalline anisotropy and demagnetizing field. (**a**) Simulated trajectory and (**b**) representation of the STT (*blue arrows*) and damping torque (*red arrows*) viewed against the 90°-orientation ($-y$-direction) of the macrospin

oscillatory motion at zero applied magnetic field [31]. A second possibility is to pin $\vec{M}_{\text{fixed}}$ in a 90° orientation with respect to the easy axis of the shape anisotropy of the free layer magnetization, i.e., the long axis of the elliptically shaped free layer [32]. In this geometry the demagnetizing field counteracts the STT in such a way that no hysteretic switching, but only precessional motion of the magnetization, is enabled. In our case [33], the role of the external field is taken by an internal field, namely the magnetocrystalline anisotropy field. Therefore, the observation of low-field excitations in the 90°-state is—as is the case for the two-step switching process presented in Fig. 2.10—a direct consequence of the interplay between magnetocrystalline anisotropy and the STT.

2.6 STT-Driven Vortex Dynamics in Nanopillars

In this section we deal with current-induced magnetization dynamics of magnetic vortices [34]. In contrast to the quasi-uniform, single-domain magnetic elements discussed in the previous sections, the vortex structure represents a highly nonuniform magnetization pattern. The magnetic vortex structure appears at certain dimensions as the ground state of ferromagnetic disks because its magnetization pattern trades off dipolar energy against exchange energy. The magnetization basically lies in plane and has a circular shape, which avoids surface charges and therefore minimizes the dipolar field energy. However, at the center of this pattern the magnetization is forced out of plane; otherwise, there would be a strong build-up of exchange energy. The direction of the out-of-plane magnetization defines the polarity; the sense of rotation of the in-plane part constitutes the vortex chirality.

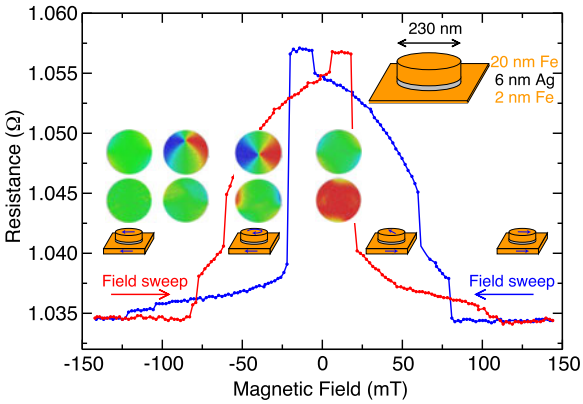

Fig. 2.16 CPP-GMR of a pillar structure as sketched in the inset. *Symbols* indicating the magnetization state and simulated micromagnetic magnetization patterns for the fixed (*bottom*) and free FM (*top*) correspond to the decreasing (*blue*) field sweep

2.6.1 Magnetic Vortices in Nanopillars

In order to promote the formation of magnetic vortices, we prepare nanopillars with a circular cross section and a slightly larger diameter of approximately 230 nm. Only the 20 nm thick top FM layer is laterally confined, while the 2 nm thick bottom FM layer is left extended with a typical width of 15 μm [see inset in Fig. 2.16]. The dimensions of the magnetic disk are in a regime where a magnetic vortex structure and a uniform in-plane magnetization are both stable states [35]. The 2 nm thick extended layer, on the other hand, is uniformly magnetized on length scales much larger than the pillar diameter as long as there is at least a small magnetic field suppressing domain formation.

The GMR response at 10 K is shown in Fig. 2.16. The magnetic field is applied in the sample plane and parallel to a magnetic easy axis of the Fe layers. Starting from saturation at 150 mT a steep increase in the resistance can be seen at 70 mT. The increase slows down until a plateau of maximum resistance is reached with a small step at a reversed field of −5 mT. At −20 mT the resistance shows a sudden drop to a level of 1.040 Ω corresponding to a normalized resistance $r(H) = [R(H) - R_{\min}]/[R_{\max} - R_{\min}]$ of 0.25, where H is the applied field. A slow decrease of the resistance down to −100 mT is followed by an abrupt decrease to the resistance of the saturated state. The reversed sweep (red curve) shows a similar behavior.

In order to interpret this data, we perform micromagnetic simulations using a custom-developed finite element algorithm [36]. The usual values for Fe material parameters were chosen: saturation magnetization $\mu_0 M_S = 2.15$ T, cubic anisotropy $K_c = 48$ kJ/m^3, exchange constant $A = 2.1 \times 10^{11}$ J/m, and a value of $\alpha = 0.01$ for the Gilbert damping constant. The results for two coplanar, decoupled disks of 230 nm diameter at a vertical distance of 6 nm and with 20 nm and 2 nm thickness, respectively, are shown in Fig. 2.16 as colored magnetization patterns. The in-plane component in the y-direction is shown for the bottom (lower row) and top (upper row) disk.

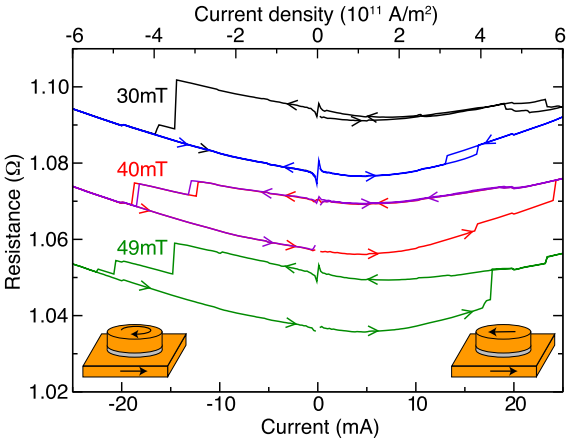

Fig. 2.17 Current-induced switching between the low-resistive vortex and high-resistive uniform state. Arrows on the curves indicate the current sweep direction. The *black* and *purple curves* start in the uniform state, all others in the vortex state. For clarity the graphs measured at 40 and 30 mT are offset by +20 and +40 mΩ, respectively, relative to the *green curve*

2.6.2 Uniform State Versus Vortex State

One of the most promising applications of STT is found in spin-torque oscillators (STOs), which make use of the current-induced steady precession of $\vec{M}_{\text{free}}$. At present, a major issue of STOs is their low output power. In order to optimize the output power, several different STOs designs have been proposed. Designs incorporating in-plane magnetized free and fixed layer with in-plane field as discussed in the previous section or out-of-plane external fields [37], in-plane magnetized free and perpendicularly magnetized fixed layer [38], in-plane magnetized fixed and perpendicularly magnetized free layer [39], and free layer magnetized in a vortex state with in-plane magnetized fixed layer [40, 41] have been studied experimentally. Comparing the characteristics—especially the output power—of HF excitations of these designs from different experiments is not conclusive, because the impedance and absolute resistance change of the samples have a very strong influence on the detected power. Here, we study HF excitations in two of the arrangements mentioned above that we are able to realize in the same sample [42]. While the fixed layer is uniformly in-plane magnetized, the free layer is either uniformly in-plane magnetized or in a vortex state. The direct comparison shows some advantages of the vortex state for the application in STOs.

Figure 2.17 shows current-induced CPP resistance changes at 10 K and various field strengths. The initial states were prepared by magnetic field sweeps according to Fig. 2.16. We observe hysteretic switching of $\vec{M}_{\text{free}}$ (e.g., the green and red curves). The high-resistive state at positive currents corresponds to uniformly and antiparallelly aligned $\vec{M}_{\text{free}}$ and $\vec{M}_{\text{fixed}}$, whereas the low-resistive state at negative currents is due to the vortex state in the free FM. This is in agreement with previous experiments on Fe/Ag/Fe nanopillars [19, 30, 33], which have established that the STT due to a positive current (see footnote 1) acts towards an antiparallel alignment. The two resistance values near 0 mA of the unshifted green curve in Fig. 2.17 measured at 49 mT indeed correspond to the values of the red and blue curves at +49 mT in Fig. 2.16. The fact that we do not observe a switching to the vortex state

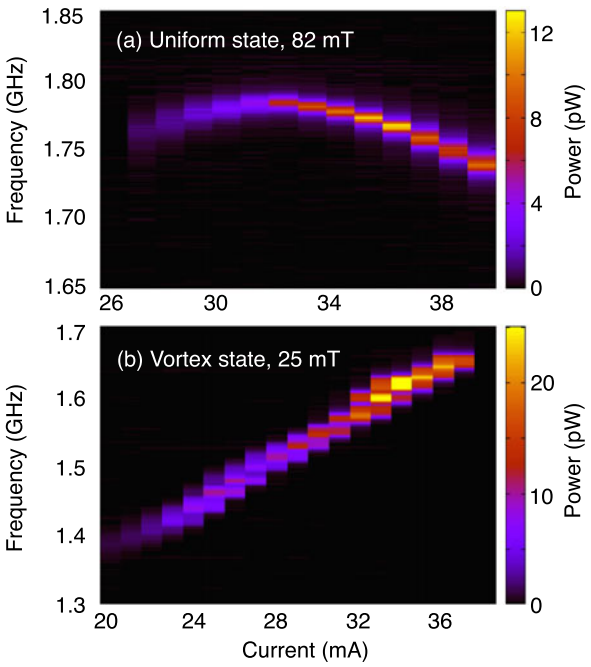

Fig. 2.18 STT-induced excitation of qualitatively different oscillatory modes in a nanodisk. (**a**) After preparation of a uniform state, a standing-wave mode with a transition from blue to red shift is excited; measurement at 82 mT. (**b**) The gyrotropic mode is excited after preparation of the vortex state; measurement at 25 mT. Note that the microwave output power generated by the gyrating vortex for a given DC current in (**b**) is much higher than that for the standing-wave mode in (**a**)

at positive currents in Fig. 2.17 proves that the prevalent torque in the switching processes does not originate from Oersted fields. These circumferential fields also tend to switch $\vec{M}_{\text{free}}$ into a vortex state at positive currents, just with the opposite vorticity compared to negative currents.

We measure DC current-induced HF excitations of the magnetization at room temperature using the setup shown in Fig. 2.13. The voltage variation arises from the GMR of the Fe/Ag/Fe stack, which reaches 2 % or 22 mΩ in Fig. 2.16. The impedance of our sample was 11 Ω at 1.5 GHz. Figure 2.18(a) shows the HF response of an STO in the uniform state measured in an in-plane field of 82 mT. The low frequencies of the excitations are the result of the cancellation of the dipolar coupling field of about 80 mT by the external field and the rather large size of the element, for which the standing-wave mode has a low frequency. The observed blue-shift behavior at low currents can be interpreted in terms of standing-wave modes, which are deformed by the Oersted field [43]. At higher currents the red shift sets in, which is explained by a predominantly homogeneous in-plane precession of the magnetization. For increasing current the angle of precession increases, thus leading to a lower frequency [44]. At the same time the peak width increases. Figure 2.18(b) shows representative HF excitations of an STO in the vortex state. Here, the gyrotropic mode [34] of the vortex is excited as previously reported by Pribiag et al. [40]. The gyrotropic mode is the lowest excitation mode of a magnetic vortex and consists of a circular motion of the vortex core around the equilibrium position. The radius of the trajectory is proportional to the excitation amplitude. When for increasing current the trajectory approaches the rim of the disk, the vortex experi-

ences a stronger restoring force that increases its precessional frequency. This results in a linear increase of the frequency, yielding a mode agility of +17 MHz/mA [Fig. 2.18(b)]. At each spot within the trajectory of the vortex core, the magnetization rotates during one period of the gyrotropic cycle by a full 2π about the sample normal. Thus, for a vortex core moving on a trajectory close to the rim of the sample the product of oscillation amplitude times area, where oscillations take place, is maximized. As a consequence, the emitted power of the STO in the vortex state is nearly three times the power emitted in the uniform state (Fig. 2.18).

The excitation of the gyrotropic mode in this geometry is in agreement with predictions of a mechanism for STT-induced gyrotropic motion of a vortex in a spin-valve nanostructure with an in-plane magnetized polarizer that has recently been proposed by Khvalkovskiy et al. [45]. The model assumes a nonuniform, i.e., symmetry-breaking magnetization of the polarizer, which is treated on the basis of a generalized Thiele equation and by micromagnetic simulations. An alternative mechanism may be related to the strong angular asymmetry of the STT in Fe/Ag/Fe(001) structures [30] as discussed in Sect. 2.5, which also breaks the symmetry in the sample plane [46].

From this direct comparison of the characteristics of an STO in either the uniform or vortex state we conclude that the higher agility, the wider tuning range, and in particular the higher output power are all advantageous for the application of the vortex state in STOs. Although this conclusion is derived from metallic, GMR-type STOs, our generic, micromagnetic arguments are also valid for the technologically more relevant tunnel magnetoresistance (TMR)-based STOs with higher output power [39].

2.6.3 Injection Locking of the Gyrotropic Vortex Excitation

In spite of improvements like those described in the previous section, the HF output power of an STO is presently far too low for applications. This is particularly true for metallic, GMR-based STOs, whose low magnetoresistance ratio of only a few percent yields output powers in the pW to low nW regime. TMR-based STOs with TMR ratios of the order of 100 % have been shown to generate about 1 μW of output power [39]. Nevertheless, ongoing research aims at strategies to significantly increase the output power. A promising route is to simultaneously operate a large number of STOs. The excitation of an array of STOs in a synchronized, phase-locked manner is believed to deliver a significant power increase, as N coherently coupled STOs emit up to the N^2-fold power. The STO-STO coupling can be achieved in two ways. One is by spin waves in a common ferromagnetic layer, as has been already demonstrated for two [47–49] and four [50] STOs. Due to the fast decay of spin waves, this interaction is short range and requires an STO-STO separation of the order of the STO's diameter, clearly below 1 μm. The second coupling mechanism via microwaves propagating in common electrodes [51, 52] permits a larger STO separation, because electrical microwave signals propagate with negligible losses over long distances. Experimentally, this situation has been addressed

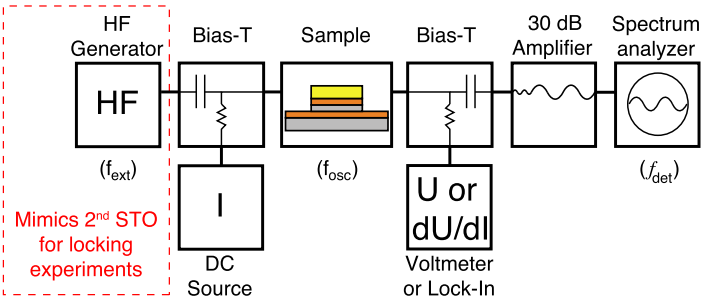

Fig. 2.19 The experimental setup for the injection locking experiments is an extension of the setup shown in Fig. 2.13. The HF generator in the *red dashed box* mimics the presence of a second STO that oscillates at the tunable frequency f_{ext}

by injection locking experiments, which study the interaction of an STO with an externally applied HF signal in order to investigate conditions for synchronization and phase locking. Rippard et al. [53] have shown the injection locking of a single-domain STO. In the following we demonstrate phase locking of the DC current-driven gyrotropic vortex motion in a vortex STO to external HF signals, and derive from the dependence of the locking on the HF amplitude criteria for the required STO output power for synchronization [54].

The layer structure and the pillar dimensions are the same as described in Sect. 2.6.1. The electrode layout allows for contacting by two microwave probes via coplanar waveguides. One of them is used to inject a DC current and an HF current of frequency f_{ext} from a network analyzer. The two currents are combined in a bias-T. The second probe is connected to a 30 dB amplifier and a spectrum analyzer (Fig. 2.19). The measurements are conducted at room temperature in a microwave probe station with an in-plane magnetic field of up to 300 mT.

Based on the data in Fig. 2.16 we know for this pillar structure how to prepare a vortex state in the nanodisk while, at the same time, the magnetization of the extended layer is saturated along a magnetic easy axis of bcc Fe, e.g. by applying 25 mT after negative saturation. Applying positive DC currents (i.e. electron flow from the nanomagnet to the extended layer (see footnote 1)) in the range of 20 to 39 mA, the vortex state is excited by STT into the gyrotropic mode; see Fig. 2.18.

We now add an external HF component of frequency f_{ext} to the driving DC current in order to mimic a second STO. This allows us to demonstrate phase locking of the DC current-induced gyrotropic motion (at frequency f_{osc}) to electric HF signals even if they are slightly out of tune, i.e., $f_{\mathrm{ext}} \neq f_{\mathrm{osc}}$. Figure 2.20(a) shows a measurement where the vortex was excited by a current of 32 mA to a frequency of $f_{\mathrm{osc}} = 1.518$ GHz, while an external signal of -17 dBm or 20 μW was swept from $f_{\mathrm{ext}} = 1.35$ to 1.7 GHz. This leads to a clear shift of the vortex frequency between 1.42 and 1.61 GHz. From 1.46 to 1.57 GHz the vortex frequency f_{osc} is completely locked to the external signal f_{ext} and is thus masked by it. Upon an amplitude increase [Fig. 2.20(b)] the phase locking range widens without qualitative changes. At -15 dBm [Fig. 2.20(c)] an additional signal of 1.65 GHz appears in

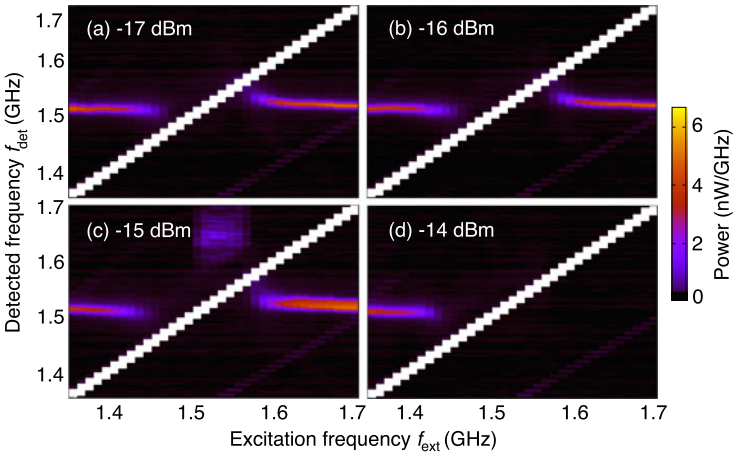

Fig. 2.20 Injection locking of the gyrotropic vortex motion. Power spectra (f_{det}, *vertical axis*) of the current-induced gyrotropic mode as a function of HF excitation frequency (f_{ext}, *horizontal axis*) measured for different excitation amplitudes as indicated. The intensity at f_{ext} exceeds the color scale and appears as *diagonal white lines*

the right-hand part of the phase locked regime, and the signal shape and intensity change for external frequencies f_{ext} above 1.6 GHz. The origin of these features is not clear. Micromagnetic simulations are required to relate them to modifications of the gyrotropic mode, e.g. periodic vortex core reversals [45] or the presence of additional excited modes at increased HF amplitude. Finally, for the strongest excitations at −14 dBm [Fig. 2.20(d)] the vortex signal is lost above 1.5 GHz when sweeping through the locking regime from low to high f_{ext}. The DC resistance after completing the frequency sweep is larger than before, which—based on Fig. 2.16—must be identified with the quasi-uniform magnetization state. Thus, the vortex has been expelled from the sample while being phase-locked to the HF signal. This may happen, when the radius of the gyrotropic trajectory strongly increases due to the excitation and the vortex finally hits the boundary of the nanodisk.

In order to evaluate the synchronization behavior in depth, we fit the frequency variation f_{osc} of the forced vortex motion with the frequency f_{ext} of the injected HF signal to a formula derived by Slavin and Tiberkevich for nonlinear oscillators [see (48b) of Ref. [55]]:

$$f_{osc} = f_{ext} + \mathrm{sign}(f_0 - f_{ext})\sqrt{(f_0 - f_{ext})^2 - \Delta^2}, \tag{2.6}$$

where $f_0 = f_{osc}(I_{HF} = 0)$ is the frequency of the free-running vortex STO and Δ is the phase locking range. An example of a fit for 32 mA DC current and −16 dBm HF excitation is shown in the inset of Fig. 2.21. The main figure shows an increase of Δ with increasing amplitude of the external signal in accordance with the linear dependence predicted by Slavin and Tiberkevich [55]. The conversion from HF power to HF current amplitudes I_{HF} is given by the impedance of the sample (11 Ω at 1.5 GHz) that we have measured with a network analyzer. However, the linear

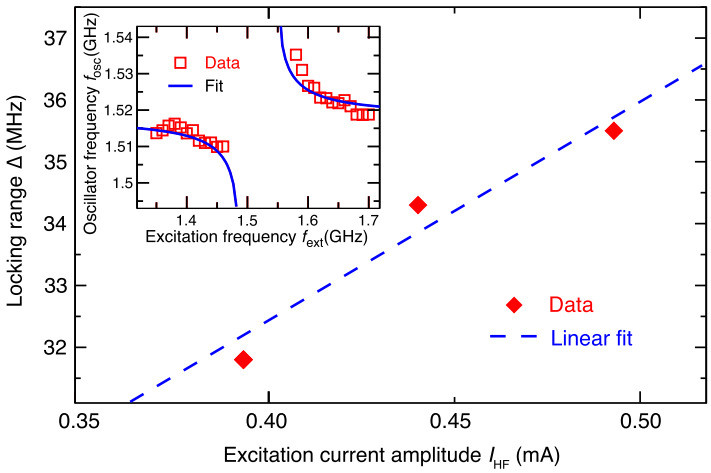

Fig. 2.21 Locking range Δ as a function of the external HF excitation amplitude. The *dashed line* is a linear fit. *Inset*: Fit (*solid line*) of (2.6) to the experimental locking behavior for $I_{DC} = 32$ mA and −16 dBm

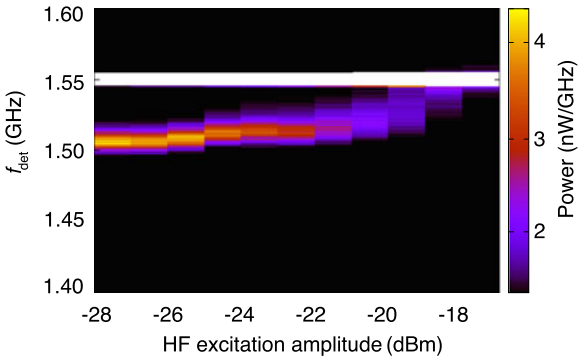

Fig. 2.22 Locking behavior of a vortex STO as a function of the HF excitation amplitude at $f_{ext} = 1.55$ GHz and $I_{DC} = 32$ mA. Locking occurs at about −18 dBm

extrapolation to zero excitation amplitude (dashed line in Fig. 2.21) yields a nonvanishing locking range of about 18 MHz. This inconsistency may be due to the fact that the theoretical model assumes only a weak excitation. Our data indicates that the widening of the locking range Δ with the excitation amplitude proceeds more slowly for strong excitation.

Figure 2.22 shows the locking behavior of the vortex STO when excited by a fixed DC current of 32 mA and an external 1.55 GHz signal of variable amplitude. For weak excitation the STO is not influenced by the HF signal and emits at its free-running frequency $f_0 \approx 1.52$ GHz. With increasing HF amplitude the STO tends to adjust to the external frequency and phase-locks for excitation amplitudes exceeding −18 dBm. The locking process is accompanied by a weakening and broadening of the STO signal. The HF signal generated by the magnetization dynamics in the pillar and the externally applied HF signal passing through the pillar reach the spec-

trum analyzer via a common pathway (right-hand branch of the setup in Fig. 2.19). Therefore, we can directly determine the ratio between the power required for phase locking and the power generated by the pillar from the measured spectra and obtain a ratio of about 3300. The HF signal is attenuated in cables, connectors, the waveguides on the sample, and due to impedance mismatch, e.g., between leads and pillar. We characterize the sum of all these effects by measuring the transmission from the HF generator to the spectrum analyzer. Based on this transmission value and the symmetry of the setup, we estimate the external HF power at -18 dBm reaching the pillar to be of the order of 1.3 μW. Thus, the vortex STO generates roughly 0.4 nW of microwave power. This low value is related to the low absolute resistance and low GMR ratio, which result in small resistance changes due to the magnetization dynamics. We emphasize that the physics of the vortex dynamics and injection locking described here is not affected by the weak conversion to output power.

Consequently, the output power of our GMR-based vortex STO is about three orders of magnitude too small to phase-lock another vortex STO. Under these conditions synchronization of an array of vortex STOs seems unlikely, unless the output power of each single STO is significantly increased, e.g., by employing highly spin-polarized ferromagnetic electrode materials (Heusler alloys [56]) or TMR-based structures with much higher MR ratios.

Thus, we have demonstrated the possibility to phase-lock the current-driven vortex motion in an STO to an external HF signal, which is a prerequisite for the synchronization of vortex STOs. The relative locking range $2\Delta/f_0 \approx 5$ % is rather large and allows for a distribution of free-running frequencies in an STO array, which seems to be compatible with present fabrication technology. However, the power requirements for synchronization call for STOs with much higher output power and for optimization of the synchronization efficiency, e.g., by appropriate phase control [57].

2.7 Summary

We have reviewed our recent work on spin-transfer torque effects in single-crystalline, Fe-based nanopillars. Measurements of the GMR effect in CPP geometry evidence the presence of bulk-like magnetocrystalline anisotropy in magnetic nanodisks, even if they are only 2 nm thick and 70 nm in diameter. The interplay between STT and magnetocrystalline anisotropy has a strong influence on current-driven magnetization dynamics of the quasi-uniform, single-domain magnetization state as follows. (i) The current-induced magnetization switching occurs in two steps with a stopover in the 90°-state, which is stabilized by the magnetocrystalline anisotropy. (ii) The internal anisotropy field in the 90°-state allows for current-induced, uniform magnetization precession even at zero field. These properties allow for a comparison with the unified theory for GMR and STT of Slonczewski [17]. In agreement with the model we observe the effect of the spin-torque asymmetry parameter Λ on the GMR and STT behaviors, from which we determine

Λ_{GMR} and Λ_{STT} independently. The values are of the order of magnitude predicted from ab initio theory [16], but differ by a factor of about two. This discrepancy is the subject of future work. The magnetocrystalline anisotropy has much less influence on the current-induced vortex dynamics, for which the geometry of the vortex averages over all in-plane directions. The vortex state can be created in the free layer of a pillar structure of suitable geometry. We demonstrated that the magnetization of the free layer can be switched between vortex and uniform state by STT as well as by external field cycles. Making use of this ability, we found (i) that the gyrotropic vortex mode can be excited in the pillar geometry with an in-plane magnetized fixed layer and (ii) that vortex STOs are generically superior to STOs operating in the quasi-uniform magnetization state, particularly concerning the output power. Finally, we demonstrated the electrical locking of the gyrotropic vortex mode to an external HF source. The described experiments contribute to a fundamental understanding of the spin-torque physics, which is required to optimize and tailor the device properties for applications.

Acknowledgements The authors gratefully acknowledge the contributions of Z. Celinski, H. Dassow, S. Gliga, P. Grünberg, F.-J. Köhne, and R. Schreiber to the results described in this review article. The work was partly funded by the German academic exchange service (DAAD) and at UCCS by the NSF (Grant No. DMR-0605629) and the ARO (Grant No. W911NF-04-1-0247).

References

1. D.C. Ralph, M.D. Stiles, J. Magn. Magn. Mater. **320**, 1190 (2008)
2. J.A. Katine, E.E. Fullerton, J. Magn. Magn. Mater. **320**, 1217 (2008)
3. J.Z. Sun, D.C. Ralph, J. Magn. Magn. Mater. **320**, 1227 (2008)
4. D.V. Berkov, J. Miltat, J. Magn. Magn. Mater. **320**, 1238 (2008)
5. T.J. Silva, W.H. Rippard, J. Magn. Magn. Mater. **320**, 1260 (2008)
6. G.S.D. Beach, M. Tsoi, J.L. Erskine, J. Magn. Magn. Mater. **320**, 1272 (2008)
7. Y. Tserkovnyak, A. Brataas, G.E.W. Bauer, J. Magn. Magn. Mater. **320**, 1282 (2008)
8. H. Ohno, T. Dietl, J. Magn. Magn. Mater. **320**, 1293 (2008)
9. P.M. Haney, R.A. Duine, A.S. Núñez, A.H. MacDonald, J. Magn. Magn. Mater. **320**, 1300 (2008)
10. J.C. Slonczewski, J. Magn. Magn. Mater. **159**, L1 (1996)
11. L. Berger, Phys. Rev. B **54**, 9353 (1996)
12. E.B. Myers, D.C. Ralph, J.A. Katine, R.N. Louie, R.A. Buhrman, Science **285**, 867 (1999)
13. J.A. Katine, F.J. Albert, R.A. Buhrman, E.B. Myers, D.C. Ralph, Phys. Rev. Lett. **84**, 3149 (2000)
14. S.I. Kiselev, J.C. Sankey, I.N. Krivorotov, N.E. Emley, R.J. Schoelkopf, R.A. Buhrman, D.C. Ralph, Nature **425**, 380 (2003)
15. M.D. Stiles, A. Zangwill, Phys. Rev. B **66**, 014407 (2002)
16. M.D. Stiles, D.R. Penn, Phys. Rev. B **61**, 3200 (2000)
17. J.C. Slonczewski, J. Magn. Magn. Mater. **247**, 324 (2002)
18. D.E. Bürgler, C.M. Schmidt, J.A. Wolf, T.M. Schaub, H.-J. Güntherodt, Surf. Sci. **366**, 295 (1996)
19. H. Dassow, R. Lehndorff, D.E. Bürgler, M. Buchmeier, P.A. Grünberg, C.M. Schneider, A. van der Hart, Appl. Phys. Lett. **89**, 222511 (2006)

20. M. Buchmeier, B.K. Kuanr, R.R. Gareev, D. Bürgler, P. Grünberg, Phys. Rev. B **67**, 184404 (2003)
21. C. Kittel, *Einführung in die Festkörperphysik* (Oldenbourg, München, 1989)
22. E.P. Wohlfarth (ed.), *Ferromagnetic Materials* (North-Holland, Amsterdam, 1980)
23. F.J. Albert, J.A. Katine, R.A. Buhrman, D.C. Ralph, Appl. Phys. Lett. **77**, 3809 (2000)
24. J. Grollier, V. Cros, A. Hamzic, J.M. George, H. Jaffrès, A. Fert, G. Faini, J.B. Youssef, H. Legall, Appl. Phys. Lett. **78**, 3663 (2001)
25. S. Urazhdin, N.O. Birge, W.P. Pratt Jr., J. Bass, Phys. Rev. Lett. **91**, 146803 (2003)
26. I.N. Krivorotov, N.C. Emley, J.C. Sankey, S.I. Kiselev, D.C. Ralph, R.A. Buhrman, Science **307**, 228 (2005)
27. J.M. George, L.G. Pereira, A. Barthélémy, F. Petroff, L. Steren, J.L. Duvail, A. Fert, R. Loloee, P. Holody, P.A. Schroeder, Phys. Rev. Lett. **72**, 408 (1994)
28. M. Buchmeier, R. Schreiber, D. Bürgler, P. Grünberg, Europhys. Lett. **63**, 874 (2003)
29. M. AlHajDarwish, H. Kurt, S. Urazhdin, A. Fert, R. Loloee, W.P. Pratt Jr., J. Bass, Phys. Rev. Lett. **93**, 157203 (2004)
30. R. Lehndorff, D.E. Bürgler, A. Kakay, R. Hertel, C.M. Schneider, Phys. Rev. B **76**, 214420 (2007)
31. O. Boulle, V. Cros, J. Grollier, L.G. Pereira, C. Deranlot, F. Petroff, G. Faini, J. Barnas, A. Fert, Nat. Phys. **3**, 492 (2007)
32. T. Devolder, A. Meftah, K. Ito, J.A. Katine, P. Crozat, C. Chappert, J. Appl. Phys. **101**, 063916 (2007)
33. R. Lehndorff, D.E. Bürgler, A. Kakay, R. Hertel, C.M. Schneider, IEEE Trans. Magn. **44**, 1951 (2008)
34. K.Y. Guslienko, B.A. Ivanov, V. Novosad, Y. Otani, H. Shima, K. Fukamichi, J. Appl. Phys. **91**, 8037 (2002)
35. R.P. Cowburn, J. Phys. D, Appl. Phys. **33**, R1 (2000)
36. R. Hertel, O. Fruchart, S. Cherifi, P.O. Jubert, S. Heun, A. Locatelli, J. Kirschner, Phys. Rev. B **72**, 214409 (2005)
37. W.H. Rippard, M.R. Pufall, S. Kaka, T.J. Silva, S.E. Russek, Phys. Rev. B **70**, 100406(R) (2004)
38. D. Houssameddine, U. Ebels, B. Delaët, B. Rodmacq, I. Firastrau, F. Ponthenier, M. Brunet, C. Thirion, J.-P. Michel, L. Prejbeanu-Buda, M.-C. Cyrille, O. Redon, B. Dieny, Nat. Mater. **6**, 447 (2007)
39. A.M. Deac, A. Fukushima, H. Kubota, H. Maehara, Y. Suzuki, S. Yuasa, Y. Nagamine, K. Tsunekawa, D.D. Djayaprawira, N. Watanabe, Nat. Phys. **4**, 803 (2008)
40. V.S. Pribiag, I.N. Krivorotov, G.D. Fuchs, P.M. Braganca, O. Ozatay, J.C. Sankey, D.C. Ralph, R.A. Buhrman, Nat. Phys. **3**, 498 (2007)
41. Q. Mistral, M. van Kampen, G. Hrkac, J.-V. Kim, T. Devolder, P. Crozat, C. Chappert, L. Lagae, T. Schrefl, Phys. Rev. Lett. **100**, 257201 (2008)
42. R. Lehndorff, D.E. Bürgler, S. Gliga, R. Hertel, P. Grünberg, C.M. Schneider, Phys. Rev. B **80**, 054412 (2009)
43. A. Kákay, S. Gliga, R. Hertel, R. Lehndorff, D.E. Bürgler, C.M. Schneider, unpublished
44. A.N. Slavin, P. Kabos, IEEE Trans. Magn. **41**, 1264 (2005)
45. A.V. Khvalkovskiy, J. Grollier, N. Locatelli, Y.V. Gorbunov, K.A. Zvezdin, V. Cros, Appl. Phys. Lett. **96**, 212507 (2010)
46. V. Sluka, A. Kákay, A.M. Deac, D.E. Bürgler, R. Hertel, C.M. Schneider, J. Phys. D, Appl. Phys. **44**, 384002 (2011)
47. S. Kaka, M. Pufall, W.H. Rippard, T.J. Silva, S.E. Russek, J. Katine, Nature **437**, 389 (2005)
48. F.B. Mancoff, N.D. Rizzo, B.N. Engel, S. Tehrani, Nature **437**, 393 (2005)
49. M.R. Pufall, W.H. Rippard, S.E. Russek, S. Kaka, J.A. Katine, Phys. Rev. Lett. **97**, 087206 (2006)
50. A. Ruotolo, V. Cros, B. Georges, A. Dussaux, J. Grollier, C. Deranlot, R. Guillemet, K. Bouzehouane, S. Fusil, A. Fert, Nat. Nanotechnol. **4**, 528 (2009)
51. J. Grollier, V. Cros, A. Fert, Phys. Rev. B **73**, 060409 (2006)

52. B. Georges, J. Grollier, M. Darques, V. Cros, C. Deranlot, B. Marcilhac, G. Faini, A. Fert, Phys. Rev. Lett. **101**, 017201 (2008)
53. W.H. Rippard, M.R. Pufall, S. Kaka, T.J. Silva, S.E. Russek, J.A. Katine, Phys. Rev. Lett. **95**, 067203 (2005)
54. R. Lehndorff, D.E. Bürgler, C.M. Schneider, Z. Celinski, Appl. Phys. Lett. **97**, 142503 (2010)
55. A. Slavin, V. Tiberkevich, IEEE Trans. Magn. **45**, 1875 (2009)
56. T. Iwase, Y. Sakuraba, S. Bosu, K. Saito, S. Mitani, K. Takanashi, Appl. Phys. Express **2**, 063003 (2009)
57. Y. Zhou, J. Persson, S. Bonetti, J. Åkerman, Appl. Phys. Lett. **92**, 092505 (2008)

Chapter 3
Origin of Ferromagnetism in Co-Implanted ZnO

Numan Akdoğan and Hartmut Zabel

Abstract The potential of room temperature ferromagnetism in many diluted magnetic semiconductor oxide systems has opened up a new route for realizing spintronic devices. Based on theoretical calculations and experimental observations, TiO_2, in both the anatase and rutile phases, and ZnO have been extensively studied as a host matrix for transition metal doping, in particular with cobalt. In this work, the structural, magnetic, and electronic properties of Co-implanted *n*-type ZnO films grown on sapphire substrates have been studied in detail. X-ray diffraction and transmission electron microscopy results show the presence of a $(10\bar{1}0)$ oriented hexagonal Co phase in the sapphire substrate, but not in the ZnO film. The diameter of the Co clusters is about 5–6 nm, forming a Co-rich layer in the substrate close to the ZnO/Al_2O_3 interface. However, the multiplet structure of the X-ray absorption spectra around the Co L_3 edge indicates that the implanted cobalt ions are in the Co^{2+} state in the ZnO film. Magnetization measurements show that there are two magnetic phases in the implanted region. One is the intrinsic room temperature ferromagnetism due to Co substitution on Zn sites in the ZnO layer, and the second magnetic phase originates from Co clusters in the sapphire substrate. The magnetic moment per substituted cobalt is about 2.81 μ_B, which is very close to the theoretical expected value of 3 μ_B/Co for Co^{2+} in its high spin state. Ferromagnetic resonance data show that the easy and hard axes have a periodicity of 60° in the film plane, in agreement with the hexagonal structure of the ZnO films. This sixfold in-plane magnetic anisotropy is attributed to the substitution of cobalt on Zn sites in the ZnO structure, and is a clear indication of long-range ferromagnetic ordering between substitutional cobalt ions in the single-crystalline ZnO films. Magnetic dichroism at the O *K* edge and the anomalous Hall effect are also observed in the Co-implanted ZnO films, supporting the intrinsic nature of the observed ferromagnetism.

N. Akdoğan (✉)
Department of Physics, Gebze Institute of Technology, 41400 Kocaeli, Turkey
e-mail: akdogan@gyte.edu.tr

H. Zabel
Institut für Experimentalphysik/Festkörperphysik, Ruhr-Universität Bochum, 44780 Bochum, Germany

B. Aktaş, F. Mikailzade (eds.), *Nanostructured Materials for Magnetoelectronics*, Springer Series in Materials Science 175, DOI 10.1007/978-3-642-34958-4_3,

3.1 Introduction

Spintronics, a short notation for spin-based electronics, is a new research area which seeks to exploit the spin of electrons in addition to their charge in semiconductors. The basic idea is to combine the characteristics of existing magnetic devices with semiconductor devices in order to realize a new generation of devices that are much smaller, more energy efficient, non-volatile, and much faster than those presently available [1–9]. There are two different approaches for realizing spintronic devices. One is metal-based spintronics, which uses ferromagnetic metals, and the second one is semiconductor-based spintronics, consisting of ferromagnetic semiconductors.

Metal-based spintronics has been the basis of information storage devices such as read heads for magnetic hard disk drives, since the discovery of the giant magnetoresistance (GMR) effect. The GMR effect[1] was reported by P. Grünberg [10] and A. Fert [11] in 1988 for layered magnetic thin film structures that consist of alternating layers of ferromagnetic and nonmagnetic layers. When the magnetization of ferromagnetic layers is parallel, the material shows very low resistance. When the magnetization of ferromagnetic layers is antiparallel, the spin-dependent scattering of carriers becomes maximum and the material exhibits higher resistance. In metal-based spintronics, researchers and developers now seek to improve the existing GMR devices by developing new materials with enhanced spin polarization and better spin filtering. A similar rapid development is expected from tunneling magnetoresistance (TMR) devices, which are composed of two ferromagnetic layers separated by an insulating metal oxide layer with a thickness of a few nanometers. In these devices, electrons can easily tunnel through the insulating barrier depending on the relative magnetization of the two ferromagnetic layers, and on the fact that the spin of the electrons is preserved as they pass through the barrier. The TMR effect leads to a more pronounced resistance change in small applied fields than is observed in GMR devices. In 1995 Moodera et al. [12] demonstrated TMR at room temperatures with very thin oxide layers. Less than a decade later, Motorola, IBM and Infineon are manufacturing fast magnetic storage devices that incorporate dense arrays of TMR elements, known as magnetic random access memory (MRAM).

In semiconductor-based spintronics, much effort is focused on producing ferromagnetism in semiconductors above room temperature. If successful, this new class of spintronic devices could be integrated much more easily with conventional semiconductor technology. The key requirement in the development of these devices is an efficient injection, transfer, and detection of spin-polarized current from a ferromagnetic material into a semiconductor. Because of the well-known problem of a resistance mismatch at metal/semiconductor interfaces, hindering an effective spin injection [13], much interest is now concentrated on the development of room temperature ferromagnetic semiconductors.

[1] In 2007, P. Grünberg and A. Fert were awarded the Nobel Prize in Physics for the discovery of this effect.

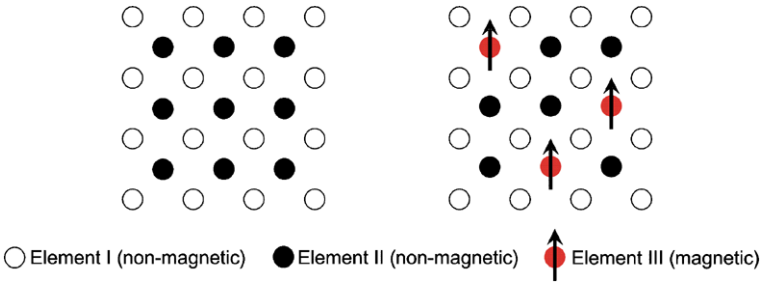

Fig. 3.1 Schematic representation of a nonmagnetic semiconductor (*left*), and a diluted magnetic semiconductor (*right*). In the style of Ref. [46]

Diluted magnetic semiconductors (DMSs) get their name from the fact that some fraction of atoms in a nonmagnetic semiconductor is replaced by magnetic ions (Fig. 3.1). DMSs are promising candidates for spintronic applications at practical temperatures, provided that their Curie temperature (T_c) is above room temperature. Therefore, a number of different semiconductor hosts have been investigated to test their magnetic properties. In the past the most attention has been paid to (Ga, Mn)As [14–37] and (In, Mn)As [38–45] systems. However, due to their reported highest Curie temperatures—around 170 K for (Ga, Mn)As [46–48] and 35 K for (In, Mn)As [48, 49]—they are disqualified for most practical applications.

Therefore, there is a great incentive for developing new DMS materials which are ferromagnetic above room temperature. In particular, the calculations of Dietl et al. [50] showed that Mn-doped ZnO would exhibit ferromagnetism above room temperature. Sato et al. have also investigated ferromagnetism of ZnO-based DMSs by ab initio electronic structure calculations based on the local spin density approximation, and they reported ferromagnetic ordering of 3*d* transition metal (TM) ions in ZnO [51, 52]. In addition, Matsumoto et al. observed room temperature ferromagnetism in Co-doped anatase TiO_2 [53]. These theoretical predictions and experimental results generated much interest in the TM-doped ZnO [54–68] and Co-doped TiO_2 systems as a potential oxide-based DMS [69–78].

While some of these works reported the observation of ferromagnetism above room temperature, the origin of ferromagnetism in these systems is not yet well understood. The main unresolved question is whether the observed ferromagnetism originates from uniformly distributed TM ions in the host matrix or whether it is due to the precipitation of secondary phases such as metallic clusters. If a DMS contains TM ions below their equilibrium solubility limit, no secondary phases are expected. In this case, since the strength of the magnetism is proportional to the number of TM ions substituted on the cation sites in a DMS, the realization of high T_c ferromagnetism is difficult. On the other hand, at higher TM dopant concentrations the doped TMs start to form unwanted metallic clusters. For this reason, to achieve a high T_c ferromagnetism in a single phase DMS, nonequilibrium sample preparation techniques such as low temperature molecular beam epitaxy (MBE) and ion implantation are required.

Ion implantation is widely used in silicon technology for integrated circuits due to its reliability, precision, and reproducibility [79]. It has also proven to be a reliable method for injecting TMs into a host semiconductor material beyond their solubility limits [80].

In this work[2] an ion implantation technique is used to implant cobalt ions into ZnO. There are two main purposes of this work. One is to produce ZnO-based ferromagnetic semiconductors which have T_c values higher than room temperature. The second aim is to shed some light on the origin of room temperature ferromagnetism, i.e., whether it originates from clusters or from uniformly distributed magnetic cobalt atoms. In an attempt to fabricate ferromagnetic semiconductors, ZnO films are exposed to magnetic cobalt ions for varying implantation doses. Rutherford backscattering spectrometry (RBS), X-ray diffraction (XRD), atomic force microscopy (AFM), and transmission electron microscopy (TEM) were used to obtain Co distribution profiles and to identify possible second phases in these systems. The magnetic properties of the implanted materials have been investigated using the magneto-optical Kerr effect (MOKE), superconducting quantum interference device (SQUID) magnetometry, ferromagnetic resonance (FMR), and X-ray resonant magnetic scattering (XRMS) as well as X-ray magnetic circular dichroism (XMCD). Hall effect measurements were also performed to determine the type of carriers in the Co-implanted ZnO films.

3.2 Overview

ZnO is a II–VI semiconductor with a wide band gap of about 3.4 eV. The stable crystal structure of ZnO is the wurtzite structure (hexagonal, with $a = 3.25$ Å and $c = 5.12$ Å) [81], in which each atom of zinc is surrounded by four oxygen atoms in tetrahedral coordination. The TM-doped ZnO is interesting from the viewpoint of forming a transparent ferromagnetic material, and it has the potential to be a highly multifunctional material with coexisting magnetic, semiconducting, and optical properties. The first observation of ferromagnetism in Co-doped ZnO was reported by Ueda et al. [54]. They prepared $Zn_{1-x}Co_xO$ thin films on sapphire substrates using a pulsed laser deposition (PLD) technique with x varying between 0.05 and 0.25. Following these initial theoretical and experimental reports, different growth methods have been used to deposit Co:ZnO films, including radio-frequency (RF) magnetron co-sputtering [82], PLD using a KrF laser [83–89], combinatorial laser molecular beam epitaxy (LMBE) [90, 91], a sol–gel method [92], and ion implantation [65–67, 93–108]. Sapphire was widely used as a substrate due to the lower mismatch (2 %) between the film and the substrate. In addition to cobalt, different 3*d* transition elements have also been used for doping, including Mn

[2]Some parts of this work are published in the articles *Intrinsic room temperature ferromagnetism in Co-implanted ZnO* [65], *Dose dependence of ferromagnetism in Co-implanted ZnO* [66], and *Six-fold in-plane magnetic anisotropy in Co-implanted ZnO (0001)* [67].

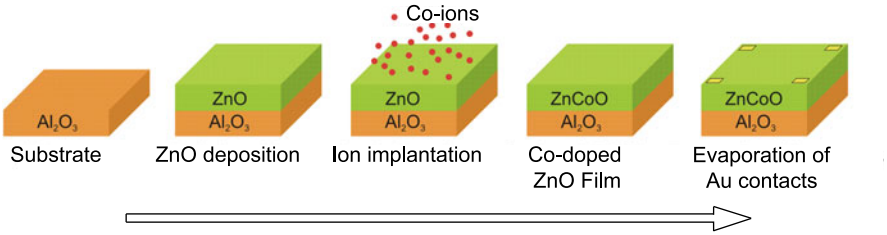

Fig. 3.2 Sample preparation stages for Co-implanted ZnO/Al_2O_3 films [66]

[54, 90, 101, 104, 109, 110], Ni [54, 68, 87, 90, 96, 100, 101, 104], V [87, 90, 111], Cr [54, 87], and Fe [54, 87, 90, 100, 101, 112, 113].

Various solubility limits for Co in ZnO have been reported by different groups. Prellier et al. [86] found that the solubility limit is about 10 % in PLD-grown films. Park et al. [114] reported that the cobalt nanoclusters start to form for $x \geq 12$ at.% in samples grown by sol–gel and RF sputtering techniques. Lee et al. [92] observed some undefined peaks for a cobalt content higher than 25 %. Kim et al. [84] showed the solubility limit to be less than 40 % in PLD-grown films. Ueda et al. [54] claimed that the solubility limit is lower than 50 %, and they clearly observed phase separations into ZnO and CoO in a film prepared using $Zn_{0.5}Co_{0.5}O$ targets. This controversy between different research groups seems to result from the growth technique used and/or from the growth conditions such as oxygen pressure and deposition temperature.

Regarding the magnetic properties of the Co:ZnO films, while some groups observed room temperature ferromagnetism [65–67, 86, 87, 89, 92, 115], others reported the absence of ferromagnetism [84, 90, 114]. The review articles on TM-doped ZnO [55, 56, 58, 60, 61, 116] provide detailed information.

3.3 Sample Preparation

About 350 Å thick ZnO films were grown on 10×10 mm^2 epi-polished single-crystalline Al_2O_3 $(11\bar{2}0)$ substrates by RF (13.56 MHz) sputtering of a ZnO target [117]. The sputtering was carried out in an atmosphere of 5×10^{-3} mbar pure Ar (99.999 %) with a substrate temperature of 500 °C. In order to increase the quality of ZnO films, we carried out post-growth annealing in an oxygen atmosphere with a partial pressure of up to 2000 mbar and a temperature of 800 °C. After annealing, the ZnO samples were implanted in an ILU-3 ion accelerator (Kazan Physical-Technical Institute of the Russian Academy of Science) by using 40 keV Co^+ ions with an ion current density of 8 μA cm^{-2}. The sample holder was cooled by flowing water during the implantation to prevent the samples from overheating. The implantation dose varied in the range of $0.25–2.00 \times 10^{17}$ ions cm^{-2}.

After implantation, the samples were cut into square pieces, and gold contacts were evaporated on the corners of the samples for anomalous Hall effect (AHE) studies (Fig. 3.2). The list of the Co-implanted ZnO films is given in Table 3.1.

Table 3.1 List of the ZnO films implanted with 40 keV Co^+ for varying Co ion dose

Sample dose	($\times 10^{17}$ ion cm^{-2})
1	0.25
2	0.50
3	0.75
4	1.00
5	1.25
6	1.50
7	2.00

3.4 Structural Properties

The depth dependence of the cobalt concentration in the Co-implanted ZnO/Al_2O_3 films was investigated using the RBS technique at the Dynamic Tandem Laboratory (DTL) at Ruhr-Universität Bochum. The RBS data show both a maximum of cobalt concentration (about 50 at.%) located close to the ZnO/Al_2O_3 interface and an extended inward tail due to cobalt diffusion into the volume of the Al_2O_3 substrate (Fig. 3.3). It is also observed that after ion implantation the thickness of the ZnO layer has decreased from originally 35 nm to 28 nm. According to the SRIM algorithm,[3] the average implanted depth of 40 keV Co ions in ZnO/Al_2O_3 is about 20.4 nm with a straggling of 9.6 nm in the Gaussian-like depth distribution (see the inset in Fig. 3.3). However, because of the surface sputtering, ion mixing, and heating of the implanted region by the ion beam, there is a redistribution of the implanted cobalt compared to the calculated profile.

The high-angle XRD experiments provide information on the structural coherence of the films and in our case also give us a chance to detect possible additional phases in the sample after ion implantation. Figure 3.4 shows high-angle Bragg scans of the ZnO films before (a) and after (b) cobalt implantation. The data were taken using synchrotron radiation at the Hamburg Synchrotron Radiation Laboratory (HASYLAB) (Fig. 3.4(a)) and at the Dortmund Electron Accelerator (DELTA) (Fig. 3.4(b)) with an energy of $E = 11000$ eV. XRD measurements yielded evidence for the $(10\bar{1}0)$ reflection of the Co hcp structure as is clearly seen on the right side of the sapphire substrate peak (Fig. 3.4(b)). The heavy ion bombarding also causes a reduction of intensity of the ZnO (0001) peak, and this intensity reduction increases with increasing cobalt concentration. After implantation, a tail (shown by an arrow in Fig. 3.4) appears around the main peak of Al_2O_3 $(11\bar{2}0)$ reflection which is not observed before implantation. This tail likely reflects the lattice expansion of the sapphire substrate upon Co implantation.

In order to further investigate both the presence of metallic cobalt clusters and the damage of the sapphire substrate, high-resolution cross-sectional TEM measurements were performed. The sample was prepared for TEM measurements by using

[3] The Stopping and Range of Ions in Matter (SRIM) [118]. SRIM software at http://www.srim.org/.

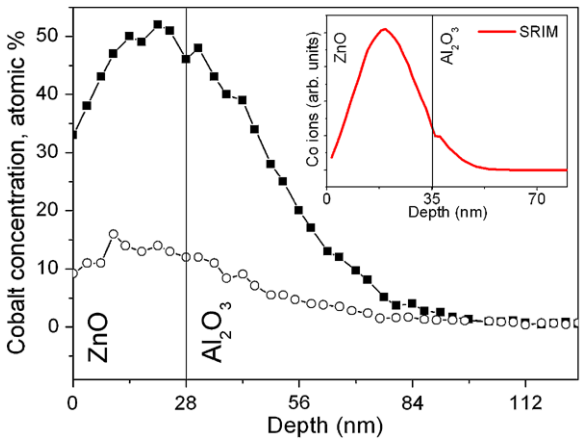

Fig. 3.3 Depth dependence of the cobalt concentration in ZnO/Al_2O_3 implanted with Co ions with a dose of 0.25×10^{17} ions cm^{-2} (*open circles*) and 1.50×10^{17} ions cm^{-2} (*closed squares*), respectively. The *inset* shows the calculated SRIM profile without taking into account ion sputtering effects [65, 66]

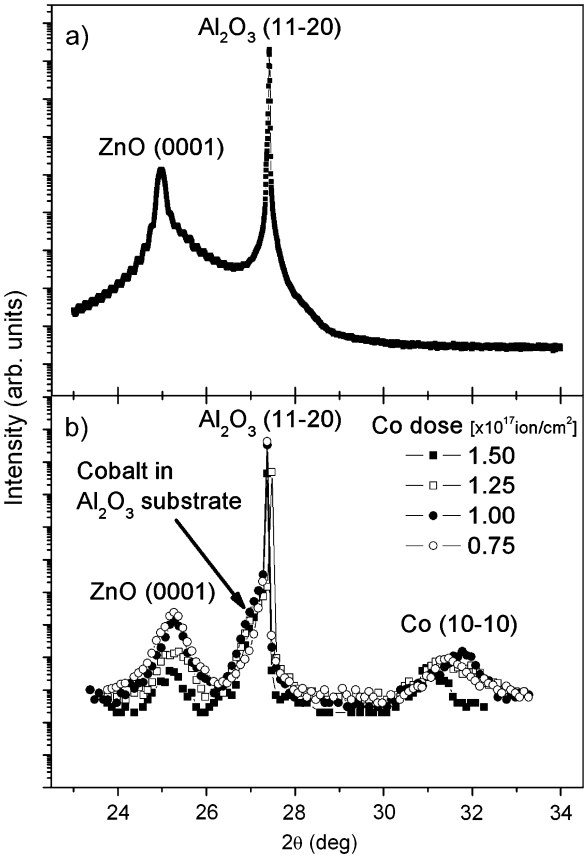

Fig. 3.4 High-angle Bragg scans of the ZnO films before (**a**) and after (**b**) cobalt ion implantation [65, 66]

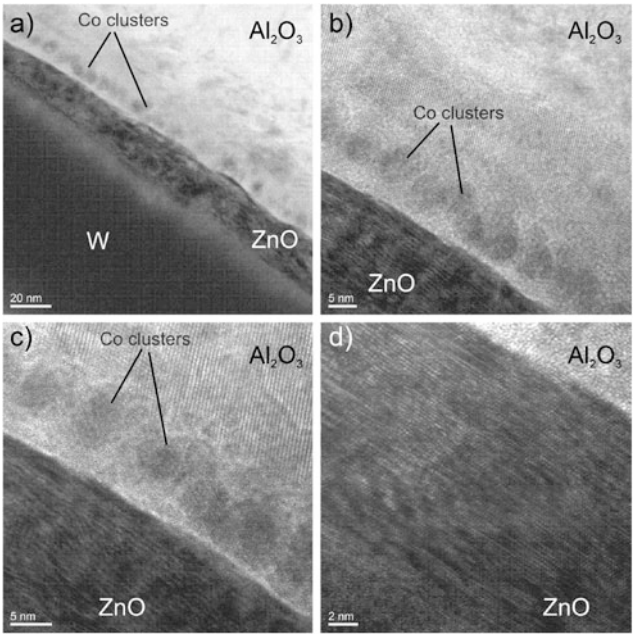

Fig. 3.5 TEM images of Co-implanted ZnO/Al_2O_3 film (sample 6). Cobalt clusters are clearly seen in Al_2O_3 substrate [65]

a focused ion beam (FIB) technique. To prevent charging effects, the sample surface was covered by tungsten (W) film, and then a very small cross-sectional piece of implanted sample was cut using FIB. Figure 3.5 presents TEM images of sample 6 (1.50×10^{17} ions cm^{-2}) with an increasing magnification from 20 nm to 2 nm. In the first image (Fig. 3.5(a)), a general overview of the ZnO/Al_2O_3 sample is shown. The cobalt clusters can be seen in the sapphire substrate located close to the ZnO/Al_2O_3 interface. The clusters most likely form because of a decomposition of Co in the Al_2O_3 substrate. Clustering occurs in Al_2O_3 at an annealing temperature of 900 °C [119]. Obviously, ion bombardment heats up the sample locally to this temperature. Figures 3.5(b) and (c) focus on the ZnO/Al_2O_3 interface. These images reveal that the cobalt clusters have a size of about 5–6 nm and that they nearly touch each other. Further information from these images is the deformation of the Al_2O_3 crystal structure close to the ZnO/Al_2O_3 interface. This results in a lattice expansion of the substrate, which is in agreement with the XRD results shown in Fig. 3.4. However, far from the interface the structure of Al_2O_3 is preserved and one can see nicely the atomic rows of Al_2O_3 presented in Fig. 3.5(c). Figure 3.5(d) shows the ZnO layer with a magnification of 2 nm. Even after heavy ion bombardment, ZnO still has a good arrangement of atomic rows. Moreover, no distinct clusters can be observed in this region.

3.5 Magnetic Properties

3.5.1 Room Temperature Magnetization Measurements

In this section the magnetization behavior of the Co-implanted ZnO films for different implantation doses is discussed. Figure 3.6 shows the hysteresis loops of Co-implanted ZnO films which were recorded at room temperature using a high-resolution MOKE setup [120–123] in the longitudinal configuration with s-polarized light. The MOKE data in Fig. 3.6 clearly indicate that, after cobalt implantation, nonmagnetic ZnO becomes ferromagnetic at room temperature with a large remanent magnetization. With increasing cobalt concentration the implanted ZnO films exhibit sequentially paramagnetic, weak ferromagnetic, and, finally, ferromagnetic response with a square-like hysteresis at room temperature for the dose of 1.50×10^{17} ions cm^{-2}. For the highest dose (2.00×10^{17} ions cm^{-2}) the square-like shape of the hysteresis disappears and the coercive field increases drastically. This indicates that at this dose cobalt atoms start to form clusters in the ZnO film. Moreover, no in-plane magnetic anisotropy is observed in Co-implanted ZnO films.

Since the MOKE technique is only sensitive to the magnetization of thin layers close to the surface (20–30 nm penetration depth), M–H measurements have also been carried out using a Quantum Design MPMS XL SQUID magnetometer. In Fig. 3.7 the MOKE and SQUID hysteresis loops of sample 6 (1.50×10^{17} ions cm^{-2}) are compared. Figure 3.7(b) presents the SQUID hysteresis loop of this sample after subtraction of a diamagnetic contribution from the sapphire substrate. The coercive field of this hysteresis is more or less the same as measured by the MOKE technique. However, some additional contributions appear, and the magnetization saturates at considerably higher fields.

3.5.2 XRMS and XAS Measurements

To study the observed ferromagnetic behavior in detail, the magnetic properties of Co-implanted ZnO films were investigated using the X-ray resonant magnetic scattering (XRMS) and X-ray absorption spectroscopy (XAS) techniques [124].

XRMS has proven to be a highly effective method for the analysis of the magnetic properties of buried layers and interfaces, including their depth dependence [125, 126]. Moreover, if the photon energy is fixed close to the energy of the corresponding absorption edges, element-specific hysteresis loops can be measured by varying the external magnetic field [127]. Since there are three elements in the Co-doped ZnO film, the analysis can be carried out separately for Co, O, and Zn.

The XRMS experiments were performed with the ALICE diffractometer [128] at the undulator beamline UE56/1-PGM at BESSY II (Berlin, Germany). The diffractometer comprises a two-circle goniometer and works in horizontal scattering geometry. A magnetic field can be applied in the scattering plane along the sample surface either parallel or antiparallel to the photon helicity, which corresponds to

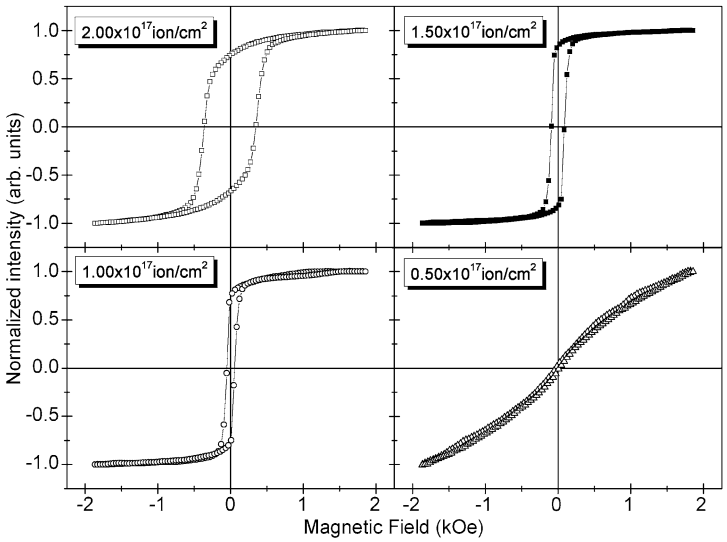

Fig. 3.6 Room temperature MOKE hysteresis curves of Co-implanted ZnO films measured for varying implantation dose [66]

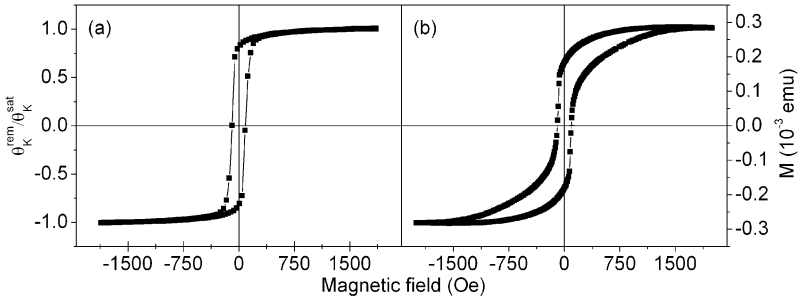

Fig. 3.7 The MOKE (**a**) and SQUID (**b**) hysteresis curves of sample 6 (1.50×10^{17} ions cm^{-2}) [65]

the longitudinal magneto-optical Kerr effect (L-MOKE) geometry. The maximum field of ± 0.27 T was high enough to fully saturate the sample. The magnetic contribution to the scattered intensity was always measured by switching the magnetic field at fixed photon helicity.

Figure 3.8 shows the specular reflectivities of sample 6 measured at the Co L_3 edge ($E = 780$ eV) in magnetic saturation. The measurements were taken at room temperature and with a magnetic field applied in the sample plane parallel (I^+, solid line) and antiparallel (I^-, open circles) to the photon helicity. Due to the high surface roughness, no Kiessig fringes are observed in the reflectivity curves. In addition the splitting of the two curves is clearly seen in Fig. 3.8. The inset in Fig. 3.8 presents the angular dependence of the asymmetry ratio to show how the magnetic

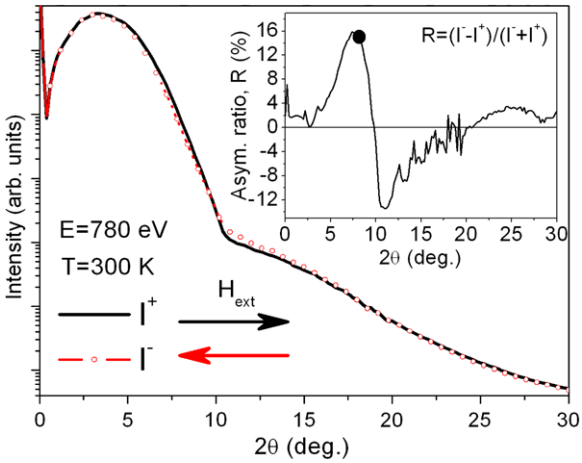

Fig. 3.8 Reflectivity scans of sample 6 taken at the Co L_3 edge ($E = 780$ eV) with a magnetic field applied in the sample plane parallel (I^+, *solid line*) and antiparallel (I^-, *open circles*) to the photon helicity. *Inset* shows the asymmetry ratio (R) as a function of angle [65]

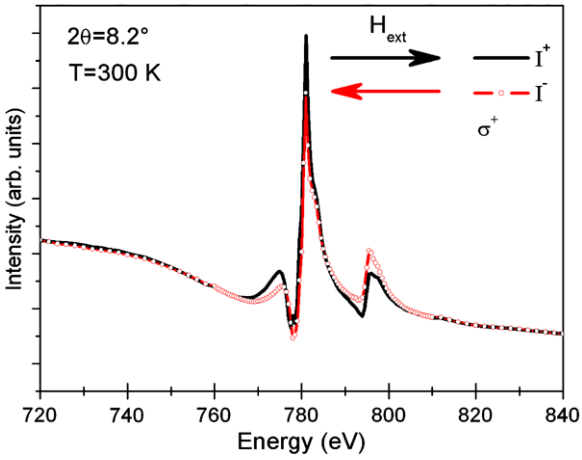

Fig. 3.9 Energy dependence of scattering intensities (XRMS) at the Co L edges for sample 6 measured at room temperature [65]

signal varies. As a compromise between high scattering intensity and high magnetic sensitivity for the investigation of the magnetic properties at the Co L edges, the scattering angle was fixed at the position of $2\theta = 8.2°$ (shown by a black circle in the inset in Fig. 3.8). For measurements at the O K edge ($E \sim 530$ eV) the scattering angle was fixed at $2\theta = 12°$, which corresponds to the same scattering vector in the reciprocal space.

The energy dependence of the intensity (XRMS) around the Co $L_{3,2}$ edges measured in positive (solid line) and negative (open circles) saturation fields is shown in Fig. 3.9 for sample 6. Since the magnetic contribution to the resonant scattering can best be visualized by plotting the asymmetry ratio, $R = (I^+ - I^-)/(I^+ + I^-)$, in Fig. 3.10 the asymmetry ratios for samples doped with different doses are presented. The asymmetry ratio shows a strong ferromagnetic signal for sample 6 (up to 30 %), and it decreases with decreasing cobalt implantation dose. The fine structure of the Co L_3 peak in Fig. 3.9 is typical for oxidized cobalt, which was observed before for

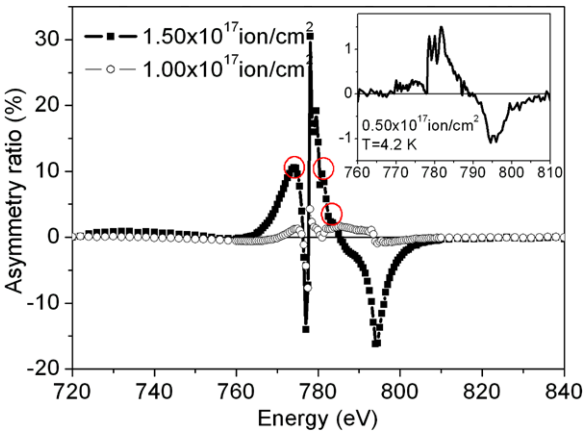

Fig. 3.10 The asymmetry ratios taken at the Co L edges for sample 6 (1.50×10^{17} ions cm^{-2}) and sample 4 (1.00×10^{17} ions cm^{-2}) shown by *closed* and *open symbols*, respectively. *Inset* presents the asymmetry ratio of sample 2 (0.50×10^{17} ions cm^{-2}) measured at 4.2 K [66]

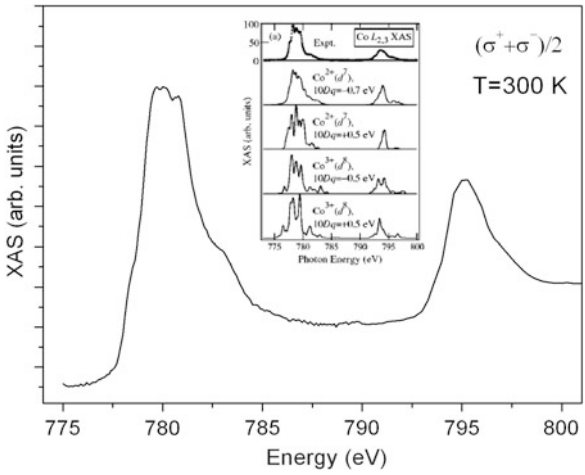

Fig. 3.11 XAS spectra of sample 6 measured at the Co $L_{2,3}$ edges by using TEY method. σ^+ and σ^- denote right and left circularly polarized light, respectively [65]. *Inset* shows the experimental Co $L_{2,3}$ edge XAS spectrum (*top*) compared with atomic multiplet calculations of Kobayashi et al. [130]

CoO by Regan et al. [129]. They also showed that in the case of metallic cobalt the Co L_3 peak consists of mainly a single component.

Recently, Kobayashi et al. [130] reported that in the presence of the Co^{2+} state in Co-doped ZnO, the XAS spectrum exhibits a multiplet structure around the Co L_3 edge (see inset in Fig. 3.11). To check whether this behavior is also present in our samples, XAS experiments were carried out at the undulator beamline UE52-SGM at BESSY II using the ALICE diffractometer. The absorption data were taken by the total electron yield (TEY) method, i.e., by measuring the sample drain current. Since the excited electron trajectories are affected by the external magnetic field, the XAS spectra were taken with fixed photon helicity at remanence. The angle of incidence was chosen to be 4.1° with respect to the surface. The spectra were normalized to the incoming photon flux. Figure 3.11 shows the averaged x-ray absorption spectra $(\sigma^+ + \sigma^-)/2$ at the Co $L_{2,3}$ edges. The XAS spectrum clearly shows a multiplet structure at the L_3 edge which is similar to that observed previously for Co-doped

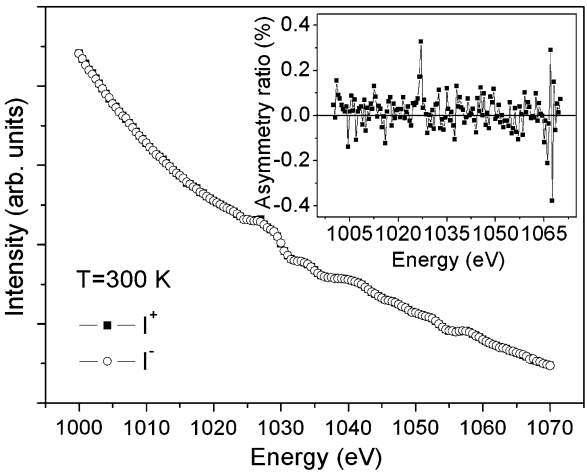

Fig. 3.12 The XRMS data for sample 6 taken at the Zn L_3 edge. The *inset* shows the asymmetry ratio [65]

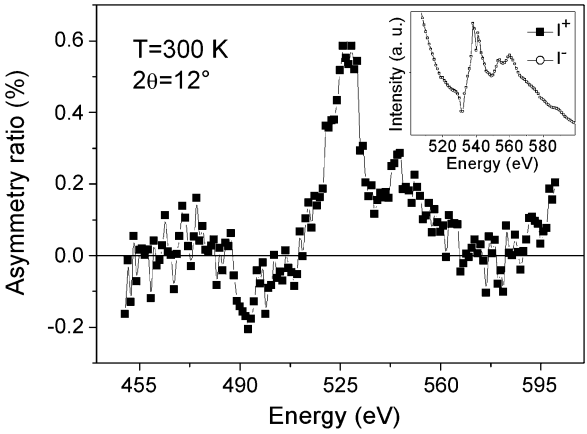

Fig. 3.13 The asymmetry ratio for sample 6 taken at the O *K* edge. The *inset* shows the XRMS data at the O *K* edge [65]

ZnO by Kobayashi et al. This multiplet structure is a clear sign of the presence of oxidized cobalt in this sample.

The magnetic signals at the Zn L_3 ($E \sim 1020$ eV) and the O *K* edges were also investigated. Within the sensitivity limit no magnetic signal could be recorded for Zn (Fig. 3.12). However, a clear magnetic signal was observed at the O *K* edge. The asymmetry ratio of sample 6 measured at the O *K* edge is presented in Fig. 3.13. Note that the maximum in the asymmetry ratio of oxygen is much smaller (by roughly a factor of 20) than the asymmetry ratio of cobalt shown by the closed symbols in Fig. 3.10. In addition to sample 6, a magnetic signal at the O *K* edge could also be observed for samples 4, 5, and 7.

In Fig. 3.14 the magnetic hysteresis curves recorded at the Co L_3 (773.4 eV) and O *K* (526.8 eV) edges are compared. The shape and the coercive field of the hysteresis curves are the same, but the intensity is much lower for the O *K* edge.

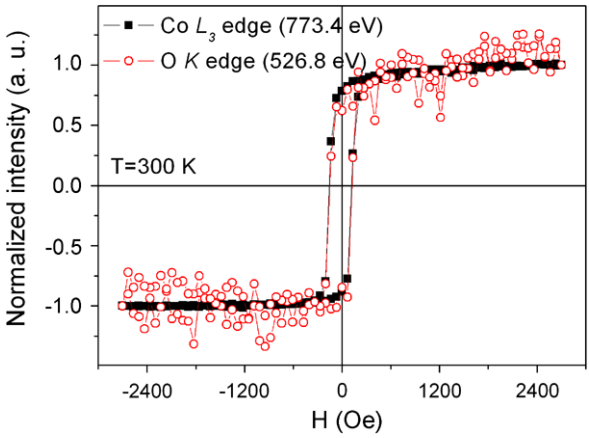

Fig. 3.14 Hysteresis curves of sample 6 measured at the Co L_3 (*closed symbols*) and O K (*open symbols*) edges [65]

This is a clear indication of a spin polarization of oxygen atoms in the ZnO host matrix.

Since an additional magnetic contribution is observed in the SQUID hysteresis curve of sample 6 (Fig. 3.7(b)), we used the XRMS technique to check whether this feature also becomes visible. For this reason, several hysteresis loops are recorded at different photon energies; a systematic change of the hysteresis loop shape is observed with changing photon energy. Here, the only three hysteresis curves shown by open red circles in Fig. 3.10 are presented. The shape of the hysteresis curve taken at 773.4 eV (closed symbols in Fig. 3.14) is practically the same as the one measured by MOKE (Fig. 3.7(a)). However, when the incoming photon energy is increased to 781 eV and 783 eV, two different hysteresis loops are observed. Figure 3.15(a) presents the hysteresis curve recorded at 781 eV. At this energy the hysteresis curve has two components with a small and a large coercive field and it is similar to the SQUID hysteresis (Fig. 3.7(b)). At higher energies the low coercive field component vanishes, and at an energy of 783 eV (Fig. 3.15(b)) the hysteresis curve consists of practically only one component with the large coercive field. This large coercive field component originates from the strong interaction between cobalt clusters in the sapphire substrate and is present even at room temperature.

The reason for the observation of different hysteresis curves using the XRMS technique can be interpreted by the change in optical parameters as a function of the incident photon energy. Depending on the energy deviation from the $L_{2,3}$ resonance condition, both types of magnetic hysteresis can be detected in sample 6. For an energy of 773.4 eV, which is very close to the L_3 resonance energy, the contribution to the scattering intensity from the phase with the large coercive field vanishes, resulting in a hysteresis loop (closed symbols in Fig. 3.14) which is similar to the one measured by MOKE (Fig. 3.7(a)). However, at a photon energy of 781 eV, at the resonance condition, both phases contribute to the scattering intensity. The hysteresis taken at this energy (Fig. 3.15(a)) presents the superposition of two phases of cobalt in the host material and is similar to the hysteresis measured with the SQUID magnetometer (Fig. 3.7(b)). The hysteresis loop recorded at an energy of

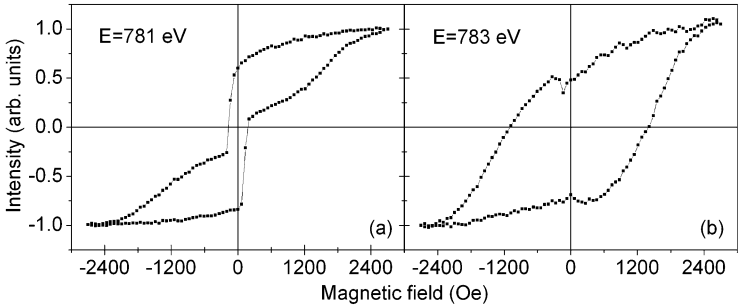

Fig. 3.15 (**a**) Hysteresis loop measured at an energy of 781 eV shows the superposition of two different phases of cobalt in the host material. (**b**) Hysteresis loop taken at an energy of 783 eV [65]

783 eV (Fig. 3.15(b)) is representative of the metallic phase of cobalt in Al_2O_3 with a large coercive field, whereas at this energy the contribution to scattering intensity from the small coercive field component is nearly zero.

3.5.3 Temperature-Dependent Magnetization Measurements

In order to check the temperature dependence of magnetization for ZnO films doped with different doses, field-cooled (FC) and zero-field-cooled (ZFC) M–T measurements have been carried out using SQUID magnetometry. For ZFC measurements, the samples are cooled in zero field to 5 K and the magnetization is recorded during warm-up to 390 K with an applied field of 0.1 kOe, parallel to the film surface. For FC measurements the applied field of 0.1 kOe is maintained during cooling to 5 K and the magnetization is recorded during field warming. Due to the clustering of cobalt in the Al_2O_3 substrate (see Fig. 3.5), the FC and ZFC curves presented in Fig. 3.16 always show evidence for the presence of a superparamagnetic phase. There is a small peak at about 20 K in the ZFC curve of sample 1 (0.25×10^{17} ions cm^{-2}) and this peak shifts to higher temperatures with increasing cobalt concentration. The trend in the M–T curve of sample 1 (0.25×10^{17} ions cm^{-2}) can be attributed to the coexistence of a ferromagnetic phase originating from substituted Co^{2+} ions in ZnO and a superparamagnetic phase due to the cluster formation in Al_2O_3. The hysteresis curve of this sample measured at 5 K (Fig. 3.17) indicates that the superparamagnetic phase in this sample is much more dominant. The M–T measurements for the samples implanted with higher doses (0.50–0.75×10^{17} ions cm^{-2}) show the occurrence of superparamagnetism with a blocking temperature of about 100 K and 250 K for sample 2 (0.50×10^{17} ions cm^{-2}) and sample 3 (0.75×10^{17} ions cm^{-2}), respectively. The hysteresis curves of these films (Fig. 3.17) also show that the superparamagnetic phase is still dominating over the ferromagnetic phase. But the hysteresis curve of sample 3 (0.75×10^{17} ions cm^{-2}) indicates that the ferromagnetic phase starts

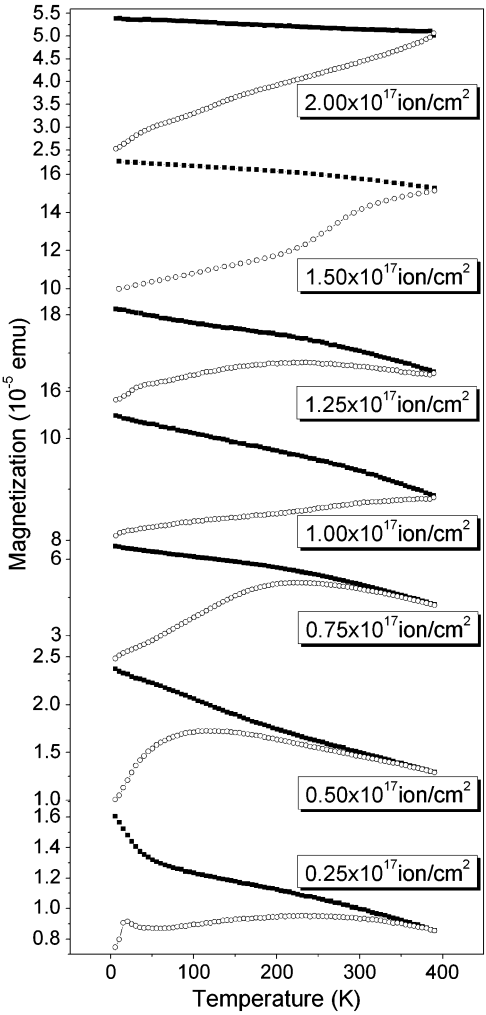

Fig. 3.16 Temperature-dependent magnetization curves of Co-implanted ZnO films taken using SQUID magnetometry for varying implantation doses [66]

to appear at this dose. The temperature-dependent magnetization curves of sample 4 (1.00×10^{17} ions cm^{-2}), sample 5 (1.25×10^{17} ions cm^{-2}), and sample 6 (1.50×10^{17} ions cm^{-2}) show that these samples have a blocking temperature of about 390 K or even more. In addition, the ferromagnetic phase is clearly seen in the SQUID hysteresis loops (Fig. 3.17) of these samples, and it is present even above room temperature (see Fig. 3.6). Since the MOKE is only sensitive to the surface layers, the superparamagnetic phase in these samples cannot be seen in the MOKE results.

Moreover, the SQUID hysteresis curves of these samples show a systematic decrease in H_c of the ferromagnetic phase with increasing cobalt dose. This behavior may be explained as follows. With increasing Co dose the magnetization becomes more homogeneous and, since magnetic inhomogeneities are the main source of

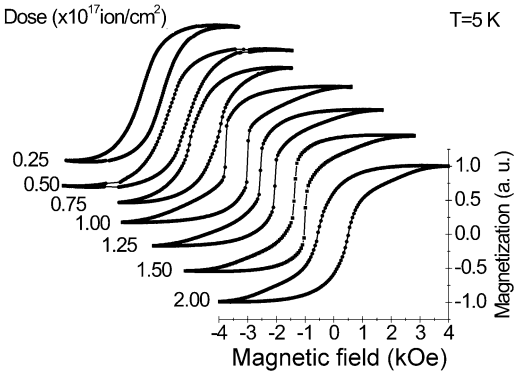

Fig. 3.17 SQUID M–H loops of Co-implanted ZnO films measured for different implantation doses at 5 K [66]

pinning for the domain walls, H_c decreases with increasing Co dose. Between 1.25×10^{17} ions cm^{-2} and 1.50×10^{17} ions cm^{-2} the potential barrier for reversal of the ferromagnetic component becomes smaller. Up to this level all inhomogeneities are filled. Any higher dose is counterproductive; it decreases the saturation magnetization and enhances the coercivity, indicating that Co goes into antisites with eventually antiferromagnetic (AF) coupling, loss of magnetization, and increase of coercivity. CoO clusters are formed in the ZnO matrix with AF spin structure and AF coupling to the remaining ferromagnetic Zn(Co)O film. The M–T data (Fig. 3.16) and the room temperature (Fig. 3.6) and low temperature (Fig. 3.17) hysteresis measurements of sample 7 (2.00×10^{17} ions cm^{-2}) clearly indicate that the cobalt atoms also start to cluster within the ZnO layer at the highest dose.

3.5.4 Magnetic Moment per Substituted Co Atom and Estimation of T_c

In order to calculate the magnetic moment per substituted Co atom we used the RBS data and SQUID hysteresis presented in Figs. 3.3 and 3.7. First we determined the percentage of cobalt atoms located within the ZnO layer from the RBS data. Integrating the area under the curve in Fig. 3.3, we estimate that 48.5 % of the implanted cobalt atoms are contained inside the ZnO layer. Secondly, we assumed that all cobalt atoms in the ZnO layer are substituted in the ZnO lattice. Indeed, the XAS data presented in Fig. 3.11 provide clear evidence for substitutional cobalt in the implanted matrix; furthermore, we could not find any indication for clustering in the ZnO layer in the TEM pictures. We also assumed that all cobalt atoms in the Al_2O_3 substrate are in the cluster phase with a magnetic moment of 1.6 μ_B per cobalt atom, as expected for metallic cobalt. Using the average magnetic moment value from the SQUID data ($\mu = 2.19\ \mu_B$/Co), finally we calculate $\mu = 2.81\ \mu_B$ per substituted cobalt atom in the ZnO layer. This value is very close to the magnetic moment of Co^{2+} in its high spin state ($\mu = 3\ \mu_B$/Co) [61, 131].

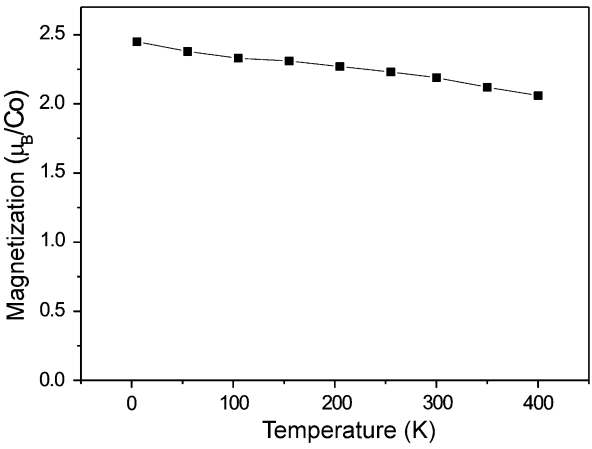

Fig. 3.18 Magnetization versus temperature curve measured at $H = 5000$ Oe by using a SQUID magnetometer. The *solid line* is a guide for the eye [65]

In Fig. 3.18 we show the temperature-dependent magnetization of the Co-implanted ZnO film. Since the annealing to very high temperatures destroys the ferromagnetism in oxide-based DMS materials [132], we only heated the sample up to 400 K. From Fig. 3.18 it is clear that the T_c is much higher than 400 K. By fitting a Brillouin curve to the M(T) data in Fig. 3.18 as a crude approximation, we estimate that the ferromagnetic Curie temperature is as high as 700 K for our film, as it was observed for Co-implanted TiO_2 rutile [132].

3.5.5 FMR Measurements

FMR measurements were carried out using a commercial Bruker EMX electron spin resonance (ESR) spectrometer at Gebze Institute of Technology operating in X-band (9.8 GHz) at room temperature. The angular dependencies of the FMR spectra have been recorded with the static magnetic field rotated either in the plane of the samples (in-plane geometry—$\theta = 90°$, φ-varied) or rotated from the sample plane to the normal (out-of-plane geometry—θ-varied, φ-fixed). The coordinate axes and relative orientation of the applied external magnetic field (H) and magnetization vector (M) are illustrated in Fig. 3.19.

In Fig. 3.20, we present the angular dependence of the in-plane resonance fields of Co-implanted ZnO films at room temperature for different implantation doses. The resonance field exhibits oscillatory behavior as a function of the azimuthal angle. The maximum and minimum values of the resonance fields correspond to the hard and easy directions for the magnetization, respectively. The periodicity of the easy and hard axes depends on the implantation dose. As seen in Fig. 3.20, for the dose of 0.75×10^{17} ions cm^{-2}, a twofold in-plane magnetic anisotropy is observed with a very small contribution from a sixfold anisotropy. The twofold in-plane magnetic anisotropy is related to the cobalt nanoparticles forming a cobalt-rich layer in the sapphire substrate, close to the ZnO/Al_2O_3 interface [65]. Indeed, when the

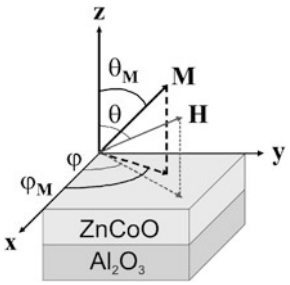

Fig. 3.19 The coordinate system for FMR measurements of Co-implanted ZnO films [67]

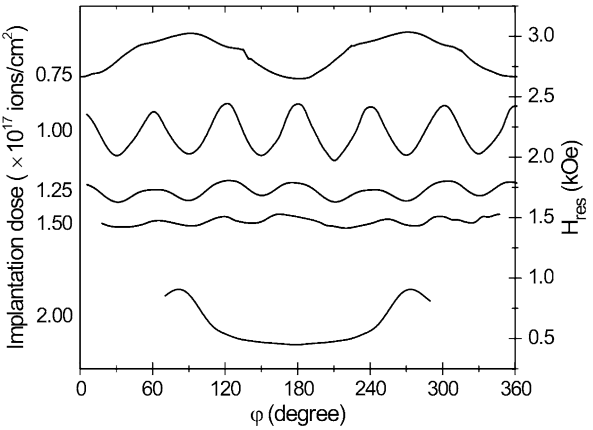

Fig. 3.20 The in-plane angular dependence of the resonance fields for different cobalt implantation doses [67]

crystalline Al_2O_3 is implanted with cobalt ions, Co nanoparticles with the hexagonal structure are aligned with their c-axis parallel to the c-axis of the host sapphire [133]. Thus, the Al_2O_3 matrix provides a magnetic anisotropy to cobalt nanoclusters [134]. In our case, the c-axis of the host Al_2O_3 is in the sample plane. Therefore, we infer that the twofold in-plane magnetic anisotropy results from cobalt nanoparticles in agreement with previous studies [133, 134]. For the dose range of 1.00–1.50 $\times$ 10^{17} ions cm^{-2}, the corresponding FMR data show that the easy and hard axes have a periodicity of 60° in the film plane, in agreement with the hexagonal structure of the ZnO films. This sixfold in-plane magnetic anisotropy is attributed to the substitution of cobalt on Zn sites in the ZnO layer and is a clear indication for long-range ferromagnetic ordering between substitutional magnetic cobalt ions in the ZnO crystal structure. At the highest implantation dose of 2.00 $\times$ 10^{17} ions cm^{-2}, a twofold in-plane magnetic anisotropy appears again. This means that for the highest dose, not only substituted cobalt ions but also metallic cobalt clusters are present in the ZnO layer, in accordance with the results published in Ref. [66]. Thus, for the highest implantation dose the resonance signal is ascribed to an overall response of the metal cobalt nanoparticles in both the ZnO layer and the sapphire substrate. In this respect, a gradual decrease in the magnitude of sixfold anisotropy for the dose of 1.5 $\times$ 10^{17} ions cm^{-2} is noteworthy. Therefore, one can expect the formation of very small cobalt clusters in the ZnO layer below the dose of 2.00 $\times$ 10^{17} ions cm^{-2}.

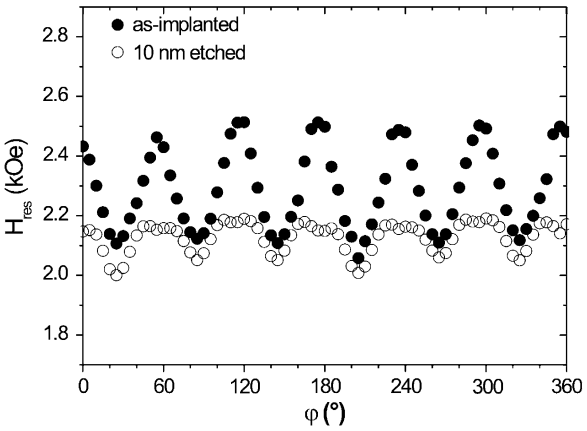

Fig. 3.21 In-plane magnetic anisotropy of Co-implanted ZnO film (Co dose: 1.00×10^{17} ions cm^{-2}) before (*closed symbols*) and after (*open symbols*) etching [67]

Thus, the maximum amplitude of the sixfold anisotropy, revealed at the dose of 1.00×10^{17} ions cm^{-2}, reflects the limit where the highest concentration for the substitutional cobalt phase in ZnO is reached. For higher doses, formation of the extrinsic ferromagnetic phase due to Co clusters starts.

In order to check whether the contribution to the sixfold in-plane magnetic anisotropy originates from ZnO only, we gradually removed the ZnO layer by 500 eV Ar-beam etching and repeated the FMR measurements. Figure 3.21 presents the in-plane magnetic anisotropies of Co-implanted ZnO film (Co dose: 1.00×10^{17} ions cm^{-2}) before and after the etching process. When the ZnO layer is etched by about 10 nm, the sixfold symmetry of the in-plane magnetic anisotropy survives, but with a significant decrease in the magnitude of anisotropy. The signal intensity also gradually decreases with etching. For the completely etched sample the signal with sixfold symmetry completely disappears. This observation shows that the FMR signal with the sixfold in-plane magnetic anisotropy originates from the substituted cobalt in the ZnO film, but not from the cobalt nanoparticles in the Al_2O_3 substrate.

3.6 Anomalous Hall Effect Measurements

In magnetic materials, in addition to the ordinary Hall effect (OHE), there is an additional voltage proportional to the sample magnetization [135], called the anomalous Hall effect (AHE). Hence, the Hall voltage can be written as follows:

$$V_{\mathrm{H}} = \left(\frac{R_0 I}{t}\right) H \cos\alpha + \left(\frac{R_{\mathrm{A}} \mu_0 I}{t}\right) M \cos\theta, \tag{3.1}$$

where t is the film thickness and I is the current. R_0 and R_{A} are the ordinary and anomalous Hall effect coefficients, respectively. μ_0 is the permeability of free space. α is the angle between the applied magnetic field (H) and the normal to the sample. θ is the angle between the sample magnetization (M) and the normal to the sample. The first term in (3.1) is the OHE and arises from the Lorentz force acting on

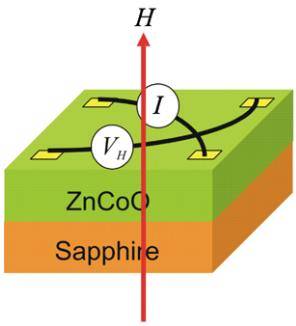

Fig. 3.22 Geometry of the AHE measurements. H is the external magnetic field applied perpendicular to the film surface [66]

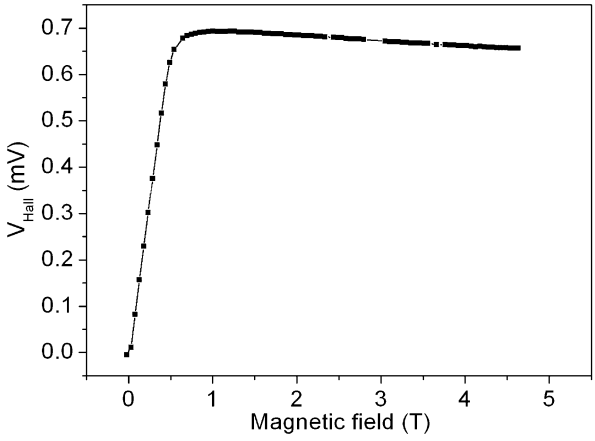

Fig. 3.23 AHE data of sample 6 (1.50×10^{17} ions cm^{-2}) taken at 4.2 K [66]

conduction electrons. This establishes an electric field perpendicular to the applied magnetic field and to the current. The second term is the AHE, and it is conventionally attributed to spin-dependent scattering mechanism involving a spin–orbit interaction between the conduction electrons and the magnetic moments of the material. At low applied magnetic fields, the Hall voltage (V_H) is dominated by the magnetic field dependence of the sample magnetization M. When the applied magnetic field is high enough to saturate the sample magnetization, the magnetic field dependence of the Hall voltage becomes linear due to the OHE.

The observation of the AHE is suggested as an important criterion for DMS materials to be intrinsic [14, 21]. In order to check whether this behavior is present in Co-implanted ZnO films and to determine the character of the majority carriers, we have carried out Hall effect experiments. The AHE measurements in this study have been performed at 4.2 K using the van der Pauw configuration presented in Fig. 3.22.

The AHE data of sample 6 (1.50×10^{17} ions cm^{-2}) are shown in Fig. 3.23. A sharp rise in the Hall voltage at low field, i.e., AHE, is followed by a slow decrease corresponding to the OHE. It is important to note that the negative slope at high fields indicates n-type carriers in Co-implanted ZnO films.

3.7 Discussion

In the literature, the reported highest solubility limit of cobalt ions in ZnO is less than 50 % using a PLD technique [54]. The measured cobalt concentration of 40–50 at.% in ZnO in this study is rather high, such that the formation of cobalt clusters in ZnO should be expected. However, no clusters could be observed within the ZnO layer for sample 6. It seems that this is due to the properties of ion implantation, which allows doping of transition metals beyond their solubility limits [80].

For the dose dependence of magnetic phases in ZnO films at room temperature we propose the following scenario: At low doses ($0.25–0.50 \times 10^{17}$ ions cm^{-2}) the number of substituted cobalt ions in the ZnO layer is very small, which results in a paramagnetic signal at room temperature. Increasing the cobalt implantation dose leads to an increasing number of substituted cobalt ions, and after a certain cobalt concentration they start to interact ferromagnetically. For this reason at a cobalt dose of 0.75×10^{17} ions cm^{-2} a weak ferromagnetic behavior is observed with a T_c below room temperature. At higher cobalt concentrations ($1.00–1.50 \times 10^{17}$ ions cm^{-2}) the substituted cobalt ions in ZnO interact strongly and stabilize room temperature ferromagnetism. At the highest dose of 2.00×10^{17} ions cm^{-2}, in addition to the substituted cobalt ions, metallic cobalt clusters are also present in the ZnO layer.

The difference in the shape of the hysteresis curves obtained by MOKE and SQUID is attributed to the surface sensitivity of the MOKE technique, which has a maximum penetration depth of about 20–30 nm. On the other hand, the SQUID technique probes the whole volume of a sample. The ZnO films have a thickness of 35 nm before implantation. Because of the surface sputtering, the ZnO thickness decreases to about 28 nm after implantation. Thus MOKE provides information only from the ZnO layer, not from the sapphire substrate; i.e., MOKE is only sensitive to the ferromagnetic contribution from the ZnO layer. In this layer a small fraction of nonmagnetic ZnO atoms are replaced by magnetic Co ions, producing the MOKE hysteresis. However, SQUID collects magnetic contributions from both the Co-implanted ZnO film and from the cobalt clusters in Al_2O_3 (Fig. 3.24). Therefore, the difference between the MOKE and SQUID data appears to be a result of the depth-dependent Co content in the implanted layer.

Another important result of this study is the observation of oxygen spin polarization in Co-implanted ZnO films. Since the shape of the hysteresis curve measured at the O *K* edge (Fig. 3.14) is the same as the one recorded by MOKE (Fig. 3.7(a)), spin polarization of oxygen atoms in this sample can not be due to the cobalt clusters in the sapphire substrate. Otherwise, the hysteretic shape of the polarized oxygen should be similar to the hysteresis of metallic cobalt clusters in sapphire with a large coercive field. This shows that the oxygen atoms are polarized due to the spontaneous ferromagnetic order in the ZnO film.

The reason for the observation of AHE and *n*-type carriers in Co-implanted ZnO films can be explained by electron doping via Zn interstitials. Normally, isovalent TM^{2+} doping of ZnO does not introduce charge carriers itself; they need to be produced by additional doping [136]. However, by using ion implantation, not only are cobalt ions introduced in ZnO, but simultaneously many other defects—such as

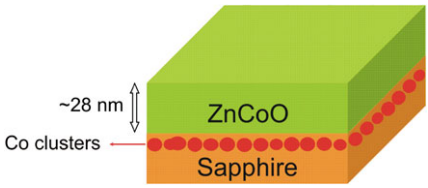

Fig. 3.24 The cluster formation in Al_2O_3 substrate after cobalt ion implantation [66]

Zn interstitials which are reported as a shallow donor in ZnO [92, 137, 138]—are also produced in the implanted region. This can be thought of as an advantage: With the ion implantation technique it is possible to introduce simultaneously both TMs and also required carriers into the ZnO.

The main question that arises here is the mechanism which leads to the observed long-range ferromagnetic ordering in Co-doped ZnO. Recently, Patterson [131] calculated the electronic structures of Co substituted for Zn in ZnO, for Zn and O vacancies, and for interstitial Zn in ZnO using the B3LYP hybrid density functional theory. He reported that the singly positively charged O vacancy is the only defect in Co-doped ZnO which can mediate ferromagnetic exchange coupling of Co ions at intermediate range (just beyond near neighbor distances). The ground state configuration is one where the majority of Co spins are parallel whereas the minority spins are parallel to each other and to the oxygen vacancy spin; thus, there are exchange couplings between these three spins which lead to an overall ferromagnetic ground state of the Co ions. No substantial exchange coupling was found for the positively charged interstitial Zn defect which also has spin half. The exchange coupling mechanism explained by Patterson is essentially the same as the impurity band model of Coey et al. [139], in which the polarons bound to the oxygen vacancies mediate ferromagnetic coupling between Co ions. In order to have the magnetic moments of the Co ions align ferromagnetically, one mediating electron is required with an oppositely directed spin. The oxygen spin polarization has not explicitly been considered in the aforementioned band structure calculations and may be due to ferromagnetic splitting of nearest neighbor oxygen *p*-levels.

3.8 Conclusions

The structural, magnetic, and electronic properties of Co-implanted ZnO films, deposited by RF sputtering methods on a $(11\bar{2}0)$ oriented sapphire substrate, have been investigated. The structural data indicate a Co cluster formation in the sapphire substrate close to the ZnO/Al_2O_3 interface. However, no indication of clustering in the ZnO layer has been found. The multiplet structure of the XAS spectra around the Co L_3 edge indicates that the implanted cobalt ions are in the Co^{2+} state in the ZnO film. A combination of room and low temperature magnetization measurements indicates that there are two magnetic phases in the Co-implanted ZnO/Al_2O_3 films. One is the ferromagnetic phase due to the Co substitution on Zn sites in the ZnO host matrix, and the second magnetic phase originates from Co clusters in the sapphire

substrate. We have found a very high magnetic moment of 2.81 μ_B per substituted cobalt atom with a very high Curie temperature ($T_c \gg 400$ K) in the Co-implanted ZnO film. Using X-ray resonant magnetic scattering at the Co L_3 edge, the magnetic contributions from the ZnO film and the substrate can be separated. Furthermore, a clear ferromagnetic signal at the O K edge is observed, which shows that the oxygen spin polarization is an important indicator for the observed long-range ferromagnetic ordering in the ZnO layer. A sixfold in-plane magnetic anisotropy of the FMR signal has also been observed in ZnO (0001) thin films implanted by Co in the dose range of 1.00–1.50 $\times$ 10^{17} ions cm^{-2}. We consider this finding to be a strong indication for intrinsic ferromagnetism in ZnO-based diluted magnetic semiconductors.

Finally, implantation of cobalt ions into the nonmagnetic ZnO film makes it ferromagnetic at room temperature with an intrinsic nature and also increases the number of n-type charge carriers without any additional doping. Of course, for successful operation of spintronic devices, in addition to a ferromagnetic semiconductor, efficient spin-polarized injection, transport, and detection are also required. In any case, the preceding results indicate that the ZnO-based DMS materials still offer promising perspectives for basic research and device applications.

Acknowledgements The authors would like to acknowledge A. Nefedov, L. Tagirov, R. Khaibullin, K. Westerholt, H.W. Becker, C. Somsen, S. Gök, B. Rameev, S. Güler, O. Öztürk and B. Aktas for their cooperation. This work was partially supported by DFG through SFB 491, the German Federal Ministry of Education and Research (BMBF) through Contract Nos. 05KS7PC1 (ALICE diffractometer) and 05ES3XBA/5 (travel to BESSY), the State Planning Organization of Turkey (DPT) through Project No. 2009K120730, TÜBİTAK through Project Nos. 209T061 and 110T855, the International Max Planck Research School-SurMat, RFBR through Grant No. 07-02-00559-a, and NK-16P/13 of the Federal Agency on Education, Russia.

References

1. R.P. Feynman, Found. Phys. **16**, 507 (1986)
2. S. Datta, B. Das, Appl. Phys. Lett. **56**, 665 (1990)
3. G.A. Prinz, Science **282**, 1660 (1998)
4. H. Ohno, N. Akiba, F. Matsukura, A. Shen, K. Ohtani, Y. Ohno, Appl. Phys. Lett. **73**, 363 (1998)
5. M. Oestreich, Nature (London) **402**, 735 (1999)
6. Y. Ohno, D.K. Young, B. Beschoten, F. Matsukura, H. Ohno, D.D. Awschalom, Nature **402**, 790 (1999)
7. S.A. Wolf, D.D. Awschalom, R.A. Buhrman, J. Daughton, S. von Molnar, M.L. Roukes, A.Y. Chtchelkanova, D.M. Treger, Science **294**, 1488 (2001)
8. S.D. Sarma, Am. Sci. **89**, 516 (2001)
9. B.T. Jonker, A.T. Hanbicki, Y.D. Park, G. Itskos, M. Furis, G. Kioseoglou, A. Petrou, Appl. Phys. Lett. **79**, 3098 (2001)
10. G. Binasch, P. Grünberg, F. Saurenbach, W. Zinn, Phys. Rev. B **39**, 4828 (1989)
11. M.N. Baibich, J.M. Broto, A. Fert, F.N.V. Dau, F. Petroff, P. Eitenne, G. Creuzet, A. Friederich, J. Chazelas, Phys. Rev. Lett. **61**, 2472 (1988)
12. J.S. Moodera, L.R. Kinder, T.M. Wong, R. Meservey, Phys. Rev. Lett. **74**, 3273 (1995)
13. G. Schmidt, D. Ferrand, L.W. Molenkamp, B.J. van Wees, Phys. Rev. B **62**, R4790 (2000)

14. H. Ohno, A. Shen, F. Matsukura, A. Oiwa, A. Endo, S. Katsumoto, Y. Iye, Appl. Phys. Lett. **69**, 363 (1996)
15. A.V. Esch, L.V. Bockstal, J. de Boeck, G. Verbanck, A.S. vas Steenbergen, R.J. Wellman, G. Grietens, R. Bogaerts, F. Herlach, G. Borghs, Phys. Rev. B **56**, 13103 (1997)
16. T. Hayashi, M. Tanaka, K. Seto, T. Nishinaga, K. Ando, Appl. Phys. Lett. **71**, 1825 (1997)
17. T. Hayashi, M. Tanaka, T. Nishinaga, H. Shimada, J. Appl. Phys. **81**, 4865 (1997)
18. T. Hayashi, M. Tanaka, T. Nishinaga, H. Shimoda, H. Tsuchiya, Y. Otsuka, J. Cryst. Growth **175**, 1063 (1997)
19. Y. Satoh, N. Inoue, Y. Nishikawa, J. Yoshino, in *Proceedings of the Third Symposium on Physics and Applications of Spin-Related Phenomena in Semiconductors* (1997), p. 23
20. K. Ando, T. Hayashi, M. Tanaka, A. Twardowski, J. Appl. Phys. **83**, 65481 (1998)
21. F. Matsukura, H. Ohno, A. Shen, Y. Sugawara, Phys. Rev. B **57**, R2037 (1998)
22. R. Shioda, K. Ando, T. Hayashi, M. Tanaka, Phys. Rev. B **58**, 1100 (1998)
23. M. Tanaka, J. Vac. Sci. Technol. B **16**, 2267 (1998)
24. B. Beschoten, P.A. Crowell, I. Malajovich, D.D. Awschalom, F. Matsukura, A. Shen, H. Ohno, Phys. Rev. Lett. **83**, 3073 (1999)
25. H. Ohno, F. Matsukura, T. Owiya, N. Akiba, J. Appl. Phys. **85**, 4277 (1999)
26. H. Shimizu, T. Hayashi, T. Nishinaga, M. Tanaka, Appl. Phys. Lett. **74**, 398 (1999)
27. A. Shen, F. Matsukura, S.P. Guo, Y. Sugawara, H. Ohno, M. Tani, A. Abe, H.C. Liu, J. Cryst. Growth **201–202**, 379 (1999)
28. A. Twardowski, Mater. Sci. Eng. B **63**, 96 (1999)
29. B. Grandidier, J.P. Hys, C. Delerue, D. Stievenard, Y. Higo, M. Tanaka, Appl. Phys. Lett. **77**, 4001 (2000)
30. R.K. Kawakami, E. Johnson-Halperin, L.F. Chen, M. Hanson, N. Guebels, J.S. Speck, A.C. Gossard, D.D. Awschalom, Appl. Phys. Lett. **77**, 2379 (2000)
31. D. Chiba, N. Akiba, F. Matsukura, Y. Ohno, H. Ohno, Appl. Phys. Lett. **77**, 1873 (2000)
32. T. Hayashi, M. Tanaka, A. Asamitsu, J. Appl. Phys. **87**, 4673 (2000)
33. N. Akiba, D. Chiba, K. Natata, F. Matsukura, Y. Ohno, H. Ohno, J. Appl. Phys. **87**, 6436 (2000)
34. Y. Nagai, T. Kurimoto, K. Nagasaka, H. Nojiri, M. Motokawa, F. Matsukura, T. Dietl, H. Ohno, Jpn. J. Appl. Phys. **40**, 6231 (2001)
35. J. Sadowski, R. Mathieu, P. Svedlindh, J.Z. Domagala, J. Bak-Misiuk, J. Swiatek, M. Karlsteen, J. Kanski, L. Ilver, H. Asklund, V. Sodervall, Appl. Phys. Lett. **78**, 3271 (2001)
36. S.J. Potashnik, K.C. Ku, S.H. Chun, J.J. Berry, N. Samarth, P. Schiffer, Appl. Phys. Lett. **79**, 1495 (2001)
37. G.M. Schott, W. Faschinger, L.W. Molenkamp, Appl. Phys. Lett. **79**, 1807 (2001)
38. H. Munekata, H. Ohno, S. von Molnar, A. Segmuller, L.L. Chang, L. Esaki, Phys. Rev. Lett. **63**, 1849 (1989)
39. H. Ohno, H. Munekata, T. Penney, S. von Molnar, L.L. Chang, Phys. Rev. Lett. **68**, 2864 (1992)
40. H. Munekata, A. Zaslevsky, P. Fumagalli, R.J. Gambino, Appl. Phys. Lett. **63**, 2929 (1993)
41. Y.L. Soo, S.W. Huang, Z.H. Ming, Y.H. Kao, H. Munekata, Phys. Rev. B **53**, 4905 (1996)
42. Y. Nishikawa, A. Tackeuchi, M. Yamaguchi, S. Muto, O. Wada, IEEE J. Sel. Top. Quantum Electron. **2**, 661 (1996)
43. S. Koshihara, A. Oiwa, M. Hirasawa, S. Katsumoto, Y. Iye, C. Urano, H. Takagi, H. Munekata, Phys. Rev. Lett. **78**, 4617 (1997)
44. K.J. Akai, Phys. Rev. Lett. **81**, 3002 (1998)
45. A. Oiwa, T. Slupinski, H. Munekata, Appl. Phys. Lett. **78**, 518 (2001)
46. H. Ohno, Science **281**, 951 (1998)
47. H. Ohno, J. Magn. Magn. Mater. **200**, 110 (1999)
48. H. Ohno, J. Vac. Sci. Technol. B **18**, 2039 (2000)
49. H. Ohno, F. Matsukura, Y. Ohno, Jpn. Soc. Appl. Phys. Int. **5**, 4 (2002)
50. T. Dietl, H. Ohno, F. Matsukura, J. Cibert, D. Ferrand, Science **287**, 1019 (2000)
51. K. Sato, H. Katayama-Yoshida, Jpn. J. Appl. Phys. **39**, L555 (2000)

52. K. Sato, H. Katayama-Yoshida, Jpn. J. Appl. Phys. **40**, L334 (2001)
53. Y. Matsumoto, M. Murakami, T. Shono, T. Hasegawa, T. Fukumura, M. Kawasaki, P. Ahmet, T. Chikyow, S.Y. Koshihara, H. Koinuma, Science **291**, 854 (2001)
54. K. Ueda, H. Tabada, T. Kawai, Appl. Phys. Lett. **79**, 988 (2001)
55. S.J. Pearton, C.R. Abernathy, D.P. Norton, A.F. Hebart, Y.D. Park, L.A. Boatner, J.D. Budai, Mater. Sci. Eng. **R 40**, 137 (2003)
56. W. Prellier, A. Fouchet, B. Mercey, J. Phys. Condens. Matter **15**, R1583 (2003)
57. A.C. Tuan, J.D. Bryan, A.B. Pakhomov, V. Shutthanandan, S. Thevuthasan, D.E. McCready, D. Gaspar, M.H. Engelhard, J.W. Rogers, K. Krishnan, D.R. Gamelin, S.A. Chambers, Phys. Rev. B **70**, 054424 (2004)
58. S.J. Pearton, W.H. Heo, M. Ivill, D.P. Norton, T. Steiner, Semicond. Sci. Technol. **19**, R59 (2004)
59. S.J. Pearton, D.P. Norton, K. Ip, Y.W. Heo, T. Steiner, J. Vac. Sci. Technol. B **22**, 932 (2004)
60. C. Liu, F. Yun, H. Morkoc, J. Mater. Sci., Mater. Electron. **16**, 555 (2005)
61. R. Janisch, P. Gopal, N.A. Spaldin, J. Phys. Condens. Matter **17**, R657 (2005)
62. J.J. Liu, M.H. Yu, W.L. Zhou, J. Appl. Phys. **99**, 08M119 (2006)
63. W. Pacuski, D. Ferrand, J. Cibert, C. Deparis, J.A. Gaj, P. Kossacki, C. Morhain, Phys. Rev. B **73**, 035214 (2006)
64. J. Zhang, X.Z. Li, Y.F. Lu, D.J. Sellmyer, J. Phys. Condens. Matter **19**, 036210 (2007)
65. N. Akdogan, A. Nefedov, K. Westerholt, H. Zabel, H.W. Becker, C. Somsen, R. Khaibullin, L. Tagirov, J. Phys. D, Appl. Phys. **41**, 165001 (2008)
66. N. Akdogan, H. Zabel, A. Nefedov, K. Westerholt, H.W. Becker, S. Gök, R. Khaibullin, L. Tagirov, J. Appl. Phys. **105**, 043907 (2009)
67. N. Akdoğan, B. Rameev, S. Güler, O. Öztürk, B. Aktaş, H. Zabel, R. Khaibullin, L. Tagirov, Appl. Phys. Lett. **95**, 102502 (2009)
68. C. Okay, B.Z. Rameev, S. Güler, R.I. Khaibullin, R.R. Khakimova, Y.N. Osin, N. Akdoğan, A.I. Gumarov, A. Nefedov, H. Zabel, B. Aktaş, Appl. Phys. A **104**, 667 (2011)
69. D.H. Kim, J.S. Yang, K.W. Lee, S.D. Bu, T.W. Noha, S.J. Oh, Y.W. Kim, J.S. Chung, H. Tanaka, H.Y. Lee, T. Kawai, Appl. Phys. Lett. **81**, 2421 (2002)
70. Y.L. Soo, G. Kioseoglou, S. Kim, Y.H. Kao, P.S. Devi, J. Parise, R.J. Gambino, P.I. Gouma, Appl. Phys. Lett. **81**, 655 (2002)
71. B.Z. Rameev, F. Yildiz, L.R. Tagirov, B. Aktas, W.K. Park, J.S. Moodera, J. Magn. Magn. Mater. **258**, 361 (2003)
72. R.I. Khaibullin, L.R. Tagirov, B.Z. Rameev, S.Z. Ibragimov, F. Yildiz, B. Aktas, J. Phys. Condens. Matter **16**, L443 (2004)
73. N. Akdogan, B.Z. Rameev, L. Dorosinsky, H. Sozeri, R.I. Khaibullin, B. Aktas, L.R. Tagirov, A. Westphalen, H. Zabel, J. Phys. Condens. Matter **17**, L359 (2005)
74. C.M. Wang, V. Shutthanandan, S. Thevuthasan, T. Droubay, S.A. Chambers, J. Appl. Phys. **97**, 073502 (2005)
75. N. Akdogan, B.Z. Rameev, R.I. Khaibullin, A. Westphalen, L.R. Tagirov, B. Aktas, H. Zabel, J. Magn. Magn. Mater. **300**, e4 (2006)
76. A. Nefedov, N. Akdogan, H. Zabel, R.I. Khaibullin, L.R. Tagirov, Appl. Phys. Lett. **89**, 182509 (2006)
77. N. Akdogan, A. Nefedov, A. Westphalen, H. Zabel, R.I. Khaibullin, L.R. Tagirov, Superlattices Microstruct. **41**, 132 (2007)
78. N. Akdogan, A. Nefedov, H. Zabel, K. Westerholt, H.W. Becker, C. Somsen, Ş. Gök, A. Bashir, R. Khaibullin, L. Tagirov, J. Phys. D, Appl. Phys. **42**, 115005 (2009)
79. L. Rubin, J. Poate, Ind. Phys. **9**, 12 (2003)
80. A.F. Hebard, R.P. Rairigh, J.G. Kelly, S.J. Pearton, C.R. Abernathy, S.N.G. Chu, R.G. Wilson, J. Phys. D, Appl. Phys. **37**, 511 (2004)
81. R.W.G. Wyckoff, *Crystal Structures*, 2nd edn. (Wiley, New York, 2001)
82. S.W. Lim, S.K. Hwang, J.M. Myoung, Solid State Commun., **125**, 231 (2003)
83. Y.Z. Yoo, T. Fukumura, Z. Jin, K. Hasagewa, M. Kawasaki, P. Ahmet, T. Chikyov, H. Koinuma, J. Appl. Phys. **90**, 4246 (2001)

84. J.H. Kim, H. Kim, D. Kim, Y.E. Ihm, W.K. Choo, J. Appl. Phys. **92**, 6066 (2002)
85. J.H. Kim, H. Kim, D. Kim, Y.E. Ihm, W.K. Choo, Physica B **327**, 304 (2003)
86. W. Prellier, A. Fouchet, B. Mercey, C. Simon, B. Raveau, Appl. Phys. Lett. **82**, 3490 (2003)
87. M. Venkatesan, C.B. Fitzgerald, J.G. Lunney, J.M.D. Coey, Phys. Rev. Lett. **93**, 177206 (2004)
88. L. Yan, C.K. Ong, X.S. Rao, J. Appl. Phys. **96**, 508 (2004)
89. S. Ramachandran, A. Tiwari, J. Narayan, Appl. Phys. Lett. **84**, 5255 (2004)
90. Z. Jin et al., Appl. Phys. Lett. **78**, 3824 (2001)
91. Y. Zheng, J.C. Boilliard, D. Demaille, Y. Bernard, J.F. Petroff, J. Cryst. Growth **274**, 156 (2005)
92. H.J. Lee, S.Y. Jeong, C.R. Cho, C.H. Park, Appl. Phys. Lett. **81**, 4020 (2002)
93. V. Ney, S. Ye, T. Kammermeier, A. Ney, H. Zhou, J. Fallert, H. Kalt, F.Y. Lo, A. Melnikov, A.D. Wieck, J. Appl. Phys. **104**, 083904 (2008)
94. K. Potzger, S. Zhou, Q. Xu, A. Shalimov, R. Groetzschel, H. Schmidt, A. Muecklich, M. Helm, J. Fassbender, Appl. Phys. Lett. **93**, 232504 (2008)
95. K. Potzger, K. Kuepper, Q. Xu, S. Zhou, H. Schmidt, M. Helm, J. Fassbender, J. Appl. Phys. **104**, 023510 (2008)
96. S. Zhou, K. Potzger, J. von Borany, R. Groetzschel, W. Skorupa, M. Helm, J. Fassbender, Phys. Rev. B **77**, 035209 (2008)
97. M.W. Khan, R. Kumar, M.A.M. Khan, B. Angadi, Y.S. Jung, W.K. Choi, J.P. Srivastava, Semicond. Sci. Technol. **24**, 095011 (2009)
98. S. Mueller, M. Zhou, Q. Li, C. Ronning, Nanotechnology **20**, 135704 (2009)
99. K. Potzger, A. Shalimov, S. Zhou, H. Schmidt, A. Muecklich, M. Helm, J. Fassbender, M. Liberati, E. Arenholz, J. Appl. Phys. **105**, 123917 (2009)
100. K. Potzger, S. Zhou, Phys. Status Solidi (b) **246**, 1147 (2009)
101. M. Schumm, M. Koerdel, S. Mueller, C. Ronning, E. Dynowska, Z. Golacki, W. Szuszkiewicz, J. Geurts, J. Appl. Phys. **105**, 083525 (2009)
102. Q. Xu, S. Zhou, D. Marko, K. Potzger, J. Fassbender, M. Vinnichenko, M. Helm, H. Hochmuth, M. Lorenz, M. Grundmann, H. Schmidt, J. Phys. D, Appl. Phys. **42**, 085001 (2009)
103. S. Zhou, K. Potzger, Q. Xu, G. Talut, M. Lorenz, W. Skorupa, M. Helm, J. Fassbender, M. Grundmann, H. Schmidt, Vacuum **83**, S13 (2009)
104. R.P. Borges, B. Ribeiro, A.R.G. Costa, C. Silva, R.C. da Silva, G. Evans, A.P. Goncalves, M.M. Cruz, M. Godinho, Eur. Phys. J. B **79**(2), 185 (2011)
105. M.H. Chu, J. Segura-Ruiz, G. Martinez-Criado, P. Cloetens, I. Snigireva, S. Geburt, C. Ronning, Phys. Status Solidi (RRL)—Rapid Res. Lett. **5**, 283 (2011)
106. J. Segura-Ruiz, G. Martinez-Criado, M.H. Chu, S. Geburt, C. Ronning, Nano Lett. **11**, 5322 (2011)
107. J.M. Wikberg, R. Knut, A. Audren, M. Ottosson, M.K. Linnarsson, O. Karis, A. Hallen, P. Svedlindh, J. Appl. Phys. **109**, 083918 (2011)
108. C.W. Zou, J. Zhang, W. Xie, L.X. Shao, L.P. Guo, D.J. Fu, Nucl. Instrum. Methods Phys. Res. B **269**, 122 (2011)
109. T. Fukumura, J. Zin, A. Ohtomo, H. Koinuma, Appl. Phys. Lett. **75**, 3366 (1999)
110. X.M. Cheng, C.L. Chien, J. Appl. Phys. **93**, 7876 (2003)
111. H. Saeki, H. Matsui, T. Kawai, H. Tabata, J. Phys. Chem. **16**, S5533 (2004)
112. Y.M. Cho, W.K. Choo, H. Kim, D. Kim, Y. Ihm, Appl. Phys. Lett. **80**, 3358 (2002)
113. R. Kumar, A.P. Singh, P. Thakur, K.H. Chae, W.K. Choi, B. Angadi, S.D. Kaushik, S. Patnaik, J. Phys. D, Appl. Phys. **41**, 155002 (2008)
114. J.H. Park, M.G. Kim, H.M. Jang, S. Ryu, Y.M. Kim, Appl. Phys. Lett. **84**, 1338 (2004)
115. Z. Yin, N. Chen, C. Chai, F. Yang, J. Appl. Phys. **96**, 5093 (2004)
116. M. Snure, D. Kumar, A. Tiwari, Int. J. Join. Mater. **61**, 72 (2009)
117. M. Ay, A. Nefedov, H. Zabel, Appl. Surf. Sci. **205**, 329 (2003)
118. J.F. Ziegler, J.P. Biersack, U. Littmark, *The Stopping and Range of Ions in Solids* (Pergamon, New York, 1985)

119. C. Morawe, H. Zabel, J. Appl. Phys. **77**, 1969 (1995)
120. T. Zeidler, F. Schreiber, H. Zabel, W. Donner, N. Metoki, Phys. Rev. B **53**, 3256 (1996)
121. T. Schmitte, Bragg-MOKE and vector-MOKE investigations: magnetic reversal of patterned microstripes. PhD thesis, Ruhr-Universität Bochum (2002)
122. A. Westphalen, Advanced MOKE investigations: remagnetization processes of microsized structures. PhD thesis, Ruhr-Universität Bochum (2007)
123. N. Akdoğan, İnce filmlerde manyeto-optik ölçümler. Master's thesis, Yıldız Technical University (2004)
124. N. Akdoğan, Origin of ferromagnetism in oxide-based diluted magnetic semiconductors. PhD thesis, Ruhr-Universität Bochum (2008)
125. J.M. Tonnerre, L. Seve, D. Raoux, G. Soullie, B. Rodmacq, P. Wolfers, Phys. Rev. Lett. **75**, 740 (1995)
126. G. van der Laan, Curr. Opin. Solid State Mater. Sci. **10**, 120 (2006)
127. J.B. Kortright, J.S. Jiang, S.D. Bader, O. Hellwig, D.T. Marguiles, E.E. Fullerton, Nucl. Instrum. Methods Phys. Res. B **199**, 301 (2003)
128. J. Grabis, A. Nefedov, H. Zabel, Rev. Sci. Instrum. **74**, 4048 (2003)
129. T.J. Regan, H. Ohldag, C. Stamm, F. Nolting, J. Lüning, J. Stöhr, R.L. White, Phys. Rev. B **64**, 214422 (2001)
130. M. Kobayashi, Y. Ishida, J.I. Hwang, T. Mizokawa, A. Fugimori, K. Mamiya, J. Okamoto, Y. Takeda, T. Okane, Y. Saitoh, Y. Muramatsu, A. Tanaka, H. Saeki, H. Tabata, T. Kawai, Phys. Rev. B **72**, 201201(R) (2005)
131. C.H. Patterson, Phys. Rev. B **74**, 144432 (2006)
132. R.I. Khaibullin, S.Z. Ibragimov, L.R. Tagirov, V.N. Popok, I.B. Khaibullin, Nucl. Instrum. Methods Phys. Res. B **257**, 369 (2007)
133. A. Meldrum, L.A. Boatner, K. Sorge, Nucl. Instrum. Methods Phys. Res. B **207**, 36 (2003)
134. J.K. Lee, M.F. Hundley, J.D. Thompson, R.K. Schulze, H.S. Jung, J.A. Valdez, M. Nastasi, X. Zhang, Appl. Phys. Lett. **89**, 182502 (2006)
135. C.M. Hurd, *The Hall Effect in Metals and Alloys* (Plenum, New York, 1972)
136. K. Nielsen, S. Bauer, M. Lübbe, S.T.B. Goennenwein, M. Opel, J. Simon, W. Mader, R. Gross, Phys. Status Solidi (a) **203**, 3581 (2006)
137. D.C. Look, D.C. Reynolds, J.R. Sizelove, R.L. Jones, C.W. Litton, G. Cantwell, W.C. Harsch, Solid State Commun. **105**, 399 (1998)
138. D.C. Look, J.W. Hemsky, J.R. Sizelove, Phys. Rev. Lett. **82**, 2552 (1999)
139. J.M.D. Coey, M. Venkatesan, C.B. Fitzgerald, Nat. Mater. **4**, 173 (2005)

Chapter 4
Magnetic Characterization of Exchange Coupled Ultrathin Magnetic Multilayers by Ferromagnetic Resonance Technique

Bekir Aktaş, Ramazan Topkaya, Mustafa Erkovan, and Mustafa Özdemir

Abstract The magnetic–nonmagnetic multilayers have been widely used in various applications. As well known the important physical parameters depend on relevant applications. For giant magneto resistance (GMR), magnetic data storage, MRAM and spintronics applications, the most important magnetic parameters in multilayered structures are interlayer exchange coupling, magnetic anisotropy, saturation magnetization and spin relaxation time. All of these parameters strictly depend on the physical size of the elements which are continuously shrinking even down to nanometer scale for ultra high density data processes. However, as the dimensions (thickness) of the films continues to decrease the magnetic signal intensity gets so weak that its detection becomes one of the major issues. But still ferromagnetic resonance (FMR) can be powerful enough to study these multilayered structures.

Recently we have developed a theoretical model to analyse the FMR data to extract magnetic parameters. We have chosen the permalloy (Py) layers separated by very thin Cr for our study because Py is one of the softest magnetic materials and its bulk form is very well characterized. The FMR measurements were carried out by using an X-band ESR spectrometer at several temperatures. The experimental data was successfully simulated by proposed model. The saturation magnetization was observed close to the value that for bulk permalloy. However a significant perpendicular anisotropy induced for thin film case. The spectra strongly depend on the thickness of Cr layer. Even the relative positions of the strong and the weak modes are interchanged for particular thickness of Cr layer. It has been found that the exchange coupling between successive layers exhibits oscillatory behaviour with respect to Cr thickness, confirming usefulness of the developed FMR model.

B. Aktaş (✉) · R. Topkaya · M. Erkovan
Department of Physics, Gebze Institute of Technology, P.K. 141, 41400 Gebze-Kocaeli, Turkey
e-mail: aktas@gyte.edu.tr

M. Özdemir
Department of Physics, Faculty of Science and Letters, Marmara University, Istanbul, Turkey

B. Aktaş, F. Mikailzade (eds.), *Nanostructured Materials for Magnetoelectronics*, Springer Series in Materials Science 175, DOI 10.1007/978-3-642-34958-4_4,

4.1 Introduction

There has recently been considerable interest in magnetic multilayers consisting of ferromagnetic and nonmagnetic films since the observation of giant magnetoresistance (GMR) [1, 2] and tunnel magnetoresistance (TMR) [3, 4] effects due to their wide applications in magnetoelectronics such as nonvolatile media and reading elements in magnetic recording technology, magnetic random access memory (MRAM), and spin transistor and information processing, etc. Many useful physical properties arise in superstructured ultrathin films. For instance, the GMR, TMR, and spin torque transfer phenomena are mainly determined by magnetic, electrical, and geometric properties of superstructured thin films. Interlayer exchange coupling between ferromagnetic layers across a nonmagnetic spacer layer is one of the most important phenomena, and was discovered by P. Grünberg in Fe/Cr/Fe multilayer structures by means of light scattering from spin waves [5]. Then, S.S.P. Parkin showed that interlayer exchange coupling oscillates depending on the nonmagnetic spacer layer thickness in NiCo/Ru/NiCo multilayers [6]. Evaluating numerous experiments in Fe/TM/Fe and Co/TM/Co (TM: Transition Metal) multilayer structures [7–9], S.S.P. Parkin concluded that the oscillation is a common property of all transition metals [10].

The exchange interactions between ferromagnetic layers through a nonmagnetic metallic spacer must be antiferromagnetic in order to have a significant GMR effect. Oscillatory interlayer exchange coupling between ferromagnetic layers was explained by A. Fert [53] using Ruderman–Kittel–Kasuya–Yosida (RKKY) interaction [11–13], which is an indirect exchange interaction of localized spins in magnetic layers mediated by conducting electrons of the nonmagnetic spacer. As the need for ultra high density data recording increases, the size of the film used in spintronic applications must be decreased [14]. Therefore, accurate magnetic characterization is one of the major issues related to magnetic multilayer structures. So far numerous superlattice structures made of ferromagnetic and nonmagnetic metallic thin layers have been investigated by using different characterization techniques [15–17].

Ferromagnetic resonance (FMR) has proven to be a well-established and useful technique to investigate magnetic materials and to determine magnetic properties, such as magnetic moment, magnetic bulk and surface anisotropies, magnetic exchange coupling, spin dynamics, and magnetic damping, etc. [40–53]. The first theory of FMR absorption was developed by C. Kittel [18]. The FMR technique was applied first by Rado and Weertman [19] to observe exchange interaction in ferromagnetic materials. These magnetic excitations in ferromagnetic bulk metals were called spin waves by Ament and Rado [20]. They developed an essential and useful theory based on Maxwell's equations to get an expression for effective permeability and surface impedance as a function of many physical parameters, such as magnitude and direction of external magnetic field, excitation field (microwave) frequency, electrical conductivity, different magnetic anisotropies, exchange interactions, dc magnetization, and even the geometric shapes of the bulk ferromagnetic metals: They showed that at least three spin wave modes localized on the surface region of ferromagnetic bulk material can be excited due

to magnetic surface anisotropy. C. Kittel [21] observed spin waves in ferromagnetic bulk materials which are excited by nonuniform (and even by uniform) rf fields.

This theory was then applied by many authors to investigate magnetic parameters of many different bulk materials. For instance, Z. Frait et al. investigated the frequency dependence of the FMR in metals [22]. H. Hurdequint et al. applied the theory to study bulk Ni-Mn alloys [23]. Then this alloy was studied in detail by Öner et al., and it was found that the magnetic symmetry is broken when the sample is cooled down to 4 K in the presence of an external magnetic field [24]. That is, the FMR absorption peaks were observed to be different for positive and negative external fields with respect to the cooling field direction. These unusual angular and temperature dependences of FMR spectra were then modeled by introducing rotational (dynamic) anisotropy, and the FMR spectra were successfully simulated on the basis of this theory by Aktas et al. [25]. Also, it was shown that the FMR spectra are very sensitive to surface conditions in which the field-induced exchange (unidirectional) anisotropy is different than that in the bulk region of the reentrant or spin-glass Ni-Mn alloys [26].

The FMR technique was applied by many authors to different structures of thin films. For instance, Tannenwald et al. observed multipeak FMR spectra in permalloy thin films (1600 Å) [27]. Wigen et al. studied permalloy and cobalt films and observed a set of spin wave modes regularly ordered in the external field axis and introduced a dynamic spin pinning model to interpret the experimental FMR data [28]. In order to explain the multipeak FMR data, Soohoo et al. introduced the magnetic surface anisotropy for surface spin pinning instead of dynamic pinning in thin films [29]. On the other hand, Portis suggested that a variation (gradient) of saturation magnetization in the surface region can cause a deviation of the resonance field of low-lying spin wave modes from Kittel's theory, which predicts the square dependence of intensities and resonance field values of the modes on mode number [30]. Wigen et al. observed nonpropagating exchange-dominated and well-resolved surface spin wave modes on YIG films and analyzed the magnetic properties using these spin wave resonance (SWR) spectra [31]. Puszkarski then retreated the SWR theory in detail and developed a rigorous theory on the basis of the surface state of films [32]. The angular dependence of SWR spectra was studied by Maksimowich et al., who obtained a practical approach to extract various contributions (from the surface anisotropy and gradient of dc magnetization) to surface spin pinning parameters using the angular dependence of SWR spectra [33]. Wigen developed an SWR theory in terms of quantum spin operator notation and determined boundary conditions for standing spin wave modes, using an appropriate transformation [34]. This theory is very suitable for analyzing the SWR spectra in continuum (long wavelength) limits. The above theories generally use resonance fields of the SWR modes to deduce relevant parameters. Full and detailed simulations of absorption curves such as resonance field, line shapes (spin damping), or absorption intensity as a function of external field for a general direction were given in the work done by Aktas et al. [35] on the SWR spectra for a monolayered magnetic thin film.

According to the conventional spin wave theory mentioned above, the separation of the SWR modes of the spectra in the external field axis is proportional to the magnitude of the exchange interactions. Therefore, a few modes can be observed in the microwave spectroscopic region if the film thickness of the usual ferromagnetic substance is about in the submicrometer scale. When the film thickness decreases below 0.1 μm, then the mode separation in the field axis drastically increases and even overreaches the positive values of the external field; i.e., the higher order SWR modes cannot be observed in a real FMR curve. Surprisingly, multipeak FMR spectra were observed even in ultrathin pure iron films with a thickness of about 15 atomic monolayers [36, 37]. However, a detailed analysis revealed that multipeaks do not belong to higher order spin wave modes, but the resonance conditions for the main FMR mode are attained two or three times due to continuous reorientation of the equilibrium direction of the static magnetization vector during the external field scan. The authors succeeded in analyzing the FMR data from ultrathin bilayers separated by sufficiently thick nonmagnetic metallic spacers to avoid any indirect exchange interactions between the magnetic layers. However, they observed that there are still dynamic indirect exchange interactions mediated by conduction electron spins through the nonmagnetic spacer. It was also shown that these conduction electrons cause spin damping in addition to the intrinsic Gilbert damping, which is a very important parameter for spintronic applications.

A detailed FMR study was done by Zang et al. on ultrathin ferromagnetic–nonmagnetic–ferromagnetic layers of various metallic materials [38, 39]. The authors observed two-peak FMR spectra and attributed them to collective excitations of individual layer magnetization due to indirect exchange interaction between thin ferromagnetic layers through a nonmagnetic conducting spacer layer. In this case the individual layers are too thin to observe the usual SWR modes to be excited in an individual magnetic layer. Thus, the magnetic spins in each layer are rigidly coupled and can be represented as a giant spin. When the resonance conditions are attained for a particular layer during the field scan, then the magnetization of this layer starts precesses around the effective field. This resonating layer magnetization also drives the magnetization of the neighboring layer to precess around its own effective field due to the exchange coupling between them. However, its precession amplitude becomes smaller compared to that for the driving layer. The magnetic excitations in the neighboring layers can take place either in phase or out of phase with respect to one another. These excitation modes are called the acoustical or optical modes, respectively. Using an appropriate magnetic free energy and also including indirect exchange coupling parameters for the multilayered thin film, the author could analyze the SWR data to deduce indirect exchange interaction parameters.

In this chapter, a detailed theoretical model [40, 41] and its applications will be cited in order to show the merit of the FMR technique in studies (even ultrathin magnetic monolayer or multilayered superstructures) to deduce many physical parameters such as static and dynamic magnetization, surface and/or bulk magnetocrystalline anisotropies, the exchange (bidirectional or unidirectional) anisotropies,

interlayer exchange coupling between ferromagnetic layers separated by nonmagnetic spacers, and the relaxation (damping) parameter of dynamic magnetization in any individual layer.

Although there are many more useful magnetic multilayer structures for applications, we have chosen Py/Cr/Py trilayers and/or multilayers as prototype systems in order to show, more clearly, the aspects of the FMR technique for investigating the magnetic properties as a function of nonmagnetic spacer thickness. Because Py is one of the magnetically soft materials with relatively weak magnetic damping, it gives a quite well-defined FMR signal with a narrow resonance line. Thus, relatively sharp peaks for different FMR excitation modes allow us to deduce magnetic parameters by fitting the theoretical values to the experimental data. The usual dc magnetization data are also used to get supplementary data to be used in the analysis of FMR spectra.

4.2 Theoretical Model

4.2.1 Magnetic Free Energy

The experimental data were analyzed for a system consisting of N magnetic multilayers with saturation magnetization M_s and layer thickness t_i by using the magnetic energy density

$$
\begin{aligned}
E = \Bigg\{ & -\sum_{i=1}^{N} t_i M_{i,s} H_0 \big[\cos(\theta_H)\cos(\theta_i) + \sin(\theta_H)\sin(\theta_i)\cos(\varphi_H - \varphi_i)\big] \\
& + \sum_{i=1}^{N} t_i K_i^{\text{eff}} \cos^2(\theta_i) + \sum_{i=1}^{N} t_i E_i^{\text{ani}}(\theta_i, \varphi_i) \\
& - \sum_{i=1}^{N-1} A_{i,i+1} \big[\cos(\theta_{i+1})\cos(\theta_i) + \sin(\theta_{i+1})\sin(\theta_i)\cos(\varphi_i - \varphi_{i+1})\big] \\
& - \sum_{i=1}^{N-1} B_{i,i+1} \big[\cos(\theta_{i+1})\cos(\theta_i) + \sin(\theta_{i+1})\sin(\theta_i)\cos(\varphi_i - \varphi_{i+1})\big]^2 \Bigg\}.
\end{aligned}
\tag{4.1}
$$

Here $(\theta_i, \theta_H, \theta_{i+1})$ and $(\varphi_i, \varphi_H, \varphi_{i+1})$ are, respectively, the polar and azimuthal angles for magnetization vector **M** and external dc field vector **H** with respect to the film normal, as shown in Fig. 4.1(a). The first term (the first line) is the usual Zeeman energy of the structure in the presence of an external dc field. The second term represents the magnetostatic energy due to the demagnetizing field and any induced perpendicular uniaxial anisotropy energy. Both of these energies qualita-

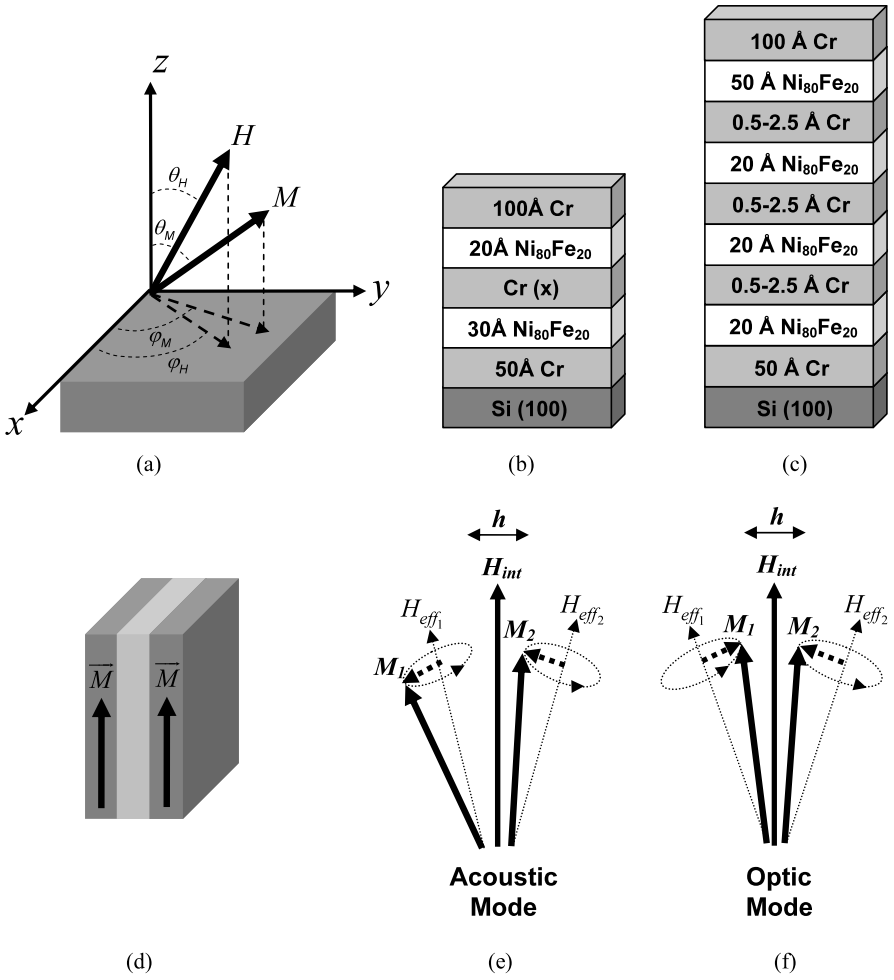

Fig. 4.1 (**a**) Relative orientations of the external dc magnetic field and magnetization vectors with respect to the sample plane and (**b**), (**c**) the stack of multilayered samples. Trilayered magnetic thin film (**d**) and relative orientations of the magnetization vectors of these layers corresponding to acoustic (**e**) and optic (**f**) modes in the external magnetic field

tively have the same angular dependence with respect to the film normal. Therefore, a single parameter, namely, K^{eff}, is used to describe these anisotropy energies. Additional terms (the second term in the second line) can also be added to describe different magnetic anisotropies as well. The last two terms (third and fourth lines) come from indirect exchange interactions of ferromagnetic layers through the nonmagnetic spacer via conduction electrons. The interlayer exchange coupling energy densities between nearest layers are determined by bilinear ($A_{i,i+1}$) and biquadratic ($B_{i,i+1}$) coupling constants. $A_{i,i+1}$ can be either positive or negative depending on

ferromagnetic or antiferromagnetic interactions, respectively. When the magnetic anisotropies (the physical and chemical structure of magnetic layers) are the same, the relative directions of magnetization vectors of neighboring layers are determined by relative values of the exchange coupling parameters in the absence of an external dc field. A positive value of $A_{i,i+1}$ dictates parallel alignments of magnetization vectors of neighboring layers. The parallel- antiparallel (perpendicular) alignments of magnetizations of neighboring layers are energetically favorable for a positive (negative) value of $B_{i,i+1}$. The biquadratic term is usually smaller compared to the bilinear term; therefore, it can be neglected for most of the ferromagnetic systems. The direct exchange interaction energy between neighboring spins is much larger compared to the other terms in total magnetic energy. On the other hand, the indirect exchange energy depends on the type of the materials and on the spacer thickness; it can even show oscillatory behavior with spacer thickness in the superstructures [7–13]. The interlayer exchange term becomes smaller and smaller as the nonmagnetic spacer becomes thicker and thicker. This term for the thinnest spacer can be comparable (or even larger) to the Zeeman and magneto-crystalline energy. In the theoretical analysis in this chapter this term is taken to be smaller compared to the other energy terms. When the directions of the magnetization vectors of neighboring layers start to deviate from each other, the system gains energy against the exchange coupling, and this energy manifests itself in FMR spectra, as will be explained later.

4.2.2 Dynamic Equation for Magnetization

As is well known, the microwave power absorption (FMR curve as a function of external dc field) by the sample is proportional to the ac magnetic susceptibility. Therefore, one has to derive a suitable theoretical expression in order to deduce the magnetic parameter for ac susceptibility. A brief description of the derivation of ac susceptibility is as follows: The equation of precessional motion for magnetization of the ith layer in an external field applied in a general direction with respect to the film plane can be written as

$$\frac{1}{\gamma}\frac{d\mathbf{M}_i}{dt} = \frac{1}{t_i}\frac{\mathbf{M}_i}{M_{i,s}} \times (\nabla_{M_i} E) - \frac{1}{t_i}\mathbf{M}_i \times \mathbf{h}^{\mathrm{rf}} + \frac{\alpha}{\gamma M_{i,s}}\left(\mathbf{M}_i \times \frac{d\mathbf{M}_i}{dt}\right) - \frac{m_{\theta_i}}{\gamma T_2}\hat{e}_{\theta_i} - \frac{m_{\varphi_i}}{\gamma T_2}\hat{e}_{\varphi_i}. \tag{4.2}$$

Here the effective field in the first term on the right-hand side is obtained from the gradient of the total magnetic energy density with respect to the magnetization vector. In polar coordinates the gradient operator is expressed as

$$\nabla_i = \hat{e}_{r_i}\frac{\partial}{\partial r_i} + \hat{e}_{\theta_i}\frac{1}{r_i \sin\theta_i}\frac{\partial}{\partial \theta_i} + \hat{e}_{\varphi_i}\frac{1}{r_i}\frac{\partial}{\partial \varphi_i}. \tag{4.3}$$

Here the symbols have their usual meanings. The second term on the right-hand side represents the ac excitation torque due to the magnetic field component of the microwave in (4.2). The third and fourth terms on the right-hand side represent the Landau–Lifshitz–Gilbert and Bloch type damping of dynamic (transverse components) magnetization, respectively in (4.2). One or both types of the damping terms can be necessary to explain the experimental data, depending on the film nature. Since the effective static field is much stronger compared to the microwave field components, the magnetization saturates along the effective dc field, **H**. When the microwave field is switched on, the magnetization vector deviates from the effective field direction, and it starts to precess around the effective dc field vector due to the perpendicular (transverse) magnetic field components of the microwave. Thus, the magnetization vector for the ith layer in the polar coordinate system in Fig. 4.1 can be written as

$$\mathbf{M}_i = M_{i,s}\hat{e}_r + m_{\theta_i}\hat{e}_{\theta_i} + m_{\varphi_i}\hat{e}_{\varphi_i}.$$

Recall that the first term represents the static component of the M lying along the effective dc field. Therefore, the z axis reference system is always chosen along the effective field for each direction of the applied dc magnetic field. The magnetization vector can be space dependent along the film normal for thicker films. But the amplitude of the ac magnetization of a very thin individual layer can be practically taken as constant throughout the layer thickness. Since the wavelength of the microwave is much longer than any dimensions of the thin film samples in the electron spin resonant (ESR) cavity, it can be taken as homogeneous over the sample volume, and so its time dependence can be written as

$$\mathbf{h}_x^{\mathrm{rf}} = h_x^o e^{j\omega t}. \tag{4.4}$$

Here w is the frequency and h_x^o the amplitude of the magnetic field component of the microwave, which is assumed to be constant throughout the layer thickness.

As mentioned above, the static torque becomes zero in the static equilibrium case (magnetization component parallel to static effective field), since the magnetization vector is parallel to the effective static field arising from the total magnetic free energy density. When a microwave field is applied, the magnetization deviates from the static equilibrium direction due to the microwave excitation torque given by the second term on the right-hand side of (4.2). Thus, the first term on the right-hand side of (4.2) makes dominant contributions to the mechanical torque, as explained below. In order to obtain the effective field, we begin with the differentials with respect to the angles of the first term of (4.2):

$$\frac{1}{\gamma_i}\delta\left(\frac{d}{dt}\mathbf{M}_i\right) = \delta\left(\frac{\mathbf{M}_i}{M_{i,s}} \times \frac{1}{t_i}\nabla_{M_{i,s}} E\right). \tag{4.5}$$

This differential arises from the small deviations of each layer magnetization from their equilibrium orientation. Contributions from the second and the third terms on the right-hand side of (4.2) will be treated later. Thus, the right-hand side of (4.5)

can be expanded as

$$\delta\left(\frac{\mathbf{M}_i}{M_{i,s}}\times\frac{1}{t_i}\nabla_{M_{i,s}}E\right)=\frac{1}{M_{i,s}}\delta\mathbf{M}_i\times\frac{1}{t_i}\nabla_{M_{i,s}}E+\frac{\mathbf{M}_i}{M_{i,s}}\times\delta\left(\frac{1}{t_i}\nabla_{M_{i,s}}E\right). \quad (4.6)$$

The first term on the right-hand side is zero since the gradient of E is zero for the equilibrium orientation. The static equilibrium conditions for the angles $\theta_i=\theta_{i,0}$, $\varphi_i=\varphi_{i,0}$ (at which the angular derivative of the energy is zero and the corresponding energy is minimum) are expressed as

$$\left.\frac{\partial E}{\partial\theta_i}\right|_{\theta_i=\theta_{i,0},\varphi_i=\varphi_{i,0}}=0,\quad\text{and}\quad\left.\frac{\partial E}{\partial\varphi_i}\right|_{\theta_i=\theta_{i,0},\varphi_i=\varphi_{i,0}}=0.$$

Expending the differential in the second term on the right side of (4.6) in polar coordinates and summing over all layers, one can get the following expression:

$$\begin{aligned}&\sum_{i=2,j=i-1}^{N-1,j+1}\left(\frac{\mathbf{M}_i}{M_{i,s}}\times\delta\left(\frac{1}{t_i}\nabla_{M_{j,s}}E\right)\right)\\&=-\sum_{i=2,j=i-1}^{N-1,j+1}\frac{1}{t_i}\frac{\mathrm{cosec}(\theta_i)}{M_j}\left(E_{\theta_j\varphi_i}m_{\theta_j}+\mathrm{cosec}(\theta_j)E_{\varphi_j\varphi_i}m_{\varphi_j}\right)\hat{e}_{\theta_i}\\&\quad+\sum_{i=2,j=i-1}^{N-1,j+1}\frac{1}{M_{j,s}}\frac{1}{t_i}\left(E_{\theta_j\theta_i}m_{\theta_j}+\mathrm{cosec}(\theta_j)E_{\theta_i\varphi_j}m_{\varphi_j}\right)\hat{e}_{\varphi_i}.\end{aligned}$$

Here $E_{\theta_j\theta_i}$, $E_{\varphi_j\varphi_i}$ and $E_{\theta_j\varphi_i}$ represent second order partial derivations of the energy density with respect to the polar angles of the magnetization for each layer. The angular derivative must be calculated for static equilibrium values of the angles. The radial components of magnetization in polar coordinates can be taken as constant when the microwave component of the magnetic field is much smaller compared to the dc component. Thus, the first term on the right-hand side of (4.2) makes the following contribution to the time dependence of the transverse components of magnetization as:

$$\frac{1}{\gamma_i}\frac{d}{dt}m_{\theta_i}=-\frac{1}{t_i}\frac{1}{\sin(\theta_i)}\sum_{j=i-1}^{i+1}\left(\frac{E_{\theta_j\varphi_i}}{M_{j,s}}m_{\theta_j}+\frac{1}{M_{j,s}}\frac{E_{\varphi_j\varphi_i}}{\sin(\theta_j)}m_{\varphi_j}\right), \quad (4.7)$$

$$\frac{1}{\gamma_i}\frac{d}{dt}m_{\varphi_i}=\frac{1}{t_i}\sum_{j=i-1}^{i+1}\left(\frac{E_{\theta_j\theta_i}}{M_{j,s}}m_{\theta_j}+\frac{E_{\theta_i\varphi_j}}{M_{j,s}\sin(\theta_j)}m_{\varphi_j}\right). \quad (4.8)$$

Note that the summations in (4.7) and (4.8) are taken only for exchange coupled nearest neighboring layers.

The contributions from the time-dependent parts (the next terms) in (4.2) to each component can be added to (4.7) and (4.8) to get:

$$\begin{aligned}
\frac{1}{\gamma_i}\frac{\mathrm{d}m_{\theta_i}}{\mathrm{d}t}\hat{e}_{\theta_i} &= -\frac{m_{\theta_j}}{t_i M_j \sin\theta_i}\mathrm{E}_{\theta_i\varphi_j}\hat{e}_{\theta_i} - \frac{m_{\varphi_j}}{t_i M_j \sin\theta_i \sin\theta_j}\mathrm{E}_{\varphi_i\varphi_j}\hat{e}_{\theta_i} - M_r h_{\varphi_i}\hat{e}_{\theta_i} \\
&\quad - \frac{m_{\theta_i}}{\gamma T_2}\hat{e}_{\theta_i} + \frac{i\omega\alpha}{\gamma}m_{\varphi_i}\hat{e}_{\theta_i}, \\
\frac{1}{\gamma_i}\frac{\mathrm{d}m_{\varphi_i}}{\mathrm{d}t}\hat{e}_{\varphi_i} &= \frac{m_{\theta_j}}{t_i M_j}\mathrm{E}_{\theta_i\theta_j}\hat{e}_{\varphi_i} + \frac{m_{\varphi_j}}{t_i M_j \sin\theta_j}\mathrm{E}_{\theta_i\varphi_j}\hat{e}_{\varphi_i} - M_r h_{\theta_i}\hat{e}_{\varphi_i} - \frac{m_{\varphi_i}}{\gamma T_2}\hat{e}_{\varphi_i} \\
&\quad - \frac{i\omega\alpha}{\gamma}m_{\theta_i}\hat{e}_{\varphi_i}.
\end{aligned} \tag{4.9}$$

4.2.3 Solution of Dynamic Equation for AC Magnetization

As seen, we have two sets of coupled linear differential equations for the theta and phi components of M. Therefore, the time dependence of the transverse components of the magnetization can also be assumed the same as for the driving torque due to this microwave excitation field, namely,

$$\begin{aligned}
m_{\theta_i} &= m^o_{\theta_i} e^{-j\omega t}, \\
m_{\varphi_i} &= m^o_{\varphi_i} e^{-j\omega t}.
\end{aligned} \tag{4.10}$$

The transverse components of $\mathbf{M}_i$ in (4.10) can be inserted in (4.2) to also include the damping torque, and one can get the following coupled equations for amplitudes of the time-varying components of each layer's magnetization, $\mathbf{M}_i$ as:

$$\begin{aligned}
-\frac{j\omega}{\gamma_i}m_{\theta_i} &= -\frac{m_{\theta_{i-1}}}{t_i M_{i-1,s}\sin\theta_i}E_{\theta_{i-1}\varphi_i} - \frac{m_{\varphi_{i-1}}}{t_i M_{i-1,s}\sin\theta_i \sin\theta_{i-1}}E_{\varphi_{i-1}\varphi_i} \\
&\quad - \frac{m_{\theta_i}}{t_i M_{i,s}\sin\theta_i}E_{\theta_i\varphi_i} - \frac{m_{\varphi_i}}{t_i M_{i,s}\sin^2\theta_i}E_{\varphi_i\varphi_i} - \frac{m_{\theta_{i+1}}}{t_i M_{i+1,s}\sin\theta_i}E_{\theta_{i+1}\varphi_i} \\
&\quad - \frac{m_{\varphi_{i+1}}}{t_i M_{i+1,s}\sin\theta_i \sin\theta_{i+1}}E_{\varphi_i\varphi_{i+1}} + \frac{i\omega\alpha}{\gamma}m_{\varphi_i} - \frac{1}{\gamma T_2} - M_{i,s}h_{\varphi_i}, \\
-\frac{j\omega}{\gamma_i}m_{\varphi_i} &= \frac{m_{\theta_{i-1}}}{t_i M_{i-1,s}}E_{\theta_{i-1}\theta_i} + \frac{m_{\varphi_{i-1}}}{t_i M_{i-1,s}\sin\theta_{i-1}}E_{\theta_i\varphi_{i-1}} + \frac{m_{\theta_i}}{t_i M_{i,s}}E_{\theta_i\theta_i} \\
&\quad + \frac{m_{\varphi_i}}{t_i M_{i,s}\sin\theta_i}E_{\theta_i\varphi_i} + \frac{m_{\theta_{i+1}}}{t_i M_{i+1,s}}E_{\theta_i\theta_{i+1}} + \frac{m_{\varphi_{i+1}}}{t_i M_{i+1}\sin\theta_{i+1}}E_{\theta_i\varphi_{i+1}} \\
&\quad - \frac{i\omega\alpha}{\gamma}m_{\theta_i} - \frac{1}{\gamma T_2} + M_{i,s}h_{\theta_i}.
\end{aligned} \tag{4.11}$$

Similar equations without damping torque were given in the literature [38, 39] to get the dispersion relations. But, in order to obtain full FMR absorption curves we have included damping torque in the dynamic equation of motion for magnetization.

4.2.4 Magnetic Susceptibility

The coupled equations (see (4.10)) can be put in a more compact matrix form in dimensions of $2N$ by $2N$,

$$C.\mathbf{Z} = Y. \tag{4.12}$$

Here C is a $2N \times 2N$ dimensional matrix whose nonzero matrix elements are:

$$C_{m,m} = j\frac{\omega}{\gamma_l} - \frac{E_{\theta_l\varphi_l}}{t_l M_{l,s}\sin\theta_l} - \frac{1}{\gamma_l T_2}; \qquad C_{m,m+1} = j\frac{\omega\alpha}{\gamma_l} - \frac{E_{\varphi_l\varphi_l}}{t_l M_{l,s}\sin^2\theta_l};$$

$$C_{m,m+2} = -\frac{E_{\theta_{l+1}\varphi_l}}{t_l M_{l+1,s}\sin\theta_l}; \qquad C_{m,m+3} = -\frac{E_{\varphi_l\varphi_{l+1}}}{t_l M_{l+1,s}\sin\theta_l\sin\theta_{l+1}};$$

$$C_{m+1,m} = \frac{E_{\theta_l\theta_l}}{t_l M_{l,s}} - j\frac{\omega\alpha}{\gamma_l}; \qquad C_{m+1,m+1} = j\frac{\omega}{\gamma_l} + \frac{E_{\theta_l\varphi_l}}{t_l M_{l,s}\sin\theta_l} + \frac{1}{\gamma_l T_2};$$

$$C_{m+1,m+2} = \frac{E_{\theta_l\theta_{l+1}}}{t_l M_{l+1,s}}; \qquad C_{m+1,m+3} = \frac{E_{\theta_l\varphi_{l+1}}}{t_l M_{l+1,s}\sin\theta_{l+1}};$$

$$C_{m+2,m} = -\frac{E_{\theta_l\varphi_{l+1}}}{t_{l+1} M_{l,s}\sin\theta_{l+1}}; \qquad C_{m+2,m+1} = -\frac{E_{\varphi_l\varphi_{l+1}}}{t_{l+1} M_{l,s}\sin\theta_l\sin\theta_{l+1}};$$

$$C_{m+3,m} = \frac{E_{\theta_l\theta_{l+1}}}{t_{l+1} M_{l,s}}; \qquad C_{m+3,m+1} = \frac{E_{\theta_{l+1}\varphi_l}}{t_{l+1} M_{l,s}\sin\theta_l},$$

where l runs from 1 to N while m runs from 1 to $2N-1$. Here $E_{\theta_j\theta_i}$, $E_{\varphi_j\varphi_i}$ and $E_{\theta_j\varphi_i}$ must be calculated for equilibrium orientations (corresponding to total energy minima) of each layer's magnetizations. In (4.12) the Z represents a column matrix whose elements are made from transverse components of all magnetic layers. The transpose of Z is a row matrix:

$$Z^T = (m_{\theta_1}, m_{\varphi_1}, m_{\theta_2}, m_{\varphi_2}, \ldots, m_{\theta_i}, m_{\varphi_i}, \ldots, m_{\theta_N}, m_{\varphi_N}). \tag{4.13}$$

On the other hand, Y is a column matrix whose elements are obtained from the multiplication of the saturation value of each layer's magnetization, $M_{i,s}$ by the projection of the external microwave field on the polar unit vectors of each magnetic layer as follows:

$$Y^T = (m_{s_1}h_{\theta_1}, m_{s_1}h_{\varphi_1}, m_{s_2}h_{\theta_2}, m_{s_2}h_{\varphi_2}, \ldots, m_{s_i}h_{\theta_i}, m_{s_i}h_{\varphi_i}, \ldots, m_{s_N}h_{\theta_N}, m_{s_N}h_{\varphi_N}), \tag{4.14}$$

where

$$\begin{aligned} h_{\theta_l} &= h_x^o \sin(\varphi_l), \\ h_{\varphi_l} &= h_x^o \cos(\theta_l).\cos(\varphi_l). \end{aligned} \tag{4.15}$$

Thus, one can obtain the components of the ac magnetization vector of each layer from elements of the following matrix, Z, as

$$Z = C^{-1}Y. \tag{4.16}$$

The microwave power absorption is proportional to the transverse magnetization averaged over all layers in the superstructure. In order to obtain power absorptions by the multilayered sample, one must project each m_i onto h_x^o and divide the resultant values by the magnetic field amplitude h_x^o of the external microwave field. That is, the average magnetic susceptibility is obtained as

$$\chi = m_x / h_x^o, \quad \text{where } m_x = \sum_{l=1}^{N} t_l \left\{ m_\theta^l \cos(\theta_l).\cos(\varphi_l) - m_\varphi^l \sin(\varphi_l) \right\}. \tag{4.17}$$

4.2.5 Computer Calculation of FMR Spectra to Get Fitted Parameters

One must use a computer program that calculates microwave power absorption as a function of external magnetic fields applied for general directions. Recall that the absorbed power by exchange coupled magnetic multilayers is proportional to the vector sum (in (4.17)) of the ac (transverse) components of the individual magnetization for each layer. The field derivative of the power corresponds to the experimental FMR spectra recorded by a conventional ESR spectrometer. The best parameter set can be obtained by fitting the theoretical spectra to experimental ones.

According to the theoretical model explained above, the program must first obtain the equilibrium orientations of exchange coupled magnetizations in each layer using assumed values of a set of magnetic parameters in magnetic free energy. It then calculates the second order derivatives of magnetic energy with respect to the polar angles at static equilibrium. Then, using a suitable iteration procedure, the static equilibrium polar angles for static magnetization can be obtained. The program then must solve the exchange coupled linear equations, (4.11), via (4.12), (4.13), and (4.14) to calculate transverse components of M as a function of the external magnetic fields that are applied for general directions. As mentioned above, the field derivative of the absorbed power corresponds to the experimental FMR spectra recorded by a conventional ESR spectrometer. Thus, the best parameter set can be obtained by fitting the theoretical spectra to experimental ones.

The damping parameters have very minor effects on the resonance field value, but they basically determine the resonance line shape. Although the model and computer program are suitable for both the Gilbert and Bloch type dampings, the Gilbert

type damping gives satisfactory agreement with the experimental data for homogeneous ferromagnetic samples. Although the line width and shapes vary with the angle of external field directions, the same Gilbert damping parameter can represent the line shape of field-derivative FMR spectra for general directions of the external dc field. This means that, for magnetically homogeneous films, one can successfully fit the data by using only the Gilbert type damping term. However, if there are magnetic inhomogeneities, the Bloch type damping term must be included as well.

4.3 Experimental

4.3.1 Sample Preparation

The Cr(50 Å)/Py(20 Å)/Cr(**x**)/Py(20 Å)/Cr(**x**)/Py(20 Å)/Cr(**x**)/Py(50 Å)/Cr(100 Å) multilayer and Cr(50 Å)/Py(30 Å)/Cr(t)/Py(20 Å)/Cr(100 Å) trilayer samples in Fig. 4.1 were grown onto a naturally oxidized p-type single crystal Si(100) substrate by magnetron sputtering. Here t denotes the thickness of the Cr spacer layer and ranges from 4 to 40 Å with 1 Å steps for three-layered films and from 0.5 to 2.5 Å with 0.5 Å steps for multilayered films. The substrates were cleaned in an ultrasonic bath by using methanol and ethanol consecutively before they were transferred into ultra-high vacuum (UHV) conditions. They were annealed up to 600 °C for 30 minutes in UHV to minimize the surface deficiencies. A water-cooled 3″ diameter target provided the thickness homogeneity.

High-purity Permalloy, $Ni_{80}Fe_{20}$ (Py), and Cr targets were sputtered by rf (20 W) and dc (30 W) power supplies, respectively. These types of applied power allow the slowest deposition rates with optimum pressure to get an ideal surface morphology. Although the base pressure in the preparation chamber is 1×10^{-8} mbar, the pressure during the sputtering was 1.6×10^{-3} mbar. The distance between the target and the substrate was 100 mm, allowing a 1 Å deposition sensitivity by decreasing the deposition rate.

A water-cooled Matek TM 350 QCM (Quartz Crystal Monitor) thickness monitor was used to measure the film deposition rate in situ. At the beginning of film growth, the QCM was calibrated for Py and Cr deposition rates. The calibration of the QCM thickness monitor was complemented by monitoring the attenuation of the substrate photoemission signal by X-ray photoemission spectroscopy (XPS) from the deposited films. For thickness determination we monitored the Si $2p$ attenuation as a function of chromium exposure by using XPS signals. Converting this to a Cr thickness, the electron mean free path was calculated by using the TPP formula developed by Tanuma, Powell, and Penn [52]. Since Py has two components, a Veeco Dektak 8 profile-meter was also used to calibrate the thickness to confirm the results of the photoemission attenuation.

The prepared trilayers were covered by a 100 Å Cr cap layer to prevent oxidation of the trilayered structures. We have investigated the suitable thickness of magnetic layers to observe measurable exchange coupling between ferromagnetic

layers through a metallic Cr spacer. The metallic films have polycrystalline structures. Small samples of 1×1.5 mm in lateral size were cut from the deposited films for the FMR measurements.

4.3.2 FMR and DC Magnetization Measurements

The FMR measurements were performed using a Bruker EMX model X-band ESR spectrometer at a microwave frequency of 9.5 GHz. The measurements were carried out as a function of the angle of the external dc field with respect to the film normal at room temperature. The sample sketch, relative orientation of the equilibrium magnetization vector **M**, the applied dc magnetic field vector **H**, and the experimental coordinate system are shown in Fig. 4.1(a). A picture of the prepared trilayered structure is shown in Fig. 4.1(b). The magnetic field component of the microwave is always kept perpendicular to the dc field during the sample rotation. The applied microwave field always remains in the sample plane for conventional geometry, and the power is kept small enough to avoid saturation. A small modulation field of 100 kHz was applied in parallel to the dc magnetic field in order to record the field derivative of the absorption power.

The magnetization measurements were performed by using a Vibrating Sample Magnetometer (VSM, Quantum Design PPMS 9T) at room temperature for both in-plane geometry (IPG; field parallel to the sample plane) and out-of-plane geometry (OPG; field perpendicular to the sample plane).

4.4 Experimental Results and Calculations

4.4.1 Three-Layered Py/Cr/Py Films

4.4.1.1 Experimental Results

FMR spectra of trilayered Py/Cr/Py films are very sensitive to the relative orientation of the external dc field. The spectra also strongly depend on both the ferromagnetic and nonmagnetic Cr spacer layer thickness. In order to find the most suitable samples to illustrate the effectiveness of the FMR method, the dependencies of the FMR spectra on the thickness of the ferromagnetic monolayered samples were studied first. Some examples of FMR spectra are given in Fig. 4.2. As can be seen from this figure, the FMR spectra are strongly dependent on the film thickness in the very thin film regime. Both the resonance field and the line width for both the perpendicular and parallel geometry cases change with the thickness. As the film thickness decreased below 10 Å the line drastically broadened (intensity decreased) and the resonance field values increased (decreased) for the IPG (OPG) case. After a few

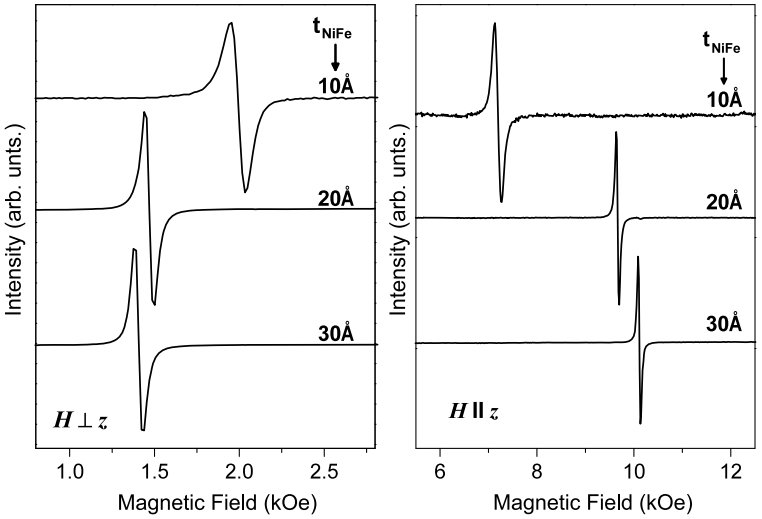

Fig. 4.2 FMR spectra of NiFe (Py) samples in parallel (*left*) and perpendicular (*right*) orientation to film plane with respect to the applied magnetic field for different thicknesses

quick trials it was seen that the thicknesses and/or magnetic anisotropies of two ferromagnetic layers should be different from each other to observe the influence of exchange interactions on the FMR spectra. Therefore, the thicknesses of the bottom and upper Py layers were chosen as 20 and 30 Å, respectively. The samples were labeled as Sx, where x is the Cr spacer thickness in Å.

The FMR spectra in Fig. 4.3 are some selected examples to show the effect of spacer thickness for the external field applied parallel (IPG case) and/or perpendicular (OPG case) to the Py(30 Å)/Cr(x Å)/Py(20 Å) trilayers. The two well-resolved FMR modes were observed for most of the samples (except S11 and S22.5 in the OPG case). These two well-resolved FMR peaks overlapping give rise to a single observed peak where the external field is applied in the film plane for all samples. As can be seen in Fig. 4.3(right), the relative intensities of the two modes depend on the spacer thickness. The weaker mode (called the optic mode) appearing at the lower field side of the strong mode (main or acoustic mode) for sample S4 shifts to the higher field side for the sample S10 as well. As seen from Fig. 4.3, the resonance field varies with the spacer thickness. The exchange coupling and resonance value exhibit roughly oscillatory behavior, as will be seen in Fig. 4.8. This value passes through a local minimum for films with a chromium thickness of 11, 22, and 33 Å. Note that the two peaks for the OPG case overlap for these thicknesses as well. There seems to be a period of 11 Å for this behavior. Note also that the thickness dependence of the resonance field for the IPG case shows opposite behavior to that for the OPG case.

Some examples of the temperature dependence of FMR spectra for samples S10 and S11 are given in Fig. 4.4 and temperature dependence of the effective magnetic anisotropy for sample S11 is given Fig. 4.9. The resonance field values, especially

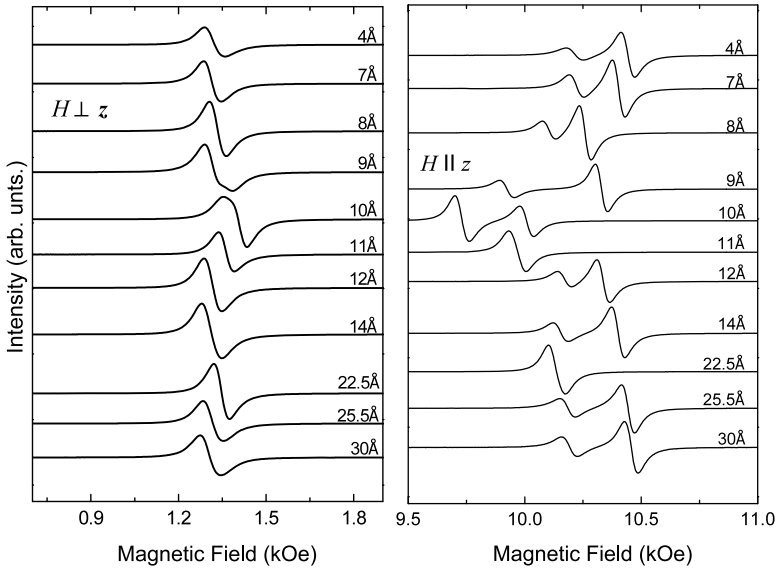

Fig. 4.3 FMR spectra of some selected trilayered films in parallel (*left*) and perpendicular (*right*) orientation to the applied magnetic field with respect to the film plane

in the OPG case, have a remarkable dependence on the temperature. Slight differences in the relative intensity of the modes and their separations in the field axis are observed as well. That is, the main characters of the FMR spectra remain almost independent of the temperature.

As mentioned above, the FMR spectra are very sensitive to the relative orientation of the external dc field. The angular variations of the FMR spectra for these two different samples are given in Fig. 4.5. Theoretical (fitted) spectra (continuous lines) obtained by the theoretical model are plotted together with the experimental ones (dotted lines). The number of peaks for S11 remains one for all angles. However, the two peaks observed for the OPG case for S10 overlap and give a single observed peak as the field direction comes close to the film plane.

As can be seen from Fig. 4.6(a), the resonance field values for both samples are almost the same for a broad range of angles. However, there are noticeable differences where the field is applied very close to the film normal; that is, the resonance field values for S4 are higher compared to those for S10. This means that the thicker spacer weakens the magnetic coupling between the ferromagnetic layers to allow more freedom for them to act as ultrathin magnetic layers. However, when the spacer becomes thinner, both layers are more strongly coupled and act almost as a single thicker layer. Since the uniaxial perpendicular anisotropy for a thinner film is generally higher than that for a thicker layer, the resonance for the OPG case is expected to occur at a higher field for S4. The strong angular dependence is mainly due to shape anisotropy (a demagnetizing field).

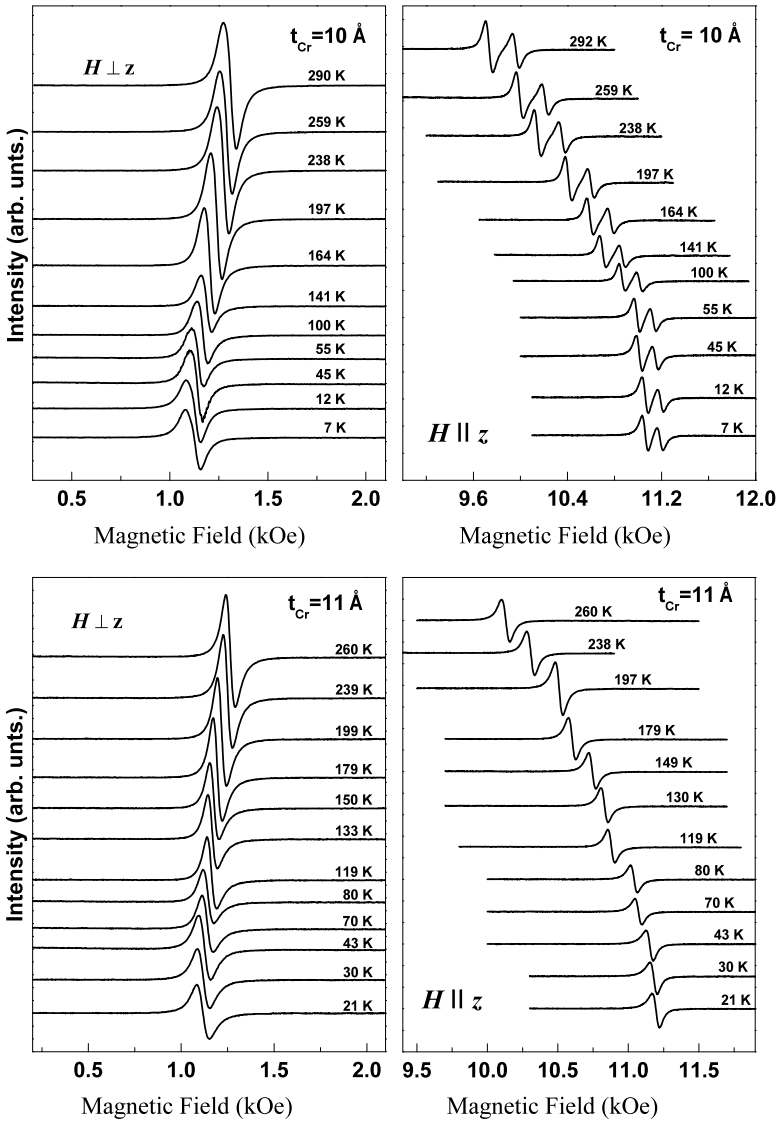

Fig. 4.4 Temperature-dependent FMR spectra of samples S10 and S11 for parallel and perpendicular geometry

Figure 4.6(b) shows the magnetic hysteresis curves of samples S4 and S10 for both the IPG and OPG cases. For OPG, the magnetization of sample S10 saturates at about 7 kOe, which corresponds to the effective uniaxial anisotropy containing the demagnetizing field and induced perpendicular axial anisotropy field. The sudden jump in the field range of 0–100 Oe for the OPG case can be attributed to a small misorientation of the external field, since the projection of the field onto the sam-

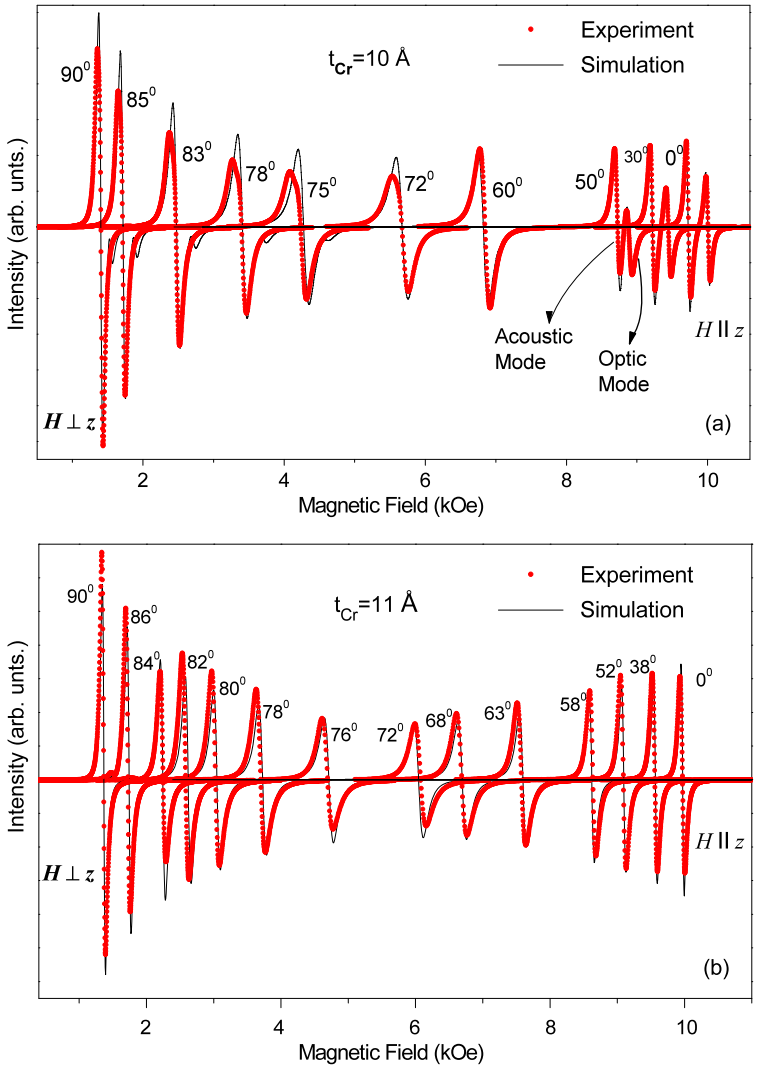

Fig. 4.5 Angular dependence of FMR spectra for samples S10 (**a**) and S11 (**b**)

ple plane can saturate magnetization in the sample plane. Thus, detection coils can detect a significant dc signal due to M saturated in the sample plane. For the IPG case, the hysteresis curves have been given as insets in Fig. 4.6(b) for both samples S4 and S10. As seen in these insets, the magnetization saturates at a very low field, even below 10 Oe, for the two samples. The hysteresis for sample S4 is wide and square-like in the IPG case, and its remanence is very close to the saturation value. However for sample S10, the remanence value in the IPG case is almost one-fifth of the saturation magnetization value, and the magnetization goes to saturation gradu-

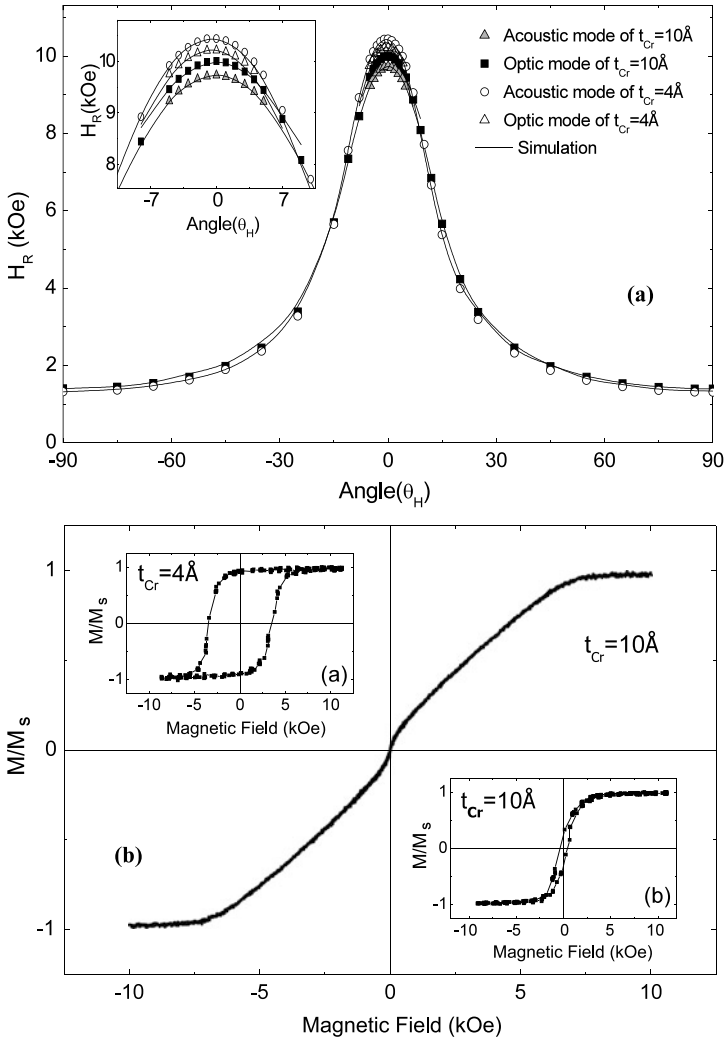

Fig. 4.6 (**a**) Dependence of the experimental and simulated resonance field values as a function of θ_H for samples S4 and S10. The *inset* shows a small region of the curves for the field oriented very close to the film normal. (**b**) Hysteresis curve recorded at room temperature of sample S10 for the external magnetic field applied along the hard magnetization axis (perpendicular to the film plane). The hysteresis curves for the easy directions (in the film plane) of the magnetizations for S4 and S10 are given in the *insets* (**a**) and (**b**), respectively

ally compared to that for S4. A similar behavior has been reported in the literature for Py/Cr/Py multilayers [50]. This could be considered as a sign for antiferromagnetic interactions between the ferromagnetic layers through the nonmagnetic spacer for sample S10.

4.4.1.2 Simulations of the FMR Spectra

For polycrystalline ultrathin Py/Cr multilayered thin films, the experimental FMR spectra could be fitted using the Zeeman, demagnetizing, and uniaxial anisotropy energies (the uniaxial axis is along the film normal). It has been found that the induced uniaxial energy strictly depends on the magnetic layer thickness. Especially for ultrathin films, this term sometimes can become comparable to the demagnetizing energy. When the magnetic layer becomes thinner than 5 Å, the magnetization does not saturate easily, which is why we used sufficiently thicker magnetic layers to saturate the magnetization to a constant value as was assumed in the development of the theory.

The angular dependencies of demagnetizing energy due to saturation magnetization and perpendicular uniaxial crystalline anisotropy for polycrystalline films have exactly the same analytical form. This means that it is very difficult (if not impossible) to extract induced perpendicular anisotropy by using FMR data only. In fact, the FMR intensity is linearly proportional to the saturation magnetization; thus, one can use a reference sample to calibrate the spectrometer signal for exact magnetization measurements. But it seems to be more convenient to use magnetization values obtained from conventional dc magnetization measurement techniques.

Some examples of simulated spectra have been plotted in Figs. 4.5 and 4.7 together with the experimental ones. As seen from these figures, there are good agreements between the experimental and the calculated FMR spectra. A careful analysis shows that the position of the resonance peaks is determined by the saturation magnetization M_s, the effective anisotropy, and the exchange coupling of the magnetic layers. In fact, in the case of magnetically equivalent layers, the ferromagnetic exchange interaction has no effect on the resonance field; that is, a single resonance peak is observed due to simultaneous excitations of precession of magnetization in all layers. However, when the magnetic properties of individual magnetic layers slightly differ from each other, the exchange coupling between successive ferromagnetic layers starts to play an important role in the FMR curve. Thus, as the external dc field is scanned in a constant microwave frequency, the magnetization vector in one of the layers comes close to the resonance condition in a particular field value, while the other layer is still far from resonance for the non-exchange coupled case. That is, the directions of dynamic magnetizations of neighboring layers become different from each other. Now when exchange coupling is switched on, it tries to make the magnetization vector in the non-resonating layer parallel to that of the resonating layer. Thus, additional inertia torque due to the magnetic field induced by the other layer arises, and this torque has to be balanced by changing the resonance field. Similarly, as the field scan is continued beyond the first resonance value, it reaches the value that would correspond to the resonance value for the non-coupled second layer. Again, due to exchange coupling with the first layer, the resonance field differs from that of the non-coupled layer.

As seen from Figs. 4.7(a3) and (b3), the optical mode occurs at the lower (higher) field side of the main (acoustic) mode for ferromagnetic (antiferromagnetic) coupling. The separation between the optic mode and acoustic mode in the field axis

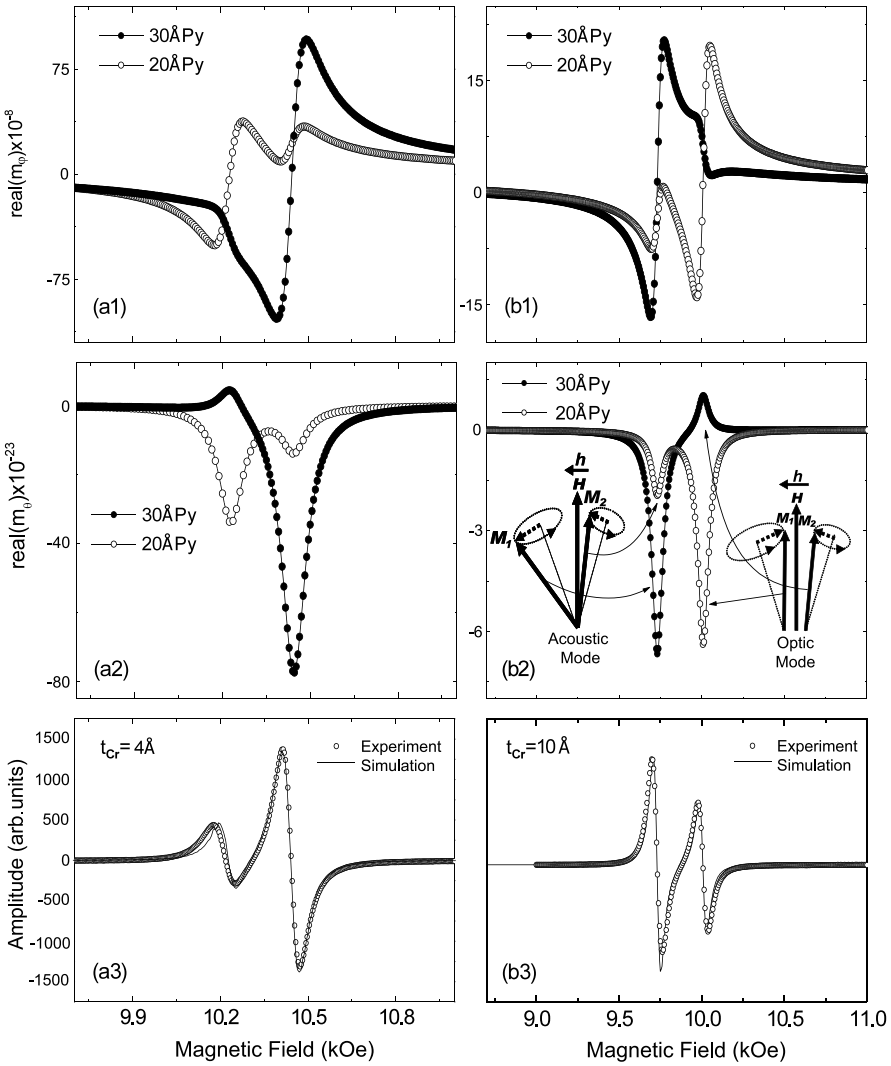

Fig. 4.7 FMR curves for two ferromagnetically (*on the left*) and antiferromagnetically (*on the right*) exchange coupled samples. The real values of the azimuthal (**a1** and **b1**) and polar (**a2** and **b2**) components of the ac magnetizations for each layer are given as a function of the external dc magnetic field to show the relative phase of the dynamic components of the magnetization for the acoustic and the optical modes. The field-derivative FMR absorption curves for S4 and S10 are given in (**a3**) and (**b3**), respectively

is determined by the orientation of the external field, the saturation magnetization, the anisotropy field, and the exchange coupling parameter. In fact, the separation between the modes generally increases with the absolute value of the exchange parameter. That is, if the interlayer exchange coupling strength increases, the optic

mode moves away from the acoustic mode, and the relative intensities and the separation between the modes increase. On the other hand, if the interlayer exchange coupling strength decreases, the optic mode comes close to the acoustic mode, while its relative intensity significantly increases.

As a result of exchange coupling of magnetically nonequivalent neighboring layers, two resonance modes are observed in the FMR curves for the OPG case. Figure 4.7 also shows the calculated real values of the azimuthal (a1 and b1) and polar (a2 and b2) components (transverse components) of the ac magnetizations for each layer of samples S4 and S10 given as a function of the external dc magnetic field. These data also allowed us to get the relative phase of the dynamic components of ac magnetization as a function of the external dc field. As can be seen in Figs. 4.7 (a1 and a2) and (b1 and b2), the real values of the azimuthal and polar components of the ac magnetizations for the two samples are different from each other. This means that the magnetization vector makes an elliptical (rather than circular) precession about the dc component of the magnetization (and about the effective dc field).

The magnetization of every layer obviously makes a contribution to the resonance absorption for each FMR mode in which all layer magnetizations are excited up to some extents. Since the excitation amplitude and the phase of precession of the dc magnetizations of neighboring layers continuously evolve with the dc field, the phase difference becomes either zero or π at the exact resonance field values of the modes. The mode for the first case (in phase) is called the acoustic mode, while the other is called the optical mode to make an analogy with phonon spectra. The relative amplitude of precession of different layers continuously changes (evolves) with the external dc magnetic field, and thus one of the layers makes a dominant contribution to the FMR signal amplitude (ac susceptibility) for each mode about the resonance field.

Since the average magnetic susceptibility is proportional to the vector sum of transverse components of the ac magnetization, the intensity of the acoustic mode is always higher than that of the optical mode at exact resonance fields. The relative positions of the modes depend on the sign of exchange coupling parameters A_{12} and B_{12} as well. As mentioned before, these parameters represent the exchange field on a magnetic layer due to the neighboring layer. This field depends on the relative orientation of the magnetization. For an independent determination of these parameters, one needs to control the relative orientations of M_1 and M_2. Unfortunately, since the demagnetizing energies of neighboring layers are close to each other and the Zeeman energy is too large compared to the exchange energy, the dc magnetization vectors of neighboring layers remain almost always parallel to each other at the FMR resonance field. Thus, the effective exchange field on one of the magnetic layer due to the other magnetic layer does not depend on the external field direction. Therefore, it is not practical to get additional information for different angles to deduce both exchange coupling terms independently. If we had been able to rotate separately the magnetization of individual magnetic layers with respect to each other, then we could have determined both parameters independently. But we do not have the ability to fix the magnetization of one layer and sweep the external field

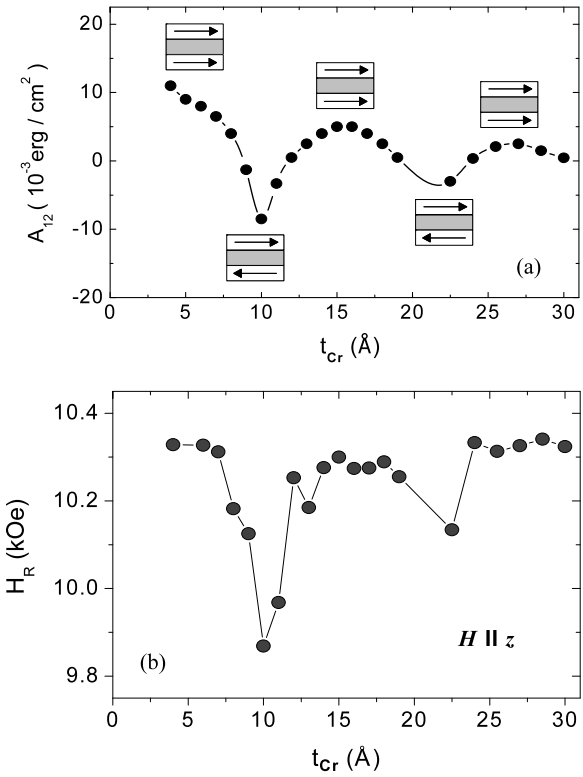

Fig. 4.8 (**a**) Effective interlayer exchange coupling parameter, A_{12}, obtained from the fitting as a function of the nonmagnetic spacer (Cr) thickness. The sign of the exchange parameter changes with the spacer thickness and causes parallel or antiparallel alignment of the magnetization of neighboring layers as shown by the *arrows* for some spacer thicknesses. (**b**) Resonance field values of the trilayered thin films at perpendicular geometry

gradually to rotate the magnetization of the second layer in order to determine A_{12} and B_{12} independently. Therefore, we have used only the bilinear term, that is, A_{12}, in the simulations. Maybe in the future we can achieve this with different multilayer structures.

The deduced interlayer exchange coupling parameter A_{12} is plotted in Fig. 4.8 as a function of the nonmagnetic spacer (Cr) thickness. Recall that both the bilinear and the biquadratic exchange energies are represented by a deduced effective parameter (A_{12}). As can be seen from this figure, the exchange parameter qualitatively exhibits oscillatory behavior. The absolute value decreases with increasing spacer thickness. However, the interlayer exchange coupling constant changes its sign and oscillates with a period of about 11 Å. Note that the spacer thickness dependence of the resonance field value shows a very similar behavior to that of the interlayer exchange coupling parameter. This result is consistent with the theory given by A. Fert et al. [53]. The deduced value of the exchange parameter for the Py (20 Å)/Cr(10 Å)/Py(30 Å) trilayer film is nearly half of the values given for the $(\text{Py/Cr(12 Å)})_{40}$ multilayer system prepared by an electron beam deposition system [50]. However the deduced value in our case is still almost 20 times less than that found for the Fe/Cr superlattice in the literature [51]. The period of oscillation of the interlayer exchange coupling is very close to that for $(\text{Py/Cr (12 Å)})_{40}$, but is

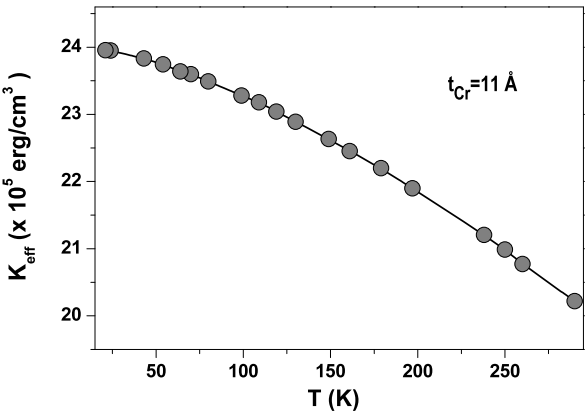

Fig. 4.9 Temperature dependence of the effective magnetic anisotropy for sample S11

significantly smaller than that given for Fe/Cr multilayers [7]. The smaller oscillation period was attributed to interface roughness or interdiffusion between the two interfaces of the trilayer [50].

4.4.2 Py/Cr/Py Multilayer

In the previous section, we investigated the magnetic properties of a Py/Cr/Py trilayer system and found that the exchange interaction depends on the nonmagnetic layer thickness and that the oscillation period was about 11 Å. This section focuses on understanding and developing descriptions of direct or indirect interactions between Cr(50 Å)/Py(20 Å)/Cr(x)/Py(20 Å)/Cr(x)/Py(20 Å)/Cr(x)/Py(50 Å)/Cr(100 Å) magnetic multilayers through sufficiently thin nonmagnetic spacer layers. For this we have continued a similar study on a multilayered structure by increasing the number of magnetic layers (three 20 Å equivalent Py layers). The nonmagnetic Cr spacer layer thickness is varied from 0.5 to 2.5 Å with 0.5 Å steps). In order to observe the influence of exchange interactions on FMR spectra, the thickness of the top Py layer was chosen as 50 Å. Thus, we induced a different effective surface magnetic anisotropy from that of the bottom ferromagnetic layers (we expect to observe optic and acoustic modes) to identify the nature and the exact value of exchange coupling between magnetic layers.

4.4.2.1 Experimental Results

Figure 4.10 shows the spacer thickness dependence of the FMR spectra for OPG and IPG cases of magnetic multilayer samples. Notice that the resonance positions are almost unaffected by the chromium thickness for the IPG case. However, in the perpendicular geometry, the spacer thickness plays an important role in the relative intensities and the resonance positions of the optic and acoustic modes in the

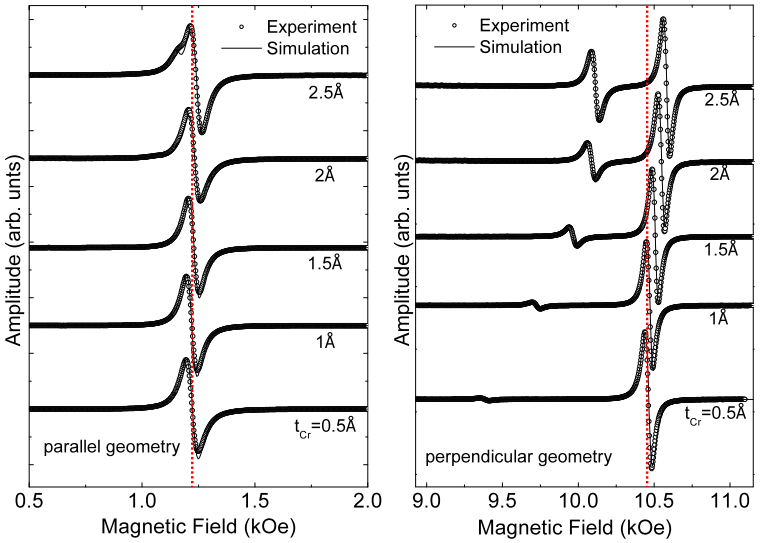

Fig. 4.10 Experimental and simulated FMR spectra of the multilayer films with different spacer thicknesses for the external field parallel (*left side*) and perpendicular (*right side*) to the sample plane

magnetic field axis. The acoustic mode intensity decreases while the optical mode intensity increases as the spacer layer thickness increases. The resonance positions of the optic and acoustic modes increase with spacer thickness as well. However, the dependence of the resonance field on the spacer thickness is much stronger for the optical mode.

The distance between the acoustic mode and optical mode is largest for the 0.5 Å Cr case. This means that the exchange coupling is ferromagnetic and largest for this sample, as can be expected from the nature of the exchange interaction. As the spacer gets thicker and thicker, the exchange coupling gets weaker and weaker. Obviously, the thicker spacer weakens the magnetic coupling between the ferromagnetic layers. Figure 4.10 also shows that the optic mode is on the left side of the acoustic mode in all samples, so all observed couplings are ferromagnetic as mentioned before.

Figure 4.11 illustrates the angular dependence of the FMR spectra for spacer layer thicknesses of 0.5 and 1 Å. When the field is applied parallel to the sample plane (IPG, $\theta = 90°$), a single FMR peak is observed. However, as the magnetic field direction approaches the film normal (OPG, $\theta = 0°$), this peak splits into two modes, an acoustic and an optic mode. This situation is rather common for all ultrathin magnetic multilayer structures in parallel and perpendicular geometry. As can be seen in the figures, the relative intensities of the two modes are very different from each other. The optical mode is much weaker than the acoustic mode for both samples. This situation implies strong interactions between successive ferromagnetic layers. The weaker mode (the optical mode) that appears at the lower field

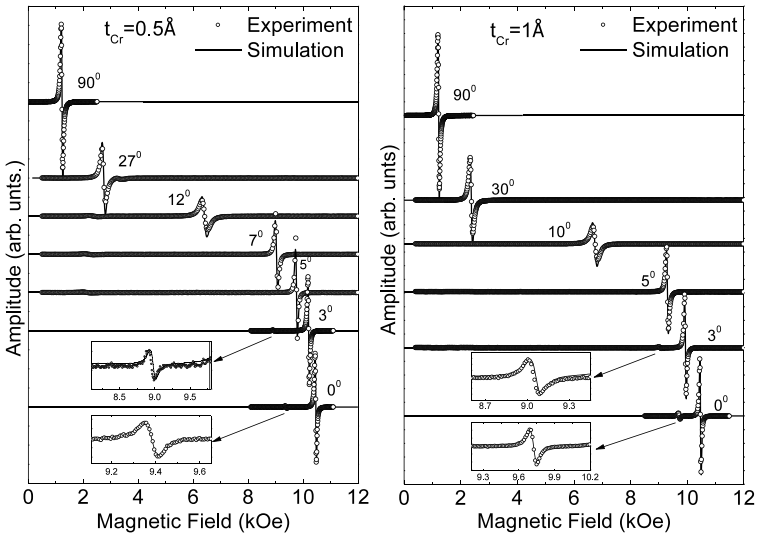

Fig. 4.11 Angular dependence of the experimental and simulated FMR spectra of the samples with $t_{Cr} = 0.5$ Å (*left*) and $t_{Cr} = 1$ Å (*right*). The weaker optical modes are magnified for clarity as shown in the *insets*

side of the strong mode (main or acoustical mode) for the spacer thickness of 1 Å shifts to a higher field, and its intensity decreases more than for the spacer thickness of 0.5 Å. This means that the magnitude of the exchange interaction between ferromagnetic layers decreased with the increase in the spacer thickness. As mentioned above, the FMR peak for the optical mode is on the left of that for the acoustic mode for both 0.5 and 1 Å spacer thicknesses. This confirms that the interaction between magnetic layers is ferromagnetic for both cases.

Figure 4.12 shows magnetic hysteresis curves of some samples for the IPG case at room temperature. The magnetization saturates at a very low field, even below 7 Oe, for each sample. The amount of reverse magnetic field, the coercive field, for all three samples is nearly 4 Oe. The hysteresis curves are wide and square-like in the IPG case, and their remanences are quite close to the saturation value. Measurements with high magnetic fields did not show an additional step. This behavior indicates that all samples have ferromagnetically exchange coupled through the nonmagnetic spacer.

4.4.2.2 Simulations of the FMR Spectra

The magnetic parameters are obtained by fitting the calculated spectra to the experimental ones. The simulated spectra obtained by using best fitting parameters were plotted in the same figures (Figs. 4.10, 4.11, and 4.13) for comparison with the experimental ones. As can be seen, there are very good agreements between the

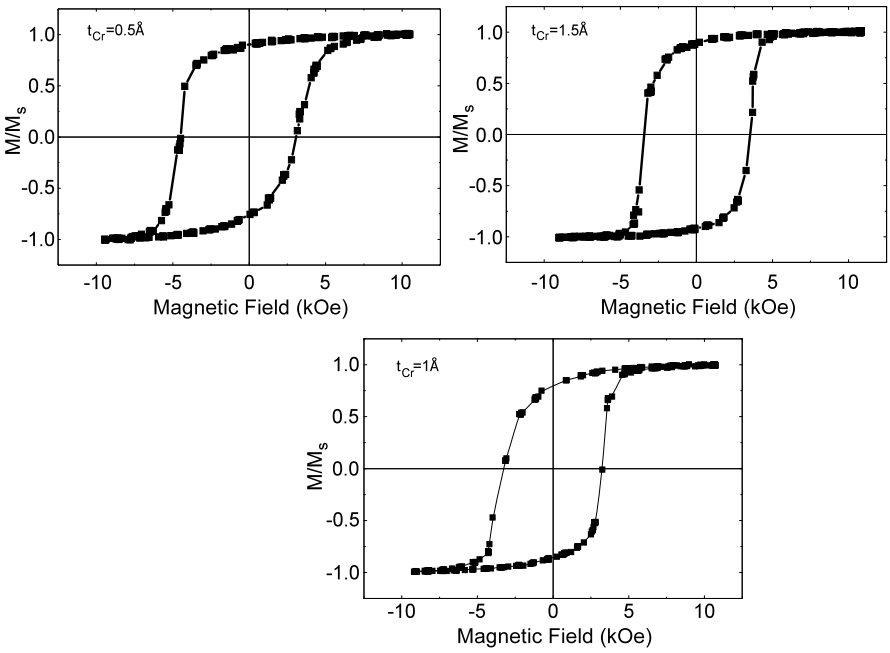

Fig. 4.12 The hysteresis curves recorded at room temperature for the external magnetic field applied along the easy directions (in the film plane) of some samples

experimental and simulated spectra. Figure 4.13 illustrates more details for the behavior of the polar components of the ac magnetizations of individual layers and the resultant SWR spectra for two different thicknesses of the Cr spacer. As can be seen from this figure, the real components of the amplitudes were given as a function of the external magnetic field applied perpendicular to the film plane. A careful examination will reveal that there are more than two peaks in the theoretical spectra, but the amplitude of higher order modes is too small to be observed in the experimental spectra. Therefore, these higher order SWR peaks have been magnified and plotted in insets just below the scaled graph to show their details. As seen from these magnified insets, the phase of the ac components of magnetization for each individual layer continuously evolves as the external magnetic field is scanned. Thus, one cannot say that some modes are purely acoustic and some optical; there is a mixture. That is, as the number of magnetic layers is sufficiently increased, one gets continuous spin waves, and their phases change step by step from one layer to the next with the k vector perpendicular to the film plane.

The angular variations of the resonance fields for two different samples are given in Fig. 4.14. The solid lines and the solid circles represent the theoretical resonance field values obtained by using the theoretical model and experimental resonance field values for the acoustic and optic modes, respectively. As one can see from the graph, there is only one FMR mode until the field direction is nearly 10° away from

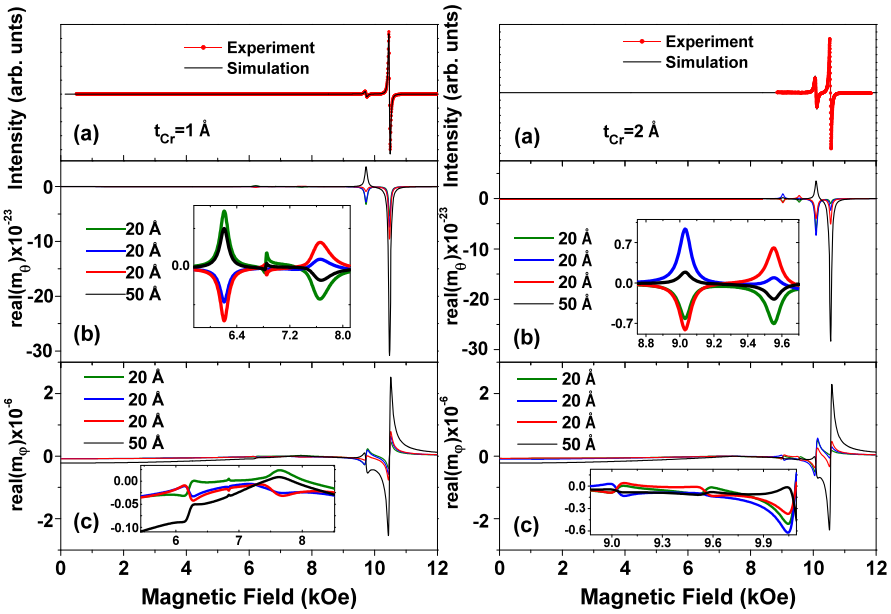

Fig. 4.13 (**a**) Experimental and simulated FMR absorption curves of the sample with $t_{\mathrm{Cr}} = 1$ and 2 Å. The real values of the polar (**b**) and azimuthal (**c**) components of the ac magnetizations for each layer are given as a function of the external dc magnetic field

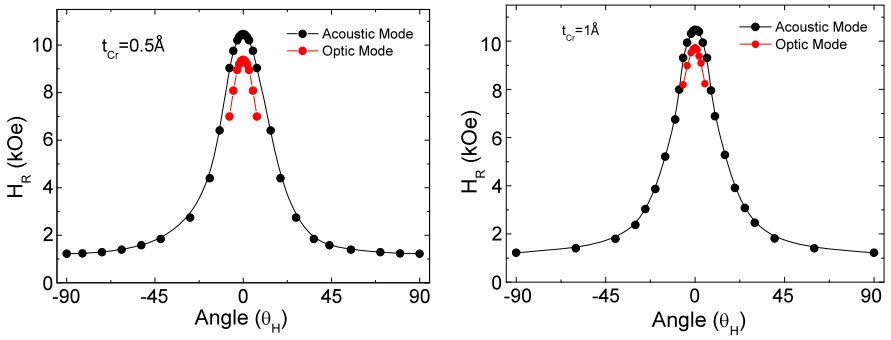

Fig. 4.14 Dependence of the experimental and simulated resonance field values as a function of θ_H for the samples with chromium thicknesses of 0.5 Å and 1.0 Å

film normal for both cases. When the field is applied very close to the film normal, an additional FMR mode (the optic mode) appears with lower resonance field values. The angular dependence of the curve of the resonance field for the acoustic mode for both samples is almost the same for a broad range of angles. However, the resonance field values for the 0.5 Å sample are lower compared to those for the 1.0 Å thick spacer where the field is applied very close to the film normal. As men-

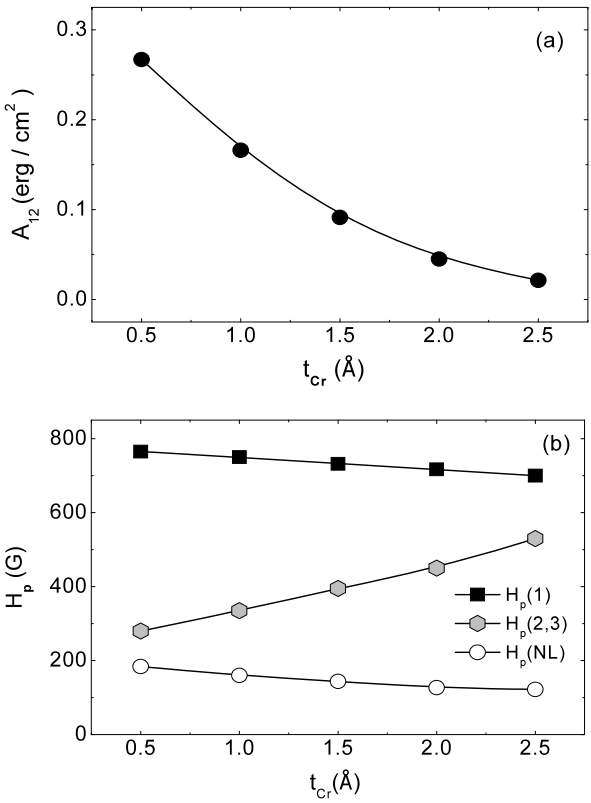

Fig. 4.15 (**a**) Effective interlayer exchange coupling parameter, A_{12}, obtained from the fitting, as a function of nonmagnetic spacer (Cr) thickness for the multilayered films. (**b**) Perpendicular magnetic anisotropy parameter, (H_p), for inner and outer layers

tioned above, this means that the magnitude of the exchange interaction between ferromagnetic layers decreases with an increase in the spacer thickness. The strong angular dependence of the resonance curves in Fig. 4.14 is mainly due to shape anisotropy (demagnetizing field).

Figure 4.15 shows the interlayer exchange interaction parameter (a) and perpendicular magnetic anisotropy parameters (b) for the inner and outer layers. The interlayer exchange interaction is obviously ferromagnetic, and its magnitude drastically decreases as the spacer thickness increases even at the sub-angstrom scale. Actually, a spacer thickness below one atomic size cannot make a continuous nonmagnetic layer. Such a thin spacer means that the very dilute Cr atoms are spread in a layer, some atoms of which consist of ferromagnetic permalloy atoms. This dilution in a layer separating two regions of permalloy can cause a drastic exchange breaking between two regions (on the opposite sides of the diluted layer) of the ferromagnetic film. The spacer thickness has a significant influence on the effective anisotropies of the magnetic layers. This can be expected from the crystalline strains due to lattice mismatch and the proximity effects of nonmagnetic chromium electrons.

4.5 Overall Evaluations

The ferromagnetic resonance (FMR) technique has been described to show its merit for the investigation of superstructures consisting of thin ferromagnetic multilayers separated by nonmagnetic thin layers. A brief history of electron spin resonance in ferromagnetic materials was given first; then its historical development for the investigation of bulk and thin films was summarized. Significant key contributions for experimental and theoretical developments were addressed in this chapter. Long-wavelength spin waves that excite across the opposite surface of a sufficiently thin film of the usual ferromagnetic materials can be recorded by an ESR spectrometer operating in the microwave frequency region. If the exchange interactions weaken, then the multi-peaks come close to each other, overlapping to give a single and possibly broad peak, making it almost impossible to deduce the direct exchange interaction parameter between spins. However, it was shown that an even weaker indirect exchange interaction between ultrathin ferromagnetic layers separated by a sufficiently thin nonmagnetic layer can still be deduced from FMR spectra by using a suitable FMR theory developed for magnetic superstructures.

For this, a macroscopic theory based on classical equations of motion for an average magnetization vector in an effective field originating from the gradient of magnetic free energy with respect to the magnetization vector was briefly described. In order to clearly illustrate the applicability of the theory, a well-known magnetically very soft magnetic material, namely an NiFe alloy, Py, was chosen as a prototype. As is well known, the FMR line of this material is sufficiently sharp to avoid the overlap of the multi-peak FMR lines in the external field axis. Thus, the FMR theory developed for magnetic multilayers was successfully applied on a multilayered (Py/Cr/Py) superstructure to analyze well-separated individual peaks corresponding to different spin-wave modes, although the technique is suitable to investigate any composite thin film sample.

Ultrathin Py/Cr/Py multilayer films grown on a Si (100) substrate by a magnetron sputtering technique under UHV conditions have been studied by VSM and FMR techniques. The dependence of the interlayer exchange coupling on the Cr spacer layer thickness in the interval from 0.5 to 40 Å was extensively studied. A computer program based on the theory has been used to deduce the interlayer exchange parameter for magnetically exchange coupled magnetic multilayers. The theoretical model can explain almost full details of the FMR spectra. The model is based on magnetic energy density including almost all the relevant parameters, such as saturation magnetization of individual magnetic layers, crystalline bulk anisotropy with different symmetries, magnetic surface anisotropy, field induced exchange bulk anisotropies (axial or unidirectional), crystalline surface and/or field induced directional exchange anisotropies, interlayer exchange interaction parameters, direction and magnitude of external dc magnetic field, and direction and frequency of the external magnetic excitation (microwave) field, etc. Obviously, any physical parameter of a system can be deduced by using any kind of experimental results. But in most cases, the experimental data are sensitive to very few physical parameters; that is, most of the techniques are practically blind for some parameters, and thus most of

the parameters cannot be accurately determined. Fortunately, FMR techniques are sensitive enough for most of the parameters in the magnetic free energy, and these parameters can be deduced by using a suitable theoretical model to analyze the FMR data. This has been shown in this chapter.

As seen in the figures, the deduced magnetic parameters strictly depend on both ferromagnetic and nonmagnetic spacer layer thicknesses. Actual line shapes, resonance positions, the relative intensities of the different FMR modes, and the angular dependence of these modes can be successfully simulated using only a single set of parameters such as M_s, K_p, A_{12} and α by using a developed computer algorithm. Particular parameters have a dominant effect on some particular aspects of the FMR spectra. For instance, the angular dependence of the resonance field is mainly determined by M_s and the perpendicular anisotropy. But relative positions and especially relative mode intensities are well accounted for by the interlayer exchange coupling. The damping parameter determines the line shapes. The angular dependence allows us to get more accurate parameters and sufficiently good fitting by using as many data as we need, since we have the freedom to perform the experiment for any direction of external static magnetic field. It was understood that FMR is a very sensitive and powerful technique to study magnetic properties of single and/or layered ferromagnetic thin films (even in the nanometer range) separated by a very thin nonmagetic spacer layer.

By fitting the theoretical values to the experimental data, it has been seen that the interlayer exchange coupling constant has qualitatively oscillatory behavior with respect to the nonmagnetic spacer thickness. The oscillation period was found to be about 11 Å for Py/Cr/Py trilayers. The value of this parameter reduces with increasing Cr thickness and becomes undetermined beyond 30 Å. If the magnetic properties of different layers are very close to each other, two modes comes close to each other; additionally, if the damping parameter is relatively large (broad peaks), then these two peaks overlap and give a distorted single line. In this case, the accuracy of the exchange parameter decreases.

We also emphasize that, although the model is developed to simulate FMR data of ferromagnetic thin layers exchange coupled through nonmagnetic spacer layers, it can also be used to simulate the SWR spectra of a sufficiently thick ferromagnetic monolayer. To do this, the individual layer thickness must be chosen to be atomic layers of ferromagnetic materials, the number of the layer will be taken as the total atomic layer of the ferromagnetic film, and the direct exchange coupling parameter is used as an interlayer indirect exchange coupling parameter in the model. In this case the same magnetic parameter set must be used for every layer. That is, the model can be used for a monolayer more easily than for multilayers, since one must use a different parameter set for each individual layer in the multilayer case. But, practically the number of layers will be dramatically increased for a single thick magnetic layer film having a thickness in the micrometer scale. However, we have seen that the program can calculate all the SWR spectra of thicker (micrometer-sized) films in less than an hour. The homogeneous thick film can be virtually divided into very thin subfilms to speed up the calculation as well.

Using this method we have simulated the dynamic behavior of spin waves and have made very instructive animations. Unfortunately, a hard copy of a book is nor

suitable to demonstrate this real animation. In the animation we have seen both circular and elliptical precessions of the spins in a magnetic multilayer or in a ferromagnetic thick layer for both IPG and OPG cases.

Acknowledgements This work was partly supported by the Ministry of Industry and Trade of TURKEY (Project No. 00185.STZ.2007-2), the State Planning Organization of Turkey (DPT-Project No. 2009K120730), and Marmara University (BAPKO Project No. FEN-KPS-100105-0073). We gratefully acknowledge that all samples used in this study were grown at Nanotechnology Center of Gebze Institute of Technology.

References

1. M.N. Baibich, J.M. Broto, A. Fert, F. Nguyen van Dau, F. Petroff, P. Eitenne, G. Creuzet, A. Friederich, J. Chazelas, Phys. Rev. Lett. **61**, 2472 (1988)
2. G. Binasch, P. Grünberg, F. Saurenbach, W. Zinn, Phys. Rev. B **39**, 4828 (1989)
3. T. Miyazaki, N. Tezuka, J. Magn. Magn. Mater. **139**, L231 (1995)
4. J.S. Moodera, L.R. Kinder, T.M. Wong, R. Meservey, Phys. Rev. Lett. **74**, 16 (1995)
5. P. Grünberg, R. Schreiber, Y. Pang, M.B. Brodsky, H. Sowers, Phys. Rev. Lett. **57**, 2442 (1986)
6. S.S.P. Parkin, D. Mauri, Phys. Rev. B **44**, 7131 (1991)
7. S.S.P. Parkin, N. More, K.P. Roche, Phys. Rev. Lett. **64**, 2304 (1990)
8. S.S.P. Parkin, R.F.C. Farrow, R.F. Marks, A. Cebollada, G.R. Harp, R.J. Savoy, Phys. Rev. Lett. **72**, 3718 (1994)
9. S.S.P. Parkin, R. Bhadra, K.P. Roche, Phys. Rev. Lett. **66**, 2552 (1991)
10. S.S.P. Parkin, Phys. Rev. Lett. **67**, 3598 (1991)
11. M.A. Ruderman, C. Kittel, Phys. Rev. **96**, 99 (1954)
12. T. Kasuya, Prog. Theor. Phys. **12**, 45 (1956)
13. K. Yosida, Phys. Rev. **106**, 893 (1957)
14. S. Parkin, X. Jiang, C. Kaiser, A. Panchula, K. Roche, M. Samant, Proc. IEEE **91**(5) (2003)
15. B. Heinrich, Z. Celinski, J.F. Cochran, W.B. Muir, J. Rudd, Q.M. Zhong, A.S. Arrott, K. Myrtle, J. Kirschner, Phys. Rev. Lett. **64**, 673 (1990)
16. J.J. de Vries, W.J.M. De Jonge, M.T. Jhonson, J. de Stegge, A. Reinders, J. Appl. Phys. **75**, 6440 (1994)
17. M. Belmeguenai, T. Martin, G. Woltersdorf, G. Bayreuther, V. Baltz, A.K. Suszka, B.J. Hickey, J. Phys. Condens. Matter **20**, 345206 (2008)
18. C. Kittel, Phys. Rev. **73**, 2 (1948)
19. F.T. Rado, J.R. Weertman, Phys. Rev. **94**, 1386 (1954)
20. W.S. Ament, G.T. Rado, Phys. Rev. **97**, 6 (1955)
21. C. Kittel, Phys. Rev. **110**, 1295–1297 (1958)
22. Z. Frait, H. Macfaden, Phys. Rev. **139**, A1173–A1180 (1965)
23. H. Hurdequint, J.S. Kouvel, H. Monod, J. Appl. Phys. **53**, 2239 (1982)
24. Y. Öner, B. Aktaş, F. Apaydin, E.A. Harris, Physica B **37**, 10 (1988)
25. B. Aktas, Y. Oner, E.A. Harris, Phys. Rev. B **39**, 1 (1989)
26. B. Aktas, Solid State Commun. **87**, 11 (1993)
27. P.E. Tannenwald, M.H. Seavey, Phys. Rev. **105**, 377–378 (1957)
28. P.E. Wigen, C.F. Kooi, M.R. Shanabarger, T.D. Rossing, Phys. Rev. Lett. **9**, 206–208 (1962)
29. R.F. Soohoo, Phys. Rev. **131**, 594 (1963)
30. A.M. Portis, Appl. Phys. Lett. **2**, 69–71 (1963)
31. P.E. Wigen, R.A. Turk, J.T. Yu, Phys. Rev. Lett. **11**, 420 (1975)
32. H. Puszkarski, Prog. Surf. Sci. **9**, 191–247 (1979)
33. L.J. Maksymowich, D. Sendorek, R. Zuberk, J. Magn. Magn. Mater. **37**, 177 (1983)

34. P.E. Wigen, Thin Solid Films **114**, 135 (1984)
35. B. Aktas, M. Ozdemir, Physica B **193**, 125–138 (1994)
36. B. Aktaş, B. Heinrich, G. Woltersdorf, R. Urban, L.R. Tagirov, F. Yildiz, K. Özdoğan, M. Özdemir, O. Yalçin, B.Z. Rameev, J. Appl. Phys. **102**, 013912 (2007)
37. B. Aktaş, B. Aktaş, B. Heinrich, G. Woltersdorf, R. Urban, L.R. Tagirov, F. Yildiz, K. Özdoğan, M. Özdemir, O. Yalçin, B.Z. Rameev, in *Magnetic Nanostructures*, ed. by B. Aktaş, L. Tagirov, F. Mikailov. Springer Series in Material Science (2007), pp. 167–184
38. Z. Zhang, Ferromagnetic resonance study in exchange coupled magnetic/non-magnetic multilayer structures. PhD Thesis, The Ohio State University, 1994
39. Z. Zang, L. Zhou, P.E. Wigen, K. Ounadjela, Phys. Rev. Lett. **73**, 336 (1994)
40. R. Topkaya, M. Erkovan, A. Öztürk, O. Öztürk, M. Özdemir, B. Aktaş, J. Appl. Phys. **108**, 023910 (2010)
41. M. Erkovan, S.T. Öztürk, R. Topkaya, B. Aktas, M. Özdemir, O. Öztürk, J. Appl. Phys. **110**, 023908 (2011)
42. B.Z. Rameev, A. Gupta, F. Yıldı z, L.R. Tagirov, B. Aktas, J. Magn. Magn. Mater. **300**, e526–e529 (2006)
43. T.G. Altincekic, İ. Boz, A. Baykal, S. Kazan, R. Topkaya, M.S. Toprak, J. Alloys Compd. **493**, 1–2 (2010)
44. R. Sahingoz, M. Erol, S. Yilmaz, S. Kazan, R. Topkaya, J. Optoelectron. Adv. Mater. **4**, 4 (2010)
45. A.R. Köymen, L.R. Tagirov, R.T. Gilmutdinov, C. Topacli, C. Birlikseven, H.Z. Durusoy, B. Aktaş, IEEE Trans. Magn. **34**, 846 (1998)
46. G. Kartopu, O. Yalcin, K.L. Choy, R. Topkaya, S. Kazan, B. Aktas, J. Appl. Phys. **109**, 3 (2011)
47. M. Farle, Rep. Prog. Phys. **61**, 755 (1998)
48. Z. Celinski, K.B. Urquhart, B. Heinrich, J. Magn. Magn. Mater. **166**, 6 (1997)
49. S. Dursun, R. Topkaya, N. Akdoğan, S. Alkoy, Ceram. Int. **38**, 5 (2012)
50. C. Peng, C. Dai, D. Dai, J. Appl. Phys. **72**, 4250 (1992)
51. S.M. Rezende, C. Chesman, M.A. Lucena, A. Azevedo, F.M. de Aguiar, S.S.P. Parkin, J. Appl. Phys. **84**, 958 (1998)
52. S. Tanuma, C.S. Powell, D.R. Penn, Surf. Sci. **192**, L849 (1987)
53. A. Fert, A. Barthelemy, P. Lequien, R. Loloee, D.K. Lottis, D.H. Mosca, F. Petroff, W.P. Pratt, P.A. Schroeder, J. Magn. Magn. Mater. **104**, 1712 (1992)

Chapter 5
Characterization of Antiferromagnetic/Ferromagnetic Perovskite Oxide Superlattices

Y. Takamura

Abstract Interfacial phenomena in perovskite oxide superlattices have the potential to provide unique functional properties for a diverse range of applications, including sensing, energy conversion, and information technology. The example of antiferromagnetic/ferromagnetic superlattices composed of $La_{0.7}Sr_{0.3}FeO_3$ (LSFO) and $La_{0.7}Sr_{0.3}MnO_3$ (LSMO) sublayers is discussed in detail. In this system, the antiferromagnetic order parameter in LSFO and the ferromagnetic order parameter in LSMO display dissimilar dependences on sublayer thickness and temperature due to the competition between different magnetic interactions. For a small range of sublayer thicknesses, a robust spin-flop coupling is observed such that the alignment of the LSMO magnetization with a magnetic field leads to the reorientation of the Fe moments in the LSFO layer to maintain a perpendicular orientation between the Fe and Mn moments.

5.1 Introduction

Perovskite oxide superlattices consisting of alternating sublayers, each with their own order parameter, exist as promising candidate materials for stimulus-sensitive applications such as sensing, energy conversion, and information technology [1]. In bulk, the functional properties of these materials, which include ferromagnetism, ferroelectricity, and superconductivity, are well characterized. However, in recent years, thin film growth techniques have matured to the point that it is possible to deposit superlattice structures via a layer-by-layer growth mode with unit cell precision of the sublayer thicknesses [2–4]. These advancements have led to a few remarkable examples which have shown the appearance of an additional order parameter at interfaces, despite the fact that it does not exist in the constituent materials. A particularly noteworthy example is the observation that a 2D electron gas with metallic conductivity exists at the interface between the two nonmagnetic insulators

Y. Takamura (✉)
Department of Chemical Engineering and Materials Science, University of California at Davis, Davis, CA 95616, USA
e-mail: ytakamura@ucdavis.edu

B. Aktaş, F. Mikailzade (eds.), *Nanostructured Materials for Magnetoelectronics*, Springer Series in Materials Science 175, DOI 10.1007/978-3-642-34958-4_5,

$SrTiO_3$ and $LaAlO_3$ [5]. Since the initial report, superconductivity and ferromagnetism have also been reported at those interfaces [6–8]. In many cases, the reasons for these unexpected interfacial properties remain highly controversial, and a number of different factors have been shown to play an important role. These factors include structural effects (lattice mismatch between the individual sublayers and the underlying substrate, rotations and tilts of the BO_6 octahedra which lie at the heart of the perovskite structure) [9–11], chemical intermixing at the interfaces [12], magnetic interactions (exchange coupling) [13, 14], electronic reconstruction [15–17], and finite size effects [18]. Therefore, a strong need exists to develop sophisticated characterization methods to probe the interfacial properties and their impact on the global properties of the superlattices, as well as to develop physical models which take into account all these interactions in order to predict the properties of nanoscale thin films and superlattices.

While numerous examples have been reported in the literature, the following article will highlight our results for superlattice structures consisting of the ferromagnetic (FM) metal $La_{0.7}Sr_{0.3}MnO_3$ (LSMO) and the antiferromagnetic (AFM) insulator, $La_{0.7}Sr_{0.3}FeO_3$ (LSFO). This system permits us to explore the exchange interactions occurring at the AFM/FM interfaces in an all-perovskite oxide system. The differing B site element allows us to independently probe the AFM and FM sublayers using soft X-ray magnetic spectroscopy by tuning to the Fe and Mn absorption edges, respectively. For this reason, this system represents an ideal model system for investigating the interfacial coupling between AFM and FM perovskite layers. This chapter is organized in the following manner. Section 5.2 discusses the background of the perovskite structured oxides and in particular the manganites and ferrites which compose the superlattices discussed. Section 5.3 provides a brief review of exchange interactions while Sect. 5.4 gives an overview of synchrotron-radiation-based characterization techniques which provide unique capabilities to characterize the functional properties of the superlattices. Finally, Sect. 5.5 highlights the functional properties of the LSFO/LSMO superlattices.

5.2 Perovskite Oxides

Many of the perovskite oxides with the chemical formula ABO_3 belong to the category of strongly correlated electron systems which are characterized by strong interactions between the charge, orbital, lattice, and spin degrees of freedom. This fact leads to many fascinating properties, including ferromagnetism, ferroelectricity, and superconductivity, which can be readily controlled with external stimuli such as applied electric and magnetic fields, external pressure, and temperature. The perovskite structure consists of an array of corner-sharing BO_6 octahedra at the body centered positions which form a network of B–O–B bonds, and the A cations at the corners with 12-fold coordination. The wide variety of physical properties associated with the perovskite structure depends on a number of factors, including:

- the possibility of various doping schemes on the A and B sites,
- the combination of valence states as long as overall charge neutrality is maintained (e.g., $A^{4+}B^{2+}$, $A^{3+}B^{3+}$, $A^{2+}B^{4+}$, and $A^{1+}B^{5+}$),
- the structure's ability to accommodate a large concentration of oxygen and cation vacancies [19],
- Jahn–Teller distortions which lead to anisotropic bond lengths within the octahedra [20],
- the relative size difference between the A and B cations, causing tilts and rotations of the octahedra relative to one another [19, 21].

The stability of the perovskite phase can be described by the Goldschmidt tolerance factor [22]:

$$t = \frac{\langle \mathrm{A} - \mathrm{O} \rangle}{\sqrt{2}\langle \mathrm{B} - \mathrm{O} \rangle} = \frac{R_\mathrm{A} - R_\mathrm{O}}{\sqrt{2}(R_\mathrm{B} - R_\mathrm{O})} \tag{5.1}$$

where the mean $\langle \mathrm{A} - \mathrm{O} \rangle$ and $\langle \mathrm{B} - \mathrm{O} \rangle$ bond lengths are obtained from the tables of ionic radii (R_A, R_O, R_B) [23]. The perovskite phase is reported to be stable for $0.78 < t < 1.05$ [21, 24], with $t = 1$ corresponding to the ideal cubic perovskite phase with space group $Pm3m$. As t decreases below unity, other perovskite structures are possible, including the rhombohedral $R\bar{3}c$ symmetry and the orthorhombic $Pbnm$ symmetry. These structures are formed through cooperative rotations of the BO_6 octahedra along the cubic [111] and [110] axes, respectively, which lead to a decrease in the B–O–B bond angles, thereby varying the strength of the B–O–B interactions along different crystallographic directions [19]. In contrast, for $t > 1$, the ABO_3 compound takes on the hexagonal structure.

External pressure and epitaxial strain in thin films can cause changes to the symmetry of the lattice by changing the bond lengths, bond angles, and the magnitude of the octahedral tilts and rotations [10, 11, 25–32]. For epitaxial thin films, the choice of the substrate can be used as a control parameter to stabilize a particular structure which differs from the thermodynamically stable bulk phase. These new structures may involve tetragonal distortions of the BO_6 octahedra [11, 28–30] and/or changes to the inherent tilts/rotation patterns of the perovskite structure [10, 31, 32], and they are theoretically predicted to dramatically impact the functional properties of the materials [33]. For example, Salvador et al. demonstrated that normally hexagonal $YMnO_3$ could be stabilized into the orthorhombic structure by growing epitaxial thin films by pulsed laser deposition on (110)-oriented $NdGaO_3$ substrates with orthorhombic symmetry [32]. In another example, epitaxial thin films of $LaCoO_3$ have been shown to possess a ferromagnetic ordering temperature, $T_\mathrm{C} \sim 85$ K [34–36] despite the fact that no FM behavior is observed down to 5 K in polycrystalline thin films or bulk samples. Two theoretical models have been developed which either ascribe the unexpected magnetization to biaxial strain alone [37, 38] or with the contribution of octahedral rotations [33].

5.2.1 Manganites and Ferrites

The family of doped rare-earth manganites $R_{1-x}A_xMnO_3$, where R = trivalent lanthanide and A = divalent alkaline earth, has received considerable interest from a technological as well as a fundamental scientific curiosity standpoint [21, 39]. For example, for the Sr-doped manganites, $La_{1-x}Sr_xMnO_3$, the temperature-composition phase diagram shows that a number of different structures with different electrical and magnetic properties are possible. These phases include the FM metal, FM insulator, paramagnetic (PM) metal, AFM insulator, and charge ordered insulator states. In most cases, these changes to the electrical and magnetic properties are accompanied by changes to the structure between the rhombohedral, orthorhombic, tetragonal, and hexagonal perovskite structures [40]. In particular, with a Sr doping level $x = 0.30$, $La_{0.7}Sr_{0.3}MnO_3$ (LSMO) is considered as a promising electrode material for information technology applications, since it exhibits colossal magnetoresistance (i.e., a large change in resistance upon the application of a magnetic field) and a high degree of spin polarization. In addition, the magnetic and electrical properties are closely linked with coincident FM/PM and metal/insulator transitions which occur at the Curie temperature, $T_C \sim 360$ K. These properties are mediated by the Mn^{3+}–O^{2-}–Mn^{4+} double exchange mechanism with Jahn-Teller distortions also playing a role [41–44]. At room temperature, the structure is rhombohedral with lattice constant $a = 5.471$ Å and $\alpha = 60.43°$ [45], though it is often assumed to have a pseudocubic structure with $a = 3.87$ Å. The replacement of Mn with Fe on the B site of the perovskite structure leads to a G-type AFM insulator state. The AFM properties are mediated by the Fe^{3+}–O^{2-}–Fe^{3+} superexchange interaction, and the AFM spin axis, $\boldsymbol{M}_{Fe}$, lies along the crystallographic $\boldsymbol{a}$-axis [46]. With increasing Sr doping level, the resistivity, Néel temperature, T_N, and the anisotropy of $La_{1-x}Sr_xFeO_3$decrease, while the crystal structure transitions from orthorhombic to rhombohedral and finally to the cubic phase. For $x = 0$ ($LaFeO_3$, LFO), $T_N \sim 740$ K and it drops to ~360 K for $x = 0.3$ ($La_{0.7}Sr_{0.3}FeO_3$, LSFO) [47, 48]. In bulk, LSFO has been reported to be a mixture of the orthorhombic ($a = 5.501$ Å, $b = 5.544$ Å, and $c = 7.846$ Å) [49] and rhombohedral phases [50].

5.3 Exchange Interactions

Exchange interactions occur at the interface between AFM and FM layers and are widely used commercially in applications such as magnetic recording read head sensors. In many all-metal or metal/oxide systems, the exchange interactions manifest themselves in the form of exchange bias [13, 14]. Upon field cooling through the Néel temperature of the AFM material, the coercive field is observed to increase and the hysteresis loops shift horizontally along the field axis. Both positive and negative shifts have been reported. The field cooling creates a locked-in state of the AFM spins which “bias” the FM spins via the exchange coupling at the interface. With a large enough shift, the FM is pinned so that only a single stable magnetic

state exists around $\boldsymbol{H} = 0$ T, and it can serve effectively as a reference FM electrode. Various models attempt to explain the magnitude and sign of exchange bias; a number of different factors have been shown to play an important role, including uncompensated spins in the AFM material, defects at the interface, spin-canted systems, and/or the FM and/or AFM domain patterns. To date however, none of these models can universally explain all the experimental data.

The situation differs at a smooth (001)-interface of a G-type AFM material with an FM material in the absence of any uncompensated spins in the AFM. In a G-type AFM material, all the nearest neighbor atoms/ions have antiparallel spin alignment such that the (001)-surface is characterized by an equal number of positive and negative spin interactions. The resulting frustrated exchange interaction, termed spin–flop coupling, has been predicted from a microscopic Heisenberg model [51–53]. In such a system, the moments in the FM layer and the AFM spin axis lower their energy when they are oriented *perpendicular* to one another in the plane of the interface. This type of spin-flop coupling has been observed experimentally in such systems as Fe_3O_4/CoO superlattices using neutron diffraction [54] and in permalloy/CoO interfaces from the shapes of hysteresis loops under different field cooling conditions [55].

However, in the case of an orthorhombic perovskite oxide such as LSFO which displays G-type antiferromagnetism, the tilting of the FeO_6 octahedra have been predicted to lead to staggered Dzyaloshinskii–Moriya interactions between nearest neighbors, thereby providing a bias field and exchange bias [56, 57]. Therefore, the nature of the exchange interactions in an all-perovskite oxide system remains unclear.

5.4 Characterization Techniques

In order to probe the global and interfacial properties of the superlattice structures, a number of sophisticated characterization techniques with sufficient depth and lateral resolution must be utilized. In the following section, we provide a brief introduction to two synchrotron-radiation-based techniques, namely soft X-ray magnetic spectroscopy and photoemission electron microscopy, that have been used to study the LSFO/LSMO superlattices. The reader is referred to more comprehensive reviews of these techniques for further details, including Refs. [58–62].

5.4.1 Soft X-Ray Magnetic Spectroscopy

Soft X-ray magnetic spectroscopy refers to the study of AFM and FM properties of materials using X-ray magnetic linear/circular dichroism (XMLD/XMCD), re-

spectively. The absorption of X-rays can excite core electrons into empty valence states above the Fermi energy of the material, thereby providing information on the electronic structure of the material. Importantly for the study of magnetism, the soft X-ray regime (50–2000 eV) covers the $2p$ core levels (L edges) of the $3d$ transition metals and the $3d$ core levels (M edges) of the rare earths, thus probing the magnetic properties of the $3d$ and $4f$ valence shells, respectively. With these techniques, element specificity is obtained by tuning the photon energy to the absorption edges of the elements, and the depth resolution is limited by the electron escape depth of the secondary electrons in the material (the top ∼2–10 nm depending on the material) for measurements of total electron yield. In a dichroism experiment, we are concerned with the difference between two X-ray absorption spectra taken under different conditions. XMCD is used to probe the ferromagnetic properties of materials. It results from the difference in the X-ray absorption spectra depending on the relative orientation of the magnetization and the helicity of circularly polarized X-rays. Spin-up photoelectrons from the core level can only be excited to an empty spin-up state in the valence shell, and the intensity of the transition is proportional to the number of empty valence states of a given spin. Since right circularly polarized X-rays transfer the opposite momentum to an electron as compared to left circularly polarized X-rays, the dichroism is a measure of the spin splitting of the valence band and therefore a probe of the magnetism. The magnitude of the dichroism follows a cosine dependence on the angle between the X-ray helicity and the magnetization, therefore showing a maximum effect between parallel and antiparallel orientations. From the analysis of the XMCD spectra, the elemental moments, including the separation of the spin and orbital contributions to the total elemental moment, can be determined [60, 61].

In contrast, XMLD measures the dichroism resulting from an asymmetry in the material relative to the $\boldsymbol{E}$ vector of the linearly polarized X-rays. Sources of asymmetry may result from crystallographic effects, such as crystal fields along different crystallographic directions [63, 64], orbital occupancy [65] or magnetic effects such as the relative orientation of the AFM spin axis, $\boldsymbol{M}_{\mathrm{Fe}}$. The crystallographic effects can be minimized by collecting the X-ray absorption spectra along the same family of directions, or if the crystallographic effects are known, they can be accounted for in the data analysis. For the magnetic effects, the polarization dependence of the intensity of the dichroism at the absorption edges can be expressed as:

$$I(\alpha) = a + b\left(3\cos^2\alpha - 1\right)\left\langle M^2\right\rangle_T \tag{5.2}$$

where a and b are constants, α is the angle between $\boldsymbol{E}$ and $\boldsymbol{M}_{\mathrm{Fe}}$, and $\langle M^2\rangle_T$ is the square of the AFM moment [66]. In this case, the maximum XMLD signal results when comparing parallel and perpendicular orientations between $\boldsymbol{E}$ and $\boldsymbol{M}_{\mathrm{Fe}}$. The XMLD effect serves as one of the few methods capable of probing the AFM properties of thin films. Other traditional techniques such as neutron diffraction require bulk materials or films on the order of >1 micrometer in thickness.

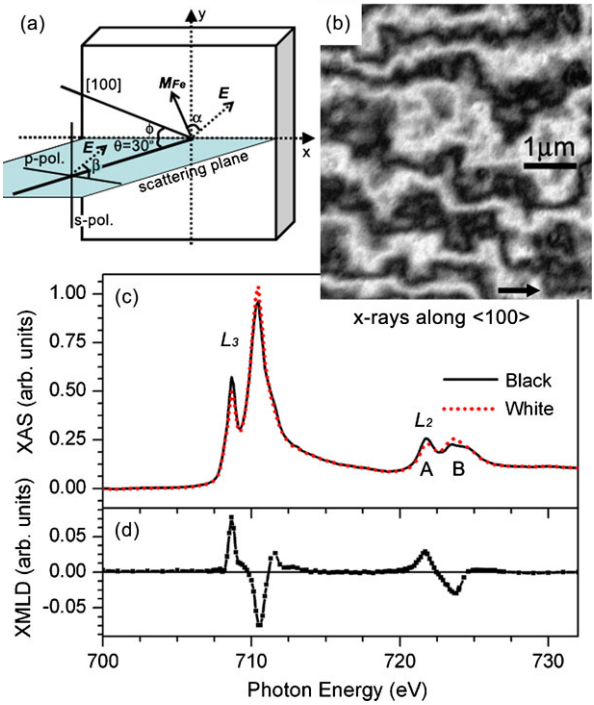

Fig. 5.1 (**a**) Schematic showing the geometry of the PEEM-3 microscope; (**b**) domain image of [12 × 12]5 superlattice taken with the ***E*** vector oriented in plane ($\beta = 90°$); (**c**) local X-ray absorption spectra taken from the white (*red dotted*) and black (*solid black*) domains; (**d**) the calculated XMLD spectra

5.4.2 Photoemission Electron Microscopy (PEEM)

Photoemission electron microscopy is based on the same fundamental principles as the soft X-ray magnetic spectroscopy measurements described above; however, an electron microscope is used to spatially capture the location from which the secondary electrons emanate [62]. A large positive sample voltage (15–20 KV) is typically applied to aid in the collection of the secondary electrons. In this way, images of the FM and AFM domain structure can be obtained with high spatial resolution, elemental and chemical specificity, and with 2–10 nm surface sensitivity. Figure 5.1(a) shows a schematic of the sample geometry of the PEEM-3 microscope located at Beamline 11.0.1 at the Advanced Light Source. The X-rays are incident upon the sample at a 30° angle relative to the sample surface and along the x-axis. For FM domains, the domain images correspond to the ratio of images taken at the photon energy corresponding to the peak in the XMCD effect with right and left circularly polarized X-rays. Because the topography and work function differences between features remain constant with the two polarizations, the divided images represent the contribution arising only from the FM domains. The contrast within each domain is determined by the relative orientation of the magnetization with the X-ray propagation direction following a cosine dependence with white/black contrast corresponding to parallel/antiparallel orientation, and gray contrast corresponding to a perpendicular orientation.

For AFM domains, the domain images correspond to the ratio of images taken with fixed orientation of the X-ray $\boldsymbol{E}$ vector at two photon energies with the opposite sign of the XMLD effect. For example, Figs. 5.1(c) and (d) show the X-ray absorption and calculated XMLD spectra taken at the Fe $L_{3,2}$ absorption edges for two different kinds of AFM domains in a LSFO/LSMO superlattice. At both the L_3 and L_2 edges, positive/negative features exist in the XMLD spectra. While the intensity of the XMLD at the L_3 edge exceeds that of the L_2 edge, the images were acquired at peaks labeled A and B of the L_2 edge since intensity of the X-ray absorption spectra are more similar, and therefore the topographical features divide out more readily in the ratio image. Figure 5.1(b) shows the resulting domain images with white/black regions correspond to domains where $\boldsymbol{M}_{\mathrm{Fe}}$ lies parallel/perpendicular to the X-ray $\boldsymbol{E}$ vector (vertical in this image). A full determination of the direction of $\boldsymbol{M}_{\mathrm{Fe}}$ can be carried out by capturing domain images as the linear polarization of the X-rays, $\boldsymbol{E}$, is rotated between p-polarization (polarized parallel to the scattering plane) and s-polarization (polarized perpendicular to the scattering plane). The rotation angle of $\boldsymbol{E}$, denoted as β, is measured relative to p-polarization such that, for $\beta = 0°$, $\boldsymbol{E}$ cants out of plane, making a 60° angle relative to the sample surface, while for $\beta = 90°$, $\boldsymbol{E}$ lies completely in the plane of the sample along the y-axis. The angle between the scattering plane and the [100] direction of the substrate is denoted by the angle, ϕ.

5.5 Characterization of LSFO/LSMO Superlattices

5.5.1 Growth of Superlattice Structures

Epitaxial LSMO and LSFO films as well as LSFO/LSMO superlattices were grown on (001)-oriented single crystal $SrTiO_3$ (STO) substrates by pulsed laser deposition (PLD). For comparison, an LSFO/LSMO solid solution film (i.e., $La_{0.7}Sr_{0.3}Mn_{0.5}Fe_{0.5}O_3$) with the same overall composition of the superlattices but without any interfaces was also deposited. A KrF laser (248 nm) was used at a frequency of 10 Hz and a fluence of ∼1.2 J/cm^2, while the substrate temperature was held at 700 °C and the oxygen pressure at 200 mTorr. In situ reflection high energy electron diffraction was used to monitor the growth rate and to verify the layer-by-layer growth mode. After deposition, the superlattices were cooled slowly to room temperature in an oxygen pressure of ∼300 Torr to ensure the proper oxygenation of the films. The notation for the superlattices consists of the following: [*# unit cells LSFO* × *# unit cells LSMO*] # *of repeats*. In all cases, the LSMO layer was grown first, so that the LSFO layer lies at the surface of the superlattice. The individual sublayer thicknesses were varied between 3 and 18 unit cells, and the total film thickness was between 36–50 nm. The uniform doping level across both layers prevents Sr diffusion between layers.

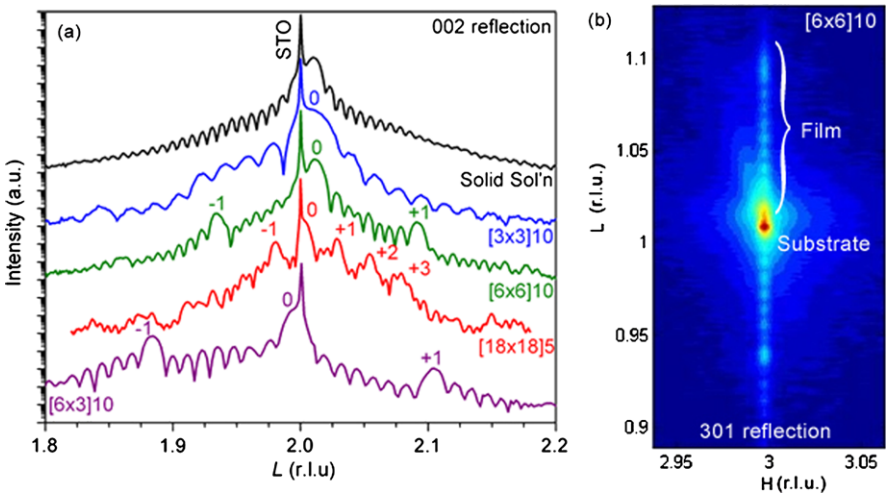

Fig. 5.2 (**a**) L scans around the (002) peak for the LSFO/LSMO superlattices and (**b**) RSM around the (301) peak for the [6 × 6]10 superlattice

5.5.2 Structural Characterization

The structural properties of the films were measured by X-ray reflectivity (XRR) and high-resolution X-ray diffraction using a Bruker D8 Discover four-circle diffractometer and beamlines 2-1 and 7-2 at the Stanford Synchrotron Radiation Lightsource (SSRL). In order to accurately characterize the individual layer thicknesses and interface roughness in these superlattices where the layers have similar density but differ chemically, resonant XRR spectra were also acquired [67]. These measurements were performed by tuning the X-ray energy to the absorption edges of the constituent elements in each layer (Mn and Fe in this case). This technique takes advantage of the fact that the real and imaginary parts of the dispersion correction factors change abruptly at the absorption edges. Satellite peaks and thickness fringes were observed in the XRR spectra and l scans of the out-of-plane 002 reflection (Fig. 5.2(a)), attesting to the smooth interfaces and permitting us to accurately confirm the periodicity of the superlattice structures. Reciprocal space maps (RSMs) around the 103, 301, 331, and 303 reflections demonstrate that the superlattices were fully strained to the underlying cubic STO substrate with an in-plane lattice parameter of $a = 3.905$ Å. Figure 5.2(b) shows an example of the RSM around the 301 reflection for the [6 × 6]10 superlattice. The features from the film and high intensity peak from the substrate appear at the same H value. The orthorhombic LSFO unit cell may be oriented with the ***c*** axis lying perpendicular to the film surface along the [001] substrate direction and with the ***a*** and ***b*** axes lying in-plane along the ⟨110⟩ substrate directions and experiencing in-plane lattice mismatch of $-/+0.39$ %, respectively. A slightly larger in-plane lattice mismatch of 0.46 % occurs if the film grows with the ***c*** axis lying along the two in-plane ⟨100⟩ substrate directions and

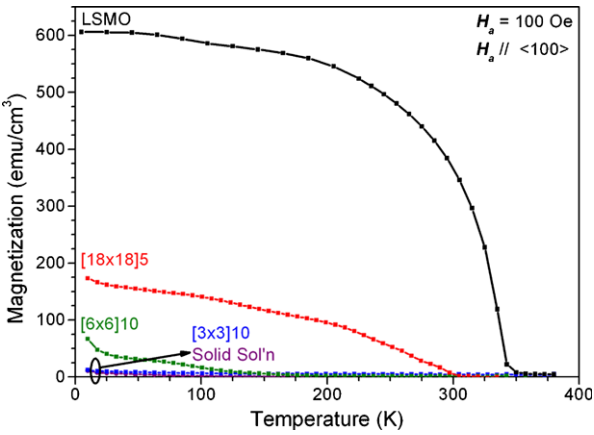

Fig. 5.3 Magnetization as a function of temperature for the superlattices, solid solution, and LSMO thin films with $\boldsymbol{H} = 0.01$ T applied along the ⟨100⟩ substrate direction [67]

the ***a*** and ***b*** axes oriented at 45° to the substrate surface, along the ⟨011⟩ substrate directions. Within the accuracy of our X-ray diffraction measurements, we cannot distinguish between these two orientations; however, both orientations consist of vertical stacks of the TiO_6, MnO_6, and FeO_6 octahedra which form the basis of the perovskite structure.

5.5.3 Bulk Magnetization Data

The bulk magnetization was measured using a Quantum Design Magnetic Properties Measurement System (superconducting quantum interference device, SQUID, magnetometer) with the magnetic field applied in the plane of the film, either along the ⟨100⟩ or the ⟨110⟩ substrate direction [67]. Figure 5.3 compares the temperature dependence of the magnetization for an LSMO and solid solution film, as well as LSFO/LSMO superlattices with $\boldsymbol{H} = 0.01$ T. The magnetization was normalized to the volume of the LSMO sublayers only. The LSMO film exhibits a bulk-like $T_C \sim 340$ K and saturation magnetization, $M_S \sim 3.8$ μ_B/Mn at 10 K. At the opposite extreme, no appreciable magnetization is observed for the solid solution film in agreement with results for Fe-doped manganites [68, 69]. With decreasing sublayer thickness, the values of T_C and M_S decrease, reaching 300 K and 150–200 K, and 1.47 μ_B/Mn and 0.57 μ_B/Mn for the [18 × 18]5 and [6 × 6]10 superlattices, respectively. Finally, the magnetization of the [3 × 3]10 superlattice approaches that of the solid solution film. This trend of reduced T_C and M_S agrees with reports for ultrathin LSMO films and LSMO/STO superlattices with LSMO sublayer thicknesses below 20 unit cells [70–75]. Hysteresis loops show that the easy magnetization direction for the [18 × 18]5 superlattice lies along the in-plane ⟨110⟩ direction, in agreement with published results for LSMO films grown on (001)-oriented STO substrates as a consequence of the 0.64 % tensile strain [76]. For the [6 × 6]10 superlattice, a slightly higher remnant magnetization is observed along the ⟨100⟩ direction over

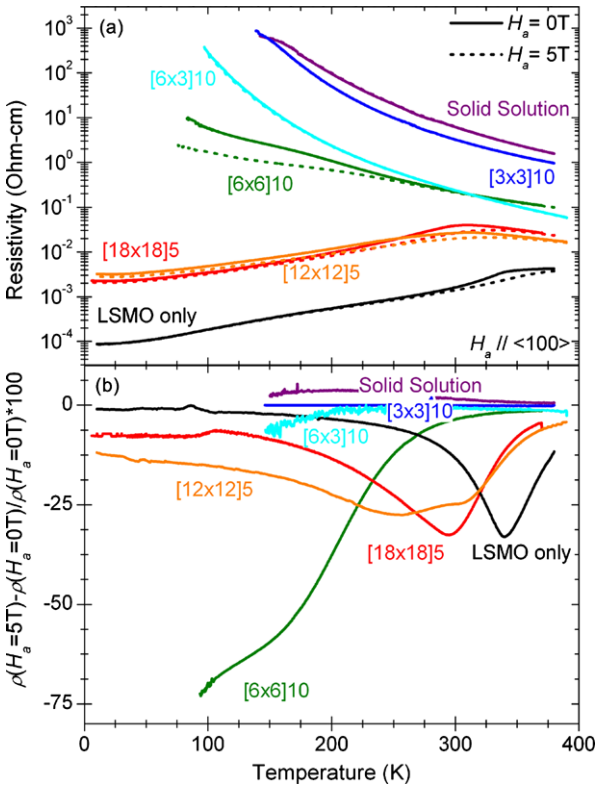

Fig. 5.4 (**a**) Resistivity and (**b**) magnetoresistance, *MR*, as a function of temperature for the LSFO/LSMO superlattices, solid solution film, and LSMO film [67]

the ⟨110⟩ direction, indicating that the magnetic easy axis has changed to the ⟨100⟩ direction. The coercive field for the [18 × 18]5 superlattice at 10 K is 0.048 T, only slightly higher than that of an LSMO film grown on an STO substrate. However, the coercive field increases dramatically to 0.17 T for the [6 × 6]10 superlattice, indicating that at small sublayer thicknesses, magnetic reversal of the LSMO sublayer is influenced by the exchange interaction with the adjacent LSFO sublayers, as discussed below.

5.5.4 Magnetotransport Properties

Magnetotransport properties as a function of temperature (Fig. 5.4) were measured using the van der Pauw geometry with $\boldsymbol{H} = 0$ and 5 T applied along the in-plane ⟨100⟩ direction [67]. The resistivity, ρ, of each superlattice was calculated from its resistance using the simplified assumption that the entire film rather than only the lower resistivity LSMO sublayers contribute to conduction. Mirroring the magnetization data, the resistivity behavior of the superlattices approaches that of the solid solution film for small sublayer thicknesses. At T_C, a well-defined metal-to-insulator transition occurs in the LSMO film as well as the [18 × 18]5 and [12 × 12]5

superlattices, and it is accompanied by a negative peak in the magnetoresistance, $MR = [\rho(H = -5\ \mathrm{T}) - \rho(H = 0\ \mathrm{T})]/\rho(H = 0\ \mathrm{T}) \times 100$. Compared to the LSMO film, the T_C for the $[18 \times 18]5$ superlattice is depressed by 40 K and the resistivity is increased by an order of magnitude across the entire temperature range. In contrast, the behavior of the superlattices with the thinnest sublayers and the solid solution film differs fundamentally. These samples display insulating behavior across the entire temperature range, no significant magnetization, and thus no *MR*. At intermediate period, the $[6 \times 6]10$ superlattice exhibits insulating characteristics with a large, negative *MR* which monotonically increases in magnitude with decreasing temperature instead of showing a peaked behavior. A similar *MR* behavior has been reported in ultrathin (approximately four unit cells) LSMO films [77] as well as LSMO films under large tensile strain [28, 29]. Alternatively, this large negative *MR* may be related to the exchange interactions between the adjacent LSFO and LSMO sublayers. Despite the fact that these superlattices have the same overall chemical composition, the resistivity ranges over several orders of magnitude, and the temperature behavior changes dramatically depending on the individual sublayer thicknesses.

5.5.5 Soft X-Ray Magnetic Spectroscopy

The soft X-ray magnetic spectroscopy measurements were taken at Beamline 4.0.2 at the Advanced Light Source using the vector magnet end station [78]. The octopole magnet incorporated in this end station provides us with the capability to apply a magnetic field (up to 0.9 T) along any arbitrary direction relative to the incoming X-ray beam, and to vary the temperature from 10–450 K. In addition, an elliptically polarizing undulator provides a high degree of right/left circularly polarized X-rays and linearly polarized X-rays with the $\boldsymbol{E}$ vector oriented at arbitrary angles.

5.5.5.1 X-Ray Absorption Spectroscopy

In order to compare the electronic structure of the superlattices, X-ray absorption spectra were collected for the Mn and Fe $L_{3,2}$ absorption edges. As shown in Fig. 5.5(a), the Mn L_2 edge remains fairly unchanged for all the superlattices; however, the L_3 main peak shifts slightly to higher photon energy for the solid solution film and the $[3 \times 3]10$ superlattice [67]. In addition, a feature about 2 eV below the main L_3 peak develops in the superlattices with the smaller sublayer thicknesses. These signatures have been ascribed to an increased concentration of Mn^{4+} ions [79, 80]. Due to the uniform Sr doping level throughout the superlattice structure, the change in the Mn^{3+}/Mn^{4+} ratio is not expected to be related to the A site chemical doping effects. Alternatively, a charge transfer involving an electron transferring

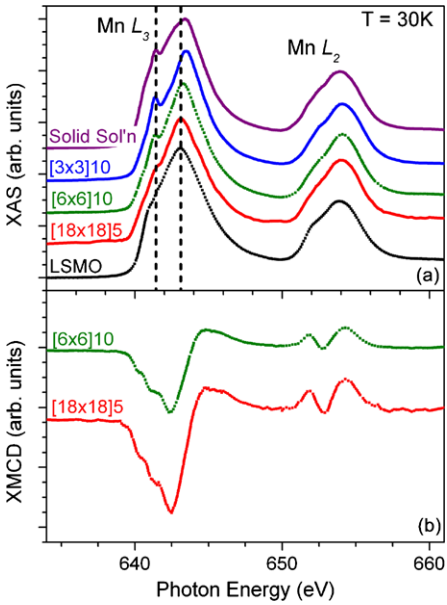

Fig. 5.5 (**a**) Mn X-ray absorption spectra and (**b**) Mn XMCD spectra for the LSMO and solid solution films as well as the LSFO/LSMO superlattices. A feature appears 2 eV below the main Mn L_3 peak for smaller sublayer thicknesses and in the solid solution film [67]

from the LSMO sublayers to the LSFO sublayers ($Mn^{3+} \rightarrow Mn^{4+}$) across the interface as proposed by Kumigashira and co-workers [17] could explain the change. The ground state of LSFO for small Sr doping ($x < 0.5$) is the Fe^{3+}-ligand hole state. Therefore, the electrons involved in the charge transfer go to states of primarily oxygen character. In accordance, no significant difference is observed in the Fe $L_{3,2}$ X-ray absorption spectra for any of the superlattices investigated. The characteristic length scales for this type of charge transfer effects reported in other perovskite systems (e.g., $SrTiO_3/LaTiO_3$ [15] and $LaMnO_3/SrMnO_3$ [16]) are on the order of a few unit cells, consistent with our observations. Because the functional properties of the perovskite oxides are strongly dependent on the valence state of the B site ions, these results suggest that one should expect a comparatively larger change in the FM properties of the LSMO sublayers than the AFM properties of the LSFO sublayers.

5.5.5.2 X-Ray Magnetic Circular Dichroism (XMCD)

The XMCD spectra were acquired with the X-rays incident upon the sample at a grazing angle of 30° relative to the sample surface with $\boldsymbol{H} = +/-0.27$ T parallel to the X-ray beam. No XMCD signal was detected at the Fe $L_{3,2}$ edge, indicating that the entire magnetic signal measured in bulk magnetometry is associated with the LSMO sublayers and that no uncompensated spins exist within the LSFO sublayers or at the LSFO/LSMO interfaces. The spectral features of the Mn $L_{3,2}$ edge XMCD signal (Fig. 5.5(b)) resembles that of LSMO single layers, and the magnitude exhibits the same sublayer thickness dependence as the bulk magnetometry,

i.e., decreasing magnetization with decreasing sublayer thickness [67]. This result demonstrates the uniformity of the magnetic properties throughout the superlattice structure, allowing us to conclude that the near-surface X-ray absorption spectrum is representative of the entire superlattice.

5.5.5.3 X-Ray Magnetic Linear Dichroism (XMLD)

The AFM properties of the LSFO/LSMO superlattices were probed using XMLD spectroscopy. The Fe $L_{3,2}$ edge XMLD spectra were obtained at 30° grazing incidence with $\boldsymbol{H} = 0$ T, and the X-ray polarization vector, $\boldsymbol{E}$, was applied either in-plane (along the [010] substrate direction) or at 60° with respect to the sample surface (referred to as the out-of-plane [001] substrate direction). Figure 5.6(a) plots the X-ray absorption spectra for the $[6 \times 6]10$ superlattice and the solid solution film for $\boldsymbol{E}//[001]$ (black curve) and $\boldsymbol{E}//[010]$ (red curve). The dichroism (Fig. 5.6(b)) was calculated as $\boldsymbol{E}//[010] - \boldsymbol{E}//[001]$ [67]. These spectra provide information on the orientation of $\boldsymbol{M}_{\mathrm{Fe}}$ with respect to the sample plane.

For the superlattices at temperatures below 100 K, the Fe XMLD spectra are nearly identical, whereas the sign of the spectra is reserved for the solid solution and LSFO films. This result suggests a common orientation of the AFM spin axis for all the superlattices, which then differs for the single layer films. To interpret these spectra, we first note that the Fe^{3+} ions in LSFO assume an octahedral coordination with the surrounding O^{2-} ions, similar to the environment for the Fe^{3+} ions on the B site of the spinel Fe_3O_4. Therefore, using the analysis of the XMLD spectra described by Arenholz et al. [81], we determine that the sign and shape of the curves is consistent with an in-plane alignment of $\boldsymbol{M}_{\mathrm{Fe}}$ in the superlattices, and an out-of-plane canting for the solid solution and LSFO films. The in-plane confinement in the superlattices is believed to occur due to the presence of a high density of horizontal interfaces. The out-of-plane canting for the single layer films is in agreement with other reports for $LaFeO_3$ films in which the canting angle varied from 20 to 45° [82, 83] and will be explored further in the following sections. These films are considered the "end member" reference points, and they allow us to conclude that the AFM properties of the superlattices do not approach these end members as a function of the sublayer thickness, unlike the case reported for the FM properties in the same superlattices. The LSFO film and the superlattices with the larger sublayer thickness display robust AFM properties with T_{N} which exceed room temperature. For the $[3 \times 3]10$ superlattice and solid solution film, the AFM signature disappears between 150 K and room temperature. Even without a full investigation of T_{N} for these samples, we clearly observe a gradual trend of decreasing T_{N} with decreasing sublayer thickness. In comparison, the observed decrease in the FM properties of the LSMO layers occurs more rapidly, such that at three unit cell thickness, the LSMO sublayers are paramagnetic while the LSFO sublayers retain their AFM properties. Comparatively fewer studies have been performed on the thickness dependence of AFM properties of thin films, particularly for the perovskite

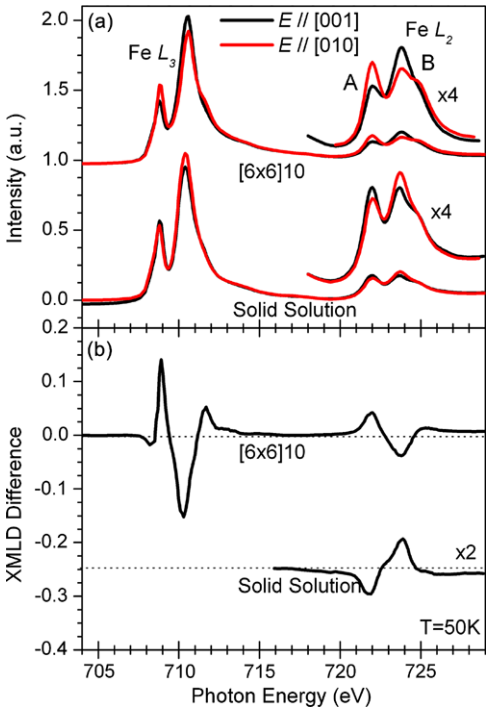

Fig. 5.6 (**a**) X-ray absorption spectra for the [6 × 6]10 superlattice and solid solution film with $\boldsymbol{E}//[001]$ (*black curve*) and $\boldsymbol{E}//[010]$ (*red curve*), and (**b**) XMLD spectra defined as $\boldsymbol{E}//[010] - \boldsymbol{E}//[001]$. Similar spectra were obtained for the superlattices with different repeat units, while the spectra for the LSFO film resembled that of the solid solution film. Due to experimental artifacts with insulating films, only the Fe L_2 edge is shown for the solid solution film [67]

oxides. The T_N of NiO thin films have been shown to decrease rapidly for thicknesses between five and ten unit cells [66]. Therefore, the AFM properties of these superlattices exhibit a fundamentally different sublayer thickness dependence than their FM counterparts.

The soft X-ray magnetic spectroscopy measurements suggest that the interfacially induced valence changes cause the different trends with respect to sublayer thickness observed for the AFM and FM properties. This charge transfer effectively pushes the LSMO sublayers towards the case of higher Sr doping (yielding an FM metal with decrease T_C). Therefore, with the decrease in long-range (dipole) interactions due to finite size effects, rapid decrease of T_C and M_S with decreasing sublayer thickness likely occurs due to the combined effects of a decrease in the long-range (dipole) interactions due to finite size effects with charge transfer. For the LSFO sublayers, the Fe valence state is nearly unchanged by the charge transfer; consequently, T_N is only weakly dependent on sublayer thickness. The observed gradual decrease in T_N is likely due to a decrease in magnetic anisotropy with decreasing thickness [66]. Additional effects (such as interfacial stabilization of oxygen vacancies within the LSFO sublayers even in the strong oxidizing conditions used during sample growth) cannot be ruled out. This charge transfer may provide an additional means of separately controlling the AFM and FM properties of superlattice structures independent of strain and chemical effects.

5.5.5.4 Anisotropic X-Ray Magnetic Linear Dichroism

Soft X-ray magnetic spectroscopy is a powerful technique for detecting the presence of spin–flop coupling in the LSFO/LSMO superlattices [81]. As described above, spin–flop coupling occurs at interfaces characterized by an equal number of positive and negative spin interactions in the absence of any uncompensated spins. The system minimizes its energy by a perpendicular alignment of the AFM spins relative to the FM spins in the adjacent FM layer. With these measurements, linearly polarized X-rays are incident upon the samples at a normal incidence angle, and the Fe $L_{3,2}$ edge XMLD spectra are calculated as the difference between X-ray absorption spectra with ($\boldsymbol{E} \perp \boldsymbol{H}$) and ($\boldsymbol{E}//\boldsymbol{H}$). The experimental geometry is shown in the inset to Fig. 5.7. An applied magnetic field, $\boldsymbol{H} = 0.3$ T (black arrows), was used to align the Mn moments along a certain crystallographic directions. Two fundamental XMLD spectra were obtained with the X-ray $\boldsymbol{E}$ vector (gray arrow) oriented along the [100] direction, $\phi = 0°$, and along the [110] direction, $\phi = 45°$. The magnetic field was applied at a small angle out of the plane of the sample in order to increase the electron-yield signal without affecting the shape of the XMLD spectra in an appreciable way. The Fe $L_{3,2}$ edge X-ray absorption and XMLD spectra at 50 K for $\phi = 0°$ and 45° are plotted in Fig. 5.7. Note that in the absence of spin–flop coupling no XMLD effect should occur, since the magnitude of the magnetic field used in the experiments should not be large enough to affect the AFM spin ordering. However, as shown in Fig. 5.7(b), a pronounced XMLD signal is obtained for both crystallographic orientations, indicating that when the magnetization of the LSMO sublayer is forced to lie parallel or perpendicular to the X-ray $\boldsymbol{E}$ vector by the magnetic field, the AFM spins are also reoriented. This reorientation of the AFM spins occurs due to the exchange interactions occurring at the AFM/FM interfaces. A large spectral change between the XMLD signal for $\phi = 0°$ and 45° indicates the influence of the crystal electric field [64].

The temperature-dependent measurements showed that the magnitude of this XMLD signal mirrored that of the Mn XMCD signal for the LSMO sublayers. Both signals showed a clear transition at $T \sim 200$ K, above which the signals disappeared. Therefore, the exchange interaction is clearly driven by the FM properties of the LSMO sublayers, as the LSFO sublayers were shown above to remain AFM to temperatures in excess of room temperature. Experimental verification of whether the reorientation of the AFM spin involves a parallel or perpendicular orientation between the Fe and Mn spins was obtained using a grazing incidence geometry similar to the one used above to probe the AFM nature of the LSFO sublayers. In this case, a magnetic field, $\boldsymbol{H} = 0.3$ T, was applied parallel to the X-ray beam, approximately along the [100] direction. In the case of *perpendicular* orientation between the Fe and Mn spins, the Mn spins would lie along the [100] direction (i.e., parallel to $\boldsymbol{H}$) and the Fe spins would be forced to lie along the [010] direction. An H XMLD spectra calculated as $\boldsymbol{E}//[010] - \boldsymbol{E}//[001]$ would result in dichroism due to the parallel vs. perpendicular relationship between the AFM spin axis and the X-ray $\boldsymbol{E}$ vector. In contrast, for a *parallel* orientation, both the Fe and Mn spins would be oriented along the [100] direction, such that the dichroism would equal zero as

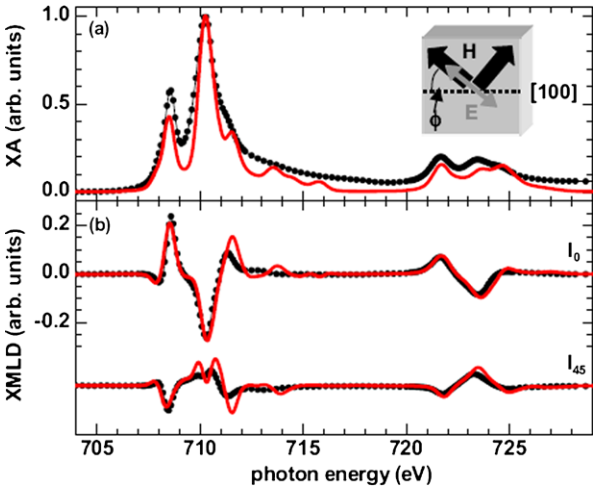

Fig. 5.7 Comparison of experimental Fe $L_{3,2}$ (**a**) X-ray absorption and (**b**) XMLD spectra obtained in normal incidence at $T = 50$ K (*black dots*) with atomic multiplet calculations (*red solid lines*). The experimental geometry is shown in the inset. The X-ray $\boldsymbol{E}$ vector (*gray arrow*) lies at an angle ϕ with respect to the [100] axis (*dashed line*). The magnetic field, $\boldsymbol{H}$ (*black arrows*), is applied at angles of ϕ and $\phi + 90°$. Fundamental XMLD spectra I_0 and I_{45} were obtained at $\phi = 0°$ and $\phi + 45°$, respectively. Reprinted with permission from Appl. Phys. Lett. 94, 072503 (2009). Copyright 2009, American Institute of Physics

the X-ray $\boldsymbol{E}$ vector would be perpendicular to the AFM spin axis in both cases. The H XMLD spectra obtained for this kind of measurement showed a spectral shape similar to that shown in Fig. 5.6, confirming the perpendicular orientation between the Fe and Mn spins as predicted by spin–flop coupling. Furthermore, its temperature dependence tracked that of the Mn XMCD signal at low temperatures. Above the T_C, the Fe H XMLD signal drops to about 30 % of its low temperature value but does not disappear completely. This reduced signal reflects the fact that in the absence of the Mn magnetization, the uniaxial alignment of the Fe AFM spins along the [010] direction disappears, so that the Fe spins are equally distributed into AFM domains with the Fe spins axis along the [100] and [010] directions.

Further confirmation of the spin–flop coupling mechanism was obtained using multiplet calculations [81, 84] of the Fe $L_{3,2}$ edge X-ray absorption and XMLD (solid red lines in Fig. 5.7). These calculations assumed a perpendicular orientation between the Fe and Mn moments in adjacent sublayers with an external magnetic field applied within the (001)-plane. The interface is assumed to be fully compensated. Additional details concerning the calculations are detailed in Ref. [81]. All spectral features in the experimental spectra were well reproduced by the calculations, including the fundamental spectra for the two in-plane orientations of $\boldsymbol{H}$ and $\boldsymbol{E}$, i.e., $\phi = 0°$ and 45°.

Upon increasing the LSFO sublayer thickness to 18 unit cells in the [18 × 18]5 superlattice, the spin–flop coupling effect disappears, as the magnetic anisotropy of the LSFO sublayers now dominates and a magnetic field, $H = 0.3$ T is not suffi-

cient to reorient the AFM spins. Thus, exchange interactions play a comparatively weaker role, and the coercive field correspondingly returns to a similar value as observed in a single layer LSMO film. On the other hand, with a decrease of the LSMO sublayer thickness to 3 unit cells as in the $[3 \times 3]10$ and $[6 \times 3]10$ superlattices, the LSMO magnetization disappears and no spin–flop coupling was detected. Therefore, spin–flop coupling only occurs for a small range of sublayer thicknesses due to the delicate balance between the exchange interactions, interfacial electronic reconstruction, and long-range (dipole) interactions.

5.5.6 Photoemission Electron Microscopy

5.5.6.1 AFM Domain Patterns

PEEM imaging was performed at the Advanced Light Source using the PEEM-3 microscope located on Beamline 11.0.1. For each angle of the X-ray $\boldsymbol{E}$ vector (β), the domain images were obtained by taking the ratio of images captured at the A and B features of the Fe L_2 edge. The AFM domain images for a 40 nm thick LSFO film are shown in Fig. 5.8 with the X-rays oriented along the ⟨100⟩ substrate direction, $\phi = 0°$. All images are shown with the same contrast conditions. As β varies from 0° to 90°, four distinct types of micrometer-sized domains can be identified. For example, the blue domains remain white for all polarizations, while the yellow domains start as white for $\beta = 0°$ and quickly transition to black by $\beta = 30°$. Quantitative analysis of the local intensity for each type of domain (Fig. 5.8(c)) was extracted from the images and then normalized to the average intensity for the entire ratio image. This procedure removes an artificial modulation of the experimental, angular-dependent XMLD curves because of small changes in the image illumination and X-ray intensity with changes in polarization and energy. This nonmagnetic artifact has equal amplitude in all types of domains and is easily removed by the normalization to the average intensity. Error values represent the sigma value for the Gaussian curves used to fit the intensity histograms of the experimental data. The formation of these four types of domains can be explained by a domain model where $\boldsymbol{M}_{\mathrm{Fe}}$ orients along the ⟨100⟩ family of directions but cants out of the plane of the film by an angle, θ. The model curves were divided by their average value to facilitate the comparison with the normalized experimental data. Good agreement exists with the domain model (Fig. 5.8(d)) with regard to the trends and, most importantly, the locations of the crossing points as a function of β assuming an out-of-plane canting angle of $30°+/-3°$. These crossing points are unchanged in polarization angle regardless of the analysis procedure (with and without the normalization to the average value); therefore, they serve as key indicators to match to the model. In comparison, previous reports on $LaFeO_3$ thin films determined canting angles ranging from 20 to 45° [82, 83]. These differences have been ascribed to differences in growth method (PLD vs. molecular beam epitaxy) and the strain state of the films in each work.

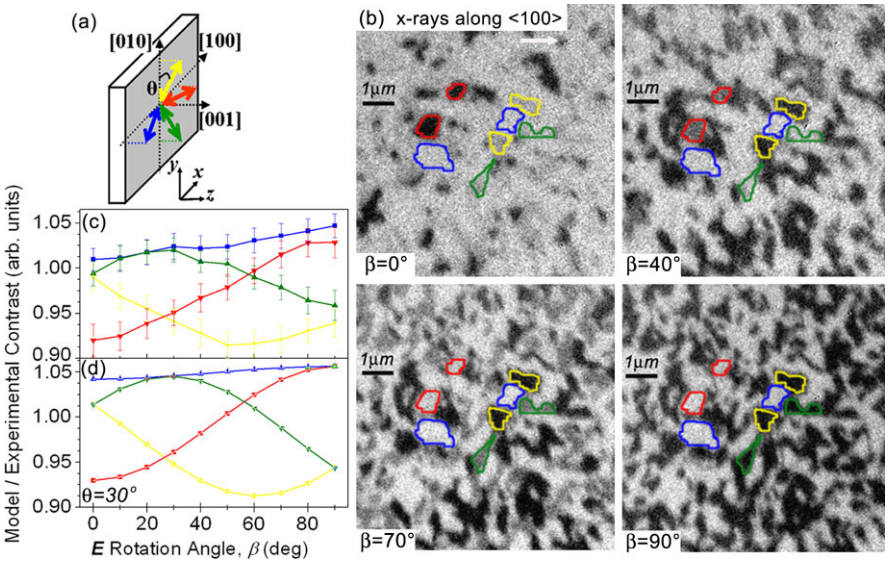

Fig. 5.8 (**a**) The AFM domain model for an LSFO thin film with four domains where $\boldsymbol{M}_{\mathrm{Fe}}$ orients along the ⟨100⟩ and ⟨010⟩ directions and canting out of the plane of the film with an angle, θ; (**b**) domain images for varying β; (**c**) experimental contrast vs. β obtained from images in (**b**) for each of the four types of domains, error bars represent the sigma value for the Gaussian curve used to fit the experimental contrast; and (**d**) model contrast vs. β for the case of $\theta = 30°$

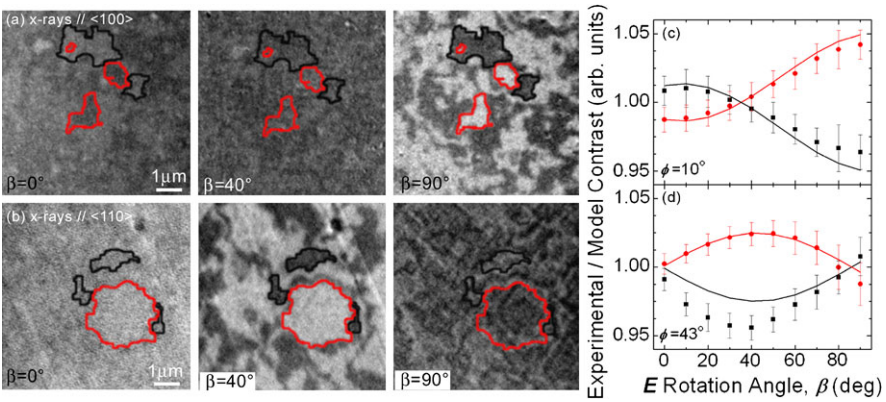

Fig. 5.9 Domain images for the [6 × 6]10 superlattice for varying β with the X-rays along the (**a**) ⟨100⟩ and (**b**) ⟨110⟩ directions; (**c**) and (**d**) experimental and model contrast vs. β obtained from images in (**a**) and (**b**) for a two-domain model with the spin axis lying in-plane ($\theta = 0°$) along the ⟨100⟩ and ⟨010⟩ directions. The *red* and *black lines* highlight the boundaries of a few domains used to extract the experimental contrast

In contrast, the domain images for a [6 × 6]10 superlattice (Fig. 5.9) taken at room temperature show only two types of AFM domains as β varies from 0° to 90°.

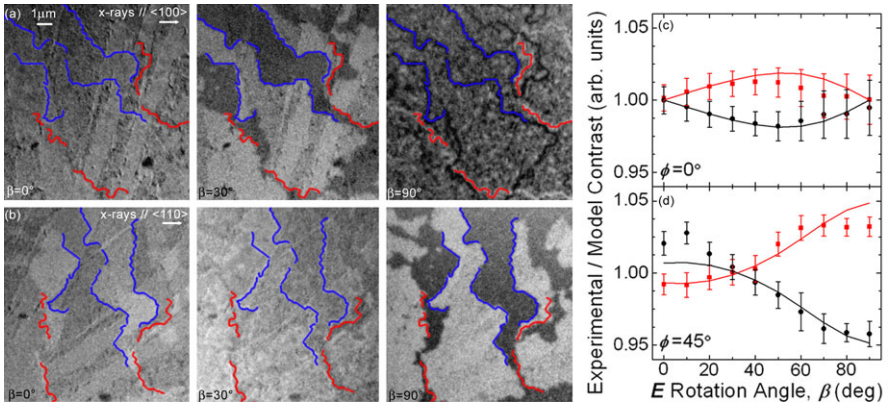

Fig. 5.10 Domain images for the [6 × 3]10 superlattice for varying β with the X-rays along the (**a**) ⟨100⟩ and (**b**) ⟨110⟩ directions; (**c**) and (**d**) experimental contrast and model contrast vs. β obtained from images in (**a**) and (**b**) for a two-domain model with the spin axis lying in-plane ($\theta = 0°$) along the ⟨110⟩ family directions. The *blue/red lines* highlight the position of the *black/white* domain walls observed in the $\beta = 90°$ or $\beta = 40°$ image with the X-rays along the ⟨100⟩ or ⟨110⟩ directions, respectively

In this sample, the LSFO sublayers retain their AFM properties for temperatures >400 K, while the T_C of the LSMO sublayer is suppressed to 150–200 K. Both sublayers are slightly tetragonally distorted due to the epitaxial strain from the underlying STO substrate. PEEM images were obtained for two different sample orientations: the X-rays oriented along the ⟨100⟩ substrate direction (Fig. 5.9(a)) and along the ⟨110⟩ substrate direction (Fig. 5.9(b)). For the former, maximum contrast is obtained for $\beta = 90°$, where in each type of domain $\boldsymbol{E}$ is either exactly parallel or perpendicular to $\boldsymbol{M}_{\mathrm{Fe}}$. The contrast is reversed and weaker for $\beta = 0°$. With the X-rays along the ⟨110⟩ substrate direction, weak domain contrast is observed at $\beta = 0°$ and 90° as in each case $\boldsymbol{E}$ forms approximately a 45° angle with $\boldsymbol{M}_{\mathrm{Fe}}$ in both types of domains, while the domain contrast is the strongest at $\beta = 40°$. This behavior can only be described with a model where $\boldsymbol{M}_{\mathrm{Fe}}$ orients along the in-plane ⟨100⟩ substrate directions, i.e., with $\theta = 0°$, such that the red and blue domains from Fig. 5.8(a) degenerate into a single type of AF domain, and similarly for the green and yellow domains. Good agreement is obtained by comparing the experimental contrast values for both sample orientations to the model contrast (Figs. 5.9(c) and (d)). The shapes of the domains are characterized by fairly straight edges which align with the in-plane ⟨100⟩ substrate directions. Seo et al. [85] reported similar angular domains in $LaFeO_3$ films which are defined by the structural twins where the c axis takes on two possible in-plane orientations parallel to the ⟨100⟩ substrate directions.

Figure 5.10 shows the AFM domain images for a [6 × 3]10 superlattice where the LSMO sublayer thickness has been decreased to three unit cells. At this thickness, the LSMO sublayers no longer display ferromagnetism at any temperature, and they may not effectively decouple the LSFO sublayers from one another. We observe

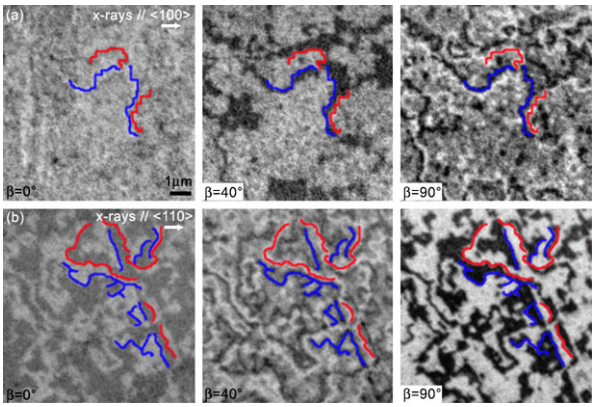

Fig. 5.11 Domain images for the [12 × 12]5 superlattice for varying β with the X-rays along the (**a**) ⟨100⟩ and (**b**) ⟨110⟩ directions. The *blue/red lines* highlight the position of the *black/white* regions observed in the $\beta = 90°$ or $\beta = 40°$ image with the X-rays along the ⟨100⟩ or ⟨110⟩ directions, respectively

weak AFM domain contrast for $\beta = 0°$ and 90° and strong domain contrast at $\beta =$ 40° with extremely large domains (tens of micrometers long) when the X-rays are oriented along the ⟨100⟩ substrate direction; i.e., the AFM spin axis is oriented 45° compared to the [6 × 6]10 superlattice. In addition, the image for $\beta = 90°$ shows a uniformly gray background highlighted by thin black and white lines at locations which correspond to the domain walls in the image for $\beta = 30°$. These domain walls are highlighted by blue and red lines in Fig. 5.10. Upon rotation of the sample by 45°, strong domain contrast is observed for $\beta = 90°$, weak reversed contrast for $\beta = 0°$, and no domain contrast for $\beta = 30°$. In this case, the experimental contrast shows good agreement with a domain model where $\boldsymbol{M}_{\mathrm{Fe}}$ lies along the in-plane ⟨110⟩ directions, while $\boldsymbol{M}_{\mathrm{Fe}}$ within the domain walls lies along the in-plane ⟨100⟩ directions.

Finally, with a thicker sublayer thickness in a [12 × 12]5 superlattice (Fig. 5.11), we observe a hybrid AFM domain structure of the previous two superlattice samples consisting of small sub-micrometer-sized domains where $\boldsymbol{M}_{\mathrm{Fe}}$ lies along the in-plane ⟨100⟩ and ⟨110⟩ substrate directions. For this superlattice, a magnetic ordering temperature of $T_{\mathrm{C}} \sim 300$ K is observed from bulk magnetometry measurements. As in the case with the [6 × 6]10 superlattice shown in Fig. 5.9, the domains have straight edges which generally align with the in-plane ⟨100⟩ substrate directions. The small size of the domains makes it difficult to extract experimental contrast values. However, similar to the [6 × 3]10 superlattice shown in Fig. 5.10, for $\phi = 0°$ and $\beta = 90°$ we observe small, uniformly gray regions highlighted by thin black and white lines at the locations which correspond to the domain walls in the image for $\beta = 40°$. After rotating the sample to $\phi = 45°$, the effect is reversed; strong domain contrast can be observed at $\beta = 90°$, and the domain walls are apparent for $\beta = 40°$. Therefore, the AF domains are interpreted as consisting of regions where $\boldsymbol{M}_{\mathrm{Fe}}$ lies along the in-plane ⟨110⟩ directions separated by domain walls in which $\boldsymbol{M}_{\mathrm{Fe}}$ lies along the in-plane ⟨100⟩ directions, as in the case of the [6 × 3]10 superlattice. These domain walls are highlighted with blue and red lines in Fig. 5.11.

Our PEEM-3 images reveal that the orientation of $\boldsymbol{M}_{\mathrm{Fe}}$ differs in LSFO thin films and superlattices, and within the superlattices depending on the structural properties

(i.e., strain state, sublayer thicknesses, presence of structural defects). For LSFO thin films, $\boldsymbol{M}_{\mathrm{Fe}}$ cants out of plane by 30° along the [100] and [010] substrate directions, while it is confined to an in-plane direction for all the superlattices. For the $[6 \times 6]10$ superlattice, a two-domain structure is observed where $\boldsymbol{M}_{\mathrm{Fe}}$ lies along the two in-plane ⟨100⟩ substrate directions. In contrast, for the $[6 \times 3]10$ and $[12 \times 12]5$ superlattices, we observe domains with $\boldsymbol{M}_{\mathrm{Fe}}$ lying along the ⟨110⟩ substrate directions, separated by thin domain walls where $\boldsymbol{M}_{\mathrm{Fe}}$ lies along the ⟨100⟩ substrate directions. The formation of the domain walls suggests that multiple competing interactions exist or that the LSFO anisotropy is lower in these samples than in the samples where the thickness of the domains walls is below the spatial resolution of the PEEM-3 microscope (<40 nm).

These results suggest that a number of parameters ultimately determine the orientation of $\boldsymbol{M}_{\mathrm{Fe}}$. First, the superlattices contain small individual layer thickness with a high density of horizontal interfaces. Reports from the literature have shown that FM and AFM moments near interfaces can deviate away from their orientations far away from the interfaces. Recently, Aruta et al. [86] reported that FM order develops at the interfaces in superlattices of the AF insulators $SrMnO_3$ and $LaMnO_3$. In these $[n\ SrMnO_3 \times 2n\ LaMnO_3]$ superlattices, for small values of n, the AFM Mn spins in the $LaMnO_3$ layers are pinned in an in-plane orientation by the ferromagnetism that develops at the interfaces. For $n > 5$, the AFM Mn spins are able to take their preferred out-of-plane orientation at the center of the layers. Furthermore, Izumi et al. [87] deduced from their magnetization and magnetotransport data that the interaction at $La_{0.6}Sr_{0.4}FeO_3/La_{0.6}Sr_{0.4}MnO_3$ interfaces resulted in a spin-canted region within the $La_{0.6}Sr_{0.4}MnO_3$ layer and that the thickness of this spin-canted region increased with increasing $La_{0.6}Sr_{0.4}FeO_3$ thickness. Though it was not investigated, it would not be unexpected that the AFM spins in the $La_{0.6}Sr_{0.4}FeO_3$ layer are also canted away from their bulk orientation at the interfaces.

Second, the LSMO sublayer thickness determines whether the individual LSFO sublayers are coupled or isolated from one another. With an LSMO sublayer thickness of three unit cells, we suspect that the LSFO sublayers may be coupled, but for larger LSMO sublayer thicknesses, the LSFO sublayers should be magnetically isolated from one another. Third, X-ray diffraction measurements show that the superlattices exist in slightly different strain states due to the epitaxial strain from the underlying STO substrate. This strain results in changes to the distortions and/or rotations of the FeO_6 octahedra as the unit cell deviates from its bulk orthorhombic symmetry towards a tetragonal/cubic symmetry. This increase in symmetry may lower the energy difference for $\boldsymbol{M}_{\mathrm{Fe}}$ to orient along different crystallographic directions or to follow the influence of external alignment forces such as those offered by the presence of horizontal or vertical interfaces. Finally, scanning transmission electron microscopy images [88] show that these superlattices are characterized by different types and densities of structural defects (stacking faults, dislocations) which can define the locations of domain walls. Due to the complex nature of these multiple interactions, it is likely that a combination of these effects contributes to the observed differences in the AF domain patterns.

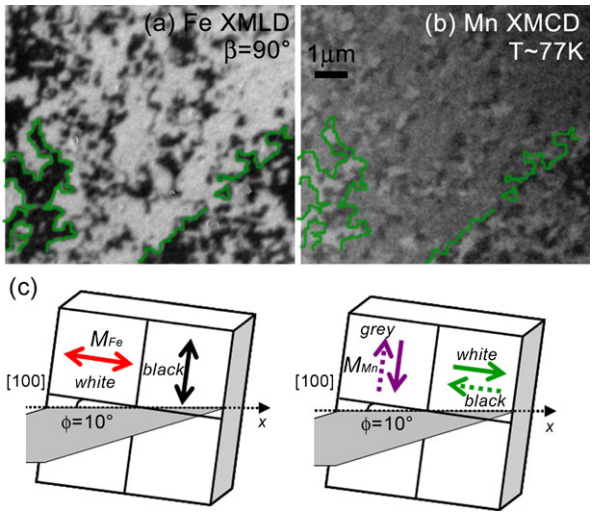

Fig. 5.12 (**a**) Fe XMLD with $\beta = 90°$ and (**b**) Mn XMCD domain images taken at $T \sim 77$ K with $\phi = 10°$. The *green lines* outline the locations of a few black AFM domains. (**c**) Schematic showing the orientation of $\boldsymbol{M}_{\mathrm{Fe}}$ in the AFM domains and $\boldsymbol{M}_{\mathrm{Mn}}$ in the FM domains

5.5.6.2 Imaging of Spin–Flop Coupling

Using the unique low temperature capabilities of the PEEM-3 microscopy, we were able to observe the perpendicular orientation of the AFM and FM spins in the [6 × 6]10 superlattice mediated by spin–flop coupling. AFM domain images captured as a function of β at low temperature show that the types of AFM domains formed in the LSFO sublayers remain unchanged in the presence of FM order in the adjacent LSMO sublayers (i.e., $\boldsymbol{M}_{\mathrm{Fe}}$ orients along the in-plane ⟨100⟩ substrate directions) [89]. However, the locations of these AFM domains change with temperature such that they form elongated stripes several micrometers in width that have predominantly white/black contrast. The edges of these stripes are aligned approximately with the ⟨110⟩ substrate directions. Figure 5.12 compares the Fe XMLD ($\beta = 90°$, first column) and Mn XMCD (second column) domain images at 77 K with the X-ray beam aligned along the [100] substrate direction, $\phi = 10°$. Based on the analysis of the AFM domain contrast described above, $\boldsymbol{M}_{\mathrm{Fe}}$ within the white and black domains lie along the [100] and [010] substrate directions, respectively, i.e. at 100° and 10° relative to the X-ray $\boldsymbol{E}$ vector, respectively (see schematic in Fig. 5.12(c)). In the region of the sample shown, the AFM domains primarily have white contrast. The locations of a few black domains are highlighted in green. The corresponding Mn XMCD images show the formation of many small, irregularly shaped FM domains with strong white (black) contrast separated by wider regions with gray contrast. These white (black) domains correspond to regions where $\boldsymbol{M}_{\mathrm{Mn}}$ is *parallel* (*antiparallel*) [i.e., 190° (10°)] to the X-ray helicity (x-axis), while the intermediate gray contrast indicates a *perpendicular* orientation [i.e., −80° (100°)] between $\boldsymbol{M}_{\mathrm{Mn}}$ and the X-ray helicity (see schematic in Fig. 5.12(c)). No clear boundaries can be observed between the gray and white (black) regions, as the AFM domain wall width lies below the spatial resolution of the microscope. Upon close inspection, we notice that the white (black) FM domains correspond to regions of

black contrast in the Fe XMLD image. Note that each of the AFM domains correlates to two types of much smaller FM domains. Similarly, the large gray FM domains correspond to the large patches of white AFM domains. As shown in the schematic in Fig. 5.12(c), this interpretation of the AFM and FM domain contrast indicates a local perpendicular orientation between the AFM spin axis and the FM moments. Further confirmation of this perpendicular orientation was obtained by examining the images for $\phi = -35°$ [89].

This perpendicular coupling remains unchanged for temperatures below the $T_C \sim 160$ K of the LSMO sublayer, where the Mn XMCD disappears. As the temperature changes, however, we observe that the locations of the AFM and FM domains move in concert with one another, such that by 160 K, the white and black AFM domains are nearly uniformly located throughout the film, instead of forming the striped patterns described above. This movement of the domains involves the 90° and 180° rotation of the Fe and Mn moments, suggesting that the strength of the spin–flop coupling is able to overcome the pinning effect of the structural defects which typically define the locations of the AFM domains [85].

5.6 Conclusions

In conclusion, we have presented our study of the structural and functional properties of perovskite oxide superlattices composed of antiferromagnetic LSFO and ferromagnetic LSMO sublayers. Despite the fact that, in the bulk, these two materials possess similar ordering temperatures, in these superlattices, they display differing behavior with decreasing temperature and sublayer thickness. For a critical range of sublayer thicknesses, a robust spin–flop coupling is observed such that the AFM spin axis and the FM magnetization in the adjacent sublayers maintain a perpendicular orientation, even upon the application of an external magnetic field. Because of the unique ability to control the direction of the AFM spin axis with an applied magnetic field, this spin–flop coupling may have potential applications in future memory or sensor devices. Furthermore, we find that the direction of the AFM spin axis and the nature of the AFM domains have a strong dependence on the structural properties of the superlattices. A detailed understanding of the interplay between the structural, chemical, magnetic, and electronic effects present in these perovskite oxide superlattice systems will facilitate their implementation into technological applications.

Acknowledgements A number of people contributed to this work, including Fan Yang, Nihan Kemik, Andreas Scholl, Anthony Young, Andrew Doran, Elke Arenholz, Gerrit van der Laan, Michael Biegalski, Hans Christen, Apurva Mehta, Matthew Bibee, Rajesh Chopdekar, and Yuri Suzuki. A portion of this research was conducted at facilities operated for the Office of Basic Energy Sciences, of the U.S. Department of Energy: the Center for Nanophase Materials Sciences is sponsored at Oak Ridge National Laboratory, the Advanced Light Source is supported by the Director, Office of Science under Contract No. DE-AC02-05CH11231, and the Stanford Synchrotron Radiation Lightsource, a Directorate of SLAC National Accelerator Laboratory and an Office of Science User Facility operated by Stanford University. Research at UC Davis is supported by UC Davis start-up funds and the National Science Foundation Contract No. DMR 0747896.

References

1. R. Ramesh, N.A. Spaldin, Multiferroics: progress and prospects in thin films. Nat. Mater. **6**, 21–29 (2006)
2. H.M. Christen, G. Eres, Recent advances in pulsed-laser deposition of complex oxides. J. Phys. Condens. Matter **20**, 264005 (2008)
3. G. Rijnders, G. Koster, D.H.A. Blank, H. Rogalla, In situ monitoring during pulsed laser deposition of complex oxides during reflection high energy electron diffraction under high oxygen pressure. Appl. Phys. Lett. **70**, 1888–1890 (1997)
4. D.G. Schlom, L.-Q. Chen, X.Q. Pan, A. Schmehl, M.A. Zurbuchen, A thin film approach to engineering functionality into oxides. J. Am. Ceram. Soc. **91**, 2429–2454 (2008)
5. A. Ohtomo, H.Y. Hwang, A high-mobility electron gas at the $LaAlO_3/SrTiO_3$ heterointerface. Nature **427**, 423–426 (2004)
6. N. Reyren, S. Thiel, A.D. Caviglia, L. Fitting Kourkoutis, G. Hammerl, C. Richter, C.W. Schneider, T. Kopp, A.-S. Ruetschi, D. Jaccard, M. Gabay, D.A. Muller, J.-M. Triscone, J. Mannhart, Superconducting interfaces between insulating oxides. Science **317**, 1196–1199 (2007)
7. A. Brinkman, M. Huijben, M. van Zalk, J. Huijben, U. Zeitler, J.C. Maan, W.G. van der Wiel, G. Rijnders, D.H.A. Blank, H. Hilgenkamp, Magnetic effects at the interface between non-magnetic oxides. Nat. Mater. **6**, 493–496 (2007)
8. M. Huijben, A. Brinkman, G. Koster, G. Rijnders, H. Hilgenkamp, D.H.A. Blank, Structure-property relation of $SrTiO_3/LaAlO_3$ interfaces. Adv. Mater. **21**, 1665–1677 (2009)
9. C. Adamo, X. Ke, H.Q. Wang, H.L. Xin, T. Heeg, M.E. Hawley, W. Zander, J. Schubert, P. Schiffer, D.A. Muller, L. Maritato, D.G. Schlom, Effect of biaxial strain on the electrical and magnetic properties of (001) $La_{0.7}Sr_{0.3}MnO_3$ thin films. Appl. Phys. Lett. **95**, 112504 (2009)
10. S.J. May, J.-W. Kim, J.M. Rondinelli, E. Karapetrova, N.A. Spaldin, A. Bhattacharya, P.J. Ryan, Quantifying octahedral rotations in strained perovskite oxide films. Phys. Rev. B **82**, 014110 (2010)
11. Y. Konishi, Z. Fang, M. Izumi, T. Manako, M. Kasai, H. Kuwahara, M. Kawasaki, K. Terakura, Y. Tokura, Orbital-state-mediated phase-control of manganites. J. Phys. Soc. Jpn. **68**, 3790–3793 (1999)
12. N. Nakagawa, H.Y. Hwang, D.A. Muller, Why some interfaces cannot be sharp. Nat. Mater. **5**, 204–209 (2006)
13. W.H. Meiklejohn, C.P. Bean, New Magnetic Anisotropy. Phys. Rev. **102**, 1413–1414 (1956)
14. J. Nogues, I.K. Schuller, Exchange bias. J. Magn. Magn. Mater. **192**, 203–232 (1999)
15. A. Ohtomo, D.A. Muller, J.L. Grazul, H.Y. Hwang, Artificial charge-modulation in atomic-scale perovskite titanate superlattices. Nature **419**, 378–380 (2002)
16. S. Smadici, P. Abbamonte, A. Bhattacharya, X. Zhai, B. Jiang, A. Rusydi, J.N. Eckstein, S.D. Bader, J.-M. Zuo, Electronic Reconstruction at $SrMnO_3$–$LaMnO_3$ Superlattice Interfaces. Phys. Rev. Lett. **99**, 196404 (2007)
17. H. Kumigashira, D. Kobayashi, R. Hashimoto, A. Chikamatsu, M. Oshima, N. Nakagawa, T. Ohnishi, M. Lippmaa, H. Wadati, A. Fujimori, K. Ono, M. Kawasaki, H. Koinuma, Inherrent charge transfer layer formation at $La_{0.6}Sr_{0.4}FeO_3/La_{0.6}Sr_{0.4}MnO_3$ heterointerfaces. Appl. Phys. Lett. **84**, 5353–5355 (2004)
18. C.A.F. Vaz, J.A.C. Bland, G. Lauhoff, Magnetism in ultrathin film structures. Rep. Prog. Phys. **71**, 056501 (2008)
19. J.B. Goodenough, General considerations, in *Localized to Itinerant Electronic Transition in Perovskite Oxides*, vol. 98 (Springer, Berlin, 2001), pp. 1–16
20. J.B. Goodenough, Jahn-Teller Phenomena in Solids. Annu. Rev. Mater. Sci. **28**, 1–27 (1998)
21. J.M.D. Coey, M. Viret, S. von Molnar, Mixed-valence manganites. Adv. Phys. **48**, 167–293 (1999)
22. V.M. Goldschmidt, Die Gesetze der Krystallochemie. Naturwissenschaften **14**, 477–485 (1926)

23. R.D. Shannon, Revised effective ionic-radii and systematic studies of interatomic distances in halides and chalcogenides. Acta Crystallogr., Ser. A **32**, 751–767 (1976)
24. C.A. Randall, A.S. Bhalla, T.R. Shrout, L.E. Cross, Classification and consequences of complex lead perovskite ferroelectrics with regard to B-site cation order. J. Mater. Res. **5**, 829–834 (1990)
25. H.Y. Hwang, S.-W. Cheong, P.G. Radaelli, M. Marezio, B. Batlogg, Lattice effects on the magnetoresistance in doped $LaMnO_3$. Phys. Rev. Lett. **75**, 914–917 (1995)
26. H.Y. Hwang, T.T.M. Palstra, S.-W. Cheong, B. Batlogg, Pressure effects on the magnetoresistance in doped manganese perovskites. Phys. Rev. B **52**, 15046–15049 (1995)
27. Y. Moritomo, A. Asamitsu, Y. Tokura, Pressure effect on the double-exchange ferromagnet $La_{1-x}Sr_xMnO_3$ $(0.15 < x < 0.5)$. Phys. Rev. B **51**, 16491–16494 (1995)
28. Y. Takamura, R.V. Chopdekar, E. Arenholz, Y. Suzuki, Control of the magnetic and magnetotransport properties of $La_{0.67}Sr_{0.33}MnO_3$ thin films through epitaxial strain. Appl. Phys. Lett. **92**, 162504 (2008)
29. F. Yang, N. Kemik, M.D. Biegalski, H.M. Christen, E. Arenholz, Y. Takamura, Strain engineering to control the magnetic and magnetotransport properties of $La_{0.67}Sr_{0.33}MnO_3$ thin films. Appl. Phys. Lett. **97**, 092503 (2010)
30. Z. Fang, I.V. Solovyev, K. Terakura, Phase diagram of tetragonal manganites. Phys. Rev. Lett. **84**, 3169–3172 (2000)
31. A. Vailionis, H. Boschker, W. Siemons, E.P. Houwman, D.H.A. Blank, G. Rijnders, G. Koster, Misfit strain accommodation in epitaxial ABO_3 perovskites: lattice rotations and lattice modulations. Phys. Rev. B **83**, 064101 (2011)
32. P.A. Salvador, T.D. Doan, B. Mercey, B. Raveau, Stabilization of $YMnO_3$ in a perovskite structure as a thin film. Chem. Mater. **10**, 2592–2595 (1998)
33. J.M. Rondinelli, N.A. Spaldin, Structural effects on the spin-state transition in epitaxially strained $LaCoO_3$ films. Phys. Rev. B **79**, 054409 (2009)
34. D. Fuchs, E. Arac, C. Pinta, S. Schuppler, R. Schneider, H.v. Lohneysen, Tuning the magnetic properties of $LaCoO_3$ thin films by epitaxial strain. Phys. Rev. B **77**, 014434 (2008)
35. D. Fuchs, C. Pinta, T. Schwarz, P. Schweiss, P. Nagel, S. Schuppler, R. Schneider, M. Merz, G. Roth, H.v. Lohneysen, Ferromagnetic order in epitaxially strained $LaCoO_3$ thin films. Phys. Rev. B **75**, 144402 (2007)
36. J.W. Freeland, J.X. Ma, J. Shi, Ferromagnetic spin-correlations in strained $LaCoO_3$ thin films. Appl. Phys. Lett. **93**, 212501 (2008)
37. A. Herklotz, A.D. Rata, L. Schultz, K. Dorr, Reversible strain effect on the magnetization of $LaCoO_3$. Phys. Rev. B **79**, 092409 (2009)
38. K. Gupta, P. Mahadevan, Strain-driven magnetism in $LaCoO_3$ thin films. Phys. Rev. B **79**, 020406(R) (2009)
39. A.P. Ramirez, Colossal magnetoresistance. J. Phys. Condens. Matter **9**, 8171–8199 (1997)
40. J. Hemberger, A. Krimmel, T. Kurz, H.-A. Krug von Nidda, V.Y. Ivanov, A.A. Mukhin, A.M. Balbashov, A. Loidl, Structural, magnetic, and electrical properties of single-crystalline $La_{1-x}Sr_xMnO_3$ $(0.4 < x < 0.85)$. Phys. Rev. B **66**, 094410 (2002)
41. P.-G. de Gennes, Effects of Double Exchange in Magnetic Crystals. Phys. Rev. **118**, 141–154 (1960)
42. C. Zener, Interaction between the d shells in the transition metals. Phys. Rev. **81**, 440 (1951)
43. P.W. Anderson, H. Hasegawa, Considerations on double exchange. Phys. Rev. **100**, 675–681. (1955)
44. A.J. Millis, P.B. Littlewood, B.I. Shraiman, Double exchange alone does not explain the resistivity of $La_{1-x}Sr_xMnO_3$. Phys. Rev. Lett. **74**, 5144–5147 (1995)
45. P.G. Radaelli, G. Iannone, M. Marezio, H.Y. Hwang, S.W. Cheong, J.D. Jorgensen, D.N. Argyriou, Structural effects on the magnetic and transport properties of perovskite $A_{1-x}A_xMnO_3$ $(x = 0.25, 0.30)$. Phys. Rev. B **56**, 8265 (1997)

46. R.L. White, Review of recent work on the magnetic and spectroscopic properties of the rare-earth orthoferrites. J. Appl. Phys. **40**, 1061–1069 (1969)
47. J.-C. Grenier, N. Ea, M. Pouchard, M. Abou-Sekkina, Proprietes electriques et magnetiques des ferrites oxydes $La_{1-x}Sr_xFeO_{3-y}$. Mater. Res. Bull. **19**, 1301–1309 (1984)
48. U. Shimony, J.M. Knudsen, Mossbauer studies on iron in the pervoskites $La_{1-x}Sr_xFeO_3$ $(0 < x < 1)$. Phys. Rev. **144**, 361–366 (1966)
49. In *Powder Diffraction File #01-089-1269*, ed. by International Centre for Diffraction Data
50. A. Fossdal, M. Menon, I. Waernhus, K. Wiik, M.-A. Einarsrud, T. Grande, Crystal structure and thermal expansion of $La_{1-x}Sr_xFeO_{3-\delta}$ materials. J. Am. Ceram. Soc. **87**, 1952–1958 (2004)
51. N.C. Koon, Calculations of exchange bias in thin films with ferromagnetic/antiferromagnetic interfaces. Phys. Rev. Lett. **78**, 4865–4868 (1997)
52. T.C. Schulthess, W.H. Butler, Consequences of spin–flop coupling in exchange biased films. Phys. Rev. Lett. **81**, 4516–4519 (1998)
53. L.L. Hinchey, D.L. Mills, Magnetic properties of ferromagnetic–antiferromagnetic superlattice structures with mixed-spin antiferromagnetic sheets. Phys. Rev. B **34**, 1689–1699 (1986)
54. Y. Ijiri, J.A. Borchers, R.W. Erwin, S.-H. Lee, P.J. van der Zaag, R.M. Wolf, Perpendicular coupling in exchange-biased Fe_3O_4/CoO superlattices. Phys. Rev. Lett. **80**, 608–611 (1998)
55. T.M. Moran, I.K. Schuller, Effects of cooling field strength on exchange anisotropy at permalloy/CoO interfaces. J. Appl. Phys. **79**, 5109–5111 (1996)
56. S. Dong, Q. Zhang, S. Yunoki, J.-M. Liu, E. Dagotto, Ab initio study of the intrinsic exchange bias at the $SrRuO_3$/$SrMnO_3$ interface. Phys. Rev. B **84**, 224437 (2011)
57. S. Dong, K. Yamauchi, S. Yunoki, R. Yu, S. Liang, A. Moreo, J.-M. Liu, S. Picozzi, E. Dagotto, Exchange bias driven by the Dzyaloshinskii–Moriya interaction and ferroelectric polarization at G-type antiferromagnetic Perovskite interfaces. Phys. Rev. Lett. **103**, 127201 (2009)
58. J.B. Kortright, D.D. Awschalom, J. Stohr, S.D. Bader, Y.U. Idzerda, S.S.P. Parkin, I.K. Schuller, H.-C. Siegmann, Research frontiers in magnetic materials at soft x-ray synchrotron radiation facilities. J. Magn. Magn. Mater. **207**, 7–44 (1999)
59. T. Funk, A. Deb, S.J. George, H. Wang, S.P. Cramer, X-ray magnetic circular dichroism—a high energy probe of magnetic properties. Coord. Chem. Rev. **249**, 3–30 (2005)
60. J. Stohr, Exploring the microscopic origin of magnetic anisotropies with X-ray magnetic circular dichroism (XMCD) spectroscopy. J. Magn. Magn. Mater. **200**, 470–497 (1999)
61. J. Stohr, R. Nakajima, Magnetic properties of transition-metal multilayers studied with X-ray magnetic circular dichroism spectroscopy. IBM J. Res. Dev. **42**, 73–88 (1998)
62. S. Anders, H.A. Padmore, R.M. Duarte, T. Renner, T. Stammler, A. Scholl, M.R. Scheinfein, J. Stohr, L. Seve, B. Sinkovic, Photoemission electron microscope for the study of magnetic materials. Rev. Sci. Instrum. **70**, 3973–3981 (1999)
63. E. Arenholz, G. van der Laan, R.V. Chopdekar, Y. Suzuki, Anisotropic X-ray magnetic linear dichroism at the Fe $L_{2,3}$ edges in Fe_3O_4. Phys. Rev. B **74**, 094407 (2006)
64. E. Arenholz, G. van der Laan, R.V. Chopdekar, Y. Suzuki, Angle-dependent Ni^{2+} X-ray magnetic linear dichroism: interfacial coupling revisited. Phys. Rev. Lett. **98**, 197201 (2007)
65. C.T. Chen, L.H. Tjeng, J. Kwo, H.L. Kao, P. Rudolf, F. Sette, R.M. Fleming, Out-of-plane orbital characters of intrinsic and doped holes in $La_{2-x}Sr_xCuO_4$. Phys. Rev. Lett. **68**, 2543 (1992)
66. D. Alders, L.H. Tjeng, F.C. Voogt, T. Hibma, G.A. Sawatzky, C.T. Chen, J. Vogel, M. Sacchi, S. Iacobucci, Temperature and thickness dependence of magnetic moments in NiO epitaxial films. Phys. Rev. B **57**, 11623–11631 (1998)
67. Y. Takamura, F. Yang, N. Kemik, E. Arenholz, M.D. Biegalski, H.M. Christen, Competing interactions in ferromagnetic/antiferromagnetic perovskite superlattices. Phys. Rev. B **80**, 180417(R) (2009)
68. K.H. Ahn, X.W. Wu, K. Liu, C.L. Chien, Magnetic properties and colossal magnetoresistance of La(Ca)MnO_3 materials doped with Fe. Phys. Rev. B **54**, 15299–15302 (1996)

69. A. Tiwari, K.P. Rajeev, Metal-insulator transition in $La_{0.7}Sr_{0.3}Mn_{1-x}Fe_xO_3$. J. Appl. Phys. **86**, 5175–5178 (1999)
70. M. Huijben, L.W. Martin, Y.-H. Chu, M.B. Holcomb, P. Yu, G. Rijnders, D.H.A. Blank, R. Ramesh, Critical thickness and orbital ordering in ultrathin $La_{0.7}Sr_{0.3}MnO_3$ films. Phys. Rev. B **78**, 094413 (2008)
71. R.V. Chopdekar, E. Arenholz, Y. Suzuki, Orientation and thickness dependence of magnetization at the interfaces of highly spin-polarized manganite thin films. Phys. Rev. B **79**, 104417 (2009)
72. A. Tebano, C. Aruta, S. Sanna, P.G. Medaglia, G. Balestrino, A.A. Sidorenko, R. De Renzi, G. Ghiringhelli, L. Braicovich, Evidence of orbital reconstruction at interfaces in ultrathin $La_{0.67}Sr_{0.33}MnO_3$ films. Phys. Rev. Lett. **100**, 137401 (2008)
73. L.F. Kourkoutis, J.H. Song, H.Y.M. Hwang, Microscopic origins for stabilizing room-temperature ferromagnetism in ultrathin manganite layers. Proc. Natl. Acad. Sci. USA **107**, 11682–11685 (2010)
74. M. Izumi, Y. Ogimoto, T. Manako, M. Kawasaki, Y. Tokura, Interface effect and its doping dependence in $La_{1-x}Sr_xMnO_3/SrTiO_3$ superlattices. J. Phys. Soc. Jpn. **71**, 2621–2624 (2002)
75. R. Herger, P.R. Willmott, C.M. Schleputz, M. Bjorck, S.A. Pauli, D. Martoccia, B.D. Patterson, D. Kumah, R. Clarke, Y. Yacoby, M. Dobeli, Structure determination of monolayer-by-monolayer grown $La_{1-x}Sr_xMnO_3$ thin films and the onset of magnetoresistance. Phys. Rev. B **77**, 085401 (2008)
76. L.M. Berndt, V. Balbarin, Y. Suzuki, Magnetic anisotropy and strain states of (001) and (110) colossal magnetoresistance thin films. Appl. Phys. Lett. **77**, 2903–2905 (2000)
77. J.Z. Sun, D.W. Abraham, R.A. Rao, C.B. Eom, Thickness-dependent magnetotransport in ultrathin manganite films. Appl. Phys. Lett. **74**, 3017–3019 (1999)
78. E. Arenholz, S.O. Prestemon, Design and performance of an eight-pole resistive magnet for soft X-ray magnetic dichroism measurements. Rev. Sci. Instrum. **76**, 083908 (2005)
79. M. Abbate, F.M.F. de Groot, J.C. Fuggle, A. Fujimori, O. Strebel, F. Lopez, M. Domke, G. Kaindl, G.A. Sawatzky, M. Takano, Y. Takeda, H. Eisaki, S. Uchida, Controlled-valence properties of $La_{1-x}Sr_xFeO_3$ and $La_{1-x}Sr_xMnO_3$ studied by soft X-ray absorption spectroscopy. Phys. Rev. B **46**, 4511–4519 (1992)
80. F.M.F. de Groot, X-ray absorption and dichroism of transition metals and their compounds. J. Electron Spectrosc. **67**, 529–622 (1994)
81. E. Arenholz, G. van der Laan, F. Yang, N. Kemik, M.D. Biegalski, H.M. Christen, Y. Takamura, Magnetic structure of $La_{0.7}Sr_{0.3}MnO_3/La_{0.7}Sr_{0.3}FeO_3$ superlattices. Appl. Phys. Lett. **94**, 072503 (2009)
82. J. Luning, F. Nolting, A.O. Scholl, H.J.W. Seo, J. Fompeyrine, J.-P. Locquet, J. Stohr, Determination of the antiferromagnetic spin axis in epitaxial $LaFeO_3$ films by X-ray magnetic linear dichroism spectroscopy. Phys. Rev. B **67**, 214433 (2003)
83. S. Czekaj, F. Nolting, L.J. Heyderman, P.R. Willmott, G. van der Laan, Sign dependence of the X-ray magnetic linear dichroism on the antiferromagnetic spin axis in $LaFeO_3$ thin films. Phys. Rev. B **73**, 020401(R) (2006)
84. G. van der Laan, B.T. Thole, Strong magnetic X-ray dichroism in $2p$ absorption spectra of $3d$ transition-metal ions. Phys. Rev. B **43**, 13401 (1991)
85. J.W. Seo, E.E. Fullerton, F. Nolting, A. Scholl, J. Fompeyrine, J.-P. Locquet, Antiferromagnetic $LaFeO_3$ thin films and their effect on exchange bias. J. Phys. Condens. Matter **20**, 264014 (2008)
86. C. Aruta, C. Adamo, A. Galdi, P. Orgiani, B. Bisogni, N.B. Brookes, J.C. Cezar, P. Thakur, C.A. Perroni, G. de Filippis, V. Cataudella, D.G. Schlom, L. Maritato, G. Ghiringhelli, Evolution of magnetic phases and orbital occupation in $(SrMnO_3)_n/(LaMnO_3)_{2n}$ superlattices. Phys. Rev. B **80** (2009)
87. M. Izumi, Y. Murakami, Y. Konishi, T. Manako, M. Kawasaki, Y. Tokura, Structural characterization and magnetic properties of oxide superlattices $La_{0.6}Sr_{0.4}MnO_3/La_{0.6}Sr_{0.4}FeO_3$. Phys. Rev. B **60**, 1211–1215 (1999)

88. M. Gu, M.D. Biegalski, H.M. Christen, C. Song, N.D. Browning, Y. Takamura, Strain relaxation defects in perovskite oxide superlattices. J. Mater. Res. **27**, 1436 (2012)
89. F. Yang, N. Kemik, A. Scholl, A. Doran, A.T. Young, M.D. Biegalski, H.M. Christen, Y. Takamura, Correlated domain structure in perovskite oxide superlattices exhibiting spin–flop coupling. Phys. Rev. B **83** (2011)

Chapter 6
Half-Metallic and Magnetic Silicon Nanowires Functionalized by Transition-Metal Atoms

Engin Durgun and Salim Ciraci

Abstract In this paper we investigate the atomic structure and the mechanical, electronic, and magnetic properties of silicon nanowires (SiNWs) using first-principles plane wave calculations within density functional theory. We examined hydrogen-passivated SiNWs along the [001] direction and studied doping of 3*d* transition-metal (TM) atoms. Nanowires of different sizes are initially cut from the bulk silicon crystal in rod-like forms, and subsequently their atomic structures are relaxed before and also after the termination of surface dangling bonds by hydrogen atoms. We have first presented an extensive analysis of the atomic structure, stability, and the elastic and electronic properties of bare and hydrogen-terminated SiNWs. The energetics of adsorption and the resulting electronic and magnetic properties are examined for different levels of 3*d* TM atom coverage. Adsorption of TM atoms generally results in the magnetic ground state. The net magnetic moment increases with increasing coverage. While specific SiNWs acquire half-metallic behavior at low coverage, at high coverage ferromagnetic nanowires become metallic for both spin directions, and some of them have very high spin polarization at the Fermi level. Our results suggest that electronic and spintronic devices with conducting interconnects between them can be fabricated on a single SiNW at a desired order. We believe that our study will initiate new research on spintronic applications of SiNWs.

6.1 Introduction

One of the major obstacles in the miniaturization of solid state electronic devices has been the fabrication of interconnects having diameters compatible with the size

E. Durgun · S. Ciraci
UNAM-Institute of Materials Science and Nanotechnology, Bilkent University, Ankara 06800, Turkey

S. Ciraci (✉)
Department of Physics, Bilkent University, Ankara 06800, Turkey
e-mail: ciraci@fen.bilkent.edu.tr

B. Aktaş, F. Mikailzade (eds.), *Nanostructured Materials for Magnetoelectronics*, Springer Series in Materials Science 175, DOI 10.1007/978-3-642-34958-4_6,

of the devices they connect. In solid state electronics and also in nanoelectronics, interconnecting nano or molecular devices has remained a challenge for several decades.

Although the search for feasible interconnects in nanoelectronics is continuing, nanosized silicon nanowires (SiNWs) appear to be an attractive 1D material because of their well-known silicon-based microelectronic fabrication technology and their ability to be used directly on the Si-based chips. SiNWs display a diversity of electronic properties depending on the number of Si atoms in their cross section. The linear monatomic Si chain is metallic with a quantum ballistic conductance three times higher than that of gold [1–3]. However, the linear Si chain is metastable, and hence it changes to a metallic zigzag chain [1–3]. Stable nanowires made of Si pentagons perpendicular to the wire axis have been reported [4]. Based on the prediction of first-principles calculations, Si can also form tubular structures made of hexagons similar to that of carbon nanotubes. Depending on their chirality and diameter, these tubular structure can exhibit metallic or semiconducting behaviors [5].

SiNWs have been produced using various experimental methods [6–10]. The formation of an oxide layer around the SiNW with a minimum thickness of 1–3 nm appears to be a disadvantage [11]. Nevertheless, rod-like SiNWs with a diameter of 1.3 to 7 nm have been prepared more recently. The oxide layer can be removed from the surface, and the dangling bonds at the surfaces can be terminated with hydrogen [12]. The experimental findings have indicated a crystalline core surrounded by an outer surface for the atomic structure of the SiNWs. Whether this crystalline core is tetrahedral (diamond-like as in bulk Si) or any other arrangement of atoms has been the subject of further investigation. Fullerene-like (cage-like) nanowires have been proposed and investigated theoretically in Refs. [13, 14].

The thinnest SiNW (radius $R \sim 0.65$–3.5 nm) synthesized so far has been grown along the [110] and the [112] directions [12]. SiNWs with sizes of less than 10 nm have been also reported along different directions such as [001] [15], [110] [15, 16], [111] [16], and [112] [16]. Theoretically [001] oriented SiNW is the most studied wire in the literature. Rurali et al. [17] studied nonpassivated and undoped [001] SiNWs consisting of 57, 114, and 171 atoms by using ab initio techniques. They obtained energetically equivalent metallic and semimetallic reconstructions. Tight-binding density functional calculations on hydrogen-passivated SiNWs [18] have reported that, while [112] are the most stable ones, [001] wires have the widest energy band gap. The interaction of hydrogen-saturated SiNWs [001] with TM atoms has also been investigated [19].

Experimental and theoretical studies so far have shown that those SiNWs exhibit a wide range of physical and chemical properties, which may be of interest in technological applications [20].[1] Depending on whether the dangling bonds on

[1]Numerous theoretical studies on SiNW have been published in recent years. See for example: [21, 22].

their outer surface are saturated with hydrogen atoms and on the shape of their cross section, they exhibit semiconducting or metallic behavior. Usually, unsaturated dangling bonds on the outer surface attribute a metallic character to a SiNW. Upon saturation of these dangling bonds, a SiNW becomes a semiconductor. Moreover, the band gaps of semiconductor SiNWs vary with their diameter. The band gap and also the stability of a SiNW strongly depend on its diameter.

SiNWs can function in various electronic and optical applications like field effect transistors (FETs) [23], light emitting diodes [24], lasers [25], and interconnects. The conductance can be tuned by doping during the production process or by applying a gate voltage in a SiNW FET. In various device applications, such as diodes and transistors, n- and p-doped SiNWs [20, 26, 27] have also attracted interest. Furthermore, a growing research interest has been devoted to the functionalization of the SiNW surface with various species to study the chemical and biological sensitivity [28–30]. Hydrogen-saturated SiNW and GeNW, which have band gaps of different widths, can form pseudomorphic heterostructures [31]. It has been predicted that the periodic, hydrogen-saturated SiNW(N)/GeNW(N) heterostructure superlattices behave as a multiple quantum well structure with confined states [31].

This paper presents an extensive study on the structural, electronic, and magnetic properties of hydrogen-passivated SiNWs oriented along the [001] direction, as well as those functionalized by 3d transition metals (TMs). The organization of the paper is as follows. In the following section, we summarize essential aspects of the method and its relevant parameters used in the calculations. In Sect. 6.3 we present a systematic and brief summary of our results on the atomic structure, reconstruction, energetics, and mechanical and electronic properties of hydrogen-terminated SiNWs of different cross sections. The quantum confinement effects on the variation of the energy band gap is also analyzed. Section 6.4 deals with the functionalization of SiNWs with light TMs, such as Ti, Fe, Co, Cr, and Mn. First, the adsorption geometry and energetics are examined for the external and internal adsorption of a single TM atom (per primitive cell designated as $\Theta = 1$) on the surface of (inside of) SiNWs with different facets. It is found that TM-doped H-saturated SiNWs have a ferromagnetic ground state and that some of them exhibit half-metallic (HM) behavior with 100 % spin polarization at the Fermi level (E_F) [32, 33]. Upon increased coverage of TM atoms (corresponding to $\Theta = n$, n being the number of TM atoms adsorbed per primitive cell) of H-saturated SiNWs, the HM character is disturbed, but spin polarization continues to be very high for specific nanowires. The high magnetic moment and also the high spin polarization for certain cases achieved at high Θ can be important for applications in biotechnology and spintronics. Our results are of fundamental and technological interest, since room temperature ferromagnetism has already been discovered in Mn^+-doped SiNW [34]. The paper ends with our conclusions in Sect. 6.5.

6.2 Method

We have performed first-principles plane wave calculations [35][2,3] within density functional theory (DFT) [39, 40]. All calculations for nonmagnetic, ferromagnetic, and antiferromagnetic states are carried out using ultra-soft pseudopotentials [36, 37, 41]. The results of these calculations have also been confirmed by calculations using the projector augmented wave (PAW) potential [42]. The exchange correlation potential has been approximated by generalized gradient approximation (GGA) [43] for both spin-polarized and spin-unpolarized cases. For partial occupancies we use the Methfessel–Paxton smearing method [44]. All structures have been treated within supercell geometry. We have used the periodic boundary conditions with cell dimensions of a and b ranging from 20 to 30 Å depending on the diameter of the SiNW in order to provide 10 Å vacuum space and along the wire axis $c = c_0$ (c_0 being the relaxed lattice constant of SiNW). In the self-consistent potential and total energy calculations the Brillouin zone (BZ) of the supercell is sampled in the **k**-space within Monkhorst–Pack scheme [45] by $(1 \times 1 \times 15)$ mesh points. A plane wave basis set with a maximum kinetic energy of 350 eV has been used.

All atomic positions and lattice constants are optimized by using the conjugate gradient method where the total energy and atomic forces are minimized. The convergence for energy is chosen as 10^{-6} eV between two ionic steps, and the maximum force allowed on each atom is 10^{-3} eV/Å. To relieve the constraints imposed by periodic boundary conditions, the calculations related to the study of reconstruction have been repeated using supercells with $c = 2c_0$ and $c = 4c_0$ (comprising double and quadruple unit cells of SiNW, respectively).

6.3 Properties of Hydrogen-Passivated Silicon Nanowires

In this paper, we consider rod-like hydrogen-passivated SiNWs oriented along the [001] direction with different diameters (or different numbers of Si atoms in their unit cell). The bare Si nanowire oriented along the [001] direction and having N Si atoms in the primitive unit cell is specified as SiNW(N). Similarly, a nanowire with all dangling bonds on the surface passivated by H atoms after relaxation is designated H-SiNW(N). If the dangling bonds are saturated before relaxation, it is specified as H-SiNW(N)-b (Fig. 6.1 upper panels). The sequence of structure optimization is crucial for the electronic properties. Here, the structure optimization of the H-SiNWs is achieved in two steps. Initially, the SiNWs are cut in rod-like forms from the bulk Si crystal. Subsequently, the initial atomic structure having the ideal bulk configuration is relaxed to yield the minimum total energy. In the second

[2]Numerical computations have been carried out by using VASP software [36, 37].

[3]Charge transfer, orbital hybridization, and local magnetic moments have been obtained from SIESTA code using local basis set [38].

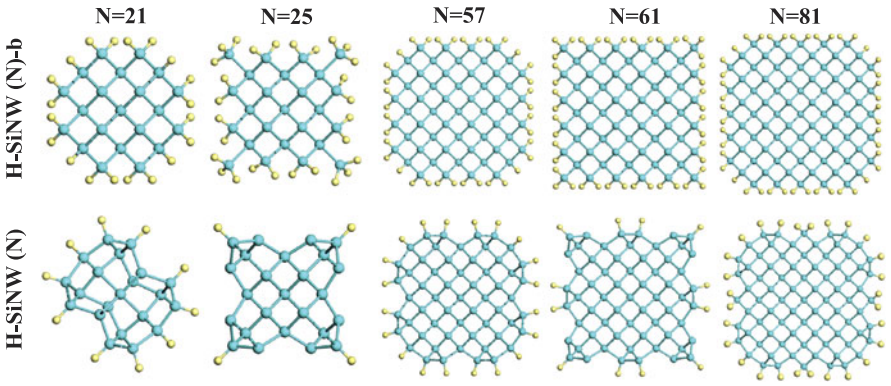

Fig. 6.1 *Upper panels*: Top views of optimized atomic structures of H-SiNW(N)-b (with $N = 21$, 25, 57, 61, and 81) (passivated before relaxation) along [001] direction. *Lower panels*: Top views of H-SiNW(N) (passivated after relaxation). *Large* (*blue*) and *small* (*yellow*) *balls* indicate Si and H atoms, respectively. Side views consist of two primitive unit cells (Color figure online)

step, hydrogen passivation of bare SiNWs is achieved by termination of the dangling bonds of Si atoms (which have a nearest neighbor coordination of less than four Si atoms) by H atoms. Subsequently, the whole structure including H atoms is optimized again (see Fig. 6.1 lower panels). An alternative method of structure optimization has also been carried out in several theoretical studies in a single step: First, the dangling bonds on the surface of the ideal bare SiNW cut from the bulk crystal are saturated by H atoms; subsequently, the whole structure has been optimized once. The latter optimization process, however, leads to a different electronic structure than the former. The two-step process is used in the present study, and note that the two-step process better mimics the actual growth process. The results for single-step relaxation, i.e., H-SiNW(N)-b, are also included for comparison. This section presents a comparative study of the atomic structure and reconstruction, electronic band structure, and elastic properties of structure optimized bare and H-passivated SiNWs.

6.3.1 Atomic Structure and Energetics

Figure 6.1 shows the atomic structures of the optimized H-SiNWs investigated in this paper. We considered wire geometries having 21, 25, 57, 61, and 81 Si atoms in the primitive unit cell. Among these wires, nanowires 21, 57, and 81 have a rather round cross section, while 25 and 61 have a square-like cross section.

The cohesive energy (per Si atom) of the bare SiNWs is calculated by $\overline{E}_c = E_T[\mathrm{Si}] - E_T[\mathrm{SiNW}(N)]/N$, in terms of the total energy of the free Si atom and the total energy of bare SiNW(N) with an optimized structure. According to this definition, $\overline{E}_c > 0$ indicates that the structure is stable with respect to the constituent free

Table 6.1 Lattice constant c_0, maximum radius R_{max}, cohesive energy per atom relative to free Si atom $\overline{E}_c$, binding energy of hydrogen relative to free H atom E_b, binding energy of hydrogen relative to H_2 molecule E'_b, minimum of band gap E_G, elastic constant κ of hydrogen-terminated SiNW(N). The κ values for hydrogen-terminated SiNWs before relaxation are given in parentheses

H-SiNW(N)	c_0 (Å)	R_{max} (Å)	$\overline{E}_c$ (eV)	E_b (eV)	E'_b (eV)	E_G	κ (eV/Å^2)
$N = 21$	5.85	11.03	4.05	4.14	0.74	0.7	172 (82)
$N = 25$	5.45	13.20	4.13	4.22	0.82	1.1	254 (96)
$N = 57$	5.39	17.76	4.24	4.28	0.88	1.7	394 (298)
$N = 61$	5.43	20.90	4.26	4.34	0.94	1.1	509 (303)
$N = 81$	5.40	21.6	4.27	4.28	0.88	1.6	532 (456)

atoms. The binding energy of hydrogen with respect to the free H atom is also of interest and is calculated by $E_b = (N_H E_T[H] + E_T[\text{SiNW}(N)] - E_T[\text{H-SiNW}])/N_H$, in terms of the total energy of structure optimized bare SiNW(N) and H-SiNW(N) terminated by N_H hydrogen atoms and the energy of the free H atom, $E_T[H]$. The binding energy of hydrogen relative to the H_2 molecule, E'_b, is obtained if $E_T[H]$ is replaced by $E_T[H_2]/2$. Calculated structure parameters, such as the lattice constant along the wire axis, c_0, the maximum radius of the cross section, the cohesive energy relative to the free Si atom, and the binding energy of the H atom are presented in Table 6.1.

In general, the lattice constant c_0 of optimized bare and H-SiNW(N) decreases with increasing N. Namely, the lattice constant is large for small N, but approaches the lattice constant of bulk Si. However, this trend is different for $N = 25$ and 61, which form a class of nanowires with square-like cross sections.

$\overline{E}_c$ is comparable with the cohesive energy of bulk crystal calculated to be 4.46 eV/atom, and as expected it increases with increasing N and converges to the bulk value (the bulk properties start to dominate with increasing diameter). The binding of H atoms is exothermic with positive binding energy for both E_b and E'_b.

The atomic structure of SiNWs has been analyzed by comparing the distribution of interatomic distances between various atoms (up to sixth nearest neighbor) with that of the ideal crystal. In Fig. 6.2, the distribution of interatomic distances is plotted for bare SiNW(N), H-SiNW(N), as well as H-SiNW(N)-b for $N = 21$, 57 (round cross section) and 25, 61 (square cross section).

The deviation from the ideal case is large for small N. The distribution of the first nearest neighbor distance is always sharp for all N. Significant deviations from the second, third, etc., nearest neighbor distances of the ideal bulk crystal are observed. In particular, already the peak related to the distribution of the second nearest neighbor distance starts to broaden. The structure of optimized bare SiNWs is healed by H-termination of the dangling bonds. This is seen by the fact that the distribution of distant nearest neighbors appears as peaks coinciding with the ideal structure. Additional peaks are related to surface reconstruction. Clearly, the distribution of H-SiNW(N)-b is very similar to that of ideal SiNW, since the surface relaxation is hindered by saturating the dangling bonds of ideal SiNW.

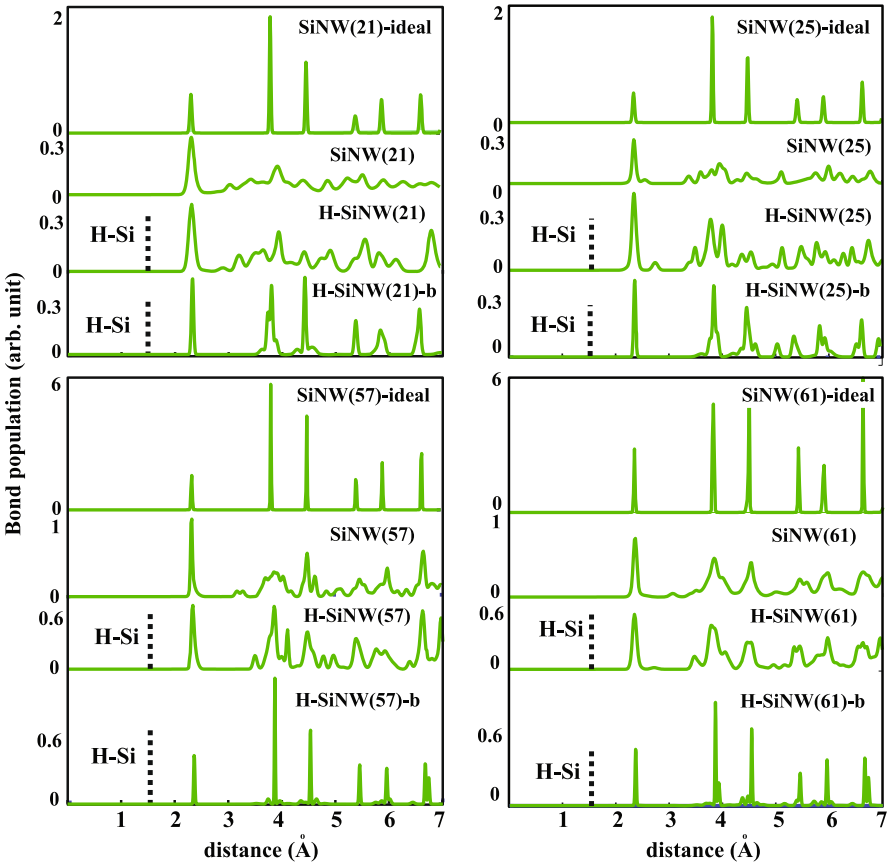

Fig. 6.2 *Upper curve* in each panel with numerals indicates the distribution of first, second, third, fourth, etc., nearest neighbor distances of ideal SiNW(N) for $N = 21$, 25, 57, and 61 as cut from the ideal Si crystal. The *second curve* is for structure optimized bare SiNW(N). The *third curve* is for structure optimized H-SiNW(N). The *bottom curve* corresponds to H-SiNW(N)-b (see text). *Vertical dashed line* corresponds to the distance of Si–H bond (Color figure online)

6.3.2 Reconstruction and Stability

The surface reconstruction of bare SiNWs is crucial for the resulting electronic properties and hence has been widely discussed [46–48]. To ensure that the structures discussed in Fig. 6.1 are minimum energy structures, we performed structure optimization by doubling and also by quadrupling the unit cell size, where the lattice constant of the supercell is taken as $c = 2c_0$ and $c = 4c_0$, respectively. As the initial structure, we always took the structure of ideal SiNW as cut from the ideal bulk crystal. All efforts to optimize the atomic structure of SiNWs resulted in the atomic structures presented in Fig. 6.1. All the surface atoms prefer to dimerize in order to minimize the total energy. Our results are in agreement with the studies consid-

ering the reconstruction patterns for the SiNWs in the same [001] growth direction [46–48]. Cao et al. [47] even labeled $N = 25$ and 61 as magic numbers, since they give the lowest energy dips in the plot of formation energies versus N. We also obtained the same geometry as Rurali et al. [48] for $N = 21$, 57, and 81 for [001] SiNWs with (110) facets, which confirms the results.

The stability of the wire structures presented in Fig. 6.1 is of prime importance. A thorough analysis of the stability of an SiNW is necessary before one considers its possible application as an electronic device. In addition to structural optimization using the conjugate gradient method, the stability of the structures has been tested by performing ab initio molecular dynamics (MD) calculations at 500 K for 1 ps with 1 fs time steps. In order to lift the constraints imposed by a single unit cell, MD calculations have been performed in a periodically repeating supercell with $c = 4c_0$.

6.3.3 Elastic Properties

The elastic properties of a SiNW can be deduced by calculating its elongation under a uniaxial tensile stress along the axis of the wire. The response of the wire to a uniaxial tensile stress can be formulated by the expression, $X_x = \kappa e_{xx}$, where κ is Young's modulus and e_{xx} is the strain along the x-direction. κ can be related to the elastic stiffness constants C_{11}, C_{12} in cubic crystals. However, since the SiNWs studied here have a high surface-to-volume ratio, it is better to define κ directly from the relation $\kappa = \partial E_T^2/\partial c_0^2$. To this end we calculated the self-consistent total energy E_T as a function of the lattice constant c_0 by relaxing all atomic positions under that constraint. The variation of κ with N is presented in Fig. 6.3 for bare and hydrogen-terminated SiNWs. One sees the following general trends from this figure. (i) The stiffness and the strength of a bare SiNW increase upon hydrogen termination of dangling bonds. (ii) The H-SiNW(N)-b is the weakest among all types, indicating that surface reconstruction makes SiNWs stronger. (iii) For bare SiNW κ increases with N almost linearly. SiNW(N)s with $N = 25$ and 61 show a slight deviation from the linear relation, perhaps due to their square-like cross section. The deviation from the linearity is enhanced in the case of H-SiNW(N)s. As compared to hydrogen-terminated SiNWs with round cross sections ($N = 21$, 57, and 81) hydrogen-terminated wires with square-like cross sections ($N = 25$ and 61) fall in a different category. It appears that upon H-termination the strength of the latter wires increases more relative to the wires with round cross sections. As with the electronic structure, these results point to the fact that the mechanical properties are sensitive to the geometry of the SiNW at small diameters.

6.3.4 Electronic Properties

Bare SiNWs are usually metallic due to the unsaturated bonds on the surface. For periodic structures these dangling bonds form surface bands, which occur in the

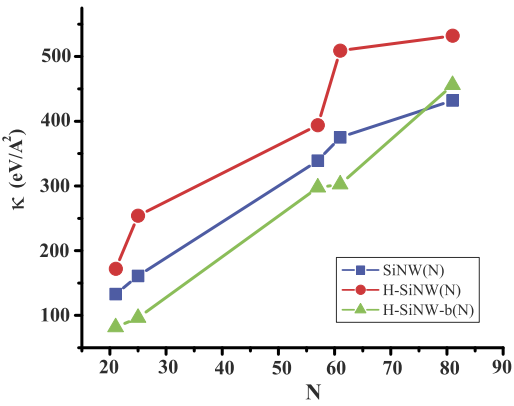

Fig. 6.3 Variation of elastic strength κ with number of atoms N in primitive unit cell of the optimized bare SiNWs, as well as H-SiNW(N) and H-SiNW(N)-b. Wires with $N = 21$, 57 and 81 have round cross section, whereas wires with $N = 25$ and 61 have square-like cross section (Color figure online)

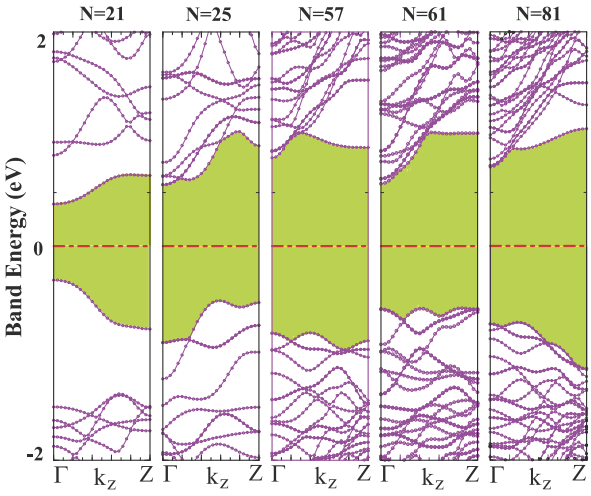

Fig. 6.4 Energy band structures of optimized H-SiNW(N) for $N = 21$, 25, 57, 61, and 81. *Shaded area* is the band gap. Zeros of band energies are set at the Fermi level (Color figure online)

band gap of the semiconductor and pin E_F. However, all these nanowires become semiconductors upon the termination of dangling bonds by H-atoms (Fig. 6.4).

Because of confinement effects E_G was known to increase with decreasing diameter D, displaying the relation $E_G \propto 1/D$. The expected variation of energy band gap with diameter is shown in Fig. 6.5. However, our study reveals that E_G depends not only on D, but also on the geometry of the cross section. In particular, we found that E_G of the structure optimized H-SiNW for a given N depends on whether the bare SiNW is relaxed before it is passivated with hydrogen or not. Note that E_G for bulk silicon is calculated as 0.65 eV, which indicates that H-SiNWs have much wider E_G than their crystal counterparts.

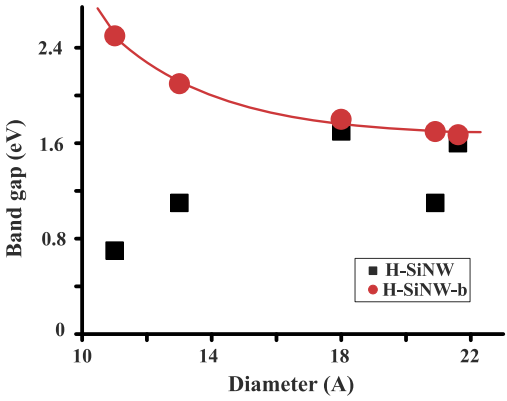

Fig. 6.5 The variation of band gap with respect to diameter for H-SiNW and H-SiNW-b (Color figure online)

6.4 Functionalization by Transition-Metal Atoms

6.4.1 Energetics of TM Adsorption

The electronic properties of hydrogen-terminated SiNWs can be modified through adsorption of transition-metal (TW) atoms on the surface of the wire. We considered the adsorption of 3*d* TM atoms (such as Ti, Cr, Mn, Fe, Co) on the surface of H-SiNW(N)s for $N = 21$, 25, and 57. The coverage of TM atoms Θ is defined as the number n of TM atoms adsorbed per primitive unit cell of the nanowire. Accordingly, one TM atom adsorbed to each primitive unit cell is designated as $\Theta = 1$. For the SiNWs under study, one can distinguish four to five different adsorption sites. The energetics of TM atom adsorption has been extensively examined for all these sites for $N = 21$, 25, and 57 (Fig. 6.6).

The binding energy corresponding to $\Theta = 1$ is calculated according to the expression, $E_B = E_T[\text{H-SiNW}(N)] + E_T[\text{TM}] - E_T[\text{H-SiNW}(N) + \text{TM}]$ in terms of the total energy of optimized H-SiNW(N) and TM adsorbed H-SiNW(N) (specified as H-SiNW(N) + TM) and the total energy of a linear chain of TM atoms having the same lattice parameter c_0 as H-SiNW(N), all calculated in the same supercell. Here the total energies, E_T, are obtained from spin-polarized calculations, since TM adsorbed H-SiNWs normally have a magnetic ground state. The calculated energy difference between spin-unpolarized and spin-polarized energy, namely, $\Delta E^m = E_T^{su} - E_T^{sp}$, is positive. Since the coupling between nearest neighbor TM atoms has been subtracted through the calculation of E_T[TM], E_B can be taken as the binding energy of a single isolated TM atom except for the effect of back donation of charge from TM–Si bonds to TM–TM bonds. As one expects, the binding energy relative to the bulk TM crystal E'_B is negative for $\Theta = 1$, indicating an endothermic process. However, in the case of high coverage of TM atoms corresponding to $\Theta = n$ with $n > 1$, $E'_B = (E_T[\text{H-SiNW}(N)] + nE_T[\text{TM}_{\text{bulk}}] - E_T[\text{H-SiNW}(N) + n\text{TM}])/n$ can be positive, since the coupling of adsorbed TM atoms is included. The calculated results for the binding energies, magnetic moments, and band gaps are presented

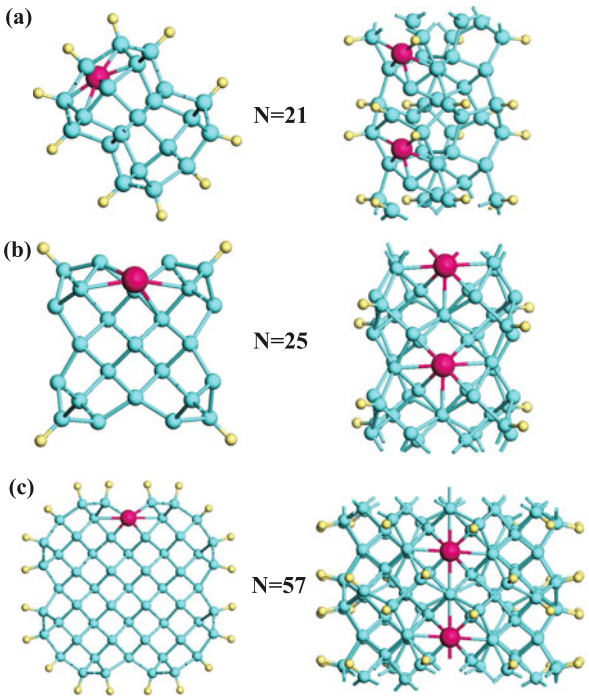

Fig. 6.6 Top and side views of (**a**) H-SiNW(21) + Co, (**b**) H-SiNW(25) + Cr(Mn), and (**c**) H-SiNW(57) + Cr(Mn)

Table 6.2 The binding energy relative to a free TM atom E_B, binding energy relative to the TM crystal E'_B, magnetic moment per unit cell μ, minimum band gap E_G (S: semiconductor, M: metal, HM: half-metal) of H-SiNW(N) covered with TM at $\Theta = 1$ for $N = 21, 25, 57$. TM = Ti, Fe, Mn, Cr, Co

	$N = 21$				$N = 25$				$N = 57$			
	E_B (eV)	E'_B (eV)	μ (μ_B)	E_G	E_B (eV)	E'_B (eV)	μ (μ_B)	E_G	E_B (eV)	E'_B (eV)	μ (μ_B)	E_G
Ti	3.74	−1.47	0	S	4.64	−0.51	0	M	3.69	−1.46	0	M
Fe	3.71	−1.07	2	S	3.52	−1.24	2	S	3.32	−1.43	2	S
Mn	1.79	–	3.12	M	2.27	–	3	HM	1.82	–	3	HM
Cr	1.81	−1.80	4.41	M	2.27	−1.34	4	HM	1.88	−1.73	4	HM
Co	4.41	−0.78	1	HM	4.12	−1.07	0	M	4.08	−1.06	1	S

for $N = 21$, 25, and 57 in Table 6.2 for the most energetic adsorption sites. In contrast to the usually weak binding of 3*d* TM atoms on single-wall carbon nanotubes, the binding energies of TM atoms on H-SiNW at $\Theta = 1$ are significant and involve charge transfer from TM atoms to Si atoms at close proximity [49, 50]. The transfer of charge from an adsorbed TM atom to the nanowire is estimated by using Mulliken analysis. It is 0.5 electron from Co to H-SiNW(21). The charge transfer from Cr to H-SiNW(25) and H-SiNW(57) is even higher and is calculated to be 0.8 and 0.9 electron, respectively. High charge transfer implies strong chemical interaction.

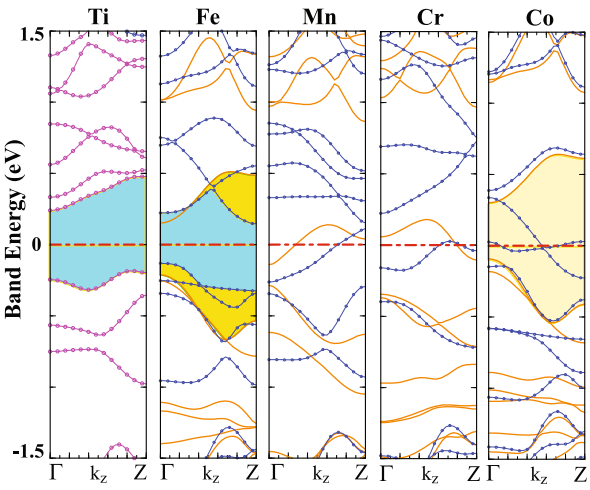

Fig. 6.7 Spin-polarized energy band structures of H-SiNW(21) covered by TM atoms at $\Theta = 1$. Band gaps of electrons with different spin directions are shown with different contrast. Bands described by *dotted* (*blue*) and *continuous* (*orange*) *lines* are for minority and majority spin states, respectively. Zeros of band energies are set at the Fermi level (Color figure online)

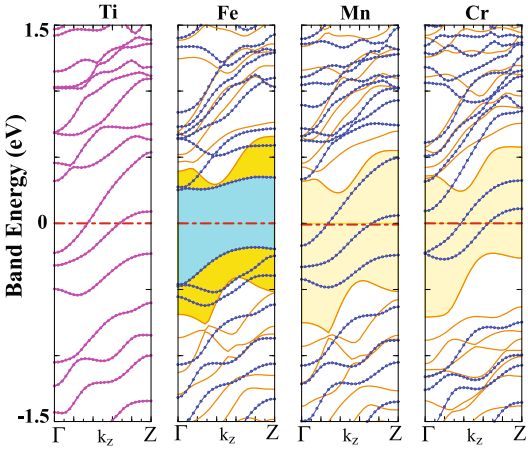

Fig. 6.8 Energy band structures of H-SiNW(25) covered by TM atoms at $\Theta = 1$. Band gaps of electrons with different spin directions are shown with different contrast. Bands described by *dotted* (*blue*) and *continuous* (*orange*) *lines* are for minority and majority spin states, respectively. Zeros of band energies are set at the Fermi level (Color figure online)

6.4.2 Electronic Band Structure

The electronic band structure of TM adsorbed H-SiNW(N)s at $\Theta = 1$ are shown in Figs. 6.7, 6.8, and 6.9. We obtain different types of electronic structures depending on the type of adsorbed TM atom and N. H-SiNW(21) + Ti is a nonmagnetic semiconductor, but it is a nonmagnetic metal for $N = 25$ and 57. For $N = 21$, 25, and 57, H-SiNW(N) + Fe is a ferromagnetic semiconductor with an integer number of spins per primitive cell. It has different band gaps for different spin directions. In contrast, H-SiNW(21) + Mn and H-SiNW(21) + Cr are ferromagnetic metals with a significant amount of net magnetic moment per primitive cell.

The situation with H-SiNW(21) + Co, H-SiNW(25) + Mn(Cr), and H-SiNW(57) + Mn(Cr) is different from the above cases (Fig. 6.10): These nanowires have a half-metallic ground state. Owing to the broken spin degeneracy,

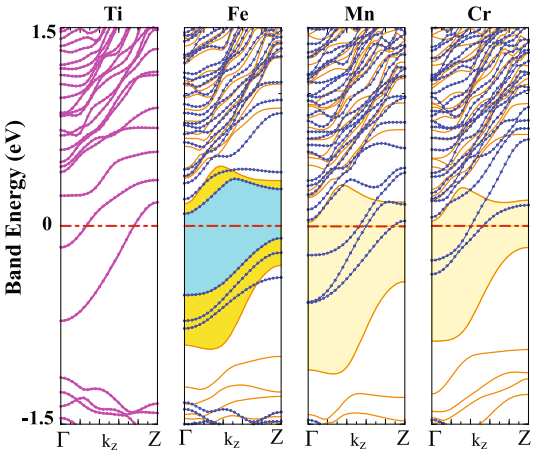

Fig. 6.9 Energy band structures of H-SiNW(57) covered by TM atoms at $\Theta = 1$. Band gaps of electrons with different spin directions are shown with different contrast. Bands described by *dotted* (*blue*) and *continuous* (*orange*) *lines* are for minority and majority spin states, respectively. Zeros of band energies are set at the Fermi level (Color figure online)

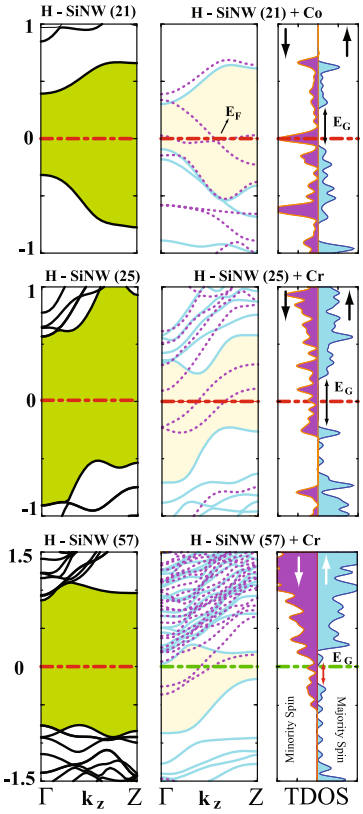

Fig. 6.10 Band structure and spin-dependent total density of states (TDOS) for $N = 21$, 25, and 57. *Left panels*: Semiconducting H-SiNW(N). *Middle panels*: Half-metallic H-SiNW(N) + TM. *Right panels*: Density of majority and minority spin states of H-SiNW(N) + TM. Bands described by *continuous and dotted lines* are majority and minority bands. Zero of energy is set to E_F

energy bands, $E_n(\mathbf{k}, \uparrow)$ and $E_n(\mathbf{k}, \downarrow)$, split, and the nanowire remains an insulator for one spin direction of the electrons, but becomes a conductor for the opposite spin

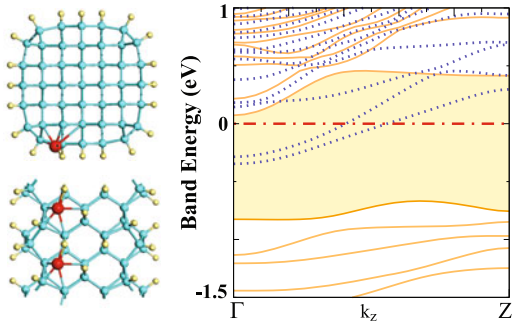

Fig. 6.11 The structure (**a**) and the energy band diagram of (**b**) H-SiNW(45) + Cr for $\Theta = 1$. Bands described by *dotted* (*blue*) and *continuous* (*orange*) *lines* are for minority and majority spin states, respectively. Zeros of band energies are set at the Fermi level

direction. The densities of the majority and minority spin states, namely $D(E, \uparrow)$ and $D(E, \downarrow)$, display a 100 % spin polarization P at E_F,

$$P = \big[D(E_F, \uparrow) - D(E_F, \downarrow)\big]/\big[D(E_F, \uparrow) + D(E_F, \downarrow)\big]. \tag{6.1}$$

The obtained results have also been checked for H-SiNW(45), which has an alternative and different facet (a more round cross section), even though it is less energetic than the other types discussed in the paper. Interestingly, external adsorption Cr(Mn) also makes H-SiNW(45) half-metallic with a similar band structure to H-SiNW(57) + Cr(Mn), as shown in Fig. 6.11.

For the half-metallic nanowires ΔE^m was calculated to be 0.04, 0.92, and 0.94 eV. A comparison of the bands of H-SiNW(N) in Fig. 6.4 with those of H-SiNW(N) + TM in Figs. 6.7, 6.8, and 6.9 reveals that the bands gaps of H-SiNW are modified and reduced for one spin direction. On the other hand, two or three bands of the opposite spin states cross E_F and attribute a metallicity to the nanowire. These metallic bands are composed of TM 3d and Si 3p hybridized states with higher TM contribution.

The half-metallic state has been a subject of interest since it was first predicted by de Groot et al. [32]. Initial efforts have been devoted to realize half-metals using Heusler alloys or TM-doped compound semiconductors in 3D crystals and in thin films [51, 52]. Qian et al. [53] have proposed that half-metallic heterostructures can be formed from δ-doped Si crystals. Recently, Son et al. [54] predicted half-metallic properties of graphene nanoribbons under bias voltage. Earlier, stable 1D half-metals were also predicted for TM atom-doped armchair single-wall carbon nanotubes [55, 56] and linear carbon chains [57].

It is well known that the band gap is underestimated by DFT. At this point we address the question of whether the half-metallic ground state predicted using DFT is realistic or an artifact. Since the present calculations predict a band gap between occupied and unoccupied majority spin bands, the semiconducting state should be realistic; the actual band gap may be larger than we predict. The metallic minority spin bands in the gap are reminiscent of the linear TM chain having the same lattice constant as H-SiNW(N) + TM. The dispersion of these bands increases in the half-metallic state due to indirect TM–TM interaction via Si atoms at the close proximity of adsorbed TM atoms. A similar band structure is obtained when the calculations are repeated with hybrid functionals [58] which yield the correct band

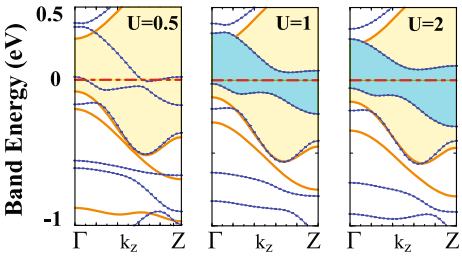

Fig. 6.12 Energy band structures of H-SiNW(21) + Co calculated by using LDA + U method for different values of U (Color figure online)

gap for bulk silicon. Briefly, we believe that the present conclusion concerning the half-metallic state is realistic and that the underestimated band gap does not have an essential affect, as long as the optical properties of a H-SiNW + TM are not concerned.

6.4.3 Stability of Half-Metallic State

Whether the half-metallic ground state is robust under deformation is another issue we address. We found that under uniaxial compression stress the minimum of the conduction band of the majority spin states rises above E_F. The minimum of the conduction band is, however, lowered under tensile stress to close the band gap. Therefore, the half-metallic state is sensitive to the tensile strain for nanowires having the conduction band edge close to E_F. In our case, since the conduction band edge of H-SiNW(25) + Cr(Mn) is away from E_F, their half-metallic state is robust. For H-SiNW(57) + Cr(Mn), with conduction band edges close to E_F, the semiconducting state for the majority spin bands may transform to semimetal at high tensile strain.

Since the H-SiNW + TM nanowire is 1D, the metallic minority spin bands crossing E_F are usually prone to Peierls distortion. The form of the bands shown in Figs. 6.8 and 6.9 eliminates the possibility of Peierls distortion. However, H-SiNW(21) + Co, which has metallic bands crossing at E_F, can become a semiconductor for both spin directions under Peierls distortion.

Another source of instability can be the on-site Coulomb interaction. It has been argued that the spin-dependent GGA may fail to properly represent localized 3d electrons. It may be possible that on-site repulsive Coulomb interaction destroys the half-metallic state. To examine the effect of on-site Coulomb repulsion, we carried out LDA + U calculations [59]. The energy band structures of half-metallic nanowires calculated for different values of U are shown in Figs. 6.12 and 6.13. Based on this analysis, although H-SiNW(21) + Co may not be stable and may change to a ferromagnetic semiconductor since the metallic bands split even at $U = 0.5$, H-SiNW(25) + Cr(Mn) can keep the half-metallic state even for $U = 4$. As an intermediatory situation, H-SiNW(57) + Cr(Mn) can keep their half-metallic states until $U \sim 1$.

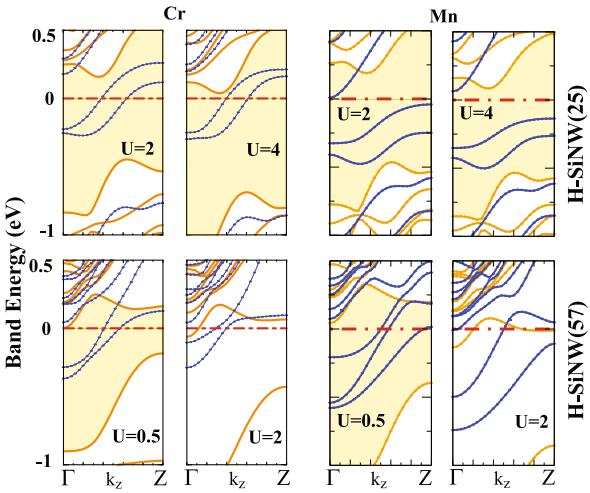

Fig. 6.13 Energy band structures of H-SiNW(25) + Cr(Mn) and H-SiNW(57) + Cr(Mn) calculated by using LDA + U method for different values of U (Color figure online)

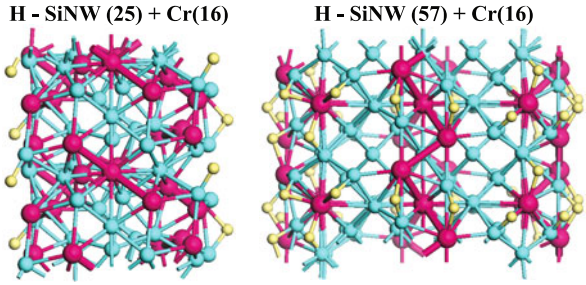

Fig. 6.14 The structure of H-SiNW(25) + Cr(16) and H-SiNW(57) + Cr(16). The *yellow*, *blue*, and *red balls* indicate H, Si, and Cr atoms, respectively

Note that the half-metallic state predicted in this study can occur in periodic and infinite structures. However, the adsorption of TM atoms on a H-SiNW cannot be perfect and periodic. The size of a half-metallic H-SiNW + TM as a spintronic device has to be finite. As a result, the deviations from the perfect and periodic structure may cause the spin polarization at E_F, P, to decrease from the perfect value $P = 1.0$. This means the destruction of the ideal half-metallicity. The ideal half-metallic state can also be destroyed when $\Theta > 1$. Nonetheless, even if $P < 1.0$, one can still meet the requirements for specific spintronic devices if a high spin polarization is achieved at E_F. Here, we have examined the electronic and magnetic properties of H-SiNW + TM at high TM coverage (Fig. 6.14) with the objective of achieving high spin polarization at high Θ.

Figure 6.15 shows the calculated density of the majority and minority spin states of H-SiNW(25) and H-SiNW(57) covered with Cr for different values of Θ. H-SiNW(25) + Cr, which is a half-metal with $\mu = 4\ \mu_B$ and $P = 1.0$ at $\Theta = 1$, becomes a ferromagnetic metal for both spin directions with $\mu = 32.3\ \mu_B$ and $P = 0.84$ at $\Theta = 8$. Clearly, the half-metallic state disappeared, but due to the high spin polarization this nanowire can still be used as a spintronic material. Upon increasing Θ to 16, spin polarization decreased to $P = 0.22$. E_F H-SiNW(57) + Cr

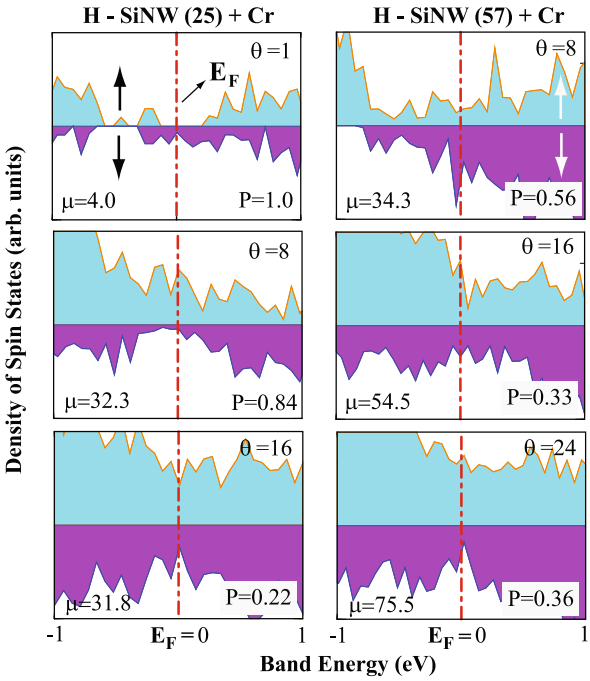

Fig. 6.15 Density of majority $D(E,\uparrow)$ (*dark*) and minority $D(E,\downarrow)$ (*light*) spin states of H-SiNW(25) + Cr and H-SiNW(57) + Cr for different coverage Θ of TM atoms (i.e., number of TM atoms per cell). For each case the calculated polarization P and net magnetic moment μ (in Bohr magnetons per cell) are shown in corresponding panels (Color figure online)

at $\Theta = 8$ has $P = 0.56$ and $\mu = 34.3\ \mu_B$. The net magnetic moment per primitive cell increases to 75.5 μ_B while P decreases to 0.36. It appears that P as well as μ exhibit variations depending on Θ, N, and the type of TM atom. One can achieve high P by covering specific H-SiNWs with TM atoms for spintronic applications.

6.4.4 *Internal Adsorption of Cr*

Having analyzed the possible adsorption sites of TM atoms on the surface of SiNW and its effects on electronic and magnetic properties, we next consider the Cr atom held at an interstitial site of H-SiNW(25) and H-SiNW(57) nanowires. This situation can be realized when a TM atom can diffuse below the surface at high temperature. A possible interstitial site is expected to be the one shown in Fig. 6.16, which is close to a hollow zone, and the others can be deep inside. After relaxation it is found that the Cr atom can settle into a cage of seven Si atoms without deforming H-SiNW(25) and [H-SiNW(57)]; their total energy is only 10 [16] meV higher than the most energetic configuration obtained for the adsorption of Cr to their surface, but E_b is slightly reduced and is calculated as 2.27 [1.86] eV. We found that the ground state of the system is metallic for H-SiNW(25), as shown in Fig. 6.16(a), with a magnetic moment of 2.93 μ_B per cell. The interaction of Cr with more Si atoms and hence the hybridization of more Cr $3d$ and Si $3p$ orbitals destroys the HM behavior and makes the wire metallic. When the energy band structure in Fig. 6.16 is compared

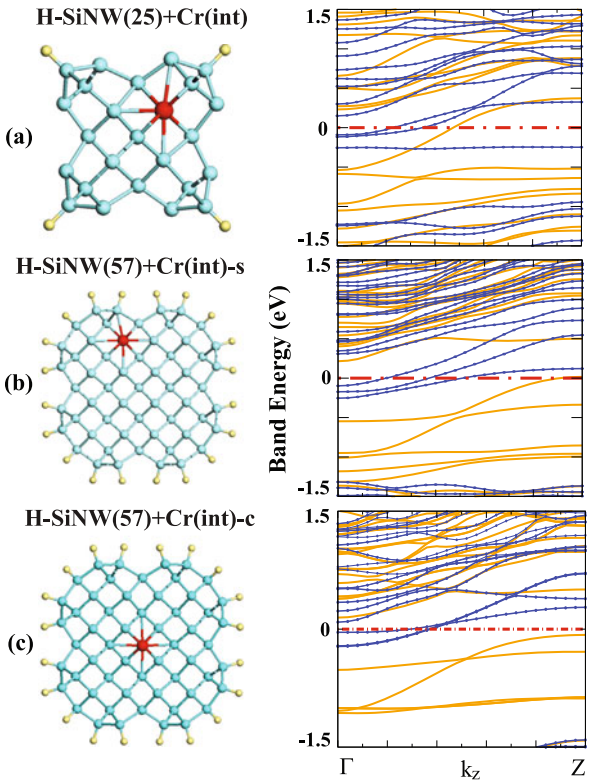

Fig. 6.16 The atomic structures of the cross section of (**a**) H-SiNW(25) + Cr(int) and (**b**), (**c**) H-SiNW(57) + Cr(int), where Cr is placed at the interstitial sites below the surface. *Light* (*orange*) and *dotted* (*blue*) bands correspond to the majority and minority spin states

with the external counterpart, it is seen that the effects of the interstitial site are more dramatic for H-SiNW(25), which has a smaller radius. According to the band structure displayed in Fig. 6.16(b), SiNW(57) + Cr(int) appears to be half-metallic except that the highest valence band of majority spins touches E_F at the Z-point of the Brillouin zone. The net magnetic moment is calculated to be 3.83 μ_B per cell. When the Cr atom diffuses inside H-SiNW(57) (Fig. 6.16(c)), the half-metallic state becomes stable again with a net $\mu = 4.0\ \mu_B$. This indicates that the position and also the deepness affect the electronic and magnetic properties for interstitial adsorption.

6.5 Conclusions

We investigated the atomic structure and the elastic, electronic, and magnetic properties of small diameter silicon nanowires oriented along the [001] direction. We considered hydrogen-passivated, and 3*d* TM (Ti, Fe, Mn, Cr, Co) decorated SiNWs. Here we summarize some important predictions of our study. (i) The structure of the ideal rods (i.e., SiNWs having ideal bond distances and bond angles) cut from the bulk Si crystal undergoes massive reconstruction as a result of structure optimization. (ii) Structure optimized bare SiNWs are generally metallic due to surface

dangling bonds. (iii) Upon passivation of dangling bonds with hydrogen atoms, the dangling bond surface states disappear, and the metallic nanowire becomes a semiconductor with a sizable band gap. It is known that, due to confinement effects, the band gap normally increases with decreasing diameter in the range of 1 to 2 nm, but is stabilized at a constant value for large diameters. However, it is found that this rule is valid if the bare SiNW is relaxed after its passivation with hydrogen atoms; it follows another trend if it is passivated before hydrogen saturation. (iv) The mechanical properties and hence the strength of bare SiNWs investigated in this paper vary when their surface is passivated with hydrogen atoms. Interestingly, square-like cross sections are found to be slightly stronger than round-like cross sections. (v) 3*d* TM atoms can be adsorbed on specific sites on the surface of hydrogen-passivated SiNWs with significant binding energy, and they attribute magnetic properties. At low coverage of TM atoms, H-SiNWs become either ferromagnetic insulators or half-metallic depending on the type of adsorbate, as well as the diameter of the nanowire. Half-metallic nanowires are insulators (semiconductors) for one spin direction of the electrons, but become metal for the opposite spin direction. Further analysis based on LDA + U calculations shows that half-metallic properties are robust for specific nanowires. (vi) When covered with more TM atoms, the perfect half-metallic state of the H-SiNW is disturbed, but for certain cases, the spin polarization at E_{F} continues to be high for applications as spin valves. The high magnetic moment obtained at high TM coverage is another remarkable result which may lead to the fabrication of nanomagnets for various applications. (vii) Cr atoms held at interstitial sites below the surface may also give rise to a half-metallic ground state.

In conclusion, we predict that silicon nanowires can gain a wide range of interesting properties when they are functionalized with TM atoms, becoming half-metals, 1D ferromagnetic semiconductors, or ferromagnetic metals and nanomagnets. The present results hold promise for the use of silicon nanowires functionalized by 3*d* TM atoms in spintronic applications including magnetoresistance, spin valves, and nonvolatile memories.

Acknowledgements This work has been partially supported by TUBITAK under Grant No. TBAG-104T536.

References

1. S. Tongay, R.T. Senger, S. Dag, S. Ciraci, Phys. Rev. Lett. **93**, 136404 (2004)
2. S. Tongay, S. Dag, E. Durgun, R.T. Senger, S. Ciraci, J. Phys. Condens. Matter **17**, 3823 (2005)
3. R.T. Senger, S. Tongay, S. Dag, E. Durgun, S. Ciraci, Phys. Rev. B **71**, 235406 (2005), and references therein
4. P. Sen, O. Gulseren, T. Yildirim, I.P. Batra, S. Ciraci, Phys. Rev. B **65**, 235433 (2002)
5. E. Durgun, S. Tongay, S. Ciraci, Phys. Rev. B **72**, 075420 (2005)
6. D.P. Yu, C.S. Lee, I. Bello, X.S. Sun, Y.H. Tang, G.W. Zhou, Z.G. Bai, Z. Zhang, S.Q. Feng, Solid State Commun. **105**, 403 (1998)
7. J. Hu, T.W. Odom, C.M. Lieber, Acc. Chem. Res. **32**, 435 (1999)

8. K. Hiruma, M. Yazawa, T. Katsuyama, K. Ogawa, K. Haraguchi, M. Koguchi, H. Kakibayashi, J. Appl. Phys. **77**, 447 (1995)
9. W.Q. Han, S.S. Fan, Q.Q. Li, Y.D. Hu, Science **277**, 1278 (1997)
10. C.R. Martin, Science **266**, 1961 (1994)
11. Y.F. Zhang, L.S. Liao, W.H. Chan, S.T. Lee, R. Sammynaiken, T.K. Sham, Phys. Rev. B **61**, 8298 (2000)
12. D.D.D. Ma, C.S. Lee, F.C.K. Au, S.Y. Tong, S.T. Lee, Science **299**, 1874 (2003)
13. M. Menon, E. Richter, Phys. Rev. Lett. **83**, 792 (1999)
14. B. Marsen, K. Sattler, Phys. Rev. B **60**, 11593 (1999)
15. J.D. Holmes, K.P. Johnston, R.C. Doty, B.A. Korgel, Science **287**, 1471 (2000)
16. Y. Wu, Y. Cui, L. Huynh, C.J. Barrelet, D.C. Bell, C.M. Lieber, Nano Lett. **4**, 433 (2004)
17. R. Rurali, N. Lorente, Phys. Rev. Lett. **94**, 026805 (2005)
18. R.Q. Zhang, Y. Lifshitz, D.D.D. Ma, Y.L. Zhao, Th. Frauenheim, S.T. Lee, S.Y. Tong, J. Chem. Phys. **123**, 144703 (2005)
19. E. Durgun, D. Cakir, N. Akman, S. Ciraci, Phys. Rev. Lett. **99**, 256806 (2007)
20. A.K. Singh, V. Kumar, R. Note, Y. Kawazoe, Nano Lett. **6**, 920 (2006)
21. Q. Wang, Q. Sun, P. Jena, Phys. Rev. Lett. **95**, 167202 (2005)
22. Q. Wang, Q. Sun, P. Jena, Nano Lett. **5**, 1587 (2005)
23. Y. Cui, Z. Zhong, D. Wang, W.U. Wang, C.M. Lieber, Nano Lett. **3**, 149 (2003)
24. Y. Huang, X. Duan, C.M. Lieber, Small **1**, 142 (2005)
25. X. Duan, Y. Huang, R. Agarwal, C.M. Lieber, Nature (London) **421**, 241 (2003)
26. M.V. Fernandez-Serra, Ch. Adessi, X. Blase, Phys. Rev. Lett. **96**, 166805 (2006)
27. E. Durgun, N. Akman, C. Ataca, S. Ciraci, Phys. Rev. B **76**, 245323 (2007)
28. Y. Cui, Q. Wei, H. Park, C.M. Lieber, Science **293**, 1289 (2001)
29. X.T. Zhou, J.Q. Hu, C.P. Li, D.D.D. Ma, C.S. Lee, S.T. Lee, Chem. Phys. Lett. **369**, 220 (2003)
30. J. Hahm, C.M. Lieber, Nano Lett. **4**, 51 (2004)
31. N. Akman, E. Durgun, S. Cahangirov, S. Ciraci, Phys. Rev. B **76**, 245427 (2007)
32. R.A. de Groot, F.M. Mueller, P.G. van Engen, K.H.J. Buschow, Phys. Rev. Lett. **50**, 2024 (1983)
33. W.E. Pickett, J.S. Moodera, Phys. Today **54**, 39 (2001)
34. H.W. Wu, C.J. Tsai, L.J. Chen, Appl. Phys. Lett. **90**, 043121 (2007)
35. M.C. Payne, M.P. Teter, D.C. Allan, T.A. Arias, J.D. Joannopoulos, Rev. Mod. Phys. **64**, 1045 (1992)
36. G. Kresse, J. Hafner, Phys. Rev. B **47**, 558 (1993)
37. G. Kresse, J. Furthmuller, Phys. Rev. B **54**, 11169 (1996)
38. P. Ordejon, E. Artacho, J.M. Soler, Phys. Rev. B **53**, R10441 (1996)
39. W. Kohn, L.J. Sham, Phys. Rev. **140**, A1133 (1965)
40. P. Hohenberg, W. Kohn, Phys. Rev. **136**, B864 (1964)
41. D. Vanderbilt, Phys. Rev. B **41**, 7892 (1990)
42. P.E. Blochl, Phys. Rev. B **50**, 17953 (1994)
43. J.P. Perdew, J.A. Chevary, S.H. Vosko, K.A. Jackson, M.R. Pederson, D.J. Singh, C. Fiolhais, Phys. Rev. B **46**, 6671 (1992)
44. M. Methfessel, A.T. Paxton, Phys. Rev. B **40**, 3616 (1989)
45. H.J. Monkhorst, J.D. Pack, Phys. Rev. B **13**, 5188 (1976)
46. S. Ismail-Beigi, T. Arias, Phys. Rev. B **57**, 11923 (1998)
47. J.X. Cao, X.G. Gong, J.X. Zhong, R.Q. Wu, Phys. Rev. Lett. **97**, 136105 (2006)
48. R. Rurali, A. Poissier, N. Lorente, Phys. Rev. B **74**, 165324 (2006)
49. E. Durgun, S. Dag, V.M.K. Bagci, O. Gulseren, T. Yildirim, S. Ciraci, Phys. Rev. B **67**, 201401(R) (2003)
50. E. Durgun, S. Dag, V.M.K. Bagci, O. Gulseren, T. Yildirim, S. Ciraci, J. Phys. Chem. B **108**, 575 (2004)
51. J.-H. Park, E. Vescovo, H.-J. Kim, C. Kwon, R. Ramesh, T. Venkatesan, Nature (London) **392**, 794 (1998)

52. H. Akinaga, T. Manago, M. Shirai, Jpn. J. Appl. Phys. **2**(39), L1118 (2000)
53. M.C. Qian, C.Y. Fong, K. Liu, W.E. Pickett, J.E. Pask, L.H. Yang, Phys. Rev. Lett. **96**, 027211 (2006)
54. Y.-W. Son, M.L. Cohen, S.G. Louie, Nature **444**, 347 (2006)
55. C.-K. Yang, J. Zhao, J.P. Lu, Nano Lett. **4**, 561 (2004)
56. Y. Yagi, T.M. Briere, M.H.F. Sluiter, V. Kumar, A.A. Farajian, Y. Kawazoe, Phys. Rev. B **69**, 075414 (2004)
57. S. Dag, S. Tongay, T. Yildirim, E. Durgun, R.T. Senger, C.Y. Fong, S. Ciraci, Phys. Rev. B **72**, 155444 (2005)
58. E. Durgun, D.I. Bilc, S. Ciraci, Ph. Ghosez, J. Phys. Chem. C **116**, 15713 (2012)
59. S.L. Dudarev, G.A. Botton, S.Y. Savrasov, C.J. Humphreys, A.P. Sutton, Phys. Rev. B **57**, 1505 (1998)

Chapter 7
Magnetic and Magnetoresistive Properties of Thin Films Patterned by Self-Assembling Polystyrene Nanospheres

Marco Coïsson, Federica Celegato, Paola Tiberto, Franco Vinai, Luca Boarino, and Natascia De Leo

Abstract Self-assembling of polystyrene nanospheres (PNs) is a powerful technique for preparing large area (several mm^2) nanostructured thin films. Compared to conventional lithographic techniques (e.g. EBL), which have more resolution and are more versatile, but are limited to very small surface areas, self-assembling PN allows preparation of large nanostructured samples. This technique limits the shaping to only circular dot and antidot geometries which can be obtained in the hexagonal close-packed configuration.

In this paper, the self-assembling PN preparation technique will be thoroughly discussed, and the magnetic and magnetoresistive properties of dot and antidot arrays of $Ni_{80}Fe_{20}$, Ni, Co and Fe-based amorphous alloys will be investigated. All dot and antidot arrays have been obtained from monolayers of PN on Si substrates. The initial diameter of the spheres is 500 nm, and is reduced to 250–400 nm by reactive ion etching. The typical thickness of the magnetic material is approximately 10–30 nm for antidot samples, and in the 30–80 nm range for dot samples.

Both dot and antidot systems have been studied by means of scanning electron microscopy, atomic force and magnetic force microscopy, and alternating gradient field magnetometry, to record hysteresis loops. On antidot samples, magnetoresistance measurements have been carried out in the 5–300 K temperature range. The expected anisotropic magnetoresistance effect is observed, superimposed to a giant

M. Coïsson (✉) · F. Celegato · P. Tiberto · F. Vinai · L. Boarino · N. De Leo
Electromagnetics Division, INRIM, strada delle Cacce 91, 10135 Torino, Italy
e-mail: m.coisson@inrim.it

F. Celegato
e-mail: f.celegato@inrim.it

P. Tiberto
e-mail: p.tiberto@inrim.it

F. Vinai
e-mail: f.vinai@inrim.it

L. Boarino
e-mail: l.boarino@inrim.it

N. De Leo
e-mail: n.deleo@inrim.it

B. Aktaş, F. Mikailzade (eds.), *Nanostructured Materials for Magnetoelectronics*, Springer Series in Materials Science 175, DOI 10.1007/978-3-642-34958-4_7,

magnetoresistance effect on some systems. Co antidots also display an exchange bias effect below approximately 150 K, as evidenced by both magnetoresistance and low temperature hysteresis loop measurements. On dot samples, a typical vortex structure is observed, which depends on the material thickness and mean dot size. Preliminary magnetoresistance measurements on dot samples are also presented.

7.1 Introduction

The science and technology of functional materials received a great impetus by the ability to produce structures on a sub-micrometer scale. Nanofabrication and nanotechnology have allowed the manipulation of materials and the engineering of innovative materials and devices [1] for fundamental studies and for applications in the fields of sensors, biomedicine, information technology and energy storage, etc. [2–5]. Nanostructures and nanodevices made of magnetic materials are currently investigated in view of applications in magnetic storage, magnetic logic and shift registers, microwave devices, nano-oscillators, magnetic sensors and 'transistors' [6–15]. When developed in large arrays, the resulting photonic and magnonic crystals are particularly suited for the magneto-recording industry and high-frequency applications. In this context, large arrays of dots and antidots, made of some magnetic material, represent a widely studied configuration of magnetic nanostructures.

However, nanopatterning over large surface areas constitutes a technological challenge which has been faced with several different approaches [16]. Electron beam lithography (EBL) is characterized by a great versatility and a high resolution, but its serial writing process severely limits the surface area which can be patterned. On the contrary, if the versatility of EBL can be given up, 'parallel' writing techniques can be exploited, which have the ability to simultaneously write over large surface areas regular arrays of dots and antidots of sub-micrometer size. Nano-imprinting, deep UV lithography, X-ray lithography and chemical methods are among the most widely used techniques [17–19]. Bottom-up self-assembly methods are also extensively studied, because of their versatility, reduced costs and ability to cover large surface areas [20–24].

Among these last methods, self-assembling of nanoparticles or nanospheres is a low-cost alternative patterning technology particularly well suited for the preparation of arrays of dots or antidots covering a surface area of several square millimeters (mm^2) or larger [25, 26]. While nanoparticles with a sharp size (diameter) distribution can be synthesized by several bottom-up chemical processes, and can even be functionalized for different purposes, their dispersion over large substrates results in well-ordered, short-range periodic templates, with a lack of a long-range order and without a precise orientation on the macroscopic scale of the whole sample, of the periodic structure. Following the pioneering work of Hulteen et al. [25], commercially available polystyrene nanospheres (PNs) are currently widely used as masks for thin film deposition or pattern etching at a sub-micrometer scale.

Obtaining a nanostructure is usually just half of the challenge, as suitable characterization techniques must be employed to study its properties or to measure or

affect its characteristics as a function of some external controlling parameter (as required in sensors and devices in general). Large area arrays of dots and antidots prepared by self-assembling techniques ease the measurement processes as larger areas and more material are available. However, the interpretation of data is usually more difficult, as a long-range disorder makes results only statistically repeatable. In the case of arrays of dots and antidots made of some magnetic material, the large areas provided by self-assembling techniques allow one to exploit with success some common measurement setups. In particular:

- optical magnetometry, e.g. the magneto-optic Kerr effect (MOKE) is limited in resolution by the wavelength of the light, usually in the visible region. As a consequence, it is hardly useful for determining the domain configuration of true nanostructures. However, in the case of large arrays of dots or antidots, collective magnetization processes can be studied by means of MOKE systems, as they have enough resolution to detect the individual nanostructures (dots or holes, with diameters usually in the range of a few hundred nanometers) and a sufficiently wide field of view to integrate a good signal. As a long-range ordering is usually lacking in self-assembled patterns, a MOKE setup must be focused precisely on a well-ordered area if orientation-dependent properties have to be investigated. If this is not a requirement, averaged values over the different orientations of the pattern due to the intrinsic long-range disorder originating from the self-assembling technique can be acquired.
- conventional magnetometers (e.g. vibrating sample magnetometer, VSM, alternating gradient field magnetometer, AGFM, superconducting quantum interference device, SQUID) lack the sensitivity to characterize small arrays of nanostructures, let alone individual nanostructures. However, if the preparation technique allows the covering of large surface areas (usually of the order of 1 mm^2 or more), conventional magnetometers have enough sensitivity to measure hysteresis loops or other magnetization curves, provided that suitable corrections for the contributions of substrates and sample holders are applied. These magnetometers are rather versatile, as they allow magnetization measurements as a function not only of the applied magnetic field intensity, but also of its direction, of temperature and of time. They can measure magnetic properties only averaged over the whole sample volume, and are not able to provide any information on the local properties of the samples.
- magnetic force microscopy (MFM) is particularly well suited for the characterization of individual magnetic nanostructures or small arrays, provided that they are not too small, as the MFM resolution is usually of the order of a few tens of nanometers or more. However, in the case of large area patterns like those obtained by self-assembling techniques, MFM can provide a useful bridge between conventional magnetometry, which averages over the whole sample volume, and the local properties of the sample (individual dots or antidot regions with a regular pattern orientation).
- magnetoresistance (MR) measurements are a powerful technique for investigating both individual nanostructures and their arrays, as they usually have enough sensitivity to detect the presence of even a single magnetic domain wall [27, 28].

However, on individual nanostructures or on small arrays, electrical contacts have to be provided by means of complex lithographic processes, sometimes involving a step made with EBL followed by an additional step requiring optical lithography. Consequently, the complexity of the system grows. On the contrary, large area percolating nanostructures (like antidots) can be characterized by means of MR measurements, at room temperature and as a function of temperature, without a significant increase in complexity of the system. In fact, electrical contacts can be more easily provided to nanostructures covering a few mm^2 surface areas. Like conventional magnetometry, MR measurements probe the magnetization of the sample over its whole volume (or at least over the whole volume where the electrical current flows); as a consequence, the intrinsic long-range disorder induced by the self-assembling techniques must be taken into account when analysing the data.

Within this context, in this chapter we will be focusing on dot and antidot arrays of soft magnetic materials prepared by self-assembling polystyrene nanospheres (PNs), which are used as masks for sputter deposition or sputter etching. The preparation technique will be described in detail in Sect. 7.2 for both dot and antidot patterns. Magnetic domain configuration, magnetic properties and magnetoresistance measurements will be discussed in Sects. 7.3 and 7.4 respectively for antidots and dots. Some peculiar features of the studied nanopatterned systems will also be discussed.

7.2 Self-Assembling

Polystyrene nanospheres are commercially available with diameters ranging in the interval 100 nm–2 μm; additionally, there are several laboratory techniques for preparing them with the desired average size. Nanospheres with a diameter distribution as monodisperse as possible can then be used to prepare 2D arrays of nanostructures on substrates and thin films by means of several techniques [25, 29–31]. The samples studied in this chapter have been prepared by dispersing the nanospheres in a water-based colloidal solution. The nanospheres form a monolayer at the liquid-air interface, with a degree of order that can be controlled by affecting the repulsive forces of electrostatic origin among the nanospheres by adding alchool (which controls the floating level of the nanospheres on water and improves their spreading) and a surfactant (which promotes the aggregation of the nanoparticles into big crystals, even if composed of domains with different orientations). The 2D crystal developed at the liquid-air interface is then transferred to the substrate (which may already have been coated with a thin film) by dipping it into the solution and lifting it carefully. The solution then dries, and the 2D array of nanospheres remains on the substrate.

Figure 7.1 shows a scanning electron microscope (SEM) image of a 2D array of PNs on a Si substrate. The spheres have a diameter of 800 nm and form an array with the hexagonal close-packed configuration, which maximizes their areal density. As

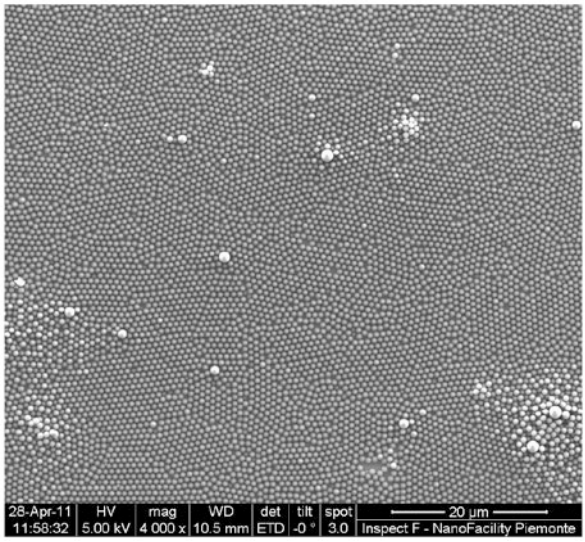

Fig. 7.1 SEM image of self-assembled PNs

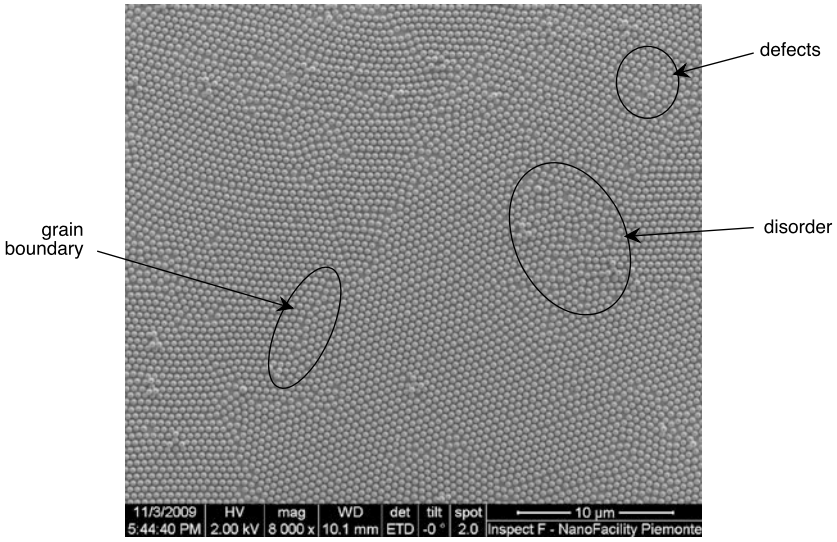

Fig. 7.2 SEM image of a monolayer of PNs. The *arrows* and the *selected regions* indicate 'grain boundaries', local disorder, point defects, as examples of possible defects of the lattice structure of the monolayer

can be seen from the figure, well-ordered crystals are formed with a typical lateral size of the order of 5–10 µm. 'Grain boundaries' develop between crystals with different orientations, and disorder and defects can be seen, e.g. in Fig. 7.2. If the solution in which the nanospheres are dispersed does not have the correct spreading

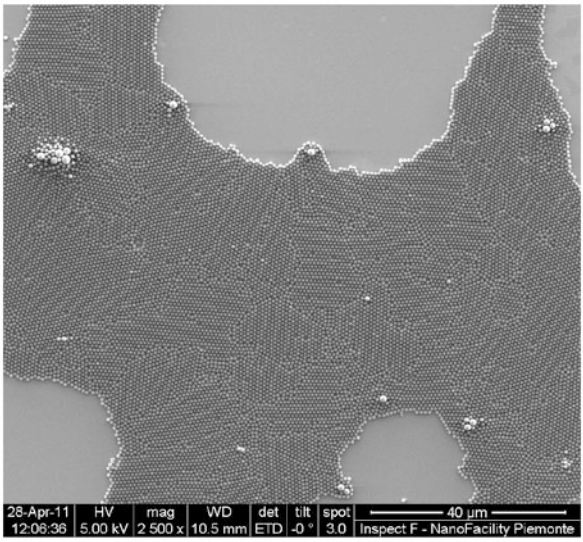

Fig. 7.3 SEM image of a very large portion of PNs, for a sample with a bad dispersion of the nanospheres. Regions not covered by the nanospheres can be seen, as well as smaller regions with two, three or more layers of nanospheres

of the nanoparticles, or if the substrate is not sufficiently clean, in certain portions of the sample the nanospheres can leave continuous portions of the substrate exposed, or occasionally arrange into multilayers (see Fig. 7.3).

A reactive ion etching (RIE) process, consisting in exposing the nanospheres to an oxygen plasma obtained by rf electromagnetic field ionization, attacks the surface of the spheres, while preserving their arrangement on the substrate. After exposure to an RIE process for a sufficiently long time (usually of the order of 100–300 s with an rf power of the order of 50–100 W), the diameter of the nanospheres can be reduced by 100–200 nm, while their center-to-center distance remains unchanged. In this way, larger portions of the substrate can be exposed to subsequent processes (such as sputter deposition or etching). Figure 7.4 shows a SEM image of an array of 500 nm spheres which have been exposed to an RIE process; as a result, their diameter is reduced to $\approx$400 nm, and significant portions of the substrate remain exposed. It has to be noted that excessive RIE power or time may result in damage to the nanospheres, which do not separate well and remain interconnected by small 'bridges' forming a percolating grid. These small 'bridges' may also result from residual monomers of surfactant present in the initial solution. An example is shown in Fig. 7.5. Depending on the applications, this effect may result in the deterioration of the properties of the final device. Additionally, if the 2D crystal of nanospheres is dispersed on a metallic film, exposure to an oxygen plasma may lead to undesired oxidation of the metal, which must be taken into account.

As the array of nanospheres can be dispersed on a bare substrate, or on a substrate on top of which a thin film (e.g. of some magnetic material) has already been prepared (e.g. by sputtering or thermal evaporation), two kinds of structures can be obtained. When the nanospheres are deposited on the bare substrate, RIE processing can be used to reduce their diameter, and subsequently a material can be deposited

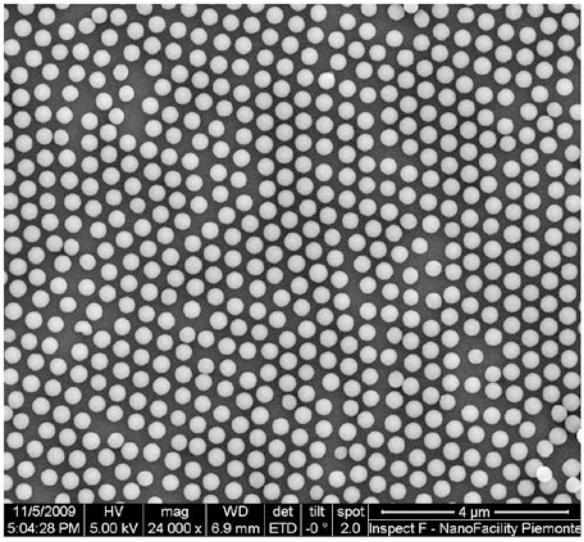

Fig. 7.4 SEM image of PNs reduced by means of RIE at 80 W for 3 minutes

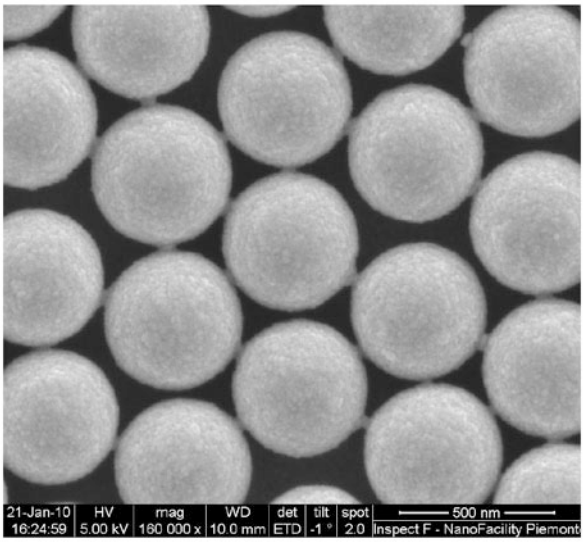

Fig. 7.5 SEM image of PNs reduced by means of RIE at 80 W for 2 minutes. Small 'bridges' connecting the nanospheres are visible

in the form of a film. The resulting structure, after the nanospheres have been removed by sonication or stripping, is an array of antidots, as shown in Fig. 7.6(a). Conversely, when the nanospheres are deposited on a thin film, RIE processing can be used to reduce their diameter and subsequently rf etching can be used to remove the material which is not protected by the nanospheres. After their removal by sonication or stripping, a dot array is obtained, as shown in Fig. 7.6(b). Both processes can be tailored with the optional RIE step. Antidot arrays are limited in thickness to ≈30–40 nm, as the gaps among the nanospheres tend to fill on top of them dur-

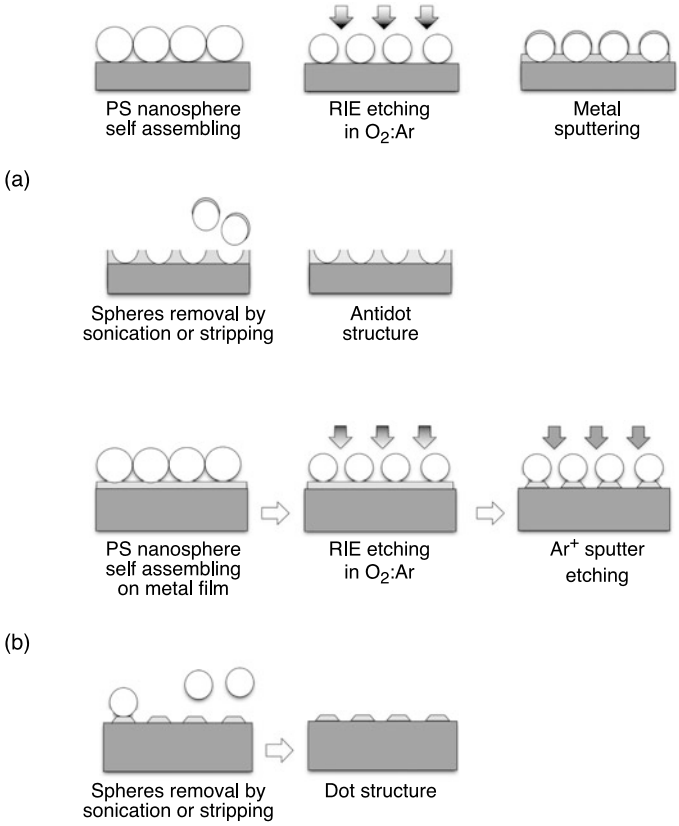

Fig. 7.6 Schematical representation of the preparation process of magnetic antidot (**a**) and dot (**b**) arrays using self-assembling of PNs [32]

ing the sputtering process, thus preventing the deposition of thicker metallic layers. In contrast, dot arrays can be obtained with fairly thick metallic layers, as the rf etching process used for removing the excess metal hardly affects the polystyrene nanospheres. Figures 7.7(a) and (b) show dot and antidot arrays with a thickness of 30 nm and 40 nm respectively, obtained with the above described preparation process.

7.3 Antidots

7.3.1 Domain Configuration

In magnetic antidot arrays prepared by self-assembling PNs, the magnetic domain configuration as observed by MFM is heavily determined by the arrangements of

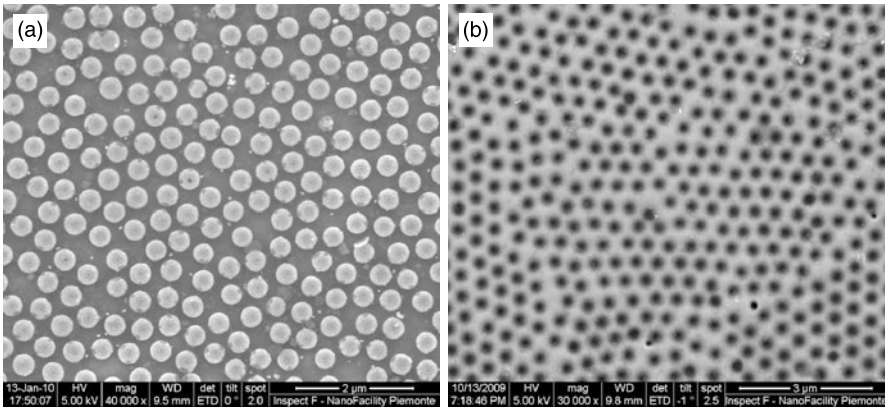

Fig. 7.7 (**a**) SEM image of a dot array of Co (30 nm thick). (**b**) SEM image of an antidot array of Ni (40 nm thick)

the holes in the film. An example is reported in Fig. 7.8, where the magnetic domain configuration (obtained through MFM) is shown at selected applied field values. The depicted region shows the interface between the patterned antidot array (on the right side of each image) and the continuous film, not previously covered by the nanospheres (on the left side of each image). A high contrast is visible between clear and dark regions, which indicate portions of the film where the field generated by the local magnetization points respectively away and toward the film. The magnetic domain configuration preserves a well-defined order over a region involving a few holes; then the orientation of the domains changes direction, even where the morphological order is excellent over a much larger scale. Upon application of a magnetic field, the magnetic domain configuration rearranges, as shown in Fig. 7.8. The applied field is not sufficient to saturate the sample, because of the high anisotropy induced by the presence of the holes, but the magnetic domains tend to align to the applied field and the degree of order of the magnetization patterns increases. Upon removing the field, the sample returns to the magnetic remanence, which is characterized by a more disordered domain configuration.

Another example, this time for a Ni antidot array, is shown in Fig. 7.9. Magnetic domain patterns extending to a few adjacent holes are visible; also in this case, the excellent order in the topography is not reflected in a long-range order of the magnetic configuration, which at the magnetic remanence appears to be irregular over a scale of the order of 1–2 micrometers. The lower contrast with respect to Fig. 7.8 is probably attributed to the lower saturation magnetization of Ni with respect to Co.

7.3.2 Magnetic and Magnetoresistive Properties

As described in Sect. 7.2, the preparation of antidot structures by means of self-assembling PNs involves the deposition of the magnetic film on top of the

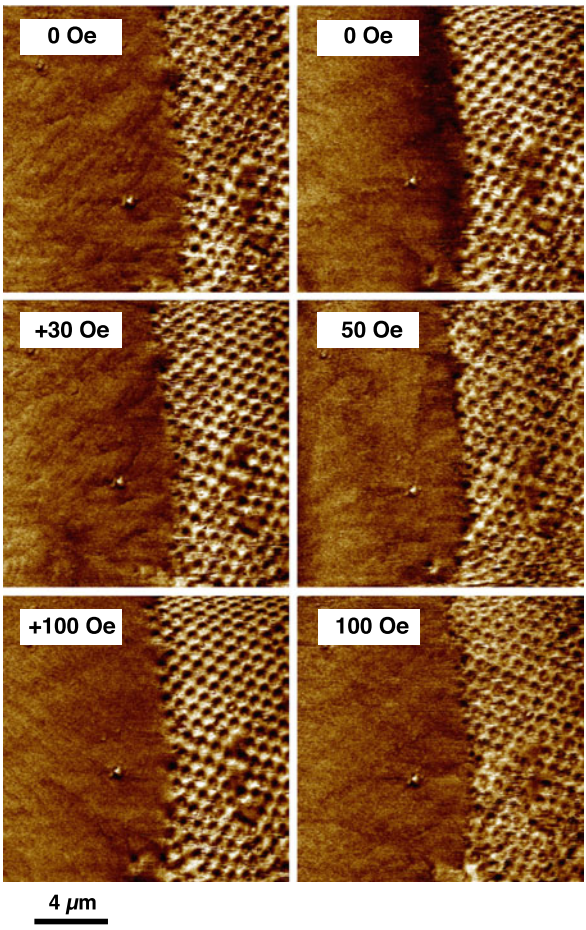

Fig. 7.8 MFM images of the interface between a continuous 25 nm thick Co film and an antidot array made of the same material. The images are taken at different applied magnetic field values. The field is applied along the *horizontal axis*

nanospheres. The magnetic material will cover the substrate in between the nanoparticles and will deposit on top of them, eventually filling the gaps among them. As a consequence, before removing the nanospheres, two magnetic layers actually exist: the antidot structure on the substrate, and the film on top of the nanoparticles, as depicted in Fig. 7.10. Hysteresis loops measured on a Co film before and after the removal of the nanospheres with the top magnetic layer are shown in Fig. 7.11. The saturating moment decreases after sonicating or stripping, as the material on top of the nanospheres is removed. The coercive field remains approximately constant, indicating that the reversal mechanisms are dominated by the antidot structure. However, the approach to saturation is very different before and after removal of the nanoparticles. Prior to sonication or stripping, a much harder magnetic phase is observed. Since the material is indeed the same as that which constitutes the underlying antidot structure, the much larger anisotropy of the topmost layer should be ascribed to its shape, which is strongly non-planar as the metallic film will coat

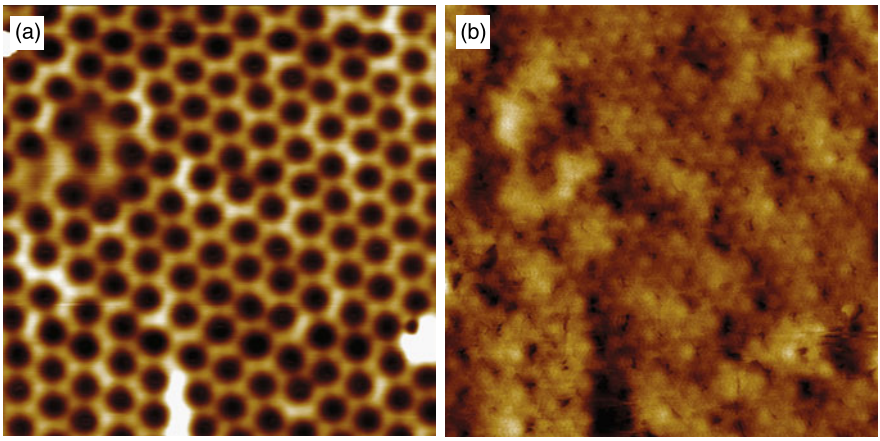

Fig. 7.9 Atomic force microscopy, AFM (**a**) and MFM (**b**) image of an antidot array of Ni (thickness: 25 nm)

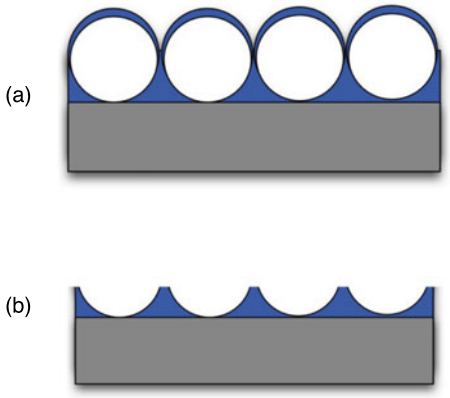

Fig. 7.10 Schematic representation of antidot preparation. (**a**) The magnetic material is deposited on the substrate and on top of the spheres. (**b**) The spheres are removed and the antidot structure remains

the nanoparticles with a variable thickness, as schematically shown in Fig. 7.10 and also reported in Refs. [33–35].

The magnetization processes and thus the loops' shape at room temperature are affected by the geometrical properties of the samples (center-to-center distance and diameter of the holes), but the specific choice of the magnetic material still has some influence, as evidenced for example in Fig. 7.12, where hysteresis loops of selected Ni, Co, $Ni_{80}Fe_{20}$ and $Fe_{73.5}Cu_1Nb_3Si_{13.5}B_9$ antidot arrays are reported. In all cases, a rather large coercive field is observed (tens of oersteds, up to more than 100 Oe for the Co sample), which can be attributed to the antidot array, where the holes act as 'defects' in the thin films which induce an anisotropy and 'pin' the domain walls through the creation of free poles at the borders of the holes. Additionally, the approach to saturation is rather slow, requiring a relatively large magnetic field to fully rotate the magnetization parallel to the applied magnetic field. Conversely,

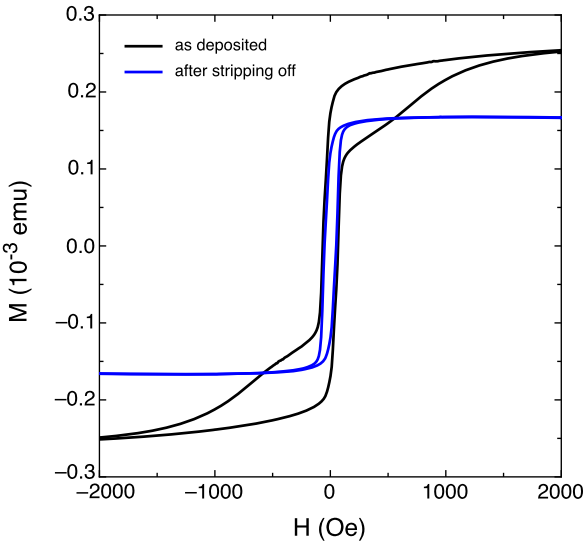

Fig. 7.11 Hysteresis loops of an antidot array of Co (thickness: 25 nm). *Black curve*: as deposited film (as in Fig. 7.10(a)). *Blue curve*: after spheres removal (as in Fig. 7.10(b))

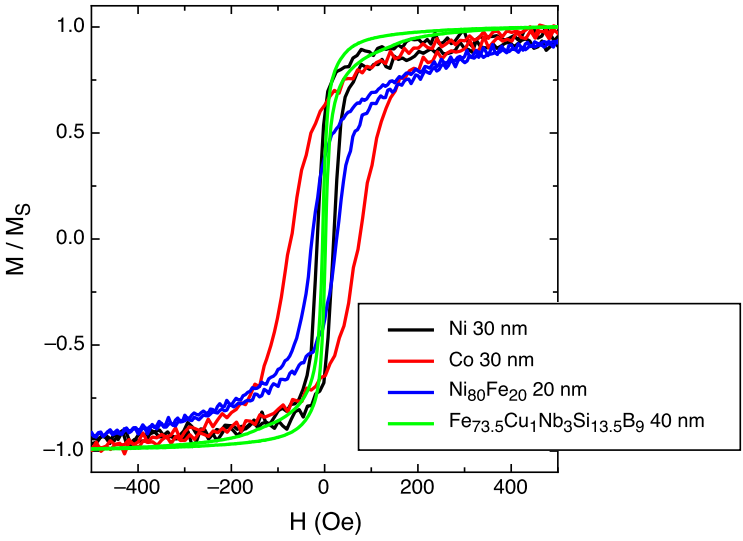

Fig. 7.12 Room temperature hysteresis loops of antidot arrays of several different compositions, normalized at their respective saturation magnetization values

there is no variation of the loops' shape when applying the magnetic field along different directions in the film plane. This is a consequence of the long-range disorder of the antidot array, which causes an averaging out of the local anisotropy directions determined by the hexagonal close-packed arrangement of the holes. For the antidots presented in Fig. 7.12, Co has the highest coercive field, whereas the

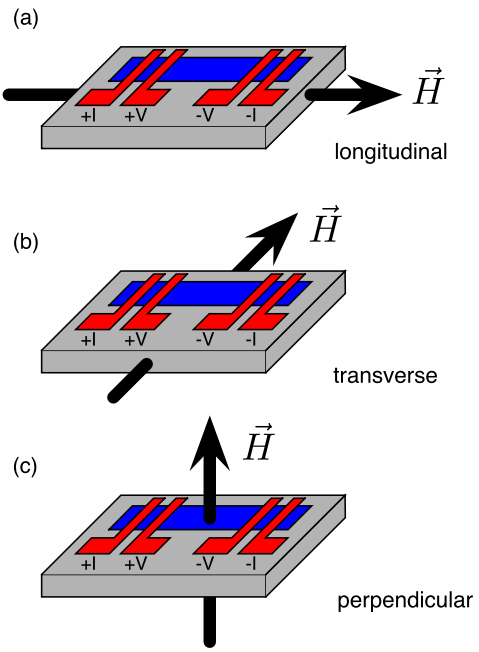

Fig. 7.13 Sketch of the geometrical configurations exploited to measure the MR (*grey*: substrate; *blue*: antidotted thin film; *red*: Cu contacts). (**a**) Longitudinal: H parallel to the electrical current flow; (**b**) transverse: H perpendicular to the electrical current flow; (**c**) perpendicular: H perpendicular to the electrical current flow and to the film plane [38]

$Fe_{73.5}Cu_1Nb_3Si_{13.5}B_9$ amorphous alloy has the lowest coercive field and the highest magnetic permeability.

A closer look at the actual magnetization processes in these antidot arrays can be obtained by means of magnetoresistance measurements. The dominant effect is the anisotropic magnetoresistance (AMR); phenomenologically, where AMR is present, a lower resistance value is observed when the electric current flows in the sample along a direction which is perpendicular to that of the magnetization; conversely, a higher resistance value is measured when the electrical current flows parallel to the magnetization vector. Usually, the direction of the current is kept constant and the magnetization is aligned along different directions through the application of a magnetic field. In this way, a varying resistance is observed as a function of the applied field.

Special care has to be taken when injecting the current in the antidot array, as the direction of the current must be well known in order to avoid incorrect interpretation of the data. In fact, as discussed e.g. in Ref. [36], point contacts are not suitable in antidot systems, as a significant portion of the path of the current is not going to flow in the desired direction. Contacts that ensure injection of the current along the whole sample width are necessary. Additionally, three different geometries can be defined, according to Fig. 7.13: 'longitudinal' means that the current and the applied field are parallel, 'transverse' means that the current and the applied field are orthogonal but both in the sample plane, 'perpendicular' means that the current and the applied field are orthogonal and the applied field is perpendicular to the sample plane.

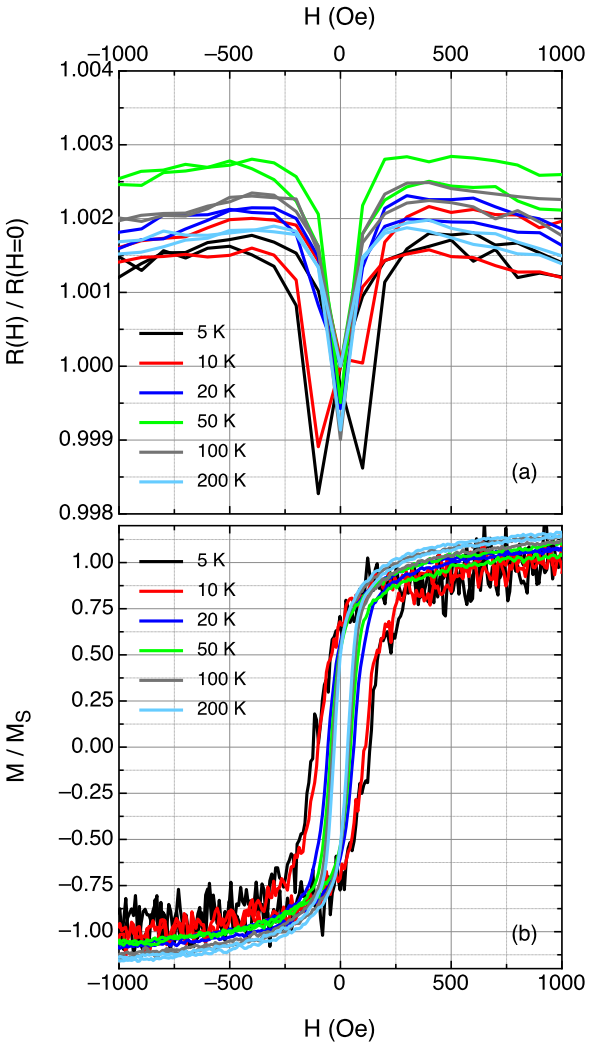

Fig. 7.14
(**a**) Magnetoresistance curves of $Ni_{80}Fe_{20}$ antidot arrays at selected temperatures. (**b**) Corresponding hysteresis loops

A set of MR curves taken at different temperatures in the longitudinal configuration is reported in Fig. 7.14. Figure 7.14(b) shows the corresponding hysteresis loops. The typical AMR behavior is observed: at high field, where saturation is achieved, the magnetization is parallel to the applied field, and since the measurements are performed in the longitudinal configuration it is also parallel to the current. In this condition, a higher resistance value is measured. When the field is reduced, the magnetization starts to deviate from the direction of the field (and thus of the current), resulting in a reduced resistance value. The condition of maximum (statistical) misalignment between the magnetization and the current is reached at the coercive field, which in fact corresponds to the minimum of the MR curves (see

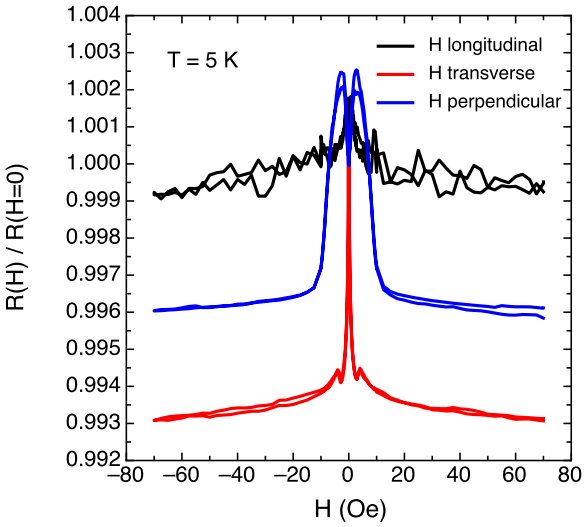

Fig. 7.15 MR curves measured at 5 K of an antidot array of $Ni_{80}Fe_{20}$ in the three different configurations described in Fig. 7.13 [38]

Figs. 7.14(a) and (b) for a comparison of the coercive field and of the MR curves minima). The hysteresis present in the magnetization curves is reflected into the MR measurements, as the minimum at $H < 0$ is reached when the field is reduced from positive saturation, and the minimum at $H > 0$ is reached when the field is increased from negative saturation. At sufficiently high fields a reduction of the resistance is observed (see Fig. 7.14(a)), which can be explained in terms of the effect of magnetic field on spin-disorder scattering in three-dimensional metals and alloys, otherwise called magnon MR [37].

MR curves measured at 5 K in the three geometries defined in Fig. 7.13 are reported in Fig. 7.15 for a $Ni_{80}Fe_{20}$ film. The longitudinal and transverse configurations display opposite behavior, as the relative orientation of current and magnetization with the application of a magnetic field is reversed. In the transverse configuration, a sufficiently high magnetic field saturates the sample along a direction perpendicular to that of the current, resulting in a low resistance value, whereas when the field is reduced the progressive misalignment of the magnetization with respect to the field increases the probability of the local magnetization lying parallel to the current, thus resulting in an increase of the resistance value. The perpendicular configuration, contrary to what is expected, does not show a monotonic decreasing behavior, indicating that the magnetization process when the field is applied perpendicular to the sample plane is rather complex and does not involve only rotations. Indeed, with respect to the transverse configuration, the field at which the maximum resistance value is observed is much larger, in agreement with the higher demagnetizing field, but some hysteresis is observed in correspondence to the maxima, indicating that an equilibrium domain configuration is reached at those field values which depends on the previous field history.

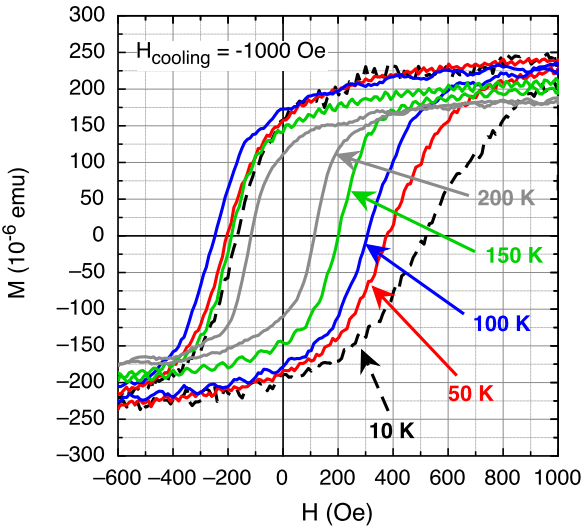

Fig. 7.16 Hysteresis loops of a Co antidot structure, measured at selected temperatures, after cooling from room temperature under a magnetic field of −1000 Oe [40]

7.3.3 Exchange Bias at Low Temperature

The relatively low thickness of the thin films patterned with an antidot geometry makes them prone to the effects of a possible oxide layer which can develop at their surface because of natural oxidation due to exposure to air. Consequences of this oxidation are detectable on the magnetic and magnetoresistive properties of the antidot arrays, provided that two conditions are fulfilled: (i) the magnetic material should spontaneously oxidize in air, and (ii) the developed oxide should be antiferromagnetic (at least at some temperatures). Both conditions are fulfilled by Co, at temperatures below ambient.

The top Co oxide layer, which below its Néel temperature is antiferromagnetic, pins the magnetization of the bottom Co layer, thus giving rise to an exchange bias effect [39]. Figure 7.16 shows selected low temperature hysteresis loops of a Co antidot array cooled from room temperature under the application of a field equal to −1000 Oe. The resulting exchange bias effect is positive (its sign can be reversed if the sign of the cooling field is reversed), as can be envisaged by the asymmetry of the loops. The exchange bias progressively reduces on increasing the temperature, until at approximately 150 K it disappears, marking that the Néel temperature of the top Co oxide layer has been overcome [40]. A more accurate estimation of the Néel temperature of the top Co oxide layer can be obtained by performing magnetization measurements as a function of temperature, under a relatively small magnetic field (+250 Oe), in two different conditions: (i) after the sample has been cooled from room temperature under an applied field of −1000 Oe and (ii) after the sample has been cooled from room temperature under an applied field of +1000 Oe. Thus, in the two conditions the signs of the measurement and of the cooling field are one time the same and the other time opposite. The results are shown in Fig. 7.17. When the measurement field has the same sign as the cooling field, no significant features

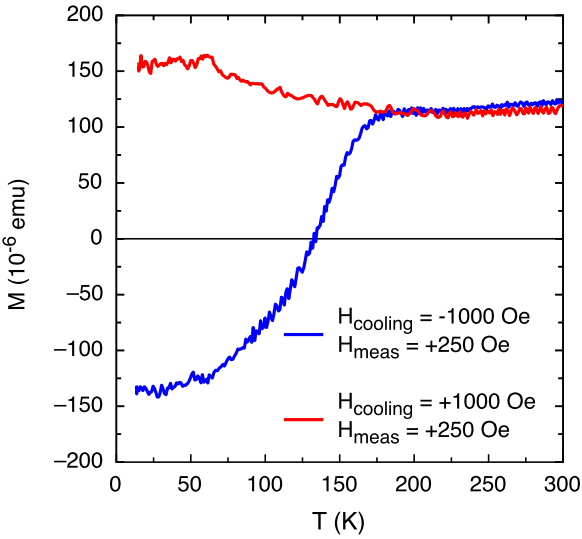

Fig. 7.17 *M* vs. *T* curves of a Co antidot array. *Red curve*: cooling and measurement fields have the same sign. *Blue curve*: cooling and measurement fields have opposite signs [40]

of the *M* vs. *T* can be observed besides the expected reduction of the magnetization with increasing temperature. Conversely, when the measurement and cooling fields have opposite sign, the exchange bias effect results in a magnetization which is negative at low temperature, and progressively increases as the interaction of the Co bottom layer with the top Co oxide layer becomes weaker. When the Néel temperature of the Co oxide layer is reached, the exchange bias effect vanishes, and the curve superimposes with that obtained in the first case.

The exchange bias effect can be observed on the same sample also through magnetoresistance measurements, which are reported at selected temperatures in Fig. 7.18 in the low-field region. The asymmetry of the resistance minima, which correspond to the coercive fields, is clearly seen to reduce on increasing temperature, and to vanish at approximately 150 K. The exchange bias field can be calculated from both hysteresis loops and MR curves, and plotted as a function of temperature. The results are perfectly consistent and are shown in Fig. 7.19, which also confirms 150 K as the Néel temperature of the top Co oxide layer.

7.4 Dots

7.4.1 Domain Configuration

An array of dots made of $Ni_{80}Fe_{20}$ with a diameter of ≈400 nm and a center-to-center distance of 500 nm and arranged in a hexagonal close-packed configuration is shown in Fig. 7.20 in a SEM image of a sample with a thickness value of 30 nm. In Fig. 7.21 similar dots are shown, made of Co, with a slightly smaller diameter (≈370 nm) and the same center-to-center distance. Both images confirm that in

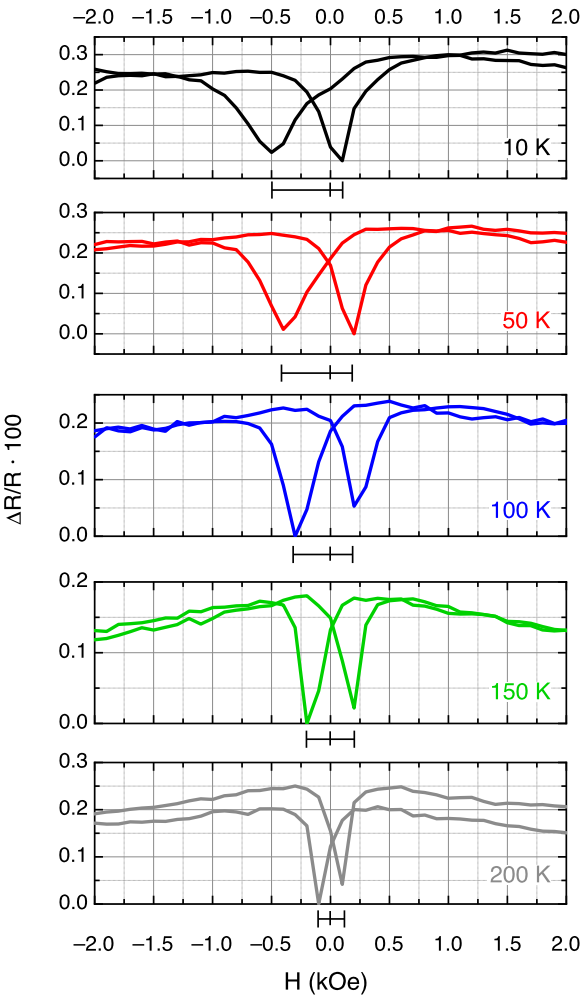

Fig. 7.18 Magnetoresistance curves of a Co antidot array, in the low-field region, at selected temperatures. The resistance variation has been normalized to its lowest value to ease comparison of the different curves. The *bars below each panel* visually indicate the bias of the curves with respect to $H = 0$ [40]

relatively small surface areas the arrays are well ordered, although small variations in the initial diameter of the nanospheres affect the degree of order of the pattern, as in the case of the Co dots.

A typical magnetic domain configuration is shown in Fig. 7.22, where an MFM image and an AFM image of the same region are presented side by side. In spite of the simple dot geometry, the possibility to create dots with small gaps among them favors magnetic interactions which are responsible for the observed complex domain configuration. In the bottom part of the MFM image of Fig. 7.22, which is taken at the magnetic remanence, some vortices can be observed, as expected in non-interacting magnetic dots of this size. However, in other portions of the image larger scale domains, involving groups of dots, or different domain configurations within individual dots can be detected, indicating that the magnetization processes

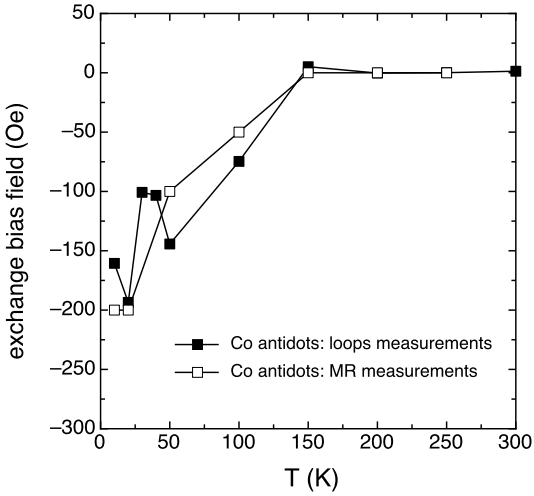

Fig. 7.19 Temperature dependence of the exchange bias field for the Co antidots sample, estimated by means of hysteresis loops (*full squares*) and magnetoresistance measurements (*open squares*) [40]

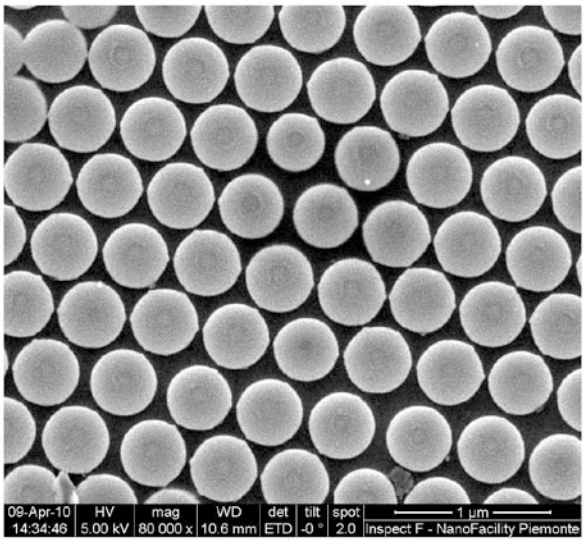

Fig. 7.20 SEM image of a $Ni_{80}Fe_{20}$ dot array with a thickness of 30 nm [41]

in these samples are rather complex. This will be confirmed by hysteresis loop measurements, as will be discussed in the next section.

7.4.2 Magnetic and Magnetoresistive Properties

Hysteresis loops measured on the dot arrays shown in Figs. 7.20 and 7.21 are reported in Figs. 7.23 and 7.24 respectively. In both cases the typical features of a magnetization reversal involving the nucleation and expulsion of a vortex can be

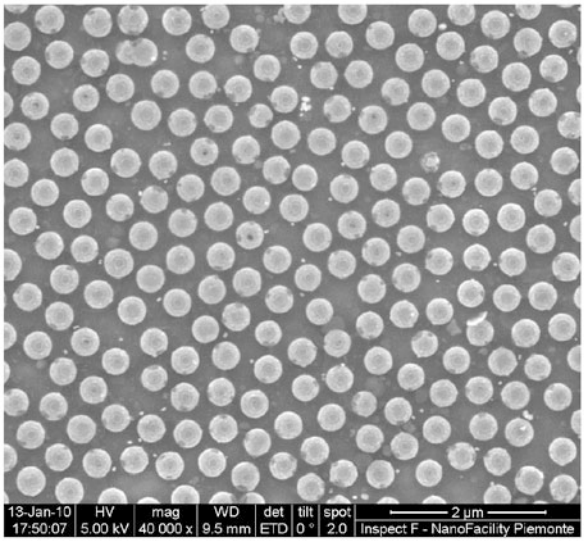

Fig. 7.21 SEM image of a Co dot array with a thickness of 30 nm [41]

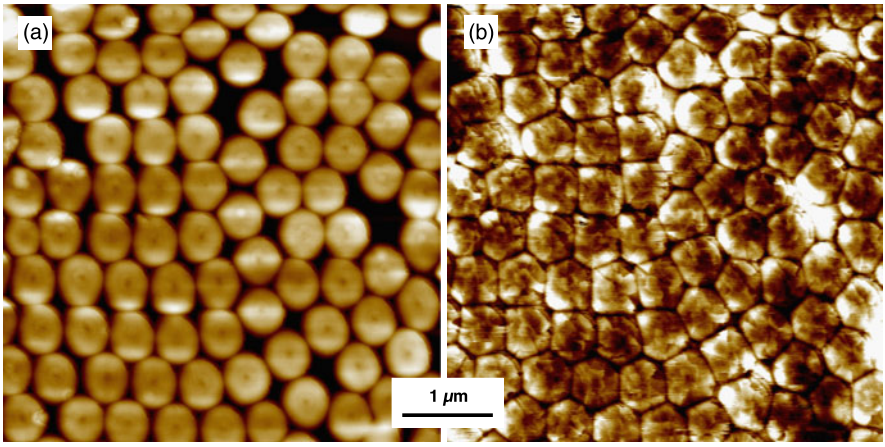

Fig. 7.22 (**a**) AFM image of $Ni_{80}Fe_{20}$ dot arrays (thickness: 30 nm). (**b**) MFM image of the same region taken at the magnetic remanence [41]

observed. These are dominant in the thinner films; the thicker ones display an additional contribution at low fields characterized by a higher permeability, which gives the loops a clear two-phase behavior. As discussed in Sect. 7.1, the magnetometers, like the AGFM, used for these loop measurements characterize the whole sample volume, and the results are thus affected by inhomogeneities in the samples which appear as additional contributions to the loops' shape. In the case of the thicker samples, the softer phase at low fields could be originated by portions of a continuous magnetic film in some parts of the samples, due to a lack of coverage of those areas

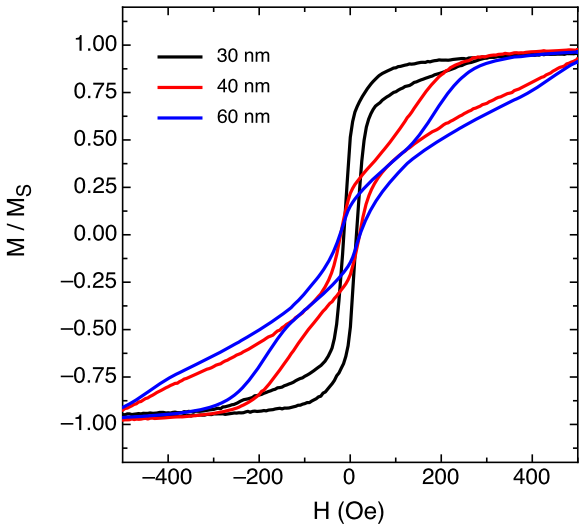

Fig. 7.23 Room temperature magnetization curves measured on $Ni_{80}Fe_{20}$ dot arrays having different thicknesses [41]

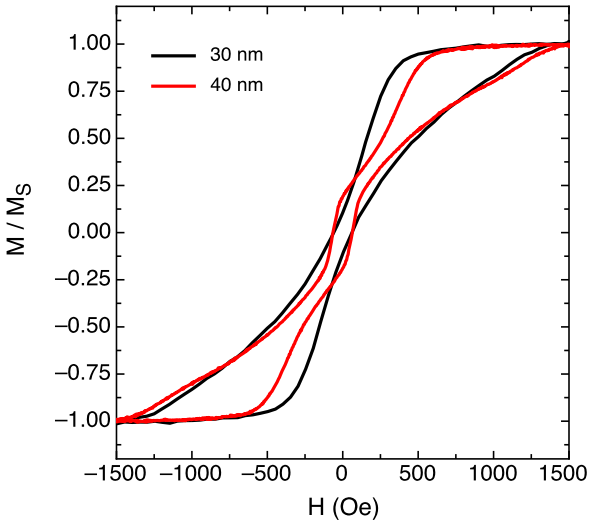

Fig. 7.24 Room temperature magnetization curves measured on Co dot arrays having different thicknesses [41]

by the PNs, or to an incomplete etching process (see Sect. 7.2) which has not completely removed the magnetic material among the dots, leaving a very thin base layer which connects the dots. This second hypothesis could justify the fact that such features are observed only in thicker samples, where the etching time is longer and a complete removal of the material could be more difficult, and is consistent with the complex domain configuration discussed in Fig. 7.22: magnetic interactions among the dots would certainly be favored by the presence of a continuous magnetic layer below them.

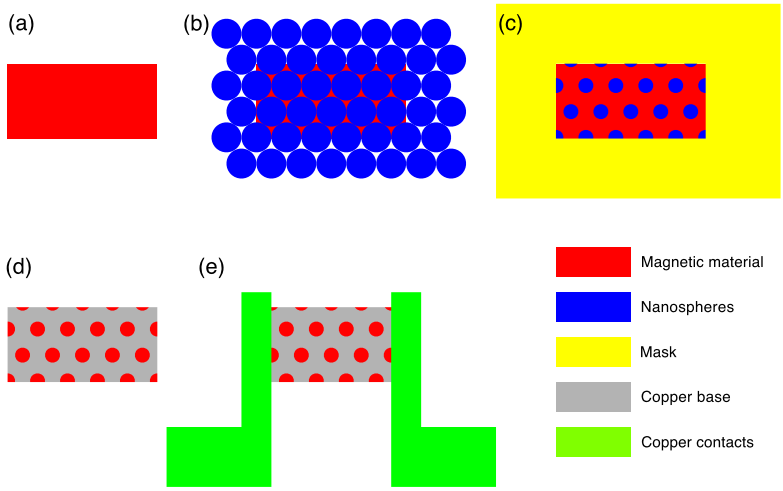

Fig. 7.25 Schematic representation of the process for preparing a dot array with contacts for magnetoresistance measurements. (**a**) Copper base + magnetic material in rectangular shape. (**b**) Deposition of nanospheres on the whole substrate. (**c**) Masking of the rectangular region with the magnetic material, RIE and plasma etching. (**d**) Removal of the nanospheres. (**e**) Deposition of copper electrical contacts for magnetoresistance measurements

The presence of a continuous conductive layer below the dots can be exploited for measuring magnetoresistance curves of arrays of dots prepared by self-assembling of PNs. The preparation process is shown schematically in Fig. 7.25. A bottom Cu layer as thin as possible is prepared: it should be thin enough to ensure that the diffusion length of the conduction electrons exceeds the thickness of the layer, but thick enough to ensure that it is continuous. In our case, the Cu layer is $\approx$3 nm thick. On top of it, the desired magnetic material is sputtered. Suitable techniques, such as EBL, optical lithography or mechanical masking during the deposition process need to be employed to shape the Cu-magnetic material bilayer into a rectangle (Fig. 7.25(a)). If a lift-off process is used, the resist with the bilayer on top of it should not be removed during this step. The nanospheres are then deposited on top of the whole substrate (Fig. 7.25(b)). A mask is then used to shade all the substrate except for the rectangular region with the Cu-magnetic material bilayer. If the rectangular region was prepared through a lift-off lithographic process, the resist used for it actually plays the role of the mask, since it was not removed in step (a) (Fig. 7.25(c)). With this masking, RIE can be used to reduce the diameter of the nanoparticles on top of the magnetic material, and plasma etching can be used to remove the excess magnetic material among them. The plasma etching rate needs to be carefully calibrated so that this step does not leave a continuous magnetic layer among the nanoparticles, but does not remove the Cu underlayer either. The nanoparticles can then be removed and the resist with the metallic bilayer on top (if used in step (a)), can be removed, thus completing the lift-off process. At the end, just a rectangular Cu underlayer with the magnetic dots on top of it

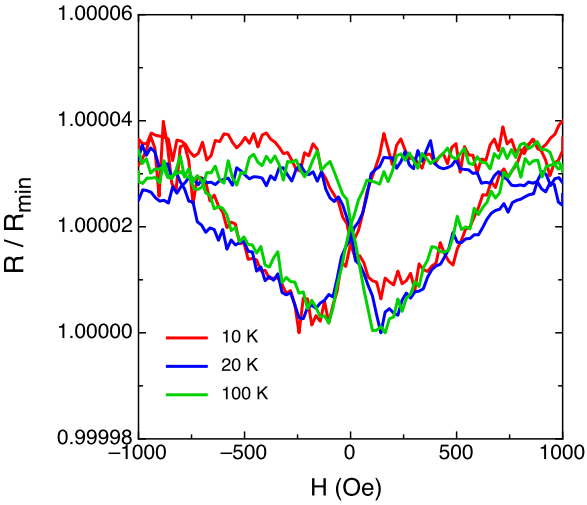

Fig. 7.26 MR curves at selected temperatures of a dot array of Co prepared according to the scheme reported in Fig. 7.25

remains on the substrate (Fig. 7.25(d)). Electrical contacts can then be deposited on top (Fig. 7.25(e)), much as in the case of antidot systems, and magnetoresistance measurements can be carried out. If the diffusion length of the electron is longer than the bottom conductive layer thickness, the conduction electrons will diffuse into the magnetic dots, and become polarized by the magnetic material. The resistance vs. field curves will then be affected by the relative orientation of the current and the magnetization of the dots (AMR effect), and possibly by the relative orientation of the magnetization between two adjacent dots (giant magnetoresistance, GMR, effect). Representative MR curves taken at different temperatures on a Co dot array 40 nm thick are shown in Fig. 7.26, in the low-field region. The magnetoresistive properties in the low-field region are almost independent of temperature; this fact suggests that Fig. 7.26 depicts an AMR effect directly linked to the magnetization reversal in the individual dots.

7.5 Conclusions

Self-assembling of polystyrene nanospheres is a powerful technique for patterning large areas (several mm^2) while keeping costs and processing time to a minimum. Compared to other techniques able to pattern large areas, like deep UV or X-ray lithography, self-assembling of nanospheres is much less expensive and does not require complex technologies or experimental setups. However, the degree of order that can be achieved in the dot and antidot structures is limited to a few micrometers, so only a statistical repeatability of the samples can be achieved. The preparation conditions need to be carefully controlled in order to prepare good monolayers of nanospheres; otherwise regions of the sample will not be covered by the nanospheres, and other regions will be covered by multilayers, thus leading to non-uniform properties of the final magnetic sample.

The advantage of having a pattern that covers a large area is that commonly available characterization techniques can be used to study the magnetic and electric properties of dot and antidot arrays prepared by means of the self-assembling of nanospheres. Several examples of magnetic domain patterns, hysteresis loops and magnetoresistance measurements have been presented, which demonstrate that complex physical processes occur in this kind of system, which concerns magnetization reversal and magneto-transport properties.

Acknowledgements This work has been partially performed at NanoFacility Piemonte, INRIM, a laboratory supported by Compagnia di San Paolo.

References

1. H.S. Nalwa, *Magnetic Nanostructures* (American Scientific, Stevenson Ranch, 2002)
2. P.P. Freitas, R. Ferreira, S. Cardoso, F. Cardoso, J. Phys. Condens. Matter **19**, 165221 (2007)
3. M. Donolato, M. Gobbi, P. Vavassori, M. Leone, M. Cantoni, V. Metlushko, B. Ilic, M. Zhang, S.X. Wang, R. Bertacco, Nanotechnology **20**, 385501 (2009)
4. P. Vavassori, M. Gobbi, M. Donolato, M. Cantoni, R. Bertacco, V. Metlushko, B. Ilic, J. Appl. Phys. **107**, 09B301 (2010)
5. C. Granata, A. Vettoliere, P. Walke, C. Nappi, M. Russo, J. Appl. Phys. **106**, 023925 (2009)
6. D.A. Allwood, G. Xiong, R.P. Cowburn, J. Appl. Phys. **100**, 123908 (2006)
7. J. Jaworowicz, N. Vernier, J. Ferre, A. Maziewski, D. Stanescu, D. Ravelosona, A.S. Jacqueline, C. Chappert, B. Rodmacq, B. Dieny, Nanotechnology **20**, 215401 (2009)
8. T. Hesjedal, T. Phung, Appl. Phys. Lett. **96**, 072501 (2010)
9. G. Reiss, D. Meyners, J. Phys. Condens. Matter **19**, 165220 (2007)
10. R. Jansen, J. Phys. D, Appl. Phys. **36**, R289 (2003)
11. J.-U. Bae, T.-Y. Lin, J.L. Reno, J.P. Bird, Appl. Phys. Lett. **93**, 143109 (2008)
12. J.H. Lee, S.N. Holmes, B. Hong, P.E. Roy, M.D. Mascaro, T.J. Hayward, D. Anderson, K. Cooper, G.A.C. Jones, M.E. Vickers, C.A. Ross, C.H.W. Barnes, Appl. Phys. Lett. **95**, 172505 (2009)
13. A. Bisig, L. Heyne, O. Boulle, M. Kläui, Appl. Phys. Lett. **95**, 162504 (2009)
14. M.R. Pufall, W.H. Rippard, S.E. Russek, S. Kada, J.A. Katine, Phys. Rev. Lett. **97**, 087206 (2006)
15. S.S.P. Parkin, M. Hayashi, L. Thomas, Science **320**, 190–194 (2008)
16. A.O. Adeyeye, N. Singh, J. Phys. D, Appl. Phys. **41**, 153001 (2008)
17. J.-S. Sohn, D. Lee, E. Cho, H.-S. Kim, B.-K. Lee, M.-B. Lee, S.-J. Suh, Nanotechnology **20**, 025302 (2009)
18. K. Galatsis, K.L. Wang, M. Ozkan, C.S. Ozkan, Y. Huang, J.P. Chang, H.G. Monbouquette, Y. Chen, P. Nealey, Y. Botros, Adv. Mater. **21** (2009)
19. A. Aktag, S. Michalski, L.P. Yue, R.D. Kirby, S.H. Liou, J. Appl. Phys. **99**, 093901 (2006)
20. D. Kitamoto, T. Morita, T. Fukuoka, M. Konishi, T. Imura, in *Self-assembling Properties of Glycolipid Biosurfactants and Their Potential Applications*. Curr. Opin. in Colloid and Interface Science, vol. 14 (2009). doi:10.1016/j.cocis.2009.05.009
21. Z.L. Xiao, C.Y. Han, U. Welp, H.H. Wang, V.K. Vlasko-Vlasov, W.K. Kwok, D.J. Mille, J.M. Hiller, R.E. Cook, G.A. Willing, G.W. Crabtree, Appl. Phys. Lett. **81**, 2869 (2002)
22. S.B. Darling, Prog. Polym. Sci. **32**, 1152 (2007)
23. Y. Sun, G.C. Walker, J. Phys. Chem. B **106**, 2217 (2002)
24. H. Shibata, M. Sato, S. Watanabe, M. Matsumoto, Colloids Surf. A, Physicochem. Eng. Asp. **346**, 58 (2009)
25. J.C. Hulteen, R.P. Val Duyne, J. Vac. Sci. Technol. A **13**, 1553 (1995)

26. A.A. Zhukov, A.V. Goncharov, P.A.J. de Groot, P.N. Bartlett, M.A. Granem, J. Appl. Phys. **93**, 7322 (2003)
27. C. Hassel, M. Brands, F.Y. Lo, A.D. Wieck, G. Dumpich, Phys. Rev. Lett. **97**, 226805 (2006)
28. R. Danneau, P. Warin, J.P. Attané, I. Petej, C. Beigné, C. Fermon, O. Klein, A. Marty, F. Ott, Y. Samson, M. Viret, Phys. Rev. Lett. **88**, 157201 (2002)
29. H.W. Deckman, J.H. Dunsmir, Appl. Phys. Lett. **41**, 377 (1982)
30. A. Kosiorek, W. Kandulski, H. Glaczynska, M. Giersig, Small **1**, 439 (2005)
31. W. Kandulsky, Thesis. http://hss.ulb.uni-bonn.de/2007/1148/1148.htm
32. L. Boarino, G. Amato, E. Enrico, N. De Leo, F. Celegato, P. Tiberto, F. Vinai, M. Coïsson, A. Chiodoni, M. Laus, in *Silicon Nanostructures by Self-assembly and Metal Assisted Etching*, ed. by P. Granitzer, K. Rumpf. Nanostructured Semiconductors: From Basic Research to Applications (Pan Stanford, New York, 2011)
33. T. Eimuller, T.C. Ulbrich, E. Amaladass, I.L. Guhr, T. Tyliszczak, M. Albrecht, Phys. Rev. B **77**, 134415 (2008)
34. C.M. Günther, O. Hellwig, A. Menzel, B. Pfau, F. Radu, D. Makarov, M. Albrecht, A. Goncharov, T. Schrefl, W.F. Schlotter, R. Rick, J. Lüning, S. Eisebitt, Phys. Rev. B **81**, 064411 (2010)
35. T.C. Ulbrich, D. Assmann, M. Albrecht, J. Appl. Phys. **104**, 084311 (2008)
36. C.C. Wang, A.O. Adeyeye, Y.H. Wu, M.B.A. Jalili, J. Appl. Phys. **97**, 023531 (2005)
37. B. Raquet, M. Viret, P. Warin, E. Sondergard, R. Mamy, Physica B **294–295**, 102 (2001)
38. P. Tiberto, L. Boarino, F. Celegato, M. Coïsson, N. De Leo, F. Vinai, P. Allia, J. Appl. Phys. **107**, 09B502 (2010)
39. W.H. Meiklejohn, C.P. Bean, Phys. Rev. **102**(5), 1413 (1956)
40. M. Coïsson, L. Boarino, F. Celegato, N. De Leo, P. Tiberto, F. Vinai, J. Nanopart. Res. **13**, 5641–5651 (2009)
41. P. Tiberto, L. Boarino, F. Celegato, M. Coisson, E. Enrico, N. De Leo, F. Vinai, P. Allia, J. Nanopart. Res. **13**, 4211–4218 (2011)

Chapter 8
Magnetic Nanoparticle Hyperthermia Treatment of Tumours

Chris Binns

Abstract Magnetic nanoparticle hyperthermia (MNH) treatment of tumours is at an advanced stage of development, having been through phase I human clinical trials and currently being tested in phase II in combination with other therapies. There is some way to go in order to achieve its original promise as a stand-alone, symptom-free treatment, but recent developments in the synthesis of a new generation of magnetic nanoparticles with a very high heating performance have brought this closer. This chapter presents the general concept of MNH and describes the heating mechanisms and limitations of currently available ferrofluids. The potential of new nanoparticles to overcome these barriers is discussed.

8.1 Background

The observation that hyperthermia can regress tumours is certainly not new. The first written record can be found in the Edwin Smith Papyrus that originates from around 1500 BC [1], though there is evidence that the papyrus is a copy of a much older text. Hippocrates, the father of modern medicine, working around 400 BC, was a great believer in treating disease by heat, and it is claimed that he treated breast and skin cancers using hyperthermia. Throughout the history of clinical medicine systemic heating of the whole body or regions of the body, induced by external heat sources such as hot baths, hot wax, or burying patients in hot mud, has been used to treat tumours [2]. Alternatively, from the nineteenth century, there were experiments in the use of pathogens to induce fever and regress tumours with some reports of success [3].

Raising the temperature of cells to around 42 °C has a number of effects including denaturing of proteins and restructuring cell membranes so they become pervious, and the release of heat shock proteins. The entire basis for systemic heating regressing tumours is that they are more sensitive to increases in temperature than healthy cells. This is not necessarily due to cancer cells being intrinsically more sensitive,

C. Binns (✉)
Department of Physics and Astronomy, University of Leicester, Leicester LE1 7RH, UK
e-mail: cb12@le.ac.uk

B. Aktaş, F. Mikailzade (eds.), *Nanostructured Materials for Magnetoelectronics*, Springer Series in Materials Science 175, DOI 10.1007/978-3-642-34958-4_8,

though this is sometimes the case. A more important factor is that in vivo the abnormal vasculature around a tumour limits heat loss by blood perfusion from the region so it tends to become a hot spot. In addition there is poor nutrient supply, so acidosis and hypoxia further increase the sensitivity of the tumour region to rises in temperature [4].

The abiding problem with systemic heating is that it is non-specific and involves a delicate balancing act between treating the tumour and causing widespread tissue damage. Interest remains however because systemic hyperthermia is a useful tool to increase the effectiveness of chemotherapy due to pre-stressing the tumour and increasing the permeability of cell membranes to drugs. In clinical trials, improved response rates were reported for the treatment of cancers when systemic hyperthermia was used in combination with doxorubicin and cyclophosphamide [5] or BCNU [6]. Introducing chemotherapy also produces the well-known side effects of these drugs, so it remains a goal for hyperthermia to be effective as a stand-alone therapy with its potential as a low morbidity treatment.

In order for hyperthermia to become an effective tool on its own it needs to utilize technologies that ensure that the only heated region is the tumour itself, and this has led to the development of high intensity focused ultrasound (HIFU) and focused microwave therapy (FMT). HIFU brings ultrasonic waves into a sharp focus of the order of millimetres in which there is sufficient energy density to heat and ablate tissue. The focus is then scanned over the volume of the tumour. Its mode of operation is not quite the same as hyperthermia in that the temperature reached within the focus is higher than the therapeutic threshold of 42 °C. The method has been found to be effective in the treatment of some cancers including prostate [7], liver, pancreatic, kidney and bladder but is ineffective for brain and lung cancers. FMT also generates temperatures in the ablation (>50 °C) as opposed to hyperthermia range and has been found to be particularly effective for breast cancer [8].

The most advanced hyperthermia method uses nanotechnology in a magic bullet approach that attaches molecular-sized heaters only to cancer cells, which are then heated by an external stimulation to which normal biological tissue is transparent. Methods include gold nanoshells [9], nanorods [10] and carbon nanotubes [11] heated by near infrared radiation, which is able to penetrate up to a centimetre into tissue or, for deep tumours, magnetic nanoparticles heated by an applied oscillating magnetic field. The latter variant of this technology is the most highly developed, having reached human clinical trials [12–15]. In magnetic nanoparticle hyperthermia (MNH) a ferrofluid containing magnetic nanoparticles is introduced into the tumour and the heating stimulation is by oscillating magnetic fields at frequencies of around 100 kHz, at which absorption of energy by normal tissue is extremely small. This chapter will focus on MNH, discussing the limitations and what improvements are required in the nanoparticles to improve the method.

The excitement surrounding MNH is that if it could be made to work as a stand-alone therapy, it offers the promise of a low morbidity and generic treatment. Phase I clinical trials of the treatment of prostate cancer by MHN alone [13] demonstrated no systemic toxicity and only a temporary impairment of quality of life. A general conclusion however is that currently it is not possible with the available

nanoparticles, based on maghemite (Fe_2O_3), to produce a sufficient temperature rise throughout the entire volume of a tumour without using an unsafe applied field energy. Clinical trials are currently focused on combining MNH with other treatment methods [15]. MNH applied to mice, in which, because of the small volume, higher field-frequency values can be used, has demonstrated complete tumour regression [16], indicating that MNH as a stand-alone therapy is possible, at least in principle.

One major limitation in attempting to reach a suitable temperature within the tumour is that the applied field and frequency combination must be such that diamagnetic tissue is not directly heated by the applied field. Originally this was taken as the Atkinson–Brezovich limit [17, 18], which, in its simplest form, can be expressed as the field-frequency ($H \times f$) product of 4.85×10^8 $\mathrm{A\,m^{-1}\,s^{-1}}$, though the actual safe value depends on the area of application in the body. For example a region in which there is a complex morphology of tissue and bone will have many local changes of refractive index, which generates internal reflections of the applied field and hotspots. Thus prostate cancers have to be treated with applied field-frequency values significantly below the Atkinson–Brezovich limit. On the other hand, brain tumours that are surrounded by homogenous tissue can be treated with a higher field excitation.

The limit on the applied field demands a high heating performance of the magnetic nanoparticles, and with the currently available material it is difficult to achieve a sufficient particle density in every part of the tumour to achieve a therapeutic temperature rise with a safe applied field. The heating power generated by a given mass of nanoparticles in W/g is denoted the specific absorption rate (SAR), and to put it simply, future development of MNH is reliant on developing nanoparticles with a much higher SAR. There are currently several new nanoparticle synthesis methods becoming available that generate SAR values up to a factor of 10 greater than Fe_2O_3, and the remainder of the chapter is devoted to high-performance nanoparticles for MNH with an emphasis on gas-phase synthesis. This is the most versatile and has so far produced the highest recorded SAR values. In the next section the mechanisms by which magnetic nanoparticles generate heat will be examined, and the important parameters that determine SAR values will be discussed.

8.2 Heating by Magnetic Nanoparticles

We begin with the most widely used model based on Néel–Brown relaxation and described by Rosensweig [19]. Although this model has been superseded, it is a useful starting point to examine the effects of various parameters on heating efficiency.

The model is based on two heating mechanisms: the Brownian mechanism due to the stochastic vibrations in the surrounding environment and the Néel mechanism due to the magnetization vector rotating within the nanoparticle. The two mecha-

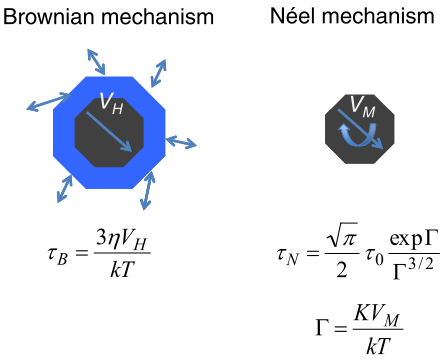

Fig. 8.1 Brownian and Néel heating mechanisms and their associated time constants τ_B and τ_N. τ_B is a function of the medium viscosity and the total hydrodynamic volume of the nanoparticles, while τ_N depends on just the magnetic volume, the anisotropy of the material and the natural time constant of the magnetic moment

nisms introduce time constants into the motion of the nanoparticle magnetization vector labelled τ_B and τ_N respectively. These are given by

$$\tau_B = \frac{3\eta V_H}{kT}, \tag{8.1}$$

where η is the medium viscosity and V_H is the hydrodynamic volume (magnetic core plus any shell) of the nanoparticle, and

$$\tau_N = \frac{\sqrt{\pi}}{2}\tau_0 \frac{e^{\Gamma}}{\Gamma^{3/2}} \quad \text{with } \Gamma = \frac{KV_M}{kT} \tag{8.2}$$

where V_M is the volume of the magnetic core, K is the anisotropy constant of the magnetic material and τ_0 is the natural time constant of the magnetic moment (high temperature rotation limit). See Fig. 8.1.

If an oscillating magnetic field is applied to the nanoparticle, the time constants introduce a phase lag between the magnetic moment and the field, which pumps energy into the system as the vector rotates. The two time constants are combined to give a single time constant:

$$\frac{1}{\tau} = \frac{1}{\tau_B} + \frac{1}{\tau_N} \tag{8.3}$$

For an applied magnetic field given by

$$H(t) = H_0 \cos \omega t$$

the imaginary (lossy) part of the complex susceptibility is given by

$$\chi'' = \frac{\omega\tau}{1 + (\omega\tau)^2}\chi_0 \tag{8.4}$$

where χ_0 is the temperature-dependent susceptibility of the nanoparticle assembly and contains the volume fraction of magnetic material in the fluid. Generally, for calculating the SAR values intrinsic to the material the volume fraction is set to 1. For superparamagnetic nanoparticles, χ_0 is described by a Langevin function and the power generated is given by

$$P = \mu_0 \pi f H_0^2 \chi''. \tag{8.5}$$

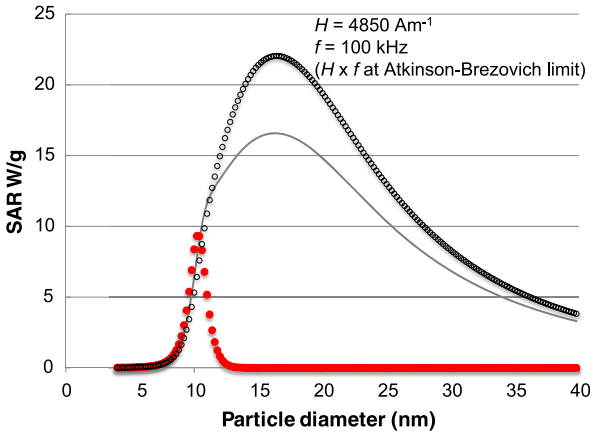

Fig. 8.2 SAR of maghemite nanoparticles calculated using the relaxation theory of Rosensweig [19] for Néel relaxation only (*filled circles*) and both Brownian and Néel relaxation (*open circles*). The parameters used for maghemite are $M_S = 4.5 \times 10^5$ A m^{-1} and $K = 4.7 \times 10^4$ J m^{-3}. The *grey line* shows the effect of adding a 1 nm thick non-magnetic shell to the nanoparticles, which only affects Brownian heating. The viscosity of the fluid is assumed to be that of blood

So in summary the three main parameters of the nanoparticles that determine their SAR are their size (both hydrodynamic and magnetic volume), which determines the time constants τ_B and τ_N, the anisotropy constant of the magnetic material, which determines τ_N and the saturation magnetization of the magnetic material, which determines χ_0 at a given temperature.

For suspended nanoparticles in a fluid it is clear that both Brownian and Néel mechanisms will contribute fully, but it is not clear how the Brownian mechanism will be affected in the case of biologically targeted nanoparticles anchored to a cell. The difference in SAR for the Brownian mechanism present and absent is demonstrated in Fig. 8.2, which shows the results of a calculation using the Rosensweig relaxation model for the case of both Brownian and Néel contributions and the Néel contribution only with an applied field at 100 kHz and an amplitude of 4850 A m^{-1} (so $H \times f$ is at the Atkinson–Brezovich limit). Also shown is the effect of a 1 nm thick non-magnetic shell, which makes a contribution to τ_B only.

It is evident that switching off the Brownian mechanism drops the peak SAR by a factor of 2 and also produces a much sharper dependence on particle size. It is also evident from both curves that good size control is essential in obtaining the peak value of SAR. The magnetic parameters used in the calculation are those published for maghemite [20]; that is, the saturation magnetization is $M_S = 4.5 \times 10^5$ A m^{-1} and the anisotropy constant is $K = 4.7 \times 10^4$ J m^{-3}. Also, the viscosity used for the fluid was that of blood to gain at least an indication of the behaviour in vivo.

The nanoparticle size for maximum SAR changes with the frequency of the excitation field, but the dependence is not a simple one, as the balance between Brownian and Néel heating changes with frequency. In general the optimum size decreases as

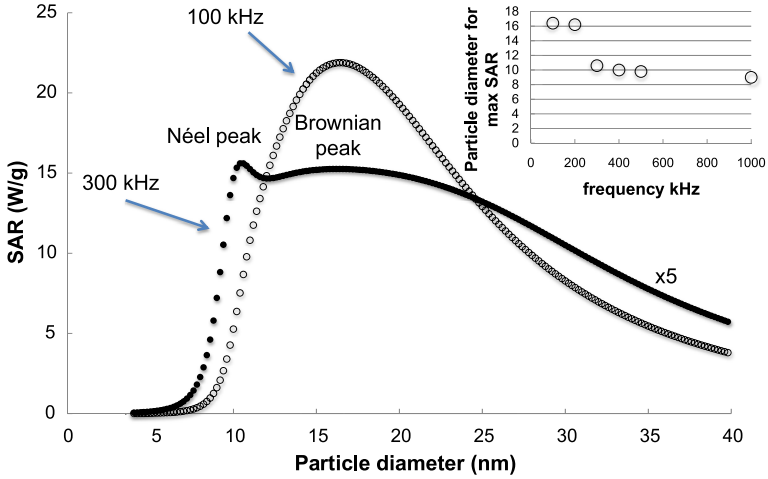

Fig. 8.3 SAR vs. particle size for different field excitation frequencies for maghemite (Fe_2O_3) nanoparticles. Generally as the frequency increases the optimum particle size decreases, but comparison between the 100 and 300 kHz curves shows that at higher frequencies the Néel peak becomes dominant. The *inset* shows the nanoparticle size for optimum SAR as a function of excitation frequency; the step between 200 and 300 kHz is due to the changeover between dominant mechanisms. Both *curves* are for $H \times f$ values at the Atkinson–Brezovich limit, so the field amplitude at 300 kHz is 1/3 that at 100 kHz

the frequency increases but, as shown in Fig. 8.3 for excitation at 100 and 300 kHz, at the higher frequency the peak SAR jumps to the Néel peak. This is reflected by the drop in optimum particle size vs. frequency shown in the inset.

Having verified the importance of nanoparticle size for different heating mechanisms, we turn to the magnetic material used. In this case there are two parameters to adjust, that is, the anisotropy constant, K and the saturation magnetization, M_S. Currently there is only one material licensed for medical use, that is, maghemite (Fe_2O_3), but as described below a number of new types of magnetic nanoparticles are being synthesized, and there is now the ability to control K and M_S over a wide range. Note that K can be controlled by changing the nanoparticle shape as well as the material.

The effect of the anisotropy is, again, complicated by the changeover between heating mechanisms. Figure 8.4 shows how the SAR curve vs. particle size for maghemite (Fe_2O_3) nanoparticles changes as the anisotropy is varied between 4.7×10^4 J m^{-3} (the measured value for maghemite nanoparticles [20]) and 1.5×10^4 J m^{-3} for an excitation field of frequency 100 kHz and amplitude 4850 A m^{-1}. As the anisotropy is reduced the Néel mechanism becomes more dominant and also increases the SAR, but not by a significant amount. It is easier to conceive of methods to increase the anisotropy, but this has a small effect on the curve.

According to the Rosensweig model, the dependence of SAR on the material saturation magnetization (M_S), shown in Fig. 8.5, is simple and clear: there is an almost

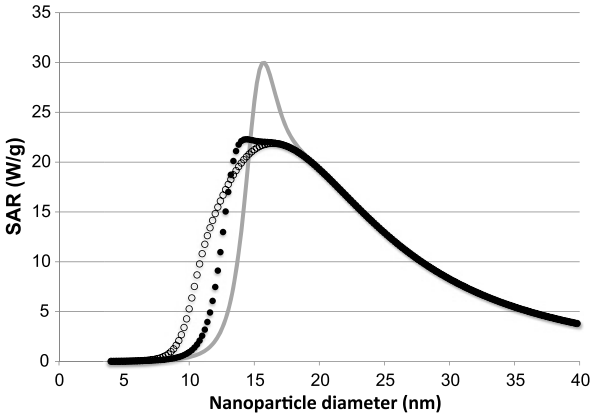

Fig. 8.4 SAR vs. particle size curve for maghemite (Fe_2O_3) nanoparticles with different anisotropy constants. *Open circles*: $K = 4.7 \times 10^4\ \mathrm{J\,m^{-3}}$ (the measured value [20]), *filled circles*: $K = 2.35 \times 10^4\ \mathrm{J\,m^{-3}}$, *grey line* $K = 1.5 \times 10^4\ \mathrm{J\,m^{-3}}$. The excitation field was 100 kHz at 4850 $\mathrm{A\,m^{-1}}$

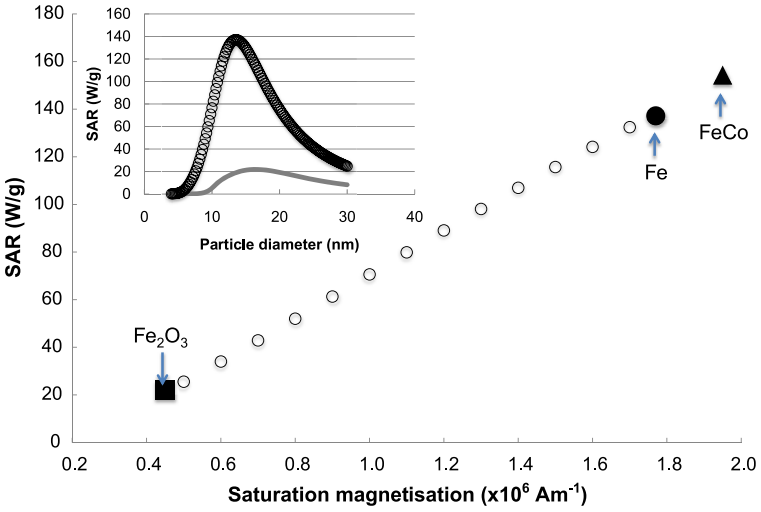

Fig. 8.5 Dependence of SAR on the saturation magnetization, M_S, of the material in the nanoparticles. The anisotropy constant, K, and M_S for Fe_2O_3 nanoparticles were taken from [20]. The K value for Fe nanoparticles was taken from [21] and the bulk M_S was assumed. For FeCo the K value for Fe nanoparticles and the bulk M_S value was used. For the M_S values between Fe_2O_3 and pure Fe, the K value and material density were interpolated between the endpoints. The excitation field was 100 kHz at 4850 $\mathrm{A\,m^{-1}}$

linear dependence between SAR and M_S. The values of K and M_S ($4.7 \times 10^4\ \mathrm{J\,m^{-3}}$ and $4.5 \times 10^5\ \mathrm{A\,m^{-1}}$) for Fe_2O_3 nanoparticles were taken from [20], the K value for Fe nanoparticles ($2 \times 10^5\ \mathrm{J\,m^{-3}}$) was taken from Binns et al. [21] and the bulk Fe M_S ($1.77 \times 10^6\ \mathrm{A\,m^{-1}}$) was assumed. For FeCo nanoparticles, we assumed the same K value as for Fe and used the bulk FeCo saturation magnetization ($1.95 \times 10^6\ \mathrm{A\,m^{-1}}$) as demonstrated for 12 nm diameter FeCo nanoparticles by Kleibert et al. [22]. For the values of M_S between Fe_2O_3 and pure Fe we inter-

polated the density and anisotropy constant between the two material endpoints. As discussed above, the anisotropy constant only plays a role if it can be changed by a large amount.

A problem in comparing nanoparticles used by different groups is that reports of SAR use different field excitation frequencies and amplitudes, often far above the Atkinson–Brezovich limit, and it is not clear how to scale them to produce a comparison of the fundamental performance of the material. A scheme that has been suggested by Kallumadil et al. [23] is to convert the measured SAR to an intrinsic loss parameter (ILP) defined by

$$ILP = \frac{SAR}{H^2 f} \tag{8.6}$$

where H and f are the amplitude and frequency of the excitation field respectively. This normalizes out the $H^2 f$ dependence of SAR (see (8.5)) and should depend only on the performance of the material. This is a helpful tool and has been used to compare the performance of a number of commercial magnetic colloids for hyperthermia [23]. We also use the ILP in our comparisons of different materials below, but it is not always valid as heating by magnetic nanoparticles may not be described by (8.5).

Recently, the limitations of the Néel–Brown relaxation model have been discussed [24, 25] and new models developed that introduce additional heating mechanisms. The fundamental assumptions in the linear theory discussed above are that

$$KV \gg kT$$

and

$$H < 3kT/(\mu_0 M_S V)$$

where V is the volume of the nanoparticles. The first condition is satisfied for all the systems considered above, but the second is satisfied only in certain applied field/particle size ranges. In addition to the second condition the particles should also be superparamagnetic (i.e. not blocked) on the timescale of $1/f$ of the applied field. The region of validity of the linear theory as a function of field and particle size has been summarized by Hergt et al. [25] and is shown by the hatched region in Fig. 8.6. The field/particle size parameter space mapped by the calculations shown so far is shown by the shaded rectangle, which extends beyond the region of validity, showing that for the larger particles we need to consider non-linear hysteresis effects. Note that for pure Fe nanoparticles for which K is larger than for Fe_2O_3, the superparamagnetic zone limits at smaller particle sizes.

The model developed by Hergt et al. [24, 25] is valid for the size range from superparamagnetic to multidomain particles and for large applied fields. A selection of results is shown in Fig. 8.7 for maghemite nanoparticles with diameters up to 54 nm and with applied fields up to 3×10^4 A m^{-1}. Superimposed on the data is an earlier calculation by Fortin et al. [26] with an applied field of 2.5×10^4 A m^{-1} using the linear relaxation model, which shows a single peak at a diameter of about 15 nm in agreement with Figs. 8.2 and 8.3 above. The new model reproduces the linear

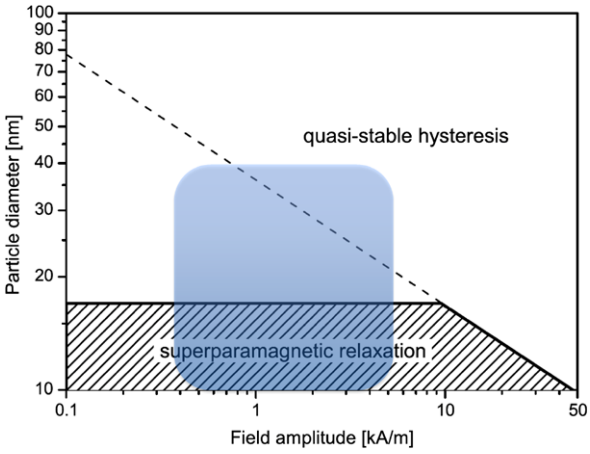

Fig. 8.6 Validity of linear Néel–Brown relaxation theory from Hergt et al. [25]. The *hatched region* shows the range of applied fields and particle sizes for which the linear theory is valid, whereas the calculations shown so far are encompassed in the *shaded rectangle*. Clearly for the parameter space considered the theory needs to be extended for non-linear hysteresis effects. Reproduced from [25] with permission from the IOP

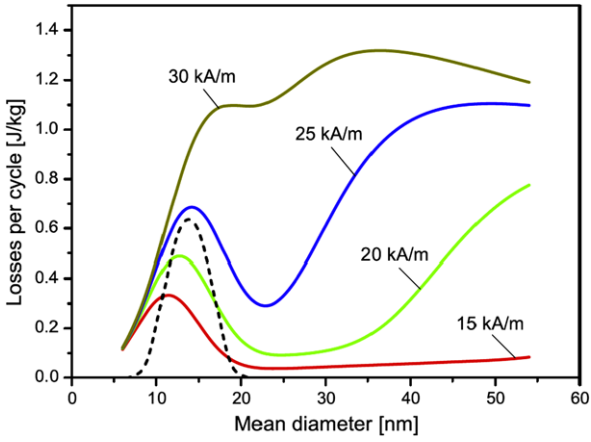

Fig. 8.7 Heat produced by Fe_2O_3 nanoparticles according to the model developed by Hergt et al. [24, 25] that includes non-linear hysteresis losses as a function of applied field amplitude and particle size. The *dashed curve* shows a calculation using the linear theory performed by Fortin et al. [26] for an applied field amplitude of $2.5 \times 10^4\ \mathrm{A\,m^{-1}}$. Reproduced from [25] with permission from the IOP

peak but with a higher value of SAR; however, it also shows that with increasing particle size the SAR value increases once more to a much higher plateau. The new work has had a significant impact on the discussion of particle size/field regimes required for optimum heating. Whereas the general opinion was that it was better to focus on small particles and very high excitation frequencies, up to 1 MHz, the calculations in [24] show that relatively large particles up to 50 nm in diameter are preferable. Large particles produce optimum power at relatively low frequencies (generally $<$100 KHz), which can be compensated by increasing the field amplitude, within the constraints of the Atkinson–Brezovich limit.

To summarize the findings so far, in order to maximize the SAR of the nanoparticle suspension the primary parameter is the saturation magnetization of the nanoparticles. Thus it is important to synthesize nanoparticles that have pure metal cores, though clearly they will require a biocompatible shell that renders them non-toxic and also protects the core from oxidation. Control over the anisotropy can also in-

crease performance within specific ranges of frequency and particle size. It appears from models that include hysteresis losses that, contrary to the general thinking, the maximum performance could be obtained from relatively large particles at low frequency and high field amplitudes. It is also apparent that the commonly used linear relaxation model may produce a significant underestimate of the heating performance of nanoparticles.

Maximizing the heat production by nanoparticles is only part of the story, as it is also important to model how the heat is distributed and transferred within living tissue in various parts of the body in order to ensure that the required volume reaches a therapeutic temperature. Models of how artificially raised temperatures are distributed in vivo go back to the Pennes equation published in 1948 [27], which describes the temperature distribution in the presence of heat conduction, cooling by blood perfusion and metabolic heating. The important thing to recognize is that the body is actively temperature controlled at a local level down to the scale of capillaries and is very effective at dissipating even highly localized heating. This is both a disadvantage and an advantage, since the body fights any attempt to generate local heat, but it also means that the temperature recovers in the unheated region back to core body temperature over a small distance, thus minimizing any damage to healthy tissue. With some simplification, assuming homogenous tissue, it can easily be shown that the Pennes equation predicts an exponential decay of temperature with distance away from the heated region given by

$$T = T_0 \exp(-x/\lambda)$$

where T_0 is the stable temperature rise achieved in the heated region (i.e. relative to core body temperature) and the decay constant, λ given by

$$\lambda = k/c_b\omega_m$$

where k is the thermal conductivity of tissue in the heated region, c_b is the specific heat of blood and ω_m is the blood perfusion rate. Putting in typical values for these parameters gives $\lambda \sim 5$ mm.

8.3 Synthesis of High-Performance Nanoparticles for Hyperthermia

There are a number of colloidal suspensions of magnetic nanoparticles based on Fe oxides that are commercially available, and a thorough comparison of their measured heating performance has been conducted by Kallumadil et al. [28]. The comparison, shown in Fig. 8.8, uses the ILP defined by (8.6), which has units $\mathrm{W\,s\,m^2/kg\,A^2}$ or $\mathrm{H\,m^2/kg}$. The best of the oxide nanoparticles, that is, sample 2 with an ILP of 3.12 $\mathrm{nH\,m^2/kg}$ and sample 11 with an ILP of 3.1 $\mathrm{nH\,m^2/kg}$, are, respectively, Nanomag-D-spio manufactured by Micromod and Resovist manufactured by Bayer–Schering. This data shows the performance of the kind of materials currently used for hyperthermia, and as discussed in the introduction marks what has to be significantly improved.

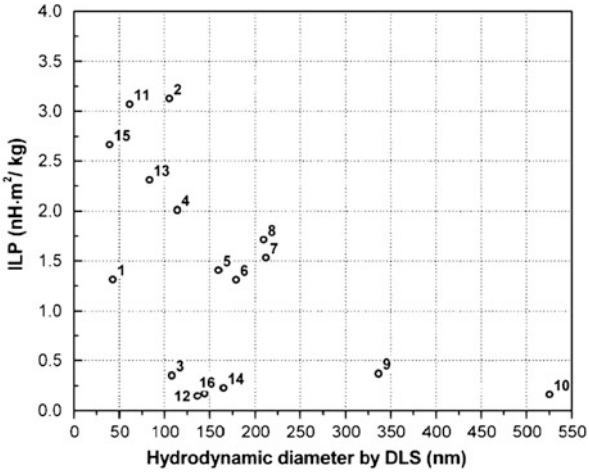

Fig. 8.8 Comparison of heating, as measured by the ILP, of a number of commercially available colloids of Fe oxide nanoparticles. Reproduced from [28] with permission from Elsevier

In the last few years a number of new synthesis routes to produce new types of magnetic nanoparticle ferrofluids have been developed in an attempt to maximize their SAR and produce values significantly higher than those currently available. These include magnetite nanoparticles produced by magnetotactic bacteria [29], Co@CoO core-shell nanoparticles prepared by thermolysis of $Co_2(CO)_8$ [30, 31], chemically synthesized Fe(0) nanocubes [32] and Fe@Fe-oxide core-shell nanoparticles produce by a new gas-phase method [33]. Details of this last method, which was developed by the authors group at the University of Leicester, UK, are presented below.

The synthesis of the core nanoparticles is carried out in ultra-high vacuum (UHV) conditions in the gas phase, which is the most flexible and controllable method. A variety of sources has been designed and built that can synthesize atomic clusters, with good size control, from the monomer to nanoparticles with diameters of tens of nanometres out of any solid element [34, 35]. The production of alloy nanoparticles in which there is control over the stoichiometry has been available for some time [36–38]. More recently, methods have been developed to produce core-shell particles in which there is free choice over the core and shell materials and good independent control over the core size and shell thickness [39].

An important feature of a gas-phase nanoparticle source is that it can operate in UHV-clean conditions [40, 41], so that both the core and the shell can be reactive materials and remain pristine without being converted to oxide. This creates a problem if one wants to extract the nanoparticles for applications or make a hydrosol out of the particle beam so that they can be applied to biology and medicine, since the majority of liquids have a vapour pressure that is incompatible with UHV operation.

The new method developed in our laboratory to deposit the nanoparticles into water while maintaining UHV-clean conditions in the rest of the source is illustrated in Fig. 8.9. The water vapour is introduced into vacuum as a molecular beam at a rate controlled by a liquid flow controller and typically of the order of 1 ml/h.

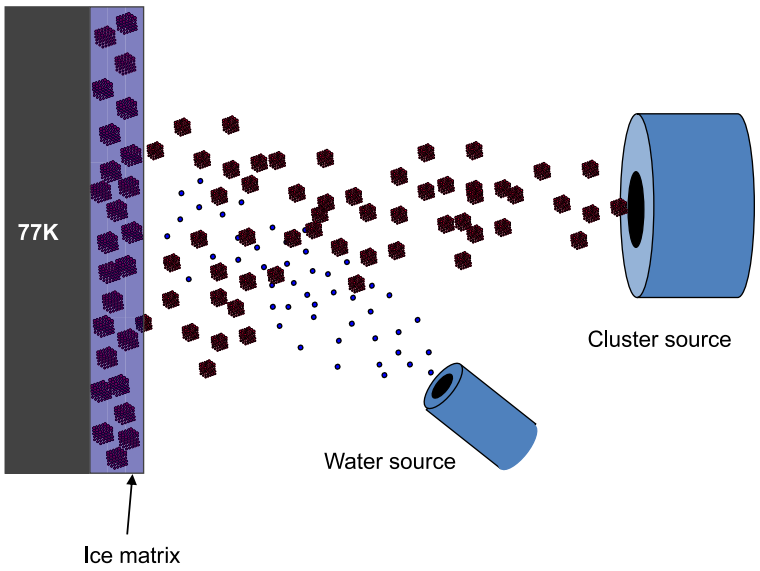

Fig. 8.9 To achieve water deposition while maintaining UHV-clean conditions in the rest of the cluster source, the nanoparticles are deposited onto a substrate maintained at 77 K onto which impinges a molecular beam of water. The clusters are thus embedded into a growing ice layer, and the volume fraction is determined by the relative deposition rates of nanoparticles and water. The vapour pressure of the ice at 77 K is in the range 10^{-12} to 10^{-14} mbar [42]

The beam impinges on a liquid nitrogen cooled surface while the nanoparticles are deposited onto the same surface and are embedded within the ice matrix. As shown by molecular dynamics simulations, the nanoparticles, which have typical speeds of around 50 ms^{-1}, are soft-landed and suffer no significant distortion as they are buried in the ice [33]. The vapour pressure of crystalline ice is less than 10^{-14} mbar at 77 K; however, the condensation method makes it is more appropriate to use the value for amorphous ice, which can be two orders of magnitude higher [43]. This is still far too low to contaminate the gas-phase nanoparticles during their formation. The injected water can either be pure or contain dissolved surfactants to prevent agglomeration, as described by Binns et al. [33].

The volume fraction of the nanoparticles in the hydrosol can be simply adjusted by varying the relative deposition rates of the particles and the water vapour. When the required amount of sample has been produced, the deposition chamber is isolated and vented to clean nitrogen while the ice is allowed to melt. The suspension is collected in a metal cup suspended beneath the conical substrate.

The core nanoparticles could be mass-filtered with a resolution of $M/\Delta M \sim 100$ using an ultra-high mass quadrupole mass filter described elsewhere [41], though for the magnetic nanoparticle suspensions this was simply used to measure the mass distribution in vacuum. The unfiltered distribution from the source is already quite narrow (see Fig. 8.10), and using the quadrupole to filter the flux produces a large drop in the deposition rate.

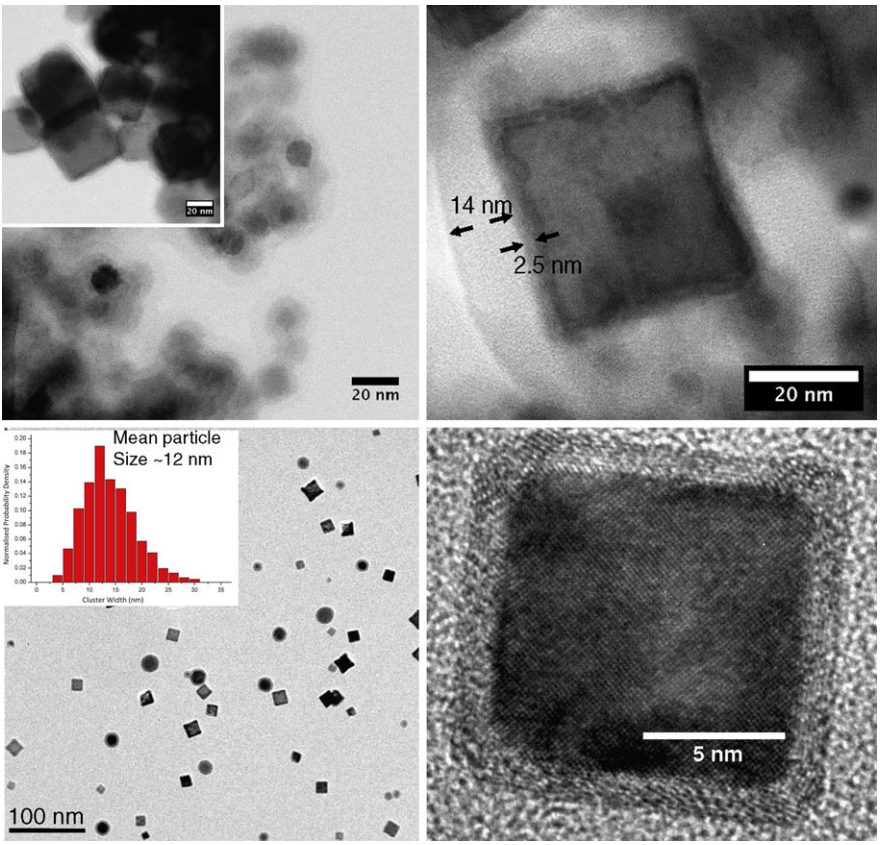

Fig. 8.10 (**a**) and (**b**) Aberration-corrected TEM images of Fe nanoparticles extracted from water with dimercapto-succinic acid and dried on a TEM grid with each showing a pure Fe core, a thin oxide shell and a thicker surfactant shell. (**c**) and (**d**) Aberration-corrected TEM images of Fe nanoparticles deposited in vacuum directly onto TEM grids allowing higher resolution. The same core-shell Fe@Fe oxide structure is observed, and the lattice spacing corresponding to bulk bcc Fe is visible in the core

The nanoparticles could also be coated with a shell of another metal, for example Au, by passing them through a tubular evaporator containing the material required. This could be an important tool to passivate the nanoparticle surfaces preventing oxidation of the core, rendering them biocompatible and encasing them in a material whose surface is easy to attach ligands to. Although suspensions of Fe@Au core-shell nanoparticles have been produced with the system [33], here we report the results of simply depositing the pure Fe nanoparticles straight into the ice matrix. As shown by the high-resolution transmission electron microscope (TEM) images in Fig. 8.10, the result is that the metal cores are coated with a thin oxide shell, which naturally passivates the nanoparticles without further processing.

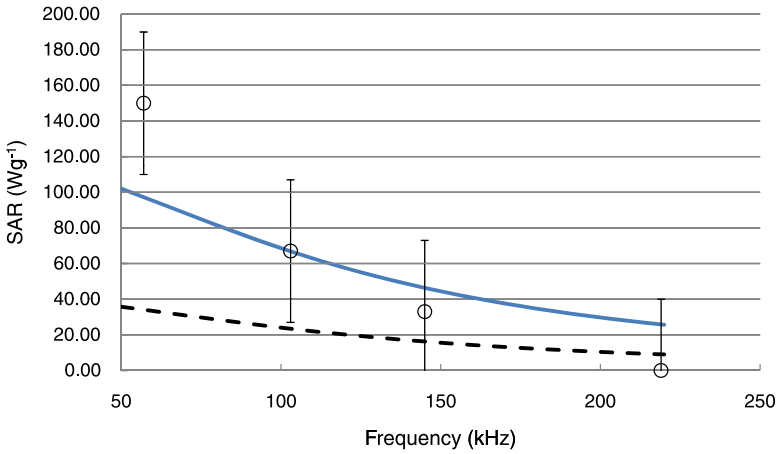

Fig. 8.11 Measured SAR values from 14 nm diameter Fe@Fe oxide core-shell nanoparticles produced by the new method at four discrete frequencies of the applied magnetic field. At each frequency the amplitude of the magnetic field was adjusted so that the product $H \times f$ was at the Atkinson–Brezovich limit (4.85×10^8 A m^{-1} s^{-1}) [17, 18]. The *solid line* shows a calculation using the linear Néel–Brown relaxation model with no adjustable parameters (see text for all the values used). For comparison the *dashed line* shows the same calculation for 14 nm diameter Fe_2O_3 nanoparticles

Figures 8.10(a) and (b) were obtained by producing the hydrosol and then putting a drop onto a TEM grid and letting it dry in air. The images show that the hydrosol comprises agglomerates of spherical and cubic particles with Fe cores around 10 nm, which is similar to the gas-phase mass spectrum. Figure 8.10(b) shows a high-resolution aberration-corrected TEM image of a single Fe nanoparticle indicating the Fe@Fe-oxide core-shell structure with a 2.5 nm thick oxide shell and a 14 nm thick layer of surfactant (dimercapto-succinic acid: $C_4H_6O_4S_2$). For comparison we also took some higher quality images of Fe nanoparticles deposited directly onto TEM grids in UHV and transferred through air into the microscope (Figs. 8.10(c) and 8.10(d)). The lower magnification image (Fig. 8.10(c)) again shows a mixture of cubes and spheres, and the high-resolution image (Fig. 8.10(d)) reveals a similar thin oxide shell to the particles in suspension. In this case further analysis shows that the oxide proceeds via the well-known Cabrera–Mott process [44].

Figure 8.11 shows the SAR measured from our Fe nanoparticles produced using the method described above at four distinct frequencies of the applied field. At all frequencies the amplitude of the magnetic field was adjusted so that the product $H \times f$ remained at the Atkinson–Brezovich limit of 4.85×10^8 A m^{-1} s^{-1} [17, 18]; thus the SAR could be determined with an excitation field that is safe for clinical use. The solid line through the data is calculated using the linear Néel–Brown relaxation model with no adjustable parameters. The median diameter of the nanoparticles (14 nm) and the shell thickness (2.5 nm) was obtained from the TEM images, the saturation magnetization of the core was taken to be that of bulk Fe

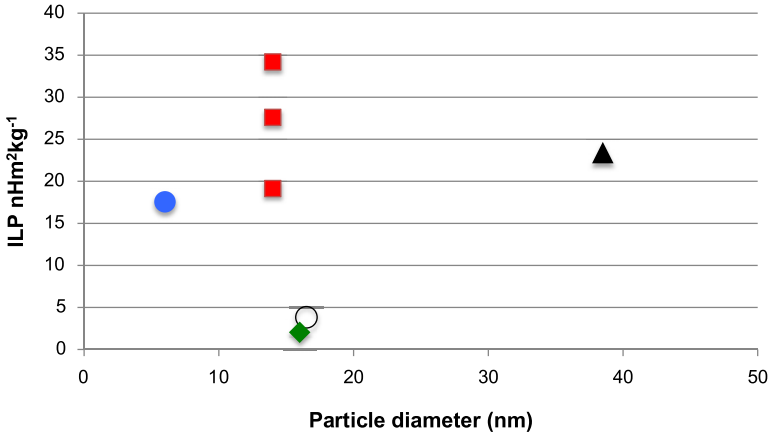

Fig. 8.12 ILP measured for various high-performance ferrofluids containing different sized nanoparticles developed for hyperthermia. *Filled circle*: Co@Co oxide nanoparticles synthesized by Bönnemann et al. [31] and measured by Hergt et al. [30]. Filled triangle: magnetite nanoparticles produced by magnetotactic bacteria measured by Hergt et al. [29]. *Filled diamond*: Fe(0) nanocubes synthesized by Mehdaoui et al. [32]. *Open circle*: Maghemite nanoparticles synthesized by Fortin et al. [44]. *Filled squares*: Fe@Fe oxide nanoparticles produced by the method described here measured at three different frequencies [33]

(1.77×10^6 A m^{-1}) and the anisotropy constant was 2×10^5 J m^{-3} as previously measured from Fe nanoparticles [21]. It was assumed in the calculation that the Fe oxide shell is non-magnetic. For comparison the calculation for 14 nm diameter Fe_2O_3 nanoparticles with no shell is shown by the dashed line.

The calculation agrees with the measurements at intermediate frequencies but underestimates the SAR at low frequency. This may well be due to the fact that the lowest frequency used (57 kHz) corresponded to the highest amplitude of the field (8.5×10^3 A m^{-1}) and the heating mechanism could be entering the non-linear regime, where it has been predicted by Hergt et al. [25] that the SAR exceeds the values predicted by the linear model.

The heating performance of the nanoparticles manufactured in the last few years intended to produce a very high SAR [29–32] are compared to the Fe@Fe-oxide core-shell particles produced by the gas-phase deposition method in Fig. 8.12. There is the usual problem that all reports use different parameters of the excitation field, so we have opted to compare the ILP values for the different materials, which despite the limitations described above does produce a normalization scheme. The value measured for maghemite nanoparticles is represented by the open circle and marks the performance of material currently used for MNH. The Co@CoO nanoparticles (filled circle) synthesized by Bönnemann et al. [31] and measured by Hergt et al. [30] and the magnetite nanoparticles produced by magnetotactic bacteria measured by Hergt et al. [29] show much higher values of ILP. Surprisingly, the Fe(0) nanocubes synthesized by Mehdaoui et al. [32], which appear quite similar to the particles produced in this work, display a low value of ILP. Although

a high value of SAR was reported in [32], this was measured with a excitation field with an $H \times f$ value over 30 times the Atkinson–Brezovich limit, which illustrates the problem in comparing SAR values in different reports. On the other hand, this sample was measured using a higher amplitude field (5.2×10^4 A m^{-1}) than any of the other samples. The $H^2 f$ scaling to obtain the ILP, which may not be a valid parameter in this case, could be artificially depressing the value for this sample.

In any case the highest performance among all the samples is displayed by the Fe@Fe oxide nanoparticles produced by the method described here with an excitation field at the Atkinson–Brezovich limit. The ILP value is shown for the three different frequencies used that showed a measurable SAR, and the fact that it is changing with frequency shows that the heating is not entirely described by the linear relaxation model. This performance is obtained without any optimization such as varying the particle size or trying to control the anisotropy by introducing antiferromagnetic shells, etc., so we are confident that even higher values can be obtained in the future.

8.4 Conclusions

Currently the use of magnetic nanoparticle hyperthermia for the treatment of tumours is restricted by the heating performance of the available nanoparticle ferrofluids. Although there is a massive amount of important biochemical and clinical work that is also required to develop this therapy, the heating issue is fundamental and needs to be solved. We have discussed the chief requirements for improving the SAR of magnetic nanoparticles and have shown that a number of novel synthesis routes developed in the last few years are producing nanoparticles with much higher SAR values than those currently licensed for clinical use, and it appears that there are still significant improvements to be made. We have focused on a new and highly flexible method for synthesizing hydrosols of nanoparticles in which the nanoparticles are manufactured and processed (e.g. coated with shells) in the gas phase in UHV-clean conditions and then deposited into liquids. The method allows the synthesis of any type of nanoparticle, including core-shell structures in which there is free choice of the materials in the core or the shells and independent control over the core size and shell thickness. No other synthesis method allows such flexibility in the design of nanoparticle suspension. and it should be possible to further optimize the SAR. Parallel developments in other synthesis methods mean that there is a range of new high-performance nanoparticles becoming available for MNH. Of course, this is just the start of the process as these must be made biocompatible, hidden from the immune system, targeted, tested in vivo, etc., but it is clear that MNH will be able to make significant strides towards the goal of working as a stand-alone treatment, which is potentially a very low morbidity and generic therapy.

References

1. J.H. Breasted, in *The Edwin Smith Surgical Papyrus*, vol. 1 (University of Chicago, Chicago, 1930)
2. R.W. Rowe-Horwege, Systemic hyperthermia, in *Encyclopedia of Medical Devices and Instrumentation*, 2nd edn., ed. by J.G. Webster (Wiley, New York, 2006), pp. 42–62
3. H.C. Nauts, Bacterial pyrogens: beneficial effects on cancer patients, in *Biomedical Thermology, Progress in Clinical Biological Research*, ed. by M. Gautherie, E. Albert (Alan R. Liss, New York, 1982), pp. 687–696
4. P. Vaupel, F. Kallinowski, Physiological effects of hyperthermia. In: *Hyperthermia and the Therapy of Malignant Tumors*, ed. by C. Streffer (Springer, Berlin, 1987)
5. H. Gerad, D.A. van Echo, M. Whitacre, M. Ashman, M. Helrich, J. Foy, S. Ostrow, P.H. Wiernik, J. Aisner, Doxorubicin, cyclophosphamide, and whole body hyperthermia for treatment of advanced soft tissue sarcoma. Cancer **53**, 2585–2591 (1984)
6. R. Engelhardt, Summary of recent clinical experience in whole-body hyperthermia combined with chemotherapy—recent results. Cancer Res. **107**, 200–224 (1988)
7. H.U. Ahmed, A. Freeman, A. Kirkham, M. Sahu, R. Scott, C. Allen, J. Van der Meulen, M. Emberton, Focal therapy for localized prostate cancer: a phase I/II trial. J. Urol. **185**, 1246–1255 (2011)
8. A.J. Fenn, *Breast Cancer Treatment by Focused Microwave Thermotherapy*, 1st edn. (Jones and Bartlett, Boston, 2006)
9. C. Loo, A. Lin, L. Hirsch, M.-H. Lee, J. Barton, N. Halas, J. West, R. Drezek, Nanoshell-enabled photonics-based imaging and therapy of cancer. Technol. Cancer Res. Treat. **3**, 33–40 (2004)
10. X. Huang, I.H. El-Sayed, W. Qian, M.A. El-Sayed, Cancer cell imaging and photothermal therapy in the near infrared region by using gold nanorods. J. Am. Chem. Soc. **128**, 2115–2120 (2006)
11. N. Wong Shi Kam, M. O'Connell, J.A. Wisdom, H. Dai, Carbon nanotubes as multifunctional biological transporters and near-infrared agents for selective cancer cell destruction. Proc. Natl. Acad. Sci. **102**, 11601 (2005)
12. K. Maier-Hauff, R. Rothe, R. Scholz, U. Gneveckow, P. Wust, B. Thiesen, A. Feussner, A. von Deimling, N. Waldoefner, R. Felix, A. Jordan, Intracranial thermotherapy using magnetic nanoparticles combined with external beam radiotherapy: results of a feasibility study on patients with glioblastoma multiforme. J. Neuro-Oncol. **81**, 53–60 (2007)
13. M. Johannsen, U. Gneveckow, M. Taymoorian, B. Thiesen, N. Waldoefner, R. Scholz, K. Jung, A. Jordan, P. Wust, S. Loening, Morbidity and quality of life during thermotherapy using magnetic nanoparticles in locally recurrent prostate cancer: results of a prospective phase I trial. Int. J. Hyperth. **23**, 315–323 (2007)
14. B. Thiesen, A. Jordan, Clinical applications of magnetic nanoparticles for hyperthermia. Int. J. Hyperth. **24**, 467–474 (2008)
15. K. Maier-Hauff, F. Ulrich, D. Nestler, H. Niehoff, P. Wust, B. Thiesen, H. Orawa, V. Budach, A. Jordan, Efficacy and safety of intratumoral thermotherapy using magnetic iron-oxide nanoparticles combined with external beam radiotherapy on patients with recurrent glioblastoma multiforme. J. Neuro-Oncol. **103**, 317–324 (2011)
16. N.A. Brusentsov, L.V. Nikitin, T.N. Brusentsova, A.A. Kuznetsov, F.S. Bayburtskiy, L.I. Shumakov, N.Y. Jurchenko, Magnetic fluid hyperthermia of the mouse experimental tumor. J. Magn. Magn. Mater. **252**, 378–380 (2002)
17. W.J. Atkinson, I.A. Brezovich, D.P. Chakraborty, Usable frequencies in hyperthermia with thermal seeds. IEEE Trans. Biomed. Eng. **BME-31**, 70 (1984)
18. Q.A. Pankhurst, N.K.T. Thanh, S.K. Jones, J. Dobson, Progress in applications of magnetic nanoparticles in biomedicine. J. Phys. D **42**, 224001 (2009)
19. R.E. Rosensweig, Heating magnetic fluid with alternating magnetic field. J. Magn. Magn. Mater. **252**, 370–374 (2002)

20. D. Fiorani, A.M. Testa, F. Lucari, F. D'Orazio, H. Romero, Magnetic properties of maghemite nanoparticle systems: surface anisotropy and interparticle interaction effects. Physica B **320**, 122–126 (2002)
21. C. Binns, M.J. Maher, Q.A. Pankhurst, D. Kechrakos, K.N. Trohidou, Magnetic behaviour of nanostructured films assembled from preformed Fe clusters embedded in Ag. Phys. Rev. B **66**, 184413 (2002)
22. A. Kleibert, J. Passig, K.-H. Meiwes-Broer, M. Getzlaff, J. Bansmann, Structure and magnetic moments of mass-filtered deposited nanoparticles. J. Appl. Phys. **101**, 114318 (2007)
23. M. Kallumadil, M. Tada, T. Nakagawa, M. Abe, P. Southern, Q.A. Pankhurst, Suitability of commercial colloids for magnetic hyperthermia. J. Magn. Magn. Mater. **321**, 1509–1513 (2009)
24. R. Hergt, S. Meffre, M. Röder, Effects of size distribution on hysteresis losses of magnetic nanoparticles for hyperthermia. J. Phys. Condens. Matter **20**, 385214 (2008)
25. R. Hergt, S. Dutz, M. Zeisberger, Validity limits of the Néel relaxation model of magnetic nanoparticles for hyperthermia. Nanotechnology **21**, 015706 (2010)
26. J.P. Fortin, F. Gazeau, C. Wilhelm, Intracellular heating of living cells through Néel relaxation of magnetic nanoparticles. Eur. Biophys. J. **37**, 223–228 (2008)
27. H. Pennes, Analysis of tissue and arterial blood temperatures in the resting human forearm. J. Appl. Physiol. **1**, 93–122 (1948)
28. M. Kallumadil, M. Tada, T. Nakagawa, M. Abe, P. Southern, Q.A. Pankhurst, Suitability of commercial colloids for magnetic hyperthermia. J. Magn. Magn. Mater. **321**, 1509–1513 (2009). Note: has incorrect correct values of the ILP of the colloids. For correct values see corrigendum by the same authors in J. Magn. Magn. Mater. **321**, 3650–3651 (2009)
29. R. Hergt, R. Hiergeist, M. Zeisberger, D. Schüler, U. Heyen, I. Hilger, W.A. Kaiser, Magnetic properties of bacterial magnetosomes as potential diagnostic and therapeutic tools. J. Magn. Magn. Mater. **293**, 80–86 (2005)
30. R. Hergt, S. Dutz, R. Müller, M. Zeisberger, Magnetic particle hyperthermia: nanoparticle magnetism and materials development for cancer therapy. J. Phys. Condens. Matter **18**, S2919–S2934 (2006)
31. H. Bönnemann, W. Brijoux, R. Brinkmann, N. Matoussevitch, N. Waldöfner, N. Palina, H. Modrow, A size-selective synthesis of air stable colloidal magnetic cobalt nanoparticles. Inorg. Chim. Acta **350**, 617–624 (2003)
32. B. Mehdaoui, A. Meffre, L.-M. Lacroix, J. Carrey, S. Lachaize, M. Gougeon, M. Respaud, B. Chaudret, Large specific absorption rates in the magnetic hyperthermia properties of metallic iron nanocubes. J. Magn. Magn. Mater. **322**, L49–L52 (2010)
33. C. Binns, P. Prieto, S. Baker, P. Howes, R. Dondi, G. Burley, L. Lari, R. Kröger, A. Pratt, S. Aktas, J.K. Mellon, Preparation of hydrosol suspensions of elemental and core-shell nanoparticles by co-deposition with water vapour from the gas-phase in ultra-high vacuum conditions. J. Nanoparticle Res. **14**, 1136 (2012)
34. C. Binns, Nanoclusters deposited on surfaces. Surf. Sci. Rep. **44**, 1–50 (2001)
35. C. Granqvist, L. Kish, W. Marlow (eds.), *Gas Phase Nanoparticle Synthesis* (Springer, Berlin, 2005), ISBN-13: 978-1402024436
36. W. Bouwen, P. Thoen, F. Vanhoutte, S. Bouckaert, F. Despa, H. Weidele, R.E. Silverans, P. Lievens, Production of bimetallic clusters by a dual-target dual-laser vaporization source. Rev. Sci. Instrum. **71**, 54–58 (2000)
37. A. Perez, P. Melinon, V. Dupuis, L. Bardotti, B. Masenelli, F. Tournus, B. Prevel, J. Tuaillon-Combes, E. Bernstein, A. Tamion, N. Blanc, D. Tainoff, O. Boisron, G. Guiraud, M. Broyer, M. Pellarin, N. Del Fatti, F. Vallee, E. Cottancin, J. Lerme, J.-L. Vialle, C. Bonnet, P. Maioli, A. Crut, C. Clavier, J.L. Rousset, F. Morfin, Functional nanostructures from clusters. Int. J. Nanotechnol. **7**, 523–574 (2010)
38. M. Getzlaff, A. Kleibert, R. Methling, J. Bansmann, K.-H. Meiwes-Broer, Mass-filtered ferromagnetic alloy clusters on surfaces. Surf. Sci. **566–568**, 332–336 (2004)
39. S.H. Baker, M. Roy, M. Qureshi, C. Binns, Probing atomic structure in magnetic core/shell nanoparticles using synchrotron radiation. J. Phys. Condens. Matter **22**, 385301 (2010)

40. S.H. Baker, S.C. Thornton, K.W. Edmonds, M.J. Maher, C. Norris, C. Binns, Characterisation of a gas aggregation source for the preparation of size-selected nanoscale transition metal clusters. Rev. Sci. Instrum. **71**, 3178 (2000)
41. G.N. Iles, S.H. Baker, S.C. Thornton, C. Binns, Enhanced capability in a gas aggregation source for magnetic nanoparticles. J. Appl. Phys. **105**, 024306 (2009)
42. A. Kouchi, Vapour pressure of amorphous ice and its astrophysical implications. Nature **330**, 550 (1987)
43. A. Pratt, private communication. Department of Physics, University of York, January 2012
44. J.-P. Fortin, C. Wilhelm, J. Servais, C. Ménager, J.-C. Bacri, F. Gazeau, Size-sorted anionic iron oxide nanomagnets as colloidal mediators for magnetic hyperthermia. J. Am. Chem. Soc. **129**, 2628–2635 (2007)

Index

B. Aktaş, F. Mikailzade (eds.), *Nanostructured Materials for Magnetoelectronics*, Springer Series in Materials Science 175, DOI 10.1007/978-3-642-34958-4,